Atomistic Modelling of Heat and Charge Transport Properties in Nanostructures

Von der Fakultät für Georessourcen und Materialtechnik der
Rheinisch-Westfälischen Technischen Hochschule Aachen

zur Erlangung des akademischen Grades eines

Doktors der Ingenieurwissenschaften

genehmigte Dissertation

vorgelegt von **Master of Engineering**

Yanguang Zhou

aus Hunan, China

Berichter: Prof. Dr.-ing. Ming Hu
Univ. Prof. Dr. rer. nat. Robert Svendsen

Tag der mündlichen Prüfung: 10. Oktober 2017

Diese Dissertation ist auf den Internetseiten der Universitätsbibliothek online verfügbar.

Declaration of Authorship

I, Yanguang ZHOU, declare that this thesis titled, "Atomistic Modelling of Heat and Charge Transport Properties in Nanostructures" and the work presented in it are my own. I confirm that:

- This work was done wholly or mainly while in candidature for a research degree at this University.
- Where any part of this thesis has previously been submitted for a degree or any other qualification at this University or any other institution, this has been clearly stated.
- Where I have consulted the published work of others, this is always clearly attributed.
- Where I have quoted from the work of others, the source is always given. With the exception of such quotations, this thesis is entirely my own work.
- I have acknowledged all main sources of help.
- Where the thesis is based on work done by myself jointly with others, I have made clear exactly what was done by others and what I have contributed myself.

Signed:

Date:

"Everyting negative - pressure, challenges - is all an opportunity for me to rise."

Kobe Bryant

Abstract

This thesis focus on the effect of nanostructuring, i.e., nanowires, grain disorder, grain size, interface and twin boundary, on thermal and electric transport properties.

Firstly, we start from the development of algorithm in the frame of non-equilibrium molecular dynamics (NEMD) which is the mimic of the method applied to measure thermal conductivity in experiments. That means, the models in NEMD are actually nanostructures. Two new algorithms named time domain direct decomposed method (TDDDM) and frequency domain direct decomposed method (FDDDM) in the frame of NEMD are proposed successfully to extract the modal (frequency) thermal conductivity. Then, we extend the FDDDM to the interface problem. By using the FDDDM, we can fully consider the harmonic and anharmonic scattering channel at interface. Four different scattering modes at interface can be characterized by FDDDM as well.

Then, we care about the thermal management through nanostructuring. Surface orientation, interface structures and diameter are used as factors to control the thermal conductivity of the nanostructures. Our results show that the thermal conductivity of Si NWs with different surface orientation can differ by as large as 2.7 $\sim$ 4.2 times, which suggests a new route to boost the thermoelectric performance. Meanwhile, the thermal conductance is found to be enhanced by around 6 times via interface designing (mass graded interface). More interesting, the thermal conductivity of Si NWs with various diameters is studied. We report that the thermal conductivity (κ) of Si nanowires (NWs) does not diverge, but converges and increases steeply when NW diameter (D) becomes extremely small ($d\kappa/dD < 0$), a long debate of one-dimensional heat conduction in history. As a consequence, the thermal conductivity for Si NWs can be modulated in a quite large range by diameter.

Finally, we studied how the thermoelectric performance is affected by nanostructuring. The grain boundary, twin boundary, anti-twin boundary and interfaces are chosen as elements to modulate the thermoelectric performance. Firstly, we found a strategy to decrease the thermal conductivity of Si NWs to a record value by polycrystallization, which means the figure of merit can be enhanced largely. Then, based on the results of first step, we designed a structure named superlattice nanocrystal heterostructures (SL-NC HSs) in which the thermal conductivity is found to be reduced by two orders of magnitude and reaches a value far below the amorphous limit of Si. Meanwhile, the power factor of such structures is found to be comparable to that of the bulk Si. As a consequence, the ZT of SL-NC HSs can reach 0.5 at room temperature. At last, we proposed a new strategy of incorporating nanotwinned structures to decouple the electronic and phononic transport. Combining the new concept of nanotwin with the previously widely used nanocrystalline approach, the power factor of the Si nanotwin-nanocrystalline heterostructures is enhanced by 120% compared to bulk crystalline Si, while the lattice thermal conductivity is reduced to a level well below the amorphous limit, yielding a theoretical

limit of 0.52 and 0.9 for ZT coefficient at room temperature and 1100 K, respectively.

Zusammenfassung

Diese Dissertation kümmert sich um dem Einfluss von Nanostrukturisation, d.h., Nanodraht, Kornstörung, Korngröße, Grenzfläche und Zwillingsgrenze, auf thermische und elektrische Transporteingenschaften.

Zuerst, fangen wir ab die Entwicklung von Algorithmen im Rahmen der Nichtgleichgewicht molekulare Dynamik (NEMD), eine der berühmteste in Untersuchung der Wärmeleitfähigkeit angewandte Methoden, die die Wärmeleitungsmessungen in Experiment imitiert. Zwei neue Algorithmen, nämlich Zeitbereich direkt zersetzte Methode (Auf Englisch: Time Domain Direct Decomposed Method TDDDM) und Frequenzbereich direkt zersetzte Methode (Auf Englisch: Frequency Domain Direct Decomposed Method FDDDM) sind in Rahmen von NEMD erfolgreich vorgeschlagen, die modale Wärmeleitfähigkeit herauszunehmen. Danach erweitern wir die FDDDM, die Grenzfläche Problem zu lösen Durch Anwendung von FDDDM können wir vollständig die harmonische und anharmonische Streukanäle an Grenzfläche zu erachten. Vier verschiedene Streumodi am Grenzfläche könnten auch durch FDDDM charakterisiert wird.

Danach kümmern wir uns um das thermische Management durch Nanostrukturisation. Oberflächenorientierung, Grenzflächenstrukturen, und Durchmesser sind als Faktoren zur Kontrolle der Wärmeleitfähigkeit von Nanostrukturen. Unsere Ergebnisse zeigen, dass die Wärmeleitfähigkeit von Silizium Nanodraht (Si NWs) mit verschiedene Oberflächenorientierungen bis 2.7 $\sim$ 4.2 fach größer sein können, was eine neue Route zur Verbesserung der Wärmeleitfähigkeitsperformanz vorschlägt. Mittlerweile ist die wärmeleitung auf 6 fach durch Grenzflächendesign verbessert. Interessanter ist die von Si NWs mit verschiedenen Durchmesser untersucht. Wir melden, dass die wärmeleitfähigkeit κ von Si NWs steigt doch divergiert nicht, als der Durchmesser der NW sehr Schmal wird $(d\kappa/dD < 0)$, was eine lange Debatte der eindimensionale Wärmeleitung in Geschichte. Als Konsequenz kann die wärmeleitfähigkeit von Si NWs in einem sehr großen Bereich durch Durchmesser moduliert werden.

Schließlich haben wir untersucht, wie die thermoelektrische Performanz durch Nanostrukturisation beeinflusst ist. Die Korngrenze, Zwillingsgrenze, Anti Zwillingsgrenze, und Flächengrenze sind als Modulierungselemente für Thermoelektrische Performanz ausgesucht. Zuerst haben wir eine Strategie zum Absteigen der wärmeleitfähigkeit von Si NWs auf Rekordwert durch Polycristalisation gefunden, was bedeutet, dass die Figur der Merit ZT weitgehend verbessert werden kann. Dann haben wir auf Basis der Ergebnisse des ersten Schrittes eine Struktur namens Supergitter Nanokristall Heterostrukturen (Auf englisch: superlattice nanocrystal heterostructures SL-NC HSs) entworfen, bei der die Wärmeleitfähigkeit um zwei größenordnungen reduziert wird und einen Wert weit unterhalb der amorphen Grenze von Si erreicht. Mittlerweile ist der Leistungsfaktor solcher Strukturen mit dem

des Bulk-Si vergleichbar. Infolgedessen kann der ZT von SL-NC HSs bei Raumtemperatur 0,5 erreichen. Schließlich haben wir eine neue Strategie vorgeschlagen, nanotwinned Strukturen zu integrieren, um den elektronischen und phononischen Transport zu entkoppeln. Durch die Kombination des neuen Konzepts von Nanotwin mit dem bisher weit verbreiteten nanokristallinen Ansatz wird der Leistungsfaktor der Si-Nanotwin-nanokristallinen Heterostrukturen um 120 % gegenüber dem kristallinen Si verstärkt, während die Gitterwärmeleitfähigkeit auf ein Niveau unterhalb der amorphen Grenze reduziert wird, was eine theoretische Grenze von 0,52 und 0,9 für den ZT-Koeffizienten bei Raumtemperatur bzw. 1100 K ergibt.

Acknowledgements

First and most, I am deeply grateful to my supervisor Prof. Ming Hu for his professional tutoring, fruitful discussions and continuous encouragement during the past three years. I appreciate a lot the anytime wechat discussions, through which I can always get new ideas and get more closed to the spirit of heat and charge transfer. I am full of gratitude to Ming for sending me to numerous conferences during my Ph.D., from which I learn a lot.

Millions of gratitudes should be sent to my former group member Dr. Xiaoliang Zhang for introducing me to the filed of nano-heat transfer. He is always very patient to answer my questions. Great thanks also go to Prof. Davide Donadio at University of Carlifornia, Davis (UCSD), from whom I acquired the Alen-Feldman theory. Prof. Ben Xu at Tsinghua University and Prof. Xiaojing Gong at Chinese Acadmy Sciences, Dr. Xiaoliang Zhang, Dr. Yang Han, Prof. Yufei Gao and Dr. Jiayue Yang at RWTH-Aachen University are greatly acknowledged for the collaborations and their useful discussions. Many thanks should also be sent to my former group member Huake Liu and the present group member Guangzhao Qin for teaching me the density functional theory.

Many thanks for the help from my colleagues and friends: Dr. Zheyong Fan at Aalto University, Dr. Shiyun Xiong at Soochow University, Mr. Lin Zhang at Utah State University, Prof. Tao Ouyang, Prof. Benhu Zhou, Prof. Chengxiao Peng, Mr. Shengying Yue, Ms. Biyao Wu, Ms. Huimin Wang, Mr. Lichuan Zhang, Dr. Long Cheng, Mr. Loay. El. Alfy. Mr. Farzad Shirazian... There are lots of happy memories with you and I will always treasure our friendship. I also thank my office fellows Dr. Niklas Mevenkamp, Mr. Miguel de la Varga, Mr. Rex Bedzra, Dr. Malte Döntgen, Ms. Rosalia Tatano, Mr. Rohite Atre, Mr. Raheel Rasool and Dr. Eduard Bader for their help on daily trivialities which makes me feel here like a home.

The Aachen Institute for Advanced Study in Computational Engineering Science (AICES) is acknowledged for the financial support.

Last but not least, I would like to thank my wife, Weiwei Yang, for her selfless and endless supporting and help. She is always with me whenever I have difficulties. This thesis would not come to be possible without her love and encouragement. I also acknowledge the continuous support from my parents. Their understand and love make me progress consecutively.

Contents

Declaration of Authorship ii

Abstract iv

Zusammenfassung vi

Acknowledgements viii

1 Introduction 1
- 1.1 Motivation . . . 1
- 1.2 State-of-art of Thermoelectrics via Nanostructuring . . . 3
  - 1.2.1 Reducing the thermal conductivity . . . 4
  - 1.2.2 Bulk comparative power factor . . . 5
- 1.3 Structure of Thesis . . . 6

2 Theoretical Background 8
- 2.1 Molecular Dynamics . . . 8
  - 2.1.1 Green-Kubo equilibrium molecular dynamics . . . 9
  - 2.1.2 Non-equilibrium molecular dynamics . . . 10
  - 2.1.3 Limitations of molecular dynamics . . . 12
- 2.2 Lattice Dynamics . . . 13
- 2.3 Density Functional Theory . . . 17
- 2.4 Boltzmann Transport Equation . . . 21
  - 2.4.1 Heat transport by phonons . . . 21
  - 2.4.2 Charge transport by carriers . . . 24
- 2.5 Conclusion . . . 26

3 New Algorithm Development Based on NEMD 28
- 3.1 Introduction . . . 28
- 3.2 Time Domain Direct Decomposition Method . . . 29
  - 3.2.1 Framework of time domain direct decomposition method . . . 29
  - 3.2.2 Validation of time domain direct decomposition method . . . 33
  - 3.2.3 Applications of time domain direct decomposition method . . . 36
- 3.3 Frequency Domain Direct Decomposed Method . . . 39
  - 3.3.1 Framework of frequency domain direct decomposed method . 39
  - 3.3.2 Validation of frequency domain direct decomposed method . . 43
  - 3.3.3 Applications of frequency domain direct decomposed method . 44

3.4 Extension based on Frequency Domain Direct Decomposed Method . 50
3.4.1 Framework of the methodology 50
3.4.2 Validation and application of the methodology 58
3.4.3 Inherent inclusion of anharmonicity in the methodology 63
3.5 Conclusion 66

4 Modulating Thermal Transport via Nanostructuring 68
4.1 Adjusting Thermal Conductivity in Nanowires via Surface Orientation 68
4.1.1 Theory and computational methods 69
4.1.2 Simulation and theory results 72
4.1.3 Phonon transport mechanism 77
4.2 Reducing Interfacial Thermal Resistance: Mass Gradient Interface . . . 79
4.2.1 Structure and simulation details 79
4.2.2 Results and discussions 81
4.3 Thermal Transport in Ultra-thin NWs 90
4.3.1 Simulation and model details 90
4.3.2 Results and discussions 92
4.4 Conclusion 100

5 Enhancing Thermoelectric Performance via Nanostruturing 103
5.1 Introduction 103
5.2 Significantly Decreasing Thermal Conductivity via Poly-crystallization 103
5.2.1 Simulation details and model generation 104
5.2.2 Record low thermal conductivity 106
5.2.3 Underlying mechanism for low thermal conductivity 110
5.3 Improving the Thermoelectric Performance via Decreasing the Thermal Conductivity 119
5.3.1 Computational details and theory framework 120
5.3.2 Results and discussions 125
5.4 Enhancing the Thermoelectric Performance by Decoupling the Heat and Charge Transport 132
5.4.1 Computational details 132
5.4.2 Results and discussions 134
5.5 Conclusion 141

6 Conclusions and Future Works 145
6.1 Conclusions 145
6.2 Future works 150

A The Static and Thermodynamic Stability Criteria 152

B Effective Mean Free Path in the Callaway Model 154

C Inherent Relaxation Time of Carriers 157

D The Power Factor of the Bulk Superlattice Nanocrystalline Heterostructures **158**

E The Calculation of Lorenz Number **159**

F Curriculum Vitae **160**

Bibliography **163**

List of Figures

1.1 The schematic of the thermoelectric module for both cooling and power generation. Figure from G. J. Snyder and E. S. Toberer. (Snyder and Toberer, 2008a) 2
1.2 The Carnot efficiency of the thermoelectric devices with various temperature difference at room temperature (b) and 600 K (c) 3

3.1 (Color online) Schematic of simulation cell used in TDDDM (NEMD) simulation. $\vec{Q}$ represents the heat current in the system. LS, LC and LR is the total length of the system, the length of the control volume, and the length of thermostats, respectively. 32
3.2 (Color online) Heat current contributions of three typical individual phonon modes of LJ Argon, normalized by total predicted heat current. (Inset) Time development of total predicted heat current of the system. The dashed lines are guide for the eyes. 33
3.3 (Color online) Mode dependent thermal conductivity contribution (left) and accumulative thermal conductivity as a function of mode frequency (right) for the case of LJ Argon calculated using SED, TDNMA, and TDDDM methods. The mode dependent thermal conductivity and accumulative thermal conductivity is normalized by the overall thermal conductivity predicted by each respective method. The dashed lines are guide for the eyes. 34
3.4 (Color online) The same as Figure 3.3 for the case of SW Si. The dashed lines are guide for the eyes. 36
3.5 (Color online) Comparison of the accumulative thermal conductivity as a function of frequency for the case of LJ Argon (left) and SW Si (right) with different total length in TDDDM. The results of SED and TDNMA are also shown for comparison with sample size of 4.2 $\times$ 4.2 $\times$ 4.2 nm^3 (LJ Argon) and 2.2 $\times$ 2.2 $\times$ 2.2 nm^3 (SW Si). 37
3.6 (Color online) Time development of heat current contributed by the Gamma point for the case of LJ Argon predicted by the TDDDM. Dashed lines denote zero heat current and are guide for the eyes. . . . 38

3.7 (Color online) Accumulative thermal conductivity as a function of mode frequency for the case of (left) LJ Argon and (right) SW Si calculated using TDNMA and FDDDM methods. The accumulative thermal conductivity is normalized by the overall thermal conductivity predicted by the respective method. (Inset) The actual accumulative thermal conductivity vs. frequency. 43
3.8 (Color online) (Left) Normalized spectral contribution to thermal conductivity and (right) corresponding normalized accumulative thermal conductivity as a function of mode frequency for the case of SW Si with different system size computed using FDDDM. The dashed lines and the arrow are guide for the eyes. (Inset) Actual thermal conductivity of SW Si vs. system length. 46
3.9 (Color online) (Left) Spectral contribution to thermal conductivity and (right) corresponding accumulative thermal conductivity as a function of mode frequency for the cases of LJ Argon with different system temperature. The arrows are guide for the eyes. 47
3.10 (Color online) Same figure as Figure 3.9 for the case of SW Si. The dashed line is guide for the eyes. 48
3.11 (Color online) (Left) Normalized spectral contribution to thermal conductivity and (right) corresponding normalized accumulative thermal conductivity as a function of mode frequency for amorphous Si computed using FDDDM and AF theory. The dashed lines are guide for the eyes. (Left inset) Comparison of VDOS between amorphous Si and crystalline Si. (Right inset) The actual accumulative thermal conductivity of c-Si and a-Si vs. frequency. 49
3.12 (Color online) Schematic of four different types of three-phonon scattering process at the interface (a-d). The situation in bulk materials (e). The blue dashed line represents the interface separating two different materials (a-d) or an imaginary interface in a bulk material (e). 57
3.13 (Color online) (a) Spectral contribution to overall heat flux of bulk Ar calculated using two-phonon process (double-dashed line), two- and three-phonon process (dashed line) and FDDDM (solid line). (b) Accumulative heat flux as a function of frequency computed using two- and three-phonon process and FDDDM. Here, the two- and three-phonon processes are only valid for the imaginary interface. 59
3.14 (Color online) (a) Spectral thermal conductance of Ar-heavy Ar interface contributed only by the two-phonon process at different temperatures. (b) The corresponding spectral thermal conductance contributed by the two- and three-phonon process. (c) The comparison of accumulative thermal conductance contributed by only two-phonon process (dashed line), two- and three-phonon process (solid line). . . . 60

3.15 (Color online) (a) The vibrational density of states (VDOS) of Ar, heavy Ar and interface (defined as the structure within the cut-off distance away from the interface). (b) Same figure as (a) for the case of Si-Ge interface. 61
3.16 (Color online) The spectral thermal conductance of different types of three-phonon process (left panel) for Ar-heavy Ar interface. The accumulative thermal conductance contributed by the individual three-phonon process (right panel). 62
3.17 (Color online) Same figure as Figure 3.14 for the case of Si-Ge interface. 63
3.18 (Color online) The spectral thermal conductance of different types of three-phonon process for Si-Ge interface (left panel). Comparison of thermal conductance contributed by individual three-phonon process (right panel). The different type of phonon process is defined in Figure 3.12. 64

4.1 (a) Schematic of NEMD simulation domain. The heat source, heat sink, and the control volume used for our FDDDM analysis are highlighted by the rectangular box. The heat flux is along the $\langle 100 \rangle$ direction. (b) The cross-sectional view of two typical Si nanowires with (100) and (110) surface orientation. The atoms are colored by their atomic potential energy. 68
4.2 Thermal conductivity of Si nanowires with different surface orientations. The highest and lowest thermal conductivity is colored in black and blue, respectively. 72
4.3 Thermal conductivity of Si nanowires as a function of RMS height of roughness for the cases of (100) and (110) surface orientation. (Inset) The dashed region is zoomed in. 73
4.4 Length dependence of thermal conductivity of Si nanowires with two typical (100) and (110) surface orientations. Three different temperatures of 200 K, 500 K, and 800 K are considered. 75
4.5 Thermal conductivity of Si nanowires with different cross-section vs. average surface atom energy. The symbols and solid lines are NEMD simulation results and theoretical predictions, respectively. 76
4.6 Vibrational density of states (VDOS) of surface and core atoms in Si nanowires with two typical (100) and (110) surface orientations. (Inset) Comparison of VDOS between the surface and core atoms. 77
4.7 Vibrational density of states (VDOS) of surface and core atoms in Si nanowires with two typical (100) and (110) surface orientations. (Inset) Comparison of VDOS between the surface and core atoms. 78

4.8 (a) Side view of three interface structures studied in this work. From left to right: perfectly abrupt interface, rough interface, mass graded interface. (b) Steady state temperature profile for the three kinds of interface structures shown in (a) calculated by nonequilibrium molecular dynamics simulation with average system temperature $T = 10\ K$. 80
4.9 The overall interfacial thermal resistance across the entire interface region calculated by the Fourier's law. The black (red) symbols represent the results of mass graded (rough) interface with various thickness (volume fraction). The arrow indicates the direction of thickness increasing. The green line is the interfacial thermal resistance of the perfectly abrupt interface. The blue line is a fitting line. (Inset) The ITR of mass graded interface goes beyond that for the perfectly abrupt interface, when the mass graded interface is thick enough (at least 300 nm). For the rough interface, the different symbols represent different thickness of the interface layer. For the mass graded interface, the different symbols mean different number of atom mass added in the mass graded layer. 82
4.10 Frequency dependent interfacial thermal conductance (FDITC) for (a) perfectly abrupt interface, (b) rough interface, and (c) mass graded interface. The first and last panel in (a) to (c) represent the FDITC in the middle of the left and right leads, respectively. The second to fifth panel is the FDITC at the positions indicated by the black lines in the corresponding structure models. The temperature at the interface is used to obtain the FDITC results. 85
4.11 (Top) Phonon energy evolvement as a function of time by wave packet simulation and (Bottom) snapshots of displacements for a longitudinal acoustic wave packet with frequency of 0.23 THz at some typical timesteps indicated by the Roman numerals for (a) perfectly abrupt interface, (b) rough interface, and (c) mass graded interface. Color coding: black, Argon; red, heavy Argon; blue, interface. The brown vertical lines in the bottom panel indicate the position of interfaces. . . 87
4.12 Phonon frequency dependent transmission coefficients for perfectly abrupt interface (black symbols), mass graded interface (red symbols) and rough interface (blue symbols) with interface thickness of (left) 8 unit cells and (right) 32 unit cells. The black and red dashed line denotes the transmission coefficient at long-wavelength limit using acoustic mismatch model for perfectly abrupt interface and mass graded interface, respectively. The filled and open symbols denote the longitude acoustic (LA) and transverse acoustic (TA) branch, respectively. (Inset) Phonon dispersion curves of regular Ar (black lines) and heavy Ar (red lines). 88

4.13 (a-c) Thermal conductivity of ultra-thin Si NWs with different diameter calculated using Tersoff potential. For comparison thermal conductivity of bulk Si with Tersoff potential (d) and thermal conductivity of the thinnest possible Si NWs using EDIP (e) and SW (f) potential are also shown. The dashed lines denote the finally converged value. . 92
4.14 Diameter dependent thermal conductivity of Si NWs calculated by GK-EMD with different interatomic potentials: (a) Tersoff, (b) EDIP and (c) SW. The dashed lines denote the thermal conductivity of bulk Si. The spline lines are guide for the eyes. Different shading color represents different heat conduction regime. 94
4.15 (Top panels) Three-phonon scattering rates for Si NWs with diameter of (a1) 1 nm, (a2) 1.5 nm and (a3) bulk Si. The blue circle is a guide for eyes. (Middle panels) The corresponding effective mean free path calculated by the single mode relaxation time approximation (SMRTA) and the Callaway model. (Bottom panels) Comparison of the corresponding modal thermal conductivity calculated by SMRTA, Callaway model and iterative Boltzmann transport equation (BTE) method. 95
4.16 Accumulative thermal conductivity calculated using the Callaway model, the relaxation time approximation (RTA) and the iterative BTE method for Si NWs with diameter of (a) 0.96 nm and (b) 1.50 nm and (c) bulk Si. The dashed lines indicate the contribution of the low frequency phonon modes ($<$ 2 THz) to the total thermal conductivity. 98
4.17 Phonon dispersion curves of the ultra-thin Si NWs with diameter of (a) 1 nm, (b) 1.5 nm and (c) 2.0 nm. For brevity only the dispersion curves below 3 THz are presented. The blue and red dots in the dispersion curves are schematic of low frequency modes for phonon scattering. The red horizontal lines are the guide for the eyes. 99
4.18 The modal phase space of ultra-thin Si NWs with diameter of (a) 1 nm, (b) 1.5 nm and (c) 2.0 nm. The different colors represent different phonon process (N/U, absorbing, emission, etc.). 99

5.1 Snapshot of (a) perfect Si NW, (b) amorphous Si NW and (c) polycrystalline Si NW used in our NEMD simulations. (Left panel) Overview and (middle panel) cross-sectional view of the structures. (Right panel) Zoom-in picture of the atomic structures. Atoms are colored using coordinate number analysis (blue and yellow atoms denote the disordered structure and the original perfect diamond structure, respectively). The red circles indicate the discontinuity (defects) between nanograins. 105

5.2 (a) The thermal conductivity of bulk Si, perfect Si NWs, amorphous Si NWs and polycrystalline NWs. The perfect crystalline Si NW and amorphous Si NW use the left-upper axes and the polycrystalline Si NW uses the left-bottom axes. The length of the polycrystalline Si NWs is 45 nm. (b) Comparison of thermal conductivity between bulk Si, perfect Si NWs, polycrystalline Si NWs and amorphous Si NWs. The thermal conductivity is normalized by the value of thermal conductivity of amorphous Si NWs (2.4 W/mK). All the NWs have the same cross-sectional size of 5.442 $\times$5.442 nm^2. 108
5.3 Length (a) and cross-sectional width (b) dependence of thermal conductivity of polycrystalline Si NWs. All the results are for the average grain size of 3.07 nm. The length used for the cross-sectional width dependence calculation is 45 nm. 111
5.4 Comparison of the participation ratio among (a) bulk Si, (b) perfect Si NW, (c) amorphous Si NW and (d) polycrystalline Si NW. The cross-sectional size of all NWs is 5.442$\times$5.442 nm^2 and the average grain size of the polycrystalline NW is 3.07 nm. 112
5.5 Comparison of the effective mean free path among (a) bulk Si, (b) perfect Si NW, (c) amorphous Si NW and (d) polycrystalline Si NW. The cross-sectional size of all NWs is 5.442 $\times$ 5.442 nm^2 and the average grain size of the polycrystalline NW is 3.07 nm. 113
5.6 The thermal conductivity as a function of effective mean free path for bulk Si, perfect Si NW, amorphous Si NW and polycrystalline Si NW. The dashed line indicates the contribution from the vibrations with effective mean free path smaller than AVD (0.22 nm), below which we regard the vibration as diffusons. The cross-sectional size of the perfect crystalline NW, amorphous NW and polycrystalline NW is 5.442 $\times$ 5.442 nm^2 and the average grain size of the polycrystalline NW is 3.07 nm. (Inset) Comparison of the relative contribution to the total thermal conductivity of propagons and diffusions. 117
5.7 Snapshot of (a) polycrystalline Si and (b) SiGe superlattice or SiGe anti-superlattice nanostructures. The schematic of SiGe superlattice (c) and SiGe anti-superlattice (d), where Si and Ge atoms are shown in different color. 122
5.8 (a) Seebeck coefficient, (b) electric conductivity, (c) electronic contribution to the thermal conductivity, and (d) the power factor, as a function of the carrier density at room temperature. 126
5.9 (a) Electric conductivity, (b) electronic contribution to the thermal conductivity, and (c) the power factor at room temperature, as a function of the grain size with a fixed carrier density of $6 \times 10^{19} cm^{-3}$ and a fixed layer thickness of around 3 nm. 127

5.10 The lattice thermal conductivity calculated by MD simulations and predicted by theory based on phonon BTE. 128
5.11 The lattice thermal conductivity from MD simulations and theoretical predictions as a function of membrane thickness. The square and diamond symbols represent the thermal conductivity of nanocrystalline structures with grain size of 3.8 and 5.5 nm, respectively. The black, red and blue color represent the results for the traditional nanocrystalline Si, SiGe superlattice nanocrystalline and SiGe anti-superlattice nanocrystalline, respectively. 129
5.12 The phonon mean free path vs. grain size and layer thickness for polycrystalline Si (a), SiGe superlattice nanocrystalline (b) and SiGe superlattice nanocrystalline (c). The solid lines use the black bottom-left axes and the dashed lines use the red up-left axes. 130
5.13 The figure of merit as a function of grain size (a) and layer thickness (b).131
5.14 The lattice thermal conductivity (left axis) and figure of merit (right axis) of the bulk polycrystalline Si, bulk SiGe superlattice nanocrystallines and bulk SiGe anti-superlattice nanocrystallines. 132
5.15 (a) The schematic of a representative nanostructure with Si nanotwinned structure. (b) The representative Si nanotwinned structure (periodic length of 1.9 nm). The atoms on the twin boundary that are stacking in the hexagonal crystal structure and the bulk atoms with the diamond crystal structure are highlighted in red and yellow, respectively. (c) The corresponding electrical charge density. (d) Change of electrical density distribution by displacing the twin boundary atoms (purple arrow). 133
5.16 The electrical transport properties of the nanotwinned structure along three directions: (a) Seebeck coefficient, (b) electrical conductivity, (c) electronic thermal conductivity and Lorenz number, (d) power factor. The X, Y, and Z direction are <111>, <110> and <112>, respectively. . . 135
5.17 Band structures of the Si nanotwinned structure with various periodic length: (a) 3.8 nm, (b) 7.6 nm, (c) 11.4 nm, and (d) 15.2 nm. The horizontal lines denote the energy level of 5 kbT. (e) The results for bulk crystalline Si. 136
5.18 (a) The lattice thermal conductivity of bulk Si and Si nanotwin with various periodic lengths. (b) The mean free path of phonons for the bulk Si and Si-TB-1. (c) The corresponding phonon dispersion as discussed in (b), the high symmetry points can be found in Figure. 5.17. 138

5.19 (a, b, c, d): the atomic structures of the Si nanotwinned membranes with different periodic lengths (a, 1.9 nm; b, 3.8 nm; c, 5.7 nm; d, 7.6 nm). Electrical transport properties of the Si nanomembranes with nanotwins inside the grains: (a) Seebeck coefficient, (b) electrical conductivity, (c) electronic thermal conductivity, and (d) power factor. . . 139
5.20 Grain size (a) and thickness (b) dependent lattice thermal conductivity of the Si nanomembranes incorporated with nanotwins. The symbols are results calculated by Green-Kubo equilibrium molecular dynamics simulation and the solid lines are theoretical results. (c) The phonon mean free path vs. grain size (using the black bottom-left axes) and thickness (using the red top-right axes). The dashed and solid lines are for layer thickness and grain size dependence, respectively. The arrows denote the increase direction of layer thickness and grain size. 140
5.21 (a) The figure of merit (ZT) of the Si-TB NMs vs. grain size (using the black axes) and layer thickness (using the red axes) at room temperature. (b) Power factor for the Si nanotwin-nanocrystalline heterostructures with different periodic lengths and nanocrystalline Si (NT-NC HSs or NC). The black horizontal line denotes the power factor for bulk crystalline Si. (c) Lattice thermal conductivity (the black axis) and figure of merit (the red axis) of the Si NT-NC HSs (solid lines) and nanocrystalline Si (long dashed lines) vs. grain size. The square symbols are the ZT coefficient for the Si-based nanostructures reported in literature with reference number labeled. The red short dashed line represents the maximum ZT (0.52) achieved in our proposed Si NT-NC HSs (theoretical limit). The blue short dashed line represents the ZT (0.26) that can be achieved in the experimentally existing Si NT-NC HSs (grain size of 5 nm). 141
5.22 The power factor (a), electrical thermal conductivity (b) and figure-of-merit (d) of the Si nanotwin-nanocrystalline heterostructures with fixed grain size of 5 nm. (c) The lattice thermal conductivity. The optimal figure-of-merit (e) and the carrier density for the corresponding grain size (f). 142

A.1 Phonon dispersion for the smallest possible Si NWs computed by Tersoff (a, b), EDIP (c, d) and SW (e, f) potential. 152
A.2 The temperature and energy of the thinnest possible (left side of the red dot-dashed line) and the largest unstable (right side of the red dot-dashed line) Si NWs using Tersoff, SW and EDIP. 153

C.1 Inherent relaxation time of electrons in bulk Si measured by experiments. 157

D.1 The power factor of the bulk nanostructures with superlattice and anti-superlattice inside the grains. 158

List of Tables

5.1 Comparison of thermal conductivity of amorphous Si NW (length of 100 unit cells) and polycrystalline Si NW (grain size of 1.26 nm) by NEMD simulations with different interatomic potentials. 110
5.2 The effective band mass at conduction band minima [Γ point for nanotwinned Si with different periodic length (Si-TB-1/2/3/4) and A point for bulk crystalline Si] 137

To my daughter...

To my wife...

To my parents...

Chapter 1

Introduction

1.1 Motivation

With the rapid development of global economy, the expense of the energy has increased progressively, which makes the energy crisis become a global issue (Snyder and Toberer, 2008a). The large energy demand of the world will exhaust the existing fossil fuels such as coal, oil and nature gas in nearly 100 years (Haile, 2014). Improving the use efficiency of energy, finding sustainable energy and recovering waste energy promises the available energy for the future. At the same time, it is well known a large amount of heat is wasted in factories, home cooking and vehicle drive due to the low efficiency of the energy conversion. Rather than just wasting this energy, it is possible to convert it to some other kinds of energy such as electric power which is quite useful for our life via the energy converters which are called thermoelectric (TE) devices [Figure 1.1].

On the other hand, massive carbon dioxide which is the main reason for the greenhouse effect, and also the carbon monoxide and dust particle such as PM 2.5 which are very harmful to the individual's health are produced during the consumption process of fossil fuels. Therefore, there is no doubt that the expansion of economic and clean energy sources (sustainable energy), such as nuclear, biomass and unconventional oil, is impending. However, developing sustainable energy of modern society is still on the baby stage (Chu and Majumdar, 2012). Meanwhile, no matter for the high-temperature materials to improve combustion efficiency, nanostructures to reach high power density batteries, or metastructures to gain light harvesting, revolutionary development in materials research will lead to the breakthrough in energy conversion and efficiency.

TE materials, which can convert the waste heat to electricity or be used as solid-state coolers, could play an important role in proving solution to global sustainable energy problem. It is easy to find the TE generators are superior to the traditional heat engine in the aspects of environment friendly, reliable and scalable and transferability since they are solid-state devices with no moving parts (Chu and Majumdar, 2012). In the early 1800s, the German physicist Thomas Johann Seebeck firstly found that a voltage can be generated when the temperature gradient is applied on the electric conductor, which is known as Seebeck effect now. Almost at the same time,

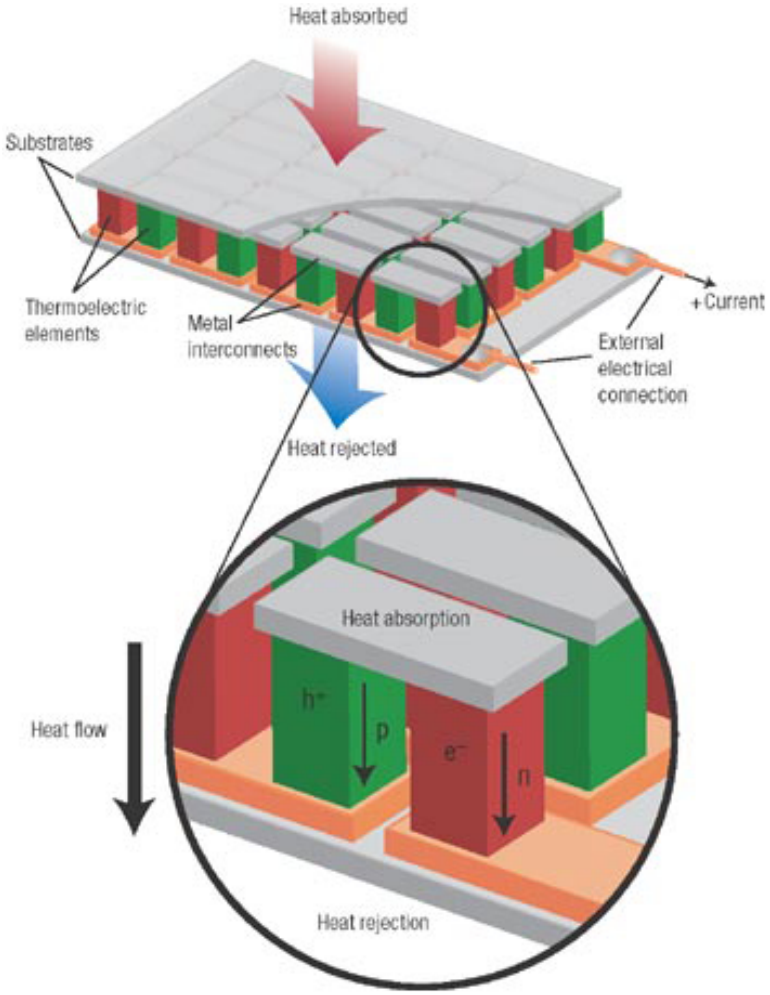


FIGURE 1.1: The schematic of the thermoelectric module for both cooling and power generation. Figure from G. J. Snyder and E. S. Toberer. (Snyder and Toberer, 2008a)

the French scientist Jean Charles Athanase Peltier observed that there was a temperature difference when a voltage is applied on the conductor, which allows people to use thermoelectric materials as cooling packages or solid state refrigeration devices. Based on the Seebeck and Peltier effect, the waste heat can be converted to electric power directly or temperature difference can be produced by the thermoelectric junction [Figure 1.1].

The efficiency of the thermoelectric materials for both power generation and cooling is characterized by the dimensionless figure-of-merit (ZT):

$$ZT = \frac{S^2 \sigma T}{\kappa} = \frac{S^2 \sigma T}{\kappa_{el} + \kappa_{ph}} \tag{1.1}$$

where S, σ , κ_{el} and κ_{ph} are the thermoelectric power (Seebeck coefficient), electrical conductivity, electronic thermal conductivity and lattice (phonon) thermal conductivity, respectively, and T is the absolute temperature. Then, the Carnot efficiency of

thermoelectric device can be written as (Lan et al., 2010)

$$\eta = \frac{T_h - T_c}{T_h} \frac{\sqrt{1+Z\overline{T}}-1}{\sqrt{1+Z\overline{T}}+T_c/T_h} \tag{1.2}$$

in which, T_h and T_c are the hot-end and cold-end temperature of the thermoelectric devices, respectively. T is the average temperature of T_h and T_c. Figure 1.2 shows that the Carnot efficiency or COP is strongly related to the ZT value: high ZT values prove the high Carnot efficiency. Based on Eq. (1.1), an ideal TE material should be an electrical conductor, but a thermal insulator. A material design challenge has been proposed by this conflicting requirement since the electrical transport properties [denominator in Eq. (1.1)] and the thermal transport properties [numerator in Eq. (1.1)] are strongly coupled. The TEs community is widely targeting $ZT \geq 3$ to make these solid-state systems competitive with traditional mechanical energy conversion systems [Figure 1.2]. Therefore, it is significant important to find a method to make the denominator and numerator in Eq. (1.1) are independent.

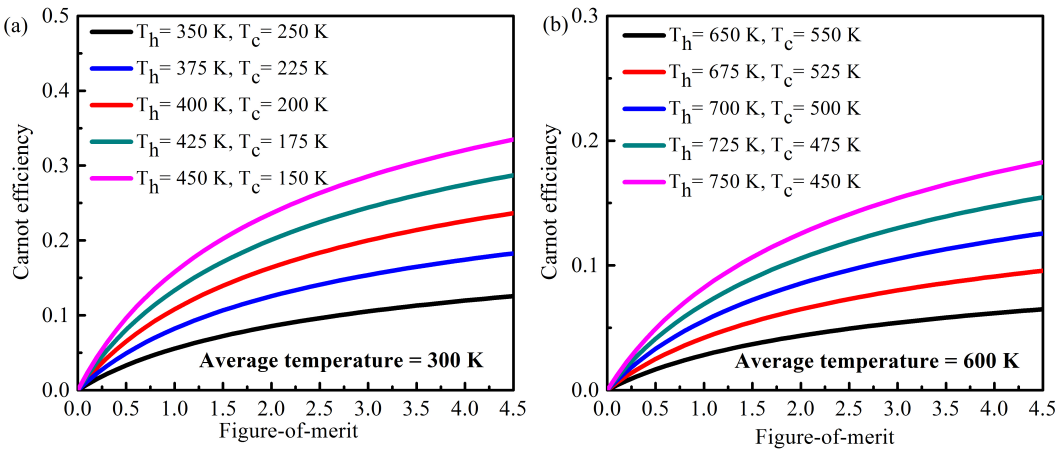


FIGURE 1.2: The Carnot efficiency of the thermoelectric devices with various temperature difference at room temperature (b) and 600 K (c).

1.2 State-of-art of Thermoelectrics via Nanostructuring

Nanostructuring the existing bulk TE materials via nanowires (NWs), superlattices (SLs) and nanocomposites (NCs), has been proved to be a quite efficient way to obtain decent thermoelectric performance (Hochbaum et al., 2008; Boukai et al., 2008; Luckyanova et al., 2012; Yu et al., 2012; Soni et al., 2012; Son et al., 2012; Zebarjadi et al., 2011), due to the faster reduction of the lattice (phonon) thermal conductivity than the slower decrease of power factor (PF, $S^2\sigma$). As a result, one of the key point to improve the figure-of-merit is to suppress the lattice thermal conductivity [Eq. (1.1)].

1.2.1 Reducing the thermal conductivity

In solid state material, the thermal conductivity is mainly contributed by lattice vibrations (phonons) and electrons. The electrons are responsible for the majority of heat conduction in metal (Al, Cu, and Au *et al.*), while the phonons are the dominant carriers in the semiconductors and insulators (Ziman, 1960), e.g. solid argon (Ar), silicon (Si), germanium (Ge) and silica-based materials. Most of good TE materials are semiconductors, and therefore, the lattice thermal conductivity is the main contributor of the total thermal conductivity. The traditional TE materials such as Si, Ge, SiGe alloy and bismuth telluride (Bi2Te3) have relative large lattice thermal conductivity, which will lead to a low figure-of-merit. Since 1960s, only slow progress has been made in enhancing the figure-of-merit, either in the widely used Bi_2Te_3 alloys or in other TE materials. Until 1990s, a pioneering work of Hicks and Dresselhaus (Hicks and Dresselhaus, 1993a; Hicks and Dresselhaus, 1993b) was conducted to theoretically prove the ZT can be enhanced significantly with nanostructured materials. Then reducing the lattice thermal conductivity via nanostructuring which actually makes phonons scattered by surface, grain boundary (GB) or interfaces, becomes the most popular method to improve the performance of thermoelectrics. For instance, Hochbaum *et al.* (Hochbaum et al., 2008) showed that using the roughed nanowires with diameter around 40 nm, the thermal conductivity of Si can be reduced from $\sim$150 $Wm^{-1}K^{-1}$ to $\sim$1.6 $Wm^{-1}K^{-1}$, and therefore, the room temperature ZT value of such roughed nanowires can be as high as around 0.63 which is the highest ZT for Si-based materials at room temperature. Almost at the same time, using the ultral thin nanowires with diameters of 10 to 20 nm, Boukai *et al.* (Boukai et al., 2008) experimentally found that the thermal conductivity of these Si nanowires can be decreased by two orders of magnitude with respect to its bulk value. As a result, a high ZT coefficient of around 0.3 can be obtained. The main reason for the super high ZT value observed in the above experiments is the extremely low lattice thermal conductivity which is caused by the significantly strong phonon-surface scattering. Following these classical experiments, a vast of studies on optimizing the thermoelectric performance via reducing the thermal conductivity by nanowires including experiments (Lee, Kim, and Hyeon, 2006; Lim et al., 2012; Li et al., 2003; Kim et al., 2015b), simulations Cartoixà et al., 2016a; Shi et al., 2009; Volz and Chen, 1999; Cartoixa, Colombo, and Rurali, 2015; Chen, Zhang, and Li, 2012; Donadio and Galli, 2010; Hu and Poulikakos, 2012; Jiang et al., 2013; Ponomareva, Srivastava, and Menon, 2007; Sansoz, 2011; Vo et al., 2008; Yang, Zhang, and Li, 2008; Zhou and Hu, 2016 and theory predictions (Martin et al., 2010; Yao, Zhang, and Li, 2008; Mingo et al., 2003; Yang, Zhang, and Li, 2010; Zhou, Zhang, and Hu, 2017; Mingo, 2003), are implemented in the recent 10 years. Meanwhile, the bulk nanostructure which introduces a plenty of grain boundaries or interfaces into the system and thus reduce the thermal conductivity to reach a quite low value which is comparable to the amorphous limit of materials via quite strong phonon-grain boundary scattering, is another popular method of nanostructuring (Zhou and Hu, 2016; Feser

et al., 2013; Joshi et al., 2008; Melis and Colombo, 2014; Garg et al., 2011; Kim et al., 2015a; Poudel et al., 2008a). In the past 15 years, excellent figure-of-merit with a value larger than one or even two has been realized experimentally in quantum nanodot bulk $AgPb_mSbTe_{2+m}$ alloys (Wang et al., 2008b), bulk nanostructured SiGe alloys (Yu et al., 2012; Wang et al., 2008b) and bulk nanostructured Bi_2Te_3 (Kim et al., 2015a; Poudel et al., 2008a) based on such an idea. The underlying mechanism behind the phenomenon of the extremely low thermal conductivity is that the phonons with mean free path (MFP) larger than the grain size is scattered by grain boundary, which has been well explained by simulations and theoretical predictions.

1.2.2 Bulk comparative power factor

A big concern about nanostructuring is that the electrical transport properties could be negatively affected by nanostructring. For example, Pan *et al.* (Pan et al., 2016) experimentally improves the electrical conductivity of Si nanowire and decrease the thermal conductivity largely. However, the low Seebeck coefficient in experiments may makes them fail to gain high figure-of-merit. Zhao *et al.* (Zhao et al., 2009) enhanced the Seebeck coefficient of the Bi2Te3 nano-/mircostructures significantly to around 210 (around twice of the bulk Bi_2Te_3) while the electrical conductivity is found to be reduced to only 1/3 of that of bulk value). Consequently, the optimized ZT of such Bi2Te3 nano-/mircostructures is only 0.66 which is even lower than the commercial Bi_2Te_3 . However, as Hicks and Dresselhaus (Hicks and Dresselhaus, 1993a; Hicks and Dresselhaus, 1993b) theoretically proved that electrons can be confined in a quantum well in nanomaterials and then the Seebeck coefficient can be enhanced largely. Meanwhile, doping is also regarded as a common method to improve the electrical conductivity. The reason in Pan *et al.*'s work may be that the superhigh doping has make the Si nanowires become metallic which means the band gap is smaller than zero. In Zhao et al.'s results, there may be defects in the grain boundary which is detrimental to the electrical conductivity. Therefore, the high electrical transport performance of nanostructures should be obtained once the quality of the sample and doping density are optimized. For example, in nanostructured bismuth antimony telluride alloy ($Bi_xSb_{2-x}Te_3$) (Hsu et al., 2004a), the power factor is found to be comparable to that of the bulk ingot at the low temperature range (around 30-250 K). As a result, the dimensionless figure-of-merit of such nanostructured $Bi_xSb_{2-x}Te_3$ can reach around 1.4 at about 100 K. By embeding dense dislocations in the grain boundaries further, the ZT value of the nanostructured $Bi_{0.5}Sb_{1.5}Te_3$ can be even increased to around 2 at room temperature, which is mainly because of the point defect scattering of phonons at the grain boundaries (Kim et al., 2015a). The nanostructured SiGe alloys are also found to hold the comparable power factor with respect to bulk Si for the cases of hole and electron doping (Yu et al., 2012; Wang et al., 2008b). Combining with the extremely low thermal conductivity, the ZT value of the nanostructured SiGe alloys can reach about 0.95 at high temperature. The power factor of the Si NWs with rough (Hochbaum et al., 2008)

and smooth (Boukai et al., 2008) surface in experiments is found to be at the same level comparing to bulk Si as well.

Based on the discussions above, it is easy to find that the key point to improve the figure-of-merit is to suppress the thermal conductivity and keep or even improve the power factor at the same time, which can be realized by nanostructuring.

1.3 Structure of Thesis

In Chapter 2, we begin with an introduction to the methods that will be used for heat and electron transport calculations and the corresponding phonon related calculations. The methods include Green-Kubo equilibrium molecular dynamics (GK-EMD) simulations, nonequilibrium molecular dynamics (NEMD) simulations, time domain normalized mode analysis (TDNMA), spectral density energy (SED), Boltzmann transport equation (BTE) and Allen-Feldman (AF) theory for thermal conductivity calculations, relaxation time approximation Boltzmann transport equation (RTA-BTE) for electrical transport calculations.

In Chapter 3, we propose two new algorithms/computational schemes named time domain direct decomposed method (TDDDM) and frequency domain direct decomposed method (FDDDM) based on the framework of NEMD. Using the TDDDM, we can investigate the size effect of each phonon mode, and find contribution of phonon modes corresponding to Gamma points is 0 as well. We find that the phonon modes with mean free path larger than the system size are truncated. Based on the FDDDM, we can study the modal contribution thermal conductivity of the complicated systems such as the nanowires and amorphous materials. The temperature effect is also included inherently in FDDDM. Then, we extend the FDDDM to the interface problem. By using the FDDDM, we can fully consider the harmonic and anharmonic scattering channel at interface. Four different scattering modes at interface can be characterized by FDDDM as well.

The thermal transport modulation via nanostructuring is investigated in Chapter 4. In this Chapter, we firstly studied the surface orientation on the thermal conductivity of Si NWs. Next, a special interface: mass graded interface is founded to enhance the thermal conductance by around 6 times. Later, the thermal conductivity of Si NWs with various diameters is studied.

In Chapter 5, we studied how the thermoelectric performance affected by nanostructuring. Firstly, we found a strategy to decrease the lattice thermal conductivity of Si NWs to a record value by polycrystallization. Then, based on the results of first step, we designed a structure named superlattice nanocrystal heterostructures (SL-NC HSs) in which the thermal conductivity is found to be reduced by two orders of magnitude and reaches a value far below the amorphous limit of Si. Meanwhile, the power factor of such structures is found to be comparable to that of the bulk Si. As a consequence, the ZT of SL-NC HSs can reach 0.5 at room temperature. At

last, we proposed a new strategy of incorporating nanotwinned structures to decouple the electronic and phononic transport. Combining the new concept of nanotwin with the previously widely used nanocrystalline approach, the power factor of the Si nanotwin-nanocrystalline heterostructures is enhanced by 120% compared to bulk crystalline Si, while the lattice thermal conductivity is reduced to a level well below the amorphous limit, yielding a theoretical limit of 0.52 and 0.9 for ZT coefficient at room temperature and 1100 K, respectively.

We conclude the thesis in Chapter 6.

Chapter 2

Theoretical Background

2.1 Molecular Dynamics

In molecular dynamics (MD) simulations, the motion of atoms is calculated by the classical Newton's second law:

$$\frac{d^2\vec{r}}{dt^2} = \frac{\vec{F}_i}{m_i} \tag{2.1}$$

where, $\{t\}$ refers to time, m_i, $\vec{r}_i$ and $\vec{F}_i$ are the mass, position and total force of atoms i, respectively. The force applied on the atom can be obtained from the first derivative of the potential energy U (Sääskilahti et al., 2014).

$$\vec{F}_i = \sum_{i \neq j} \vec{F}_{ij} = -2 \sum_j \frac{\partial U_j}{\partial \vec{r}_i} \tag{2.2}$$

where, $\vec{F}_{ij}$ is the force on atom i results from atom j. $\vec{r}_i$ is the position of atom i. From the equation above, it is easy to know that the potential energy U is the most important known quantity. The accuracy of the results strongly depends on the reasonability of the potential energy used to describe the system. The general formula for the total potential can be written as

$$U = \sum_i U_1(\vec{r}_i) + \sum_i \sum_{j>i} U_2(\vec{r}_i,\ \vec{r}_j) + \sum_i \sum_{j>i} \sum_{k>j>i} U_3(\vec{r}_i,\ \vec{r}_j,\ \vec{r}_k) + \dots \tag{2.3}$$

From the expression above, it is easy to know that the second, third and so on represent the interactions between two atoms, three atoms and so on. The first term in Eq. (2.3) stands for the external field acting on the system. To solve Eq. (2.1) , the most popular method is the Verlet arithmetic (Verlet, 1967) which compute the atomic position at $t - \delta t$ via the atomic positions at t and $t - \delta t$

$$\vec{r}_i(t + \delta t) = 2\vec{r}_i(t) - \vec{r}_i(t - \delta t) + (\delta t)^2 \vec{a}_i(t) \tag{2.4}$$

in which, $\vec{a}_i(t)$ is the acceleration and can be calculated using

$$\vec{a}_i(t) = \frac{\vec{r}_i(t + \delta t) - \vec{r}_i(t - \delta t) - 2\vec{r}_i(t)}{(\delta t)^2} \tag{2.5}$$

At the same time, the atomic velocity can be written in the form of

$$\vec{v}_i(t) = \frac{\vec{r}_i(t+\delta t) - \vec{r}_i(t-\delta t)}{2\delta t} \tag{2.6}$$

Based on Eq. (2.6), it is impossible to compute the atomic velocity at $t = 0$. The initial atomic velocity at temperature T can be generated via the Maxwell-Boltzmann distribution function

$$p\left(v_{ix}\right) = \left(\frac{m_i}{2\pi k_B T}\right)^{1/2} \exp\left(-\frac{1}{2}\frac{m_i v_{ix}^2}{k_B T}\right) \tag{2.7}$$

It gives out the probability of velocity along direction of atom i.

MD simulations usually run under some constraints which are normally called ensembles. The most widely adopted statistical sampling ensembles are the micro-canonical ensemble (*NVE*, constant particles, volume and no thermostat), the canonical ensemble (*NVT*, constant particles, volume and temperature) and the isobaric-isothermal ensemble (*NPT*, constant particles, pressure and temperature). Following the statistical physics, all the macroscopic properties can be derived from the fluctuation-dissipation. The total energy of the system, E, is the summation of potential energy U and the kinetic energy K_T:

$$\langle E\rangle = \langle U\rangle + \langle K_T\rangle = \langle U\rangle + \frac{1}{2}\sum_i^N m_i v_i^2 \tag{2.8}$$

where$N$ is the total number of atoms in the system. Based on the ideal gas law, we can know

$$\langle E\rangle = \langle U\rangle + \langle K_T\rangle = \frac{3}{2}NTk_B \tag{2.9}$$

Comparing Eq. (2.8) with Eq. (2.9), we have

$$T = \frac{2\langle K_T\rangle}{3Nk_B} = \frac{1}{3Nk_B}\sum_i^N m_i|\vec{v}_i|^2 \tag{2.10}$$

Another important quantity in MD simulations is the pressure, which can be written in the form of

$$P = \frac{Nk_BT}{V} + \frac{1}{dV}\sum_i^N \vec{r}_i \cdot \vec{F}_i \tag{2.11}$$

in which, V is the volume of the system of interest.

2.1.1 Green-Kubo equilibrium molecular dynamics

In equilibrium molecular dynamic (EMD) simulations, the fluctuation-dissipation theorem based on the linear response theory can provide the connection between the energy dissipation in irreversible processes and the thermal fluctuations (Kubo, 1966). The net flow of heat in a solid, $\vec{Q}$, fluctuates around zero at equilibrium. The

expression of $\vec{Q}$ can be shown as

$$\vec{Q} = \sum_i E_i \vec{v}_i + \sum_n \sum_{S_1} \sum_{S_1<S_2} \cdots \sum_{S_{n-1}<S_n} \left[\sum_{\alpha=1}^{n-1} \sum_{\beta=\alpha+1}^{n} \vec{F}_{S_\alpha S_\beta} \cdot (P^n_{S_\alpha} \vec{v}_{S_\alpha} + P^n_{S_\beta} \vec{v}_{S_\beta}) \cdot (\vec{r}_{S_\alpha} - \vec{r}_{S_\beta}) \right] \tag{2.12}$$

where $\vec{Q}$ is the heat current, the sum is taken over all atoms which are described by n-body potential in the control volume, S_i denotes the atoms, E_i and $\vec{r}_i$ are the energy and position of atoms, respectively. P stands for the distribution of the interaction potential and satisfies (Kubo, 1966)

$$\sum_n P_i = 1 \tag{2.13}$$

In the classical systems, equal partition of potential energy between atoms $P^n_i = 1/n$ is usually assumed. Then, for the pair-potential (two-body potential), we can know

$$\vec{Q} = \sum_i E_i \vec{v}_i + \sum_{i<j} \vec{F}_{ij} \cdot \vec{v}_j \cdot (\vec{r}_i - \vec{r}_j) = \sum_i E_i \vec{v}_i + \frac{1}{2} \sum_{i<j} \vec{F}_{ij} \cdot (\vec{v}_i + \vec{v}_j) \cdot (\vec{r}_i - \vec{r}_j) \tag{2.14}$$

In the Green-Kubo method, the thermal conductivity can be obtained by the heat current auto correlation function (HCACF), $\left\langle \vec{Q}(t) \otimes \vec{Q}(0) \right\rangle$, and can be defined by (Kubo, 1957)

$$\kappa = \frac{V}{k_B T^2} \int_0^\infty \left\langle \vec{Q}(t) \otimes \vec{Q}(0) \right\rangle dt \tag{2.15}$$

From the expression above, it is easy to know the thermal conductivity κ is a second order tensor. In the case of an isotropic material, Eq. (2.15) can be written as

$$\kappa = \frac{V}{k_B T^2} \int_0^\infty \left\langle \vec{Q}_x(t) \cdot \vec{Q}_x(0) \right\rangle dt = \frac{V}{3 k_B T^2} \int_0^\infty \left\langle \vec{Q}(t) \cdot \vec{Q}(0) \right\rangle dt \tag{2.16}$$

In crystals where the fluctuations have long life times, i.e., the mean free path (MFP) is large, the HCACF decays slowly. The thermal conductivity is accordingly large since it is related to the integral of the HCACF. In the materials such as amorphous and polycrystalline solids, where the MFP of vibrations is small, thermal fluctuations are quickly damped, leading to a small thermal conductivity (McGaughey and Kaviany, 2004a; McGaughey and Kaviany, 2004b).

2.1.2 Non-equilibrium molecular dynamics

The non-equilibrium molecular dynamics (NEMD), which is based on the concept of experiment, is known as direct method as well. In NEMD, the thermal conductivity along the specified direction is extracted using Fourier's law

$$\kappa = \frac{1}{V} \frac{\left\langle \vec{Q}_x \right\rangle}{\nabla T} = \frac{1}{V} \frac{\left\langle \vec{Q}_x \right\rangle}{dT/dx} \tag{2.17}$$

In this method, the temperature gradient on a simulation cell is formed by allowing an energy exchange E between the heat source and sink. The heat current is

$$\left\langle \vec{Q}_x \right\rangle = \frac{dE}{dt} \tag{2.18}$$

An alternative, but equivalent way is to inducing a stable heat current via imposing a fixed temperature gradient. In both cases, the system is allowed to reach a steady state firstly, after which long simulations are implemented for obtaining the correct statistical measurements.

In NEMD simulations, the size effects cannot be avoided due to the thermostats at two ends, which indicates the system is actually a film rather than a bulk structure. Only when the length of simulation cell L is larger than the dominant MFP, the phonons can be thought to not be scattered by the interfaces at the heat source and sink. As a result, the phonon MFP is limited by the system size. To eliminate the size effect, a method based on Matthiessen's rule is usually used to determine the mean free path for an infinite system τ_∞:

$$\frac{1}{\tau_{eff}(\nu,\ \vec{k})} = \frac{1}{\tau_\infty(\nu,\ \vec{k})} + \frac{1}{\tau_b(\nu,\ \vec{k})} \tag{2.19}$$

where τ_{eff} is the effective relaxation time for the system with length of L. τ_b is the phonon boundary relaxation time and can be written as

$$\frac{1}{\tau_b(\nu,\ \vec{k})} = \frac{L/2}{\left| v_{g,\ z}(\nu,\ \vec{k}) \right|} \tag{2.20}$$

On the other hand, following the kinetic theory, the thermal conductivity can be written in the form of

$$\kappa = \frac{1}{3} \sum_{\nu} \sum_{\vec{k}} C_v v_{g,\ z}^2(\nu,\ \vec{k}) \tau_\infty(\nu,\ \vec{k}) \times \left[1 + \frac{2 \left| v_{g,\ z}(\nu,\ \vec{k}) \right| \tau_\infty(\nu,\ \vec{k})}{L} \right] \tag{2.21}$$

Therefore, we can find that the length dependent thermal conductivity can be described using a function of (Sellan et al., 2010b)

$$\frac{1}{\kappa_{eff}} = \chi\left(\frac{1}{L}\right) \tag{2.22}$$

And the inherent thermal conductivity can be obtained by

$$\frac{1}{\kappa_\infty} = \lim_{L \to \infty} \chi\left(\frac{1}{L}\right) = \chi(0) = \chi(1/L) + \frac{\chi(1/L)}{1!}\left[-\frac{1}{L}\right] + \frac{\chi(1/L)}{2!}\left[-\frac{1}{L}\right]^2 + \dots \tag{2.23}$$

Obviously, when L is large, the high-order derivates at the right side can be ignored and will lead to

$$\frac{1}{\kappa_\infty} = \chi\left(1/L\right) + \frac{\chi\left(1/L\right)}{1!}\left[-\frac{1}{L}\right] \tag{2.24}$$

From the expression above, we know the inherent thermal conductivity can be obtained by extrapolating to $1/L = 0$, which is most popular approach to obtain the inherent thermal conductivity in NEMD (Schelling, Phillpot, and Keblinski, 2002a).

2.1.3 Limitations of molecular dynamics

MD simulations have been used to study various properties such as mechanical properties, chemical reaction and transport properties for the bulk and nanomaterials. It has successfully provided quite a lot meaningful underlying mechanisms at atomic scale, and therefore, assist the experimental designs. However, apart from these successful applications, several limitations exist in it as well.

The first limitation is the size and time of the MD simulations. With the help of the supercomputing, the size of the usual MD simulations can contain as many as millions of atoms corresponding to size of the system around 50 nm in cubic. However, such a system size is far from enough in some cases. For instance, in the three dimensional bulk heterostructures (HS) constituted by the grains whose typical size can be in the range of ∼nm to ∼um, the number of atoms in the system can reach several billions which is big challenge for MD simulations. On the other hand, the simulation time in normal MD simulations is from several picoseconds to hundreds of nanoseconds, which is too short for some virtual experiments. Examples can be listed from the studies of mechanical deformations simulated by MD. the strain rate of loading process in the mechanical experiments is usually in the range of $1 \sim 10^3 s^{-1}$, while in the MD simulations, due to the short running time, the strain rate is as high as $10^8 \sim 10^{11} s^{-1}$. Such big difference of strain rate between experiments and MD simulations make the results of these mechanical problems questionable. The challenges from the simulation size and time are important but not fundamental and can be solved with development of the future supercomputing. The most fundamental limitation in MD simulations is the classical distribution, that is, the trajectory of atoms is integrated according to the classical Newtonian mechanics and therefore the quantum effect is ignored. Due to the classical assumptions, phonons follow the Boltzmann distribution, i. e., $f = Ae^{E_i/k_BT}$instead of Bose-Einstein distribution, i. e., $f = A(e^{E_i/k_BT} - 1)$. As a result, the energy equipartition theory is applied in the MD simulations, which means that at any temperature, all the phonons are activated and each phonon mode has the energy of k_BT This assumption is only valid when the temperature of the system $T$is much higher than the Debye temperature T_D ($T \gg T_D$), at which the Bose-Einstein distribution can be simplified to Boltzmann distribution. At temperatures below the Debye temperature, the high frequency phonons are at least partially activated rather than fully

occupied as in MD simulations. Therefore, MD simulations are usually conducted above the Debye temperature or at least half of the Debye temperature, in which the atomic mass is sufficiently large and then the de Broglie wavelength is smaller than the interatomic distance and atoms can be treated classically. In order to overcome this fundamental limitation, different quantum corrections in MD simulations have been proposed such as temperature correction (Wang, Chan, and Ho, 1990) and quantum thermal bath (Dammak et al., 2009). What is more, for the low dimensional materials, the size scaling in NEMD calculations of thermal conductivity is far beyond resolved (Yang, Zhang, and Li, 2010).

2.2 Lattice Dynamics

Firstly, let us start with defining the lattice energy, E_{Lat}, as a sum over all atom-atom interactions:

$$E_{Lat} = \frac{1}{2} \sum_{jl,\ j'l'} \varphi(jl,\ j'l') \tag{2.25}$$

where j denotes an atom in the j-th unit cell, and the interaction energy φ is for the pair of atoms (jl) and $(j'l')$. Then, the energy caused by the harmonic displacement can written in the form of

$$E^{harm} = \frac{1}{2} \sum_{jl,\ j'l'} \vec{u}(jl) \cdot \mathrm{K} \cdot \vec{u}(j'l') = \frac{1}{2} \sum_{jl,\ j'l'} \sum_{\alpha,\ \beta} u_\alpha(jl) \cdot K_{\alpha\beta}(jl,\ j'l') \cdot u_\beta(j'l') \tag{2.26}$$

in which, the displacement matrix $\vec{u}(jl)$ is defined as

$$\vec{u}(jl) = \frac{1}{2}(u_x(jl),\ u_y(jl),\ u_z(jl))^T \tag{2.27}$$

and the elements in the 3×3 force constant matrix K can be expressed as

$$K_{\alpha\beta}(jl,\ j'l') = \frac{\partial^2 E_{Lat}}{\partial u_\alpha(jl) \partial u_\beta(j'l')} \tag{2.28}$$

The equation of motion for the (jl) atom can be given in this matrix formulation by

$$m_j \vec{u}(jl,\ t) = \sum_{j'l'} \mathrm{K}(jl,\ j'l') \vec{u}(jl,\ t) \tag{2.29}$$

where m_j is the mass of the j-th atom. It is worth noting that here the displacement is time dependent. The solution of $\vec{u}(jl,\ t)$ will be a linear superposition of travelling waves of different modes $(\vec{k},\ \nu)$ and can be expressed as

$$\vec{u}(jl,\ t) = \sum_{(\vec{k},\ \nu)} \vec{U}(j,\ \vec{k},\ \nu) \exp\left(i \left[\vec{k} \cdot \vec{r}(jl) - \omega(\vec{k},\ \nu)t\right]\right) \tag{2.30}$$

in which, $\vec{r}(jl)$ can be taken as either the equilibrium (or mean) position of the atom (jl) or the origin of the unit cell (l). The amplitude vector $\vec{U}(j,\ \vec{k},\ \nu)$ (known as

the *displacement vector*) is independent on (l) since the differences in motions between neighboring unit cell are completely described by the exponential phase factor. $\omega(\vec{k},\ \nu)$ is the phonon vibration frequency. Combining Eq. (2.29) and Eq. (2.30), we have

$$m_j\omega^2(\vec{k},\ \nu)\vec{U}(j,\ \vec{k},\ \nu) = \sum_{j'l'} \mathrm{K}(j0,\ j'l')\vec{U}(j,\ \vec{k},\ \nu)\exp\left(i\vec{k}\left[\vec{r}(jl) - \vec{r}(j0)\right]\right) \tag{2.31}$$

where the reference atom is in the unit cell $(l = 0)$. If we define the dynamic matrix $D_{\alpha\beta}(jj',\ \vec{k})$ as

$$D_{\alpha\beta}(jj',\ \vec{k}) = \frac{1}{\left(m_j m_{j'}\right)^{1/2}} \sum_{jj'} \mathrm{K}(j0,\ j'l')\exp\left(i\vec{k}\left[\vec{r}(jl) - \vec{r}(j0)\right]\right) \tag{2.32}$$

then, the Eq. (2.31) can be rewritten in the form of

$$m_j\omega^2(\vec{k},\ \nu)\vec{U}(j,\ \vec{k},\ \nu) = \frac{1}{-}\sum_{j'l'} \left(m_j m_{j'}\right)^{1/2}\vec{U}(j',\ \vec{k},\ \nu)D_{\alpha\beta}(jj',\ \vec{k}) \tag{2.33}$$

Defining the column vector $\vec{e}(\vec{k},\ \nu)$ (enginvector) as

$$\vec{e}(\vec{k},\ \nu) = \frac{\left(\sqrt{m_1}\vec{U}(1,\ \vec{k},\ \nu), \ldots, \sqrt{m_n}\vec{U}(n,\ \vec{k},\ \nu)\right)^T}{\left(\left(\sqrt{m_1}\vec{U}(1,\ \vec{k},\ \nu)\right)^2 + \ldots + \left(\sqrt{m_n}\vec{U}(n,\ \vec{k},\ \nu)\right)^2\right)^{1/2}} \tag{2.34}$$

then, Eq. (2.33) can be recast into

$$\omega^2(\vec{k},\ \nu)\vec{e}(\vec{k},\ \nu) = \mathrm{D}(\vec{k})\vec{e}(\vec{k},\ \nu) \tag{2.35}$$

From above, we know that the dynamic matrix includes both the force constant for any particular atom-atom interaction and the phase factor for the atomic motion of any wave. Therefore, Eq. (2.35) stands for the equation of motion. It generates the complete set of atomic motions associate with each wave. These waves are linearly independent (orthogonal), which means the motion associated with one wave do not affect the motions for any other. This can expressed as

$$\left(\vec{e}(\vec{k},\ \nu)\right)^T \vec{e}^*(\vec{k},\ \nu) = \delta_{\nu\nu'} \tag{2.36}$$

where $\delta_{\nu\nu'}$ is the delta function. These vibration modes are called *normal modes*, and are fundamental vibrational motions. What is also worth noting is that, for Eq. (2.35), the phonon frequency $\omega(\vec{k},\ \nu)$and enginvector $\vec{e}(\vec{k},\ \nu)$ are q point dependent. Such relation is called *phonon dispersion* in lattice dynamics. Further, we introduce

normal mode coordinates $Q(\vec{k},\ \nu)$, such that

$$\vec{u}(jl,\ t) = \frac{1}{(Nm_j)^{1/2}} \sum_{\vec{k},\ \nu} \vec{e}(j,\ \vec{k},\ \nu) \exp(i\vec{k}\cdot\vec{r}(jl)) X(\vec{k},\ \nu) \tag{2.37}$$

and

$$\dot{\vec{u}}(jl,\ t) = \frac{1}{(Nm_j)^{1/2}} \sum_{\vec{k},\ \nu} \vec{e}(j,\ \vec{k},\ \nu) \exp(i\vec{k}\cdot\vec{r}(jl)) \dot{X}(\vec{k},\ \nu) \tag{2.38}$$

On the other hand, the Hamiltonian of the dynamic system η can be written as

$$\eta = \frac{1}{2}\sum_{jl} m_j \left|\dot{\vec{u}}_j(jl,\ t)\right|^2 + \frac{1}{2}\sum_{jl,\ j'l'} \vec{u}_j^T(jl,\ t) K(jl,\ j'l') \vec{u}_j^T(j'l',\ t) \tag{2.39}$$

Recasting the Eq. (2.37) and Eq. (2.38) into Eq. (2.39), the first term of Eq. (2.39) can be written as

$$\begin{aligned}\frac{1}{2}\sum_{jl} m_j \left|\dot{\vec{u}}_j(jl,\ t)\right|^2 =& \frac{1}{2N}\sum_{l}\sum_{\vec{k},\ \nu}\sum_{\vec{k}',\ \nu'} \Big\{\vec{e}(j,\ \vec{k},\ \nu)\cdot\vec{e}^*(j,\ \vec{k}',\ \nu) \exp\left(i(\vec{k}-\vec{k}')\cdot\vec{r}(l)\right) \\ & \cdot\dot{X}(\vec{k},\ \nu)\dot{X}^*(\vec{k}',\ \nu')\Big\}\end{aligned} \tag{2.40}$$

where the mode enginvector $\vec{e}(\vec{k},\ \nu)$ has summed all the components of each atom in the unit cell. Meanwhile for the crystals with periodic boundary conditions, we can know (Ziman, 1960)

$$\frac{1}{N}\sum_{\vec{r}} \exp(i\vec{k}\cdot\vec{r}) = \delta_{\vec{k},\ 0} \tag{2.41}$$

and

$$\frac{1}{N}\sum_{\vec{k}} \exp(i\vec{k}\cdot\vec{r}) = \delta_{\vec{r},\ 0} \tag{2.42}$$

Therefore, the only terms that do not sum to zero in Eq. (2.40) are those for $\vec{k} = \vec{k}'$, Eq. (2.40) can be recast into

$$\begin{aligned}\frac{1}{2}\sum_{jl} m_j \left|\dot{\vec{u}}_j(jl,\ t)\right|^2 =& \frac{1}{2N}\sum_{\vec{k},\ \nu,\ \nu'} \Big\{\vec{e}(j,\ \vec{k},\ \nu)\cdot\vec{e}^*(j,\ \vec{k}',\ \nu)\cdot\dot{X}(\vec{k},\ \nu)\dot{X}^*(\vec{k}',\ \nu')\Big\} \\ =& \frac{1}{2}\sum_{\vec{k},\ \nu}\dot{X}(\vec{k},\ \nu)\dot{X}^*(\vec{k},\ \nu) = \frac{1}{2}\sum_{\vec{k},\ \nu}\left|\dot{X}(\vec{k},\ \nu)\right|^2\end{aligned} \tag{2.43}$$

In the same way, we can yield the expression of second term of Eq. (2.39) by substitutingEq. (2.37) and Eq. (2.38) into Eq. (2.39)

$$\begin{aligned}
&\frac{1}{2}\sum_{jl,\ j'l'}\vec{u}_j^T(jl,\ t)K(jl,\ j'l')\vec{u}_j^T(j'l',\ t)=\sum_{jl}\sum_{j'l'}\sum_{\vec{k},\ \nu}\sum_{\vec{k}',\ \nu'}\frac{1}{2N\left(m_jm_{j'}\right)^{1/2}}\left\{\vec{e}^T(j,\ \vec{k},\ \nu)\right.\\
&\left.K(jl,\ j'l')\vec{e}(j',\ \vec{k}',\ \nu')\cdot exp\left(i\left[\vec{k}\cdot\vec{r}(jl)+\vec{k}'\cdot\vec{r}(j'l')\right]\right)X(\vec{k},\ \nu)\ X(\vec{k}',\ \nu')\right\}\\
&=\sum_{jl}\sum_{j'l'}\sum_{\vec{k},\ \nu}\sum_{\vec{k}',\ \nu'}\frac{1}{2N\left(m_jm_{j'}\right)^{1/2}}\left\{\vec{e}^T(j,\ \vec{k},\ \nu)\ K(jl,\ j'l')\vec{e}(j',\ \vec{k}',\ \nu')\cdot\right.\\
&\left.exp\left(i\left(\vec{k}+\vec{k}'\right)\cdot\vec{r}(jl)\right)\cdot exp\left(i\vec{k}'\left[\vec{r}(j'l'')-\vec{r}(j0)\right]\right)\cdot X(\vec{k},\ \nu)\ X(\vec{k}',\ \nu')\right\}
\end{aligned}\tag{2.44}$$

in which, we use the definition of

$$\vec{r}(j'l')-\vec{r}(jl)=\vec{r}(j'l'')-\vec{r}(j0)\tag{2.45}$$

Based on Eq. (2.41) and Eq. (2.42), Eq. (2.44) can be simplified into

$$\begin{aligned}
&\frac{1}{2}\sum_{jl,\ j'l'}\vec{u}_j^T(jl,\ t)K(jl,\ j'l')\vec{u}_j^T(j'l',\ t)=\sum_{jl}\sum_{j'l'}\sum_{\vec{k},\ \nu,\ \nu'}\frac{1}{2N\left(m_jm_{j'}\right)^{1/2}}\left\{\vec{e}^T(j,\ \vec{k},\ \nu)\cdot\right.\\
&\left.K(jl,\ j'l')\vec{e}(j',\ \vec{k}',\ \nu')exp\left(i\vec{k}'\left[\vec{r}(j'l'')-\vec{r}(j0)\right]\right)\cdot X(\vec{k},\ \nu)\ X(\vec{k}',\ \nu')\right\}\\
&=\frac{1}{2}\sum_{\vec{k},\ \nu,\ \nu'}\left\{\vec{e}^T(\vec{k},\ \nu)\mathrm{D}(\vec{k})\vec{e}^*(\vec{k},\ \nu')\cdot X(\vec{k},\ \nu)\ X(\vec{k}',\ \nu')\right\}\\
&=\frac{1}{2}\sum_{\vec{k},\ \nu}\omega^2(\vec{k},\ \nu)\cdot X(\vec{k},\ \nu)X^*(\vec{k},\ \nu)
\end{aligned}\tag{2.46}$$

Then, the Hamiltonian of the dynamic system H can also be written in the form of

$$H=\frac{1}{2}\sum_{\vec{k},\ \nu}\dot{X}(\vec{k},\ \nu)\dot{X}^*(\vec{k},\ \nu)+\frac{1}{2}\sum_{\vec{k},\ \nu}\omega^2(\vec{k},\ \nu)\cdot X(\vec{k},\ \nu)X^*(\vec{k},\ \nu)\tag{2.47}$$

For the harmonic normal modes, one can have

$$\dot{X}(\vec{k},\ \nu)=i\omega(\vec{k},\ \nu)X(\vec{k},\ \nu)\tag{2.48}$$

Therefore, for the harmonic system, the Hamiltonian of the dynamic system can be approximated to

$$H\approx\sum_{\vec{k},\ \nu}\dot{X}(\vec{k},\ \nu)\dot{X}^*(\vec{k},\ \nu)\tag{2.49}$$

Knowing the normal mode coordinates, the relaxation time of vibration in crystals can be calculated, which will be discussed below. Another important parameter

to calculate lattice thermal conductivity is phonon group velocity $\vec{v}_g(\vec{k},\ \nu)$

$$\vec{v}_g(\vec{k},\ \nu) = \frac{\partial\omega(\vec{k},\ \nu)}{\partial\vec{k}} \tag{2.50}$$

From the expression above, we can know $\vec{v}_g(\vec{k},\ \nu)$ can be obtained once the phonon dispersion is solved.

2.3 Density Functional Theory

In principle, any solid can be completely described by solving the time-dependent Schrodinger equation (Schrödinger, 1926).

$$\hat{H}\Psi = i\hbar\frac{\partial\Psi}{\partial t} \tag{2.51}$$

where Ψ is a many body wavefunction which depends on the set of spatial coordinates of electrons, nuclei and spin at each point in time.

$$\Psi = \Psi(\vec{r}^{\,e}_1, \ldots, \vec{r}^{\,e}_{N_e};\ \vec{r}^{\,n}_1, \ldots, \vec{r}^{\,n}_{N_n};\ t) \tag{2.52}$$

where $\vec{r}^{\,e}_i$and $\vec{r}^{\,n}_i$ are the electronic and nuclear positions. To simplify the notion, we implicitly ignore the spin coordinate for the electrons in $\vec{r}^{\,e}_i$. The Hamiltonian operator of a non-relativistic system of N_e interacting electrons and N_n nuclei can be written as

$$\hat{H} = \hat{K}_e + \hat{K}_n + \hat{P}_{ee} + \hat{P}_{en} + \hat{P}_{nn} \tag{2.53}$$

where $\hat{K}_e$and $\hat{K}_n$ are the kinetic energies of electrons and nuclei, and have the form of

$$\hat{K}_e = -\sum_{i=1}^{N_e}\frac{\hbar}{2m_e}\nabla_i^2 \tag{2.54}$$

and

$$\hat{K}_n = -\sum_{i=1}^{N_n}\frac{\hbar}{2m_n}\nabla_i^2 \tag{2.55}$$

in which, m_e and m_n are the mass of the electron and nucleus, respectively. Indices i run over the electronic and nuclei degrees of freedom.

The electron-electron Coulomb interactions $\hat{P}_{ee}$ and nuclear-nuclear interactions $\hat{P}_{nn}$ have the formula of

$$\hat{P}_{ee} = -\sum_{i\neq j}^{N_e}\frac{e^2}{\left|\vec{r}^{\,e}_i - \vec{r}^{\,e}_j\right|} \tag{2.56}$$

and

$$\hat{P}_{nn} = -\frac{1}{2}\sum_{k\neq l}^{N_n}\frac{Z_k Z_l e^2}{\left|\vec{r}^{\,n}_k - \vec{r}^{\,n}_l\right|} \tag{2.57}$$

where e, $Z_{k\ or\ l}$ and $-eZ_{k\ or\ l}$ are the negative charge of electron, the atomic number and positive charge of nuclei k or l. The potential energy of the interaction between electron and nuclei $\hat{P}_{en}$ can be written as

$$\hat{P}_{nn} = -\sum_{i}^{N_e}\sum_{k}^{N_n}\frac{Z_k e}{|\vec{r}_i^{\,e} - \vec{r}_k^{\,n}|} \tag{2.58}$$

The resulting Eq. (2.51) can be only exactly solved for the simplest system. The most popular way to solve it is to use the Born-Oppenheimer approximation, in which, we firstly separate the nuclei and electronic degrees of the freedom due to the great difference in masses. The kinetic energy of the nuclei is so small since $m_e/m_n = 10^{-3}$, we then can treat the $\hat{K}_n$ as a perturbation to the rest of the Hamiltonian and are left with

$$\hat{H}_0 = \hat{K}_e + \hat{P}_{ee} + \hat{P}_{en} + \hat{P}_{nn} \tag{2.59}$$

Meanwhile, since the nuclei moves more slowly than the electrons, we can assume that the electronic configuration is determined by the instantaneous nuclear configuration and will relax to its ground state more rapidly than the timescale of nuclear vibrations. It indicates the nuclear potential $\hat{P}_{nn}$ at an instantaneous configuration can be fixed for the electronic problem. That means, for the electrons, we can solve Eq. (2.51) for the fixed nuclear positions, and the electronic wavefunction depends on the position of the nuclei only parametrically via $\vec{r}_k^{\,n}$ at any given time

$$\hat{H}_e = \hat{K}_e + \hat{P}_{ee} + \hat{P}_{ne} \tag{2.60}$$

and

$$\hat{H}_e\Psi(\vec{r}_1^{\,e},\ldots,\vec{r}_{N_e}^{\,e};\ \vec{r}_1^{\,n},\ldots,\vec{r}_{N_n}^{\,n}) = i\hbar\frac{\partial\Psi(\vec{r}_1^{\,e},\ldots,\vec{r}_{N_e}^{\,e};\ \vec{r}_1^{\,n},\ldots,\vec{r}_{N_n}^{\,n})}{\partial t} \tag{2.61}$$

The Eq. (2.61) is still too complex to solve. The most successful method to solve this equation is using the density functional theory (DFT) which is generated by Hohenberg and Kohn in 1964 (Hohenberg and Kohn, 1964). The key idea is to replace the many body problem in Eq. (2.61) with an equation of electron density which only depends on three spatial coordinates $\vec{r}(\vec{x},\ \vec{y},\ \vec{z})$ containing the electronic degrees of freedom implicitly. Two theorems make this formulation possible:
I, the potential $\hat{P}_{ne}$ is uniquely determined by the ground state density $\eta_0(\vec{r})$, up to an arbitrary constant.
II, any potential $\hat{P}_{ne}$ has a universal function $E^{HK}(\eta)$ and can be determined by the density. The ground state for any specific external potential $\hat{P}_{ne}$ can be found by minimizing the total functional $E_t(\eta)$.

The Hohenberg-Kohn functional is defined as

$$E^{HK}(\eta) = E_t(\eta) + \int d\vec{r}^{\,e}\,\hat{P}_{en}(\vec{r})\eta(\vec{r}) \tag{2.62}$$

The Kohn-Sham (KS) ansatz (Kohn and Sham, 1965) is to replace the real electrons with non-interacting quasi-particles that produce the correct ground state density, and gather all the unknown terms in one term named exchange and correlation. The universal functional then can be written as

$$\begin{aligned} E^{HK}(\eta) &= K(\eta) + E_{XC}(\eta) + P_{ee}(\eta) + \int d\vec{r}\hat{P}_{en}(\vec{r})\eta(\vec{r}) \\ &= K(\eta) + E_{XC}(\eta) + \frac{1}{2}\int\int \frac{\eta(\vec{r}) - \eta(\vec{r}')}{|\vec{r} - \vec{r}'|} d\vec{r}d\vec{r}' + \int d\vec{r}\hat{P}_{en}(\vec{r})\eta(\vec{r}) \end{aligned} \tag{2.63}$$

where the second term on the right of Eq. (2.63) E_{XC} is the *exchange-correlation functional*, which is the remaining non-coulombic electron-electron interaction. Then, a set of Schrodinger-like equations can be obtained

$$\hat{H}_{KS}\varphi_i(\vec{r}) = \varepsilon_i\varphi_i(\vec{r}) \tag{2.64}$$

in which, $\hat{H}_{KS}$ is the KS Hamiltonian operator, and has the form of

$$\hat{H}_{KS} = -\frac{\hbar^2}{2m_e}\nabla_i^2 + P_{en}(\vec{r}) + P_{ee}(\vec{r}) + E_{XC}(\vec{r}) \tag{2.65}$$

The electron density then can be recovered from the KS orbitals $\varphi_i(\vec{r})$ using

$$\eta(\vec{r}) = \sum_{i=1}^{N} |\varphi_i(\vec{r})|^2 \tag{2.66}$$

The KS equation [Eq. (2.64)] can be solved via the method of Lagrange multipliers, subject to the constraint of

$$N_e = \int \eta(\vec{r})d\vec{r} \tag{2.67}$$

It indicates that the number of electrons should be constant. Since the electron density $\eta(\vec{r})$ appears in both sides of the KS equation, the KS equation must be solved self-consistently. In principle, the KS equation can be solved exactly. However, the exchange-correlation functional $E_{XC}(\vec{r})$ has no known analytic form. The most popular way to approximate it is to rewrite exchange-correlation functional using a Taylor expansion

$$E_{XC} = \int \varepsilon_{XC}(\eta)\eta(\vec{r})d\vec{r} + \int \varepsilon_{XC}^2(\eta)|\nabla\eta(\vec{r})|^2 d\vec{r} + \dots \tag{2.68}$$

where ε_{XC} is the exchange-correlation energy per electron. Firstly, we can assume that the exchange and correlation effects are short-ranged in solids, and the electron density then varies slowly. In such systems, the Eq. (2.68) can be truncated after the first term which is called *local density approximation* (LDA). The second way is to introduce the gradient of the electron density in $E_{XC}(\vec{r})$, which is more complicated than just including the second order expansion in Eq. (2.68). Such method is named

the *generalized gradient approximation* (GGA).

The natural representation of electronic wavefunctions in crystalline systems is planes waves, which are periodic by definition. Bloch's theorem states that a wavefunction can be expanded in plane waves with exponential wave-like component and a cell-periodic component ξ

$$\varphi_j(\vec{r}) = \xi_j(\vec{r})e^{i\vec{k}\cdot\vec{r}} \tag{2.69}$$

where $\vec{k}$ is the wave vector in reciprocal space. The cell-periodic component ξ can be expanded as

$$\xi_j(\vec{r}) = \sum_G \varsigma_j(\vec{k}+\vec{G})e^{i\vec{G}\vec{r}} \tag{2.70}$$

in which, $\vec{G}$ is the reciprocal space lattice vector, and ς is the coefficient to be determined. Then, Eq. (2.69) can rewritten as

$$\varphi_j(\vec{r}) = \sum_G \varsigma_j(\vec{k}+\vec{G})e^{i(\vec{G}+\vec{k})\vec{r}} \tag{2.71}$$

The precision of the practical calculation in DFT is determined by the cutoff of the plane wave. It determines the maximum kinetic energy $\hbar^2\left|\vec{G}+\vec{k}\right|^2/2$ are kept in the calculation. Another point we need to care is the translational symmetry of the system, which can be expressed via the Born-Von Karman or cyclic boundary conductions. In such condiction, the wavefunction must have the periodicity of the lattice

$$\varphi_j(\vec{r}+\vec{R}) = \varphi_j(\vec{r}) \tag{2.72}$$

where $\vec{R}$ is the lattice vector, and $e^{i\vec{R}\vec{G}} = 1$. All the wavefunction solutions will be reduced to the first Brillouin zone when the lattice vector is transformed to reciprocal space, which means

$$\varphi_j(\vec{k}+\vec{G}) = \varphi_j(\vec{k}) \tag{2.73}$$

Theoretically, the wavefunctions in the reciprocal unit cell, or equivalently the first Brillouin zone, are sufficient since the lattice of the crystalline is infinite. However, in practice, it is impossible to perform a continuous sampling of the Brillouin zone, and a numerical quadrature has to replace any integral. The nodes of this quadrature are called "k-points" in the DFT calculations. A converge test of "k-points" must be implemented for the DFT calculations.

Two problems should be noticed when a plane wave is used. Firstly, the plane wave is cell-dependent, so it is expensive to deal with systems including large vacuum in the same way with that of bulk material. The second one is that core electrons have wavefuctions that vary significant rapidly near the atomic nuclei, and therefore require high frequency plane waves, i.e., high cutoff, in the expansion.

2.4 Boltzmann Transport Equation

2.4.1 Heat transport by phonons

It is commonly known that the heat flux will exist in the medium when a temperature gradient $\nabla T$is applied in the system. The flux of heat $\vec{Q}$ in the system, which is related to the phonon energy $\hbar\omega(\vec{k},\ \nu)$, phonon group velocity $\vec{v}_g(\vec{k},\ \nu)$, the perturbed phonon population $n(\vec{k},\ \nu)$ and equilibrium phonon population $n_0(\vec{k},\ \nu)$ can be written as

$$\vec{Q} = \frac{1}{V}\sum_{\vec{k},\ \nu} \hbar\omega(\vec{k},\ \nu)\vec{v}_g(\vec{k},\ \nu)\Big[n(\vec{k},\ \nu) - n_0(\vec{k},\ \nu)\Big] \tag{2.74}$$

where V is the volume of system. The equilibrium phonon population $n_0(\vec{k},\ \nu)$ is usually took the form of Bose-Einstein distribution function

$$n_0(\vec{k},\ \nu) = \frac{1}{e^{\hbar\omega(\vec{k},\ \nu)/k_BT} - 1} \tag{2.75}$$

where k_B is the Boltzmann constant. In order to solve the above equations, the control equation, namely Boltzmann transport equation (BTE) (Peierls, 1955), is requested

$$-\vec{v}_g(\vec{k},\ \nu)\cdot\nabla n(\vec{k},\ \nu) + \left.\frac{\partial n(\vec{k},\ \nu)}{\partial t}\right|_{scattering} = 0 \tag{2.76}$$

In the general approach, for small perturbation from the equilibrium, we can rewrite the first term of Eq. (2.76) into

$$\vec{v}_g(\vec{k},\ \nu)\cdot\nabla n(\vec{k},\ \nu) = \vec{v}_g(\vec{k},\ \nu)\cdot\frac{\partial n(\vec{k},\ \nu)}{\partial T}\nabla T \approx \vec{v}_g(\vec{k},\ \nu)\cdot\frac{\partial n_0(\vec{k},\ \nu)}{\partial T}\nabla T \tag{2.77}$$

Using the single relaxation time approximation (RTA), the second term in Eq. (2.76) can be substituted using the relaxation time $\tau(\vec{k},\ \nu)$

$$\left.\frac{\partial n(\vec{k},\ \nu)}{\partial t}\right|_{scattering} = \frac{n(\vec{k},\ \nu) - n_0(\vec{k},\ \nu)}{\tau(\vec{k},\ \nu)} \tag{2.78}$$

Combining Eq. (2.74) to Eq. (2.78) with the Fourier law $\vec{Q} = -\kappa\nabla T$, in which is the thermal conductivity, we can find that

$$\kappa = \sum_{\vec{k},\ \nu} c(\vec{k},\ \nu)\tau(\vec{k},\ \nu)\vec{v}_g(\vec{k},\ \nu)\otimes\vec{v}_g(\vec{k},\ \nu) \tag{2.79}$$

where $c(\vec{k},\ \nu)$ is the volumetric phonon specific heat and has the form of

$$c(\vec{k},\ \nu) = \frac{1}{V}\left[\frac{\hbar\omega(\vec{k},\ \nu)}{k_BT}\right]^2 n_0(\vec{k},\ \nu)\Big[n_0(\vec{k},\ \nu) + 1\Big] \tag{2.80}$$

On the other hand, the Eq. (2.76), which is also called Cattaneo-Vernotte's relation (Cattaneo, 1958; Vernotte, 1958), implies the heat flux fluctuation around the equilibrium state. Therefore, when the macroscopic heat flux takes a zero value, the right part of Eq. (2.78) can be written as (Ladd, Moran, and Hoover, 1986)

$$n(\vec{k},\ \nu;\ t) - n_0(\vec{k},\ \nu) = \Big[n(\vec{k},\ \nu;\ 0) - n_0(\vec{k},\ \nu)\Big]\, e^{-t/\tau(\vec{k},\ \nu)} \tag{2.81}$$

Then, the most popular form used to calculate the relaxation time in the MD simulation which is also called time domain normal mode analysis (TDNMA) (Henry and Chen, 2008), can be obtained using the autocorrelation of the phonon population function

$$\Big\langle \delta n(\vec{k},\ \nu;\ t)\delta n(\vec{k},\ \nu;\ 0)\Big\rangle = \Big\langle \delta n(\vec{k},\ \nu;\ t)\delta n(\vec{k},\ \nu;\ 0)\Big\rangle\, e^{-t/\tau(\vec{k},\ \nu)} \tag{2.82}$$

in which,

$$\delta n(\vec{k},\ \nu) = n(\vec{k},\ \nu) - n_0(\vec{k},\ \nu) \tag{2.83}$$

Furthermore, since $n(\vec{k},\ \nu)$ is proportional to the phonon energy $E(\vec{k},\ \nu)$, which can be obtained by Eq. (2.47), the expression above can also be written in the form of

$$\Big\langle \delta E(\vec{k},\ \nu;\ t)\delta E(\vec{k},\ \nu;\ 0)\Big\rangle = \Big\langle \delta E(\vec{k},\ \nu;\ t)\delta E(\vec{k},\ \nu;\ 0)\Big\rangle\, e^{-t/\tau(\vec{k},\ \nu)} \tag{2.84}$$

in which, $\delta E(\vec{k},\ \nu)$ means the transient phonon energy difference with respect to the equilibrium phonon energy. Therefore, the phonon life time can be computed

$$\tau(\vec{k},\ \nu) = \int_0^{t^*} \frac{\Big\langle \delta E(\vec{k},\ \nu;\ t)\delta E(\vec{k},\ \nu;\ 0)\Big\rangle}{\Big\langle \delta E(\vec{k},\ \nu;\ t)\delta E(\vec{k},\ \nu;\ 0)\Big\rangle} dt \tag{2.85}$$

Then, the thermal conductivity can be calculated using Eq. (2.79). On the other hand, assuming the scattering term expanded to its first-order perturbation $f^1_{(\vec{k},\ \nu)}$ (Fugallo et al., 2013; Omini and Sparavigna, 1995) we have

$$n(\vec{k},\ \nu) \approx n_0(\vec{k},\ \nu) + n_0(\vec{k},\ \nu)\Big[n_0(\vec{k},\ \nu) + 1\Big]\frac{\partial T}{\partial z} f^1_{(\vec{k},\ \nu)} \tag{2.86}$$

Combing Eq. (2.74) and Eq. (2.86), we can find

$$\vec{Q} = \frac{1}{NV_0}\sum_{\vec{k},\ \nu} \hbar\omega(\vec{k},\ \nu)\vec{v}_g(\vec{k},\ \nu)n_0(\vec{k},\ \nu)\Big[n_0(\vec{k},\ \nu) + 1\Big]\nabla T \cdot f^1_{(\vec{k},\ \nu)} \tag{2.87}$$

where N and V_0 are the number and volume of unit cell, respectively. Basing on the Fourier law $\vec{Q} = -\kappa\nabla T$, the thermal conductivity tensor κ can be written as

$$\kappa = \frac{1}{NV_0}\sum_{\vec{k},\ \nu} \hbar\omega(\vec{k},\ \nu)\Big[\vec{v}_g(\vec{k},\ \nu)\otimes\vec{l}\Big]n_0(\vec{k},\ \nu)\Big[n_0(\vec{k},\ \nu) + 1\Big] f^1_{(\vec{k},\ \nu)} \tag{2.88}$$

From the expression above, it is easy to know the key point to calculate the thermal conductivity is to compute the first-order perturbation. We firstly write the linearized BTE of Eq. (2.76)

$$-c(\vec{k},\ \nu)(\frac{\partial n_0(\vec{k},\ \nu)}{\partial T}) = \sum_{(\vec{k}',\ \nu'),\ (\vec{k}'',\ \nu'')} \Big[\Gamma^{(\vec{k},\ \nu)}_{(\vec{k}',\ \nu'),\ (\vec{k}'',\ \nu'')}(f^1_{(\vec{k},\ \nu)} + f^1_{(\vec{k}',\ \nu')} - f^1_{(\vec{k}'',\ \nu'')}) \\ \frac{1}{2}\Gamma^{(\vec{k}',\ \nu'),\ (\vec{k}'',\ \nu'')}_{(\vec{k},\ \nu)}(f^1_{(\vec{k},\ \nu)} - f^1_{(\vec{k}',\ \nu')} - f^1_{(\vec{k}'',\ \nu'')})\Big] \tag{2.89}$$

where Γ is the scattering rate at equilibrium of a process where a phonon mode is scattered by absorbing another phonon to generate the third phonon or decayed to two different phonons. The scattering rate matrix can be obtained based on the Fermi's golden rule

$$\begin{aligned}\Gamma^{(\vec{k},\ \nu)}_{(\vec{k}',\ \nu'),\ (\vec{k}'',\ \nu'')} &= \frac{2\pi}{N\hbar^2}\sum_{\vec{G}}\left|\Xi^3(\vec{k},\ \nu;\ \vec{k}',\ \nu';\ \vec{k}'',\ \nu'')\right|^2 \\ &\times n_0(\vec{k},\ \nu)n_0(\vec{k}',\ \nu')[n_0(\vec{k}'',\ \nu'')+1]\delta(\vec{k}+\vec{k}'-\vec{k}''\pm\vec{G}) \\ &\times \delta\left[\hbar\omega(\vec{k},\ \nu)+\hbar\omega(\vec{k}',\ \nu')-\hbar\omega(\vec{k}'',\ \nu'')\right]\end{aligned} \tag{2.90}$$

and

$$\begin{aligned}\Gamma^{(\vec{k}',\ \nu'),\ (\vec{k}'',\ \nu'')}_{(\vec{k},\ \nu)} &= \frac{2\pi}{N\hbar^2}\sum_{\vec{G}}\left|\Xi^3(\vec{k},\ \nu;\ -\vec{k}',\ \nu';\ -\vec{k}'',\ \nu'')\right|^2 \\ &\times n_0(\vec{k},\ \nu)\left[n_0(\vec{k}',\ \nu')+1\right]n_0(\vec{k}'',\ \nu'')\delta(\vec{k}-\vec{k}'-\vec{k}''\pm\vec{G}) \\ &\times \delta\left[\hbar\omega(\vec{k},\ \nu)-\hbar\omega(\vec{k}',\ \nu')-\hbar\omega(\vec{k}'',\ \nu'')\right]\end{aligned} \tag{2.91}$$

with $\vec{G}$ is the reciprocal lattice vector. Ξ^3 is the three-phonon matrix element and can be given by

$$\Xi^3(\vec{k},\ \nu;\ -\vec{k}',\ \nu';\ -\vec{k}'',\ \nu'') = \frac{\partial^3 E^{cell}}{\partial X(\vec{k},\ \nu)\partial X(\vec{k}',\ \nu')\partial X(\vec{k}'',\ \nu'')} \tag{2.92}$$

with E^{cell} is the energy of the unit cell. X is *normal mode like coordinate* and can be shown as

$$X(\vec{k},\ \nu) = \frac{1}{N}\sum_{j}^{N_b}\sum_{i}^{N}\sqrt{\frac{2M\omega(\vec{k},\ \nu)}{\hbar}}\vec{e}^*(j;\ \vec{k},\ \nu)\vec{u}(\vec{R}_l)exp(-\vec{k}\cdot\vec{R}_l) \tag{2.93}$$

where j and i are the indices of the atoms in the unit cell and the unit cell, respectively. Then, the only unknown parameter in Eq. (2.89) is the first-order perturbation $f^1_{(\vec{k},\ \nu)}$. Such an equation can be solved iteratively with the inputs of scattering rate Eq. (2.90) and Eq. (2.91), or equivalently, the relaxation time. This is the most popular (or may be only valid) method to calculate the lattice thermal conductivity in first principle calculations.

2.4.2 Charge transport by carriers

The electron distribution function $N_0^{F-D}(i,\ \vec{k};\ \vec{r})$ follows the Fermi-Dirac function. It undergoes deformation with an external field and the BTE assumes that the scatterings restore the distribution function to the original one, which means in the steady conduction, we have (Ziman, 1960)

$$\left.\frac{\partial N_0^{F-D}(i,\ \vec{k};\ \vec{r})}{\partial t}\right|_{diff}+\left.\frac{\partial N_0^{F-D}(i,\ \vec{k};\ \vec{r})}{\partial t}\right|_{drift}+\left.\frac{\partial N_0^{F-D}(i,\ \vec{k};\ \vec{r})}{\partial t}\right|_{scattering}=0 \quad (2.94)$$

when only a weak external direct current electric field is considered, we can know

$$\left.\frac{\partial N_0^{F-D}(i,\ \vec{k};\ \vec{r})}{\partial t}\right|_{drift}=-\vec{k}\frac{\partial N_0^{F-D}(i,\ \vec{k};\ \vec{r})}{\partial \vec{k}}=\frac{e}{\hbar}\vec{E}\nabla_{\vec{k}}N_0^{F-D}(i,\ \vec{k};\ \vec{r}) \quad (2.95)$$

Ignoring the diffusion term in Eq. (2.94), then we have

$$-\frac{e}{\hbar}\vec{E}\nabla_{\vec{k}}N_0^{F-D}(i,\ \vec{k};\ \vec{r})=\left.\frac{\partial N_0^{F-D}(i,\ \vec{k};\ \vec{r})}{\partial t}\right|_{scattering} \quad (2.96)$$

where $\vec{E}$ is the external electric field and i is the index of the band structure. Under the relaxation time approximation, we can know

$$-\frac{e}{\hbar}\vec{E}\nabla_{\vec{k}}N_0^{F-D}(i,\ \vec{k};\ \vec{r})=\frac{N^{F-D}(i,\ \vec{k};\ \vec{r})-N_0^{F-D}(i,\ \vec{k};\ \vec{r})}{\tau_e(i,\ \vec{k};\ \vec{r})} \quad (2.97)$$

in which, $N^{F-D}(i,\ \vec{k};\ \vec{r})$ is the local concentration of electrons in the state $(i,\ \vec{k})$ in the neighborhood of the point $\vec{r}$ in the real space and is assumed to deviate not far from the $N_0^{F-D}(i,\ \vec{k};\ \vec{r})$. $\tau_e(i,\ \vec{k};\ \vec{r})$ is the relaxation time from $N^{F-D}(i,\ \vec{k};\ \vec{r})$ to $N_0^{F-D}(i,\ \vec{k};\ \vec{r})$ when the external filed is removed. Combing Eq. (2.96) and Eq. (2.97), we have

$$N^{F-D}(i,\ \vec{k};\ \vec{r})=N_0^{F-D}(i,\ \vec{k};\ \vec{r})+e\tau_e(i,\ \vec{k};\ \vec{r})\frac{\partial N_0^{F-D}(i,\ \vec{k};\ \vec{r})}{\partial\varepsilon(i,\ \vec{k})}\vec{E}\cdot\vec{v}(i,\ \vec{k}) \quad (2.98)$$

where $\vec{v}(i,\ \vec{k})$ and $\varepsilon(i,\ \vec{k})$ are the group velocity and band energy, respectively. Meanwhile, the scattering term can be expressed as

$$\begin{aligned}\left.\frac{\partial N_0^{F-D}(i,\ \vec{k};\ \vec{r})}{\partial t}\right|_{scattering}=\sum_{(j,\ \vec{k}')}\Big\{&\Theta(j,\ \vec{k}';\ i,\ \vec{k})N^{F-D}(j,\ \vec{k}')\left[1-N^{F-D}(i,\ \vec{k})\right]\\&-\Theta(i,\ \vec{k};\ j,\ \vec{k}')N^{F-D}(i,\ \vec{k})[1-N^{F-D}(j,\ \vec{k}')]\Big\}\end{aligned} \quad (2.99)$$

where $\Theta(j,\ \vec{k}';\ i,\ \vec{k})$ is the transition probability from electronic state $(j,\ \vec{k}')$ to $(i,\vec{k})$ and can written as

$$\Theta(j,\ \vec{k}';\ i,\vec{k}) = \frac{2\pi}{\hbar}\left|M(i,\vec{k};\ j,\ \vec{k}')\right|^2 \delta[\varepsilon(j,\ \vec{k}') - \varepsilon(i,\vec{k})] \tag{2.100}$$

in which,

$$M(i,\vec{k};\ j,\ \vec{k}') = \left\langle (i,\vec{k}) \right| \Delta P \left| (j,\ \vec{k}') \right\rangle) \tag{2.101}$$

which describes the scattering from state $(j,\vec{k}')$ to $(i,\vec{k})$ by deviating the potential (ΔP) arising from the atomic displacement associated with the phonons or the perturbation potential (ΔP) caused by the defects or impurities. At the equilibrium state, we have

$$\begin{aligned}&\Theta(j,\ \vec{k}';\ i,\ \vec{k})N^{F-D}(j,\ \vec{k}')[1 - N^{F-D}(i,\ \vec{k})] = \\ &\Theta(i,\ \vec{k};\ j,\ \vec{k}')N^{F-D}(i,\ \vec{k})[1 - N^{F-D}(j,\ \vec{k}')]\end{aligned} \tag{2.102}$$

Eq. (2.102) can be simplified further by using the Fermi-Dirac function

$$\Theta(j,\ \vec{k}';\ i,\ \vec{k}) \exp\left[\frac{\varepsilon(i,\ \vec{k})}{k_B T}\right] = \Theta(i,\ \vec{k};\ j,\ \vec{k}') \exp\left[\frac{\varepsilon(j,\ \vec{k}')}{k_B T}\right] \tag{2.103}$$

For the elastic scattering, $\varepsilon(i,\ \vec{k}) = \varepsilon(j,\ \vec{k}')$, we can have

$$\Theta(j,\ \vec{k}';\ i,\ \vec{k}) = \Theta(i,\ \vec{k};\ j,\ \vec{k}') \tag{2.104}$$

Therefore, Eq. (2.99) can be rewritten in the form of

$$\left.\frac{\partial N_0^{F-D}(i,\ \vec{k};\ \vec{r})}{\partial t}\right|_{scattering} = -\sum_{(j,\ \vec{k}')} \left\{\Theta(j,\ \vec{k}';\ i,\ \vec{k})\left[N^{F-D}(j,\ \vec{k}') - N^{F-D}(i,\ \vec{k})\right]\right\} \tag{2.105}$$

Combining Eq. (2.97), Eq. (2.98) and Eq. (2.105), the relaxation time of electrons can be obtained

$$\begin{aligned}\frac{1}{\tau_e(i,\ \vec{k})} =& \frac{2\pi}{\hbar}\sum_{j,\ \vec{k}'}\left|M(j,\ \vec{k}';\ i,\ \vec{k})\right|^2 \delta[\varepsilon(j,\ \vec{k}') - \varepsilon(i,\ \vec{k})] \\ &\times\left[1 - \frac{\tau_e(j,\ \vec{k}')\vec{v}(j,\ \vec{k}')\cdot\vec{e}_E}{\tau_e(i,\ \vec{k})\vec{v}(i,\ \vec{k})\cdot\vec{e}_E}\right]\end{aligned} \tag{2.106}$$

where $\vec{e}_E$ is the unit vector along the electric filed. Clearly, Eq. (2.106) has only one unknown variable $\tau_e(i,\ \vec{k})$, which means it can be solved iteratively. For the external field direction of β, Eq. (2.106) can be also approximated as

$$\frac{1}{\tau_e(i,\ \vec{k})} = \frac{2\pi}{\hbar}\sum_{j,\ \vec{k}'}\left|M(j,\ \vec{k}';\ i,\ \vec{k})\right|^2 \delta[\varepsilon(j,\ \vec{k}') - \varepsilon(i,\ \vec{k})]\cdot\left[1 - \frac{v_\beta(j,\ \vec{k}')}{v_\beta(i,\ \vec{k})}\right] \tag{2.107}$$

To calculate the electronic transport properties, the most popular approach assumes that the electronic band structure is unchanged with doping and only the Fermi level is shifted. Then, we have

$$\sigma(T;\ \mu) = \frac{1}{V_0}\int \mathbf{\Pi}(\xi)\left[-\frac{\partial N_0^{F-D}(T;\ \mu)}{\partial \xi}\right]d\xi \tag{2.108}$$

$$\kappa_e(T;\ \mu) = \frac{1}{e^2 T V_0}\int \mathbf{\Pi}(\xi)(\xi-\mu)^2\left[-\frac{\partial N_0^{F-D}(T;\ \mu)}{\partial \xi}\right]d\xi \tag{2.109}$$

$$\mathrm{S}(T;\ \mu) = \frac{1}{eTV_0\sigma(T;\ \mu)}\int \mathbf{\Pi}(\xi)(\xi-\mu)\left[-\frac{\partial N_0^{F-D}(T;\ \mu)}{\partial \xi}\right]d\xi \tag{2.110}$$

where μ is the Fermi level. $\mathbf{\Pi}$ is the transport distribution function tensor and can be written as

$$\mathbf{\Pi}(\xi) = \frac{1}{N}\sum_{i,\ \vec{k}} e^2\tau_e(i,\ \vec{k})[\vec{v}(i,\ \vec{k})\otimes\vec{v}(i,\ \vec{k})]\left[-\frac{\delta(\xi-\xi_{i,\ \vec{k}})}{d\xi}\right] \tag{2.111}$$

in which, N is the number of k-points sampling.

2.5 Conclusion

In this chapter, we firstly introduce the methods for thermal conductivity in molecular dynamics:-GK-EMD and NEMD simulations. GK-EMD method is based on the fluctuation of heat flux and inherently including all the order scattering processes. While the NEMD simulations apply a temperature gradient and measuring the corresponding heat flux or vice versa. Thermal conductivity can be then extracted via Fourier's law. The inherent shortcoming in the NEMD simulations is the size effect, which can be avoided via doing the expansion of the thermal conductivity. MD simulations have been proved to provide the fairly robust thermal conductivity. The main challenge is that the classic distribution in the simulations which limits the simulations only valid in the high temperature range ($T > T_D/2$), in which the quantum effect is not important.

In order to study the phonon mode properties, lattice dynamics method is proposed. The *phonon dispersion*, *phonon group velocity* and *phonon energy* which can be used to calculate the relaxation time in the MD simulations, can be calculated in the frame of lattice dynamics. Finally, combing with BTE, both the modal and total thermal conductivity can be obtained in lattice dynamics. Such information is quite useful to help better understand heat transport behaviors in different systems.

To calculate the electrical transport properties or the thermal transport via first principles calculations. Density function theory is used as a principle tool to provide the basic information such as force constants and band structure. A brief introduction of DFT is introduced in this chapter.

Finally, the methods used to calculate the thermal and electrical transport properties based on the BTE, including TDNMA and iterative method of solving BTE (both for the phonons and electrons) are deduced in details in this chapter.

In the following chapters, these methods introduced here will be either used as a foundation and validation tool for my new method or implemented directly to provide the underlying information such as phonon relaxation time and modal thermal conductivity.

Chapter 3

New Algorithm Development Based on NEMD

3.1 Introduction

Understanding the mechanisms of heat transfer, especially at small scales, is of crucial importance to improve the function and performance of devices in many nanotechnology applications (Cahill et al., 2014), such as thermal barrier coatings, novel thermoelectrics (energy conversion), heat sink materials (Bergman et al., 2011), etc. Traditionally, some methods from continuum level have been proposed and applied to predict the phonon mode contribution of thermal conductivity. Klemens (Klemens, 1955; Klemens, 1951) and other researchers (Casimir, 1938; Holland, 1964; Berman, Simon, and Ziman, 1953; Herring and Vogt, 1956) obtained the spectral contribution to thermal conductivity based on long-wave approximation and Debye model. The third-order anharmonic lattice dynamic (ALD) calculation was firstly proposed by Maradudin *et al*. (Maradudin and Fein, 1962) and then extended by Debernardi *et al*. (Debernardi, Baroni, and Molinari, 1995) and Deinze *et al*. (Deinzer, Birner, and Strauch, 2003). Later on, Omini and Sparaviga (Omini and Sparavigna, 1996) proposed an iterative scheme to give exact solutions to the linearized BTE and then obtained the lattice thermal conductivity. However, all these methods can only deal with relatively simple systems such as perfect bulk crystalline materials and cannot assess the effect of defects from the real atomic model.

In principle, heat transfer at nanosacle may differ significantly from that in macro- and micro-scales (Lienhard, 2013). With characteristic length of devices or structures becoming comparable to or even smaller than the phonon MFP and wavelength of heat carriers (mainly refers to phonons herein), conventional heat transfer theory is no longer valid. Tremendous progress has been made in the past two decades to understand and characterize heat transfer at nanoscales or in nanostructures (Luo and Chen, 2013). From numerical modeling point of view, atomistic simulations such as classical MD and Green's function method, and the phonon-level calculations such as Boltzmann transport equation (BTE) combined with *ab initio*, are quite useful approaches to characterize the intrinsic properties of heat transfer at nanoscale (Feng and Ruan, 2014). Here, we focus on classical MD method where the phonon-phonon

interactions at all levels of orders are described exactly. So far, the two most commonly used approaches to predict the thermal conductivity in MD simulations are the GK method (Kubo, 1966) and the direct method (Schelling, Phillpot, and Keblinski, 2002a). Usually the former is also called EMD simulation and the latter is called NEMD simulation. Both GK-EMD and NEMD methods can predict the overall thermal conductivity, but give limited insight of the detailed phonon mode contribution. Recently, rigorous calculation of individual phonon mode contribution to the overall thermal transport based on EMD simulation has become available, namely the spectral energy density (SED) (Turney et al., 2009) and equivalently the TDNMA (Ladd, Moran, and Hoover, 1986; Henry and Chen, 2008) methods. Although they have successfully predicted the phonon behavior in perfect bulk systems, in particular mode specific phonon lifetime, both methods need some assumptions to obtain the modal thermal conductivity when they are deal with complicated systems, such as materials with interfaces or disorder materials. Furthermore, fitting the Lorentzian function in SED and the normalized autocorrelation function of the mode energy in TDNMA is sometimes nontrivial and may bring significant errors to the final result. Therefore, generating algorithms in the frame of NEMD to study the modal thermal conductivity is quite necessary.

3.2 Time Domain Direct Decomposition Method

In this section, we first propose a new method named time domain direct decomposition method (TDDDM), which is directly based on NEMD simulations, to calculate the contributions of individual phonon mode contribution to the overall thermal conductivity. Thus, in principle the TDDDM can be used as a tool to study the phonon behavior in nanostructures or the length of system along which the phonon travel is limited. It was well documented in literature that the size effect is very important when the average MFP is comparable to the system size (Schelling, Phillpot, and Keblinski, 2002a). Using the new method, we are able to investigate the size effect of individual phonon mode contribution, which cannot be realized by the previous SED and TDNMA methods that are based on EMD simulation. We find that the phonon modes with mean free path larger than the system size are truncated. Meanwhile, the thermal conductivity contributed by the Gamma point is rigorously proved to be zero by our TDDDM approach directly.

3.2.1 Framework of time domain direct decomposition method

The molecular dynamics expression of heat current was first derived by Irving and Kirkwood (Irving and Kirkwood, 1950), and then extended by Daichi *et. al.* (Torii, Nakano, and Ohara, 2008). The detailed formula of heat current can be written as

$$\vec{Q} = \left\langle \sum_j E_j \vec{v}_j - \mathrm{S}_j \vec{v}_j \right\rangle \tag{3.1}$$

where $\vec{Q}$ is the heat current, the sum is taken over all atoms in the interested volume, $\langle\rangle$ denotes the time average, E_j and $\mathbf{S}_j$ are the total energy and symmetric second order stress tensor of atom j, respectively. The detailed expression of $\mathbf{S}_j$ can be found in Ref. (McGaughey and Kaviany, 2004a).

According to the theory of lattice dynamics, we can write the displacement equation of any atom as (Dove, 1993)

$$\vec{u}(jl,\ t) = \sum_{\vec{k},\ \nu} \vec{U}(j,\ \vec{k},\ \nu) \exp(i[\vec{k} \cdot \vec{r}(jl) - \omega(\vec{k},\ \nu)t]) \tag{3.2}$$

where the sum is taken over all the wave vectors $\vec{k}$ and all phonon branches ν, $\vec{U}(j,\ \vec{k},\ \nu)$ is the amplitude vector that tells us how the atom j in the unit cell l moves induced by the phonon mode $(\vec{k},\ \nu)$, which gives the direction and the amplitude of the motion, and $\omega(\vec{k},\ \nu)$ is the vibrational frequency of the phonon mode $(\vec{k},\ \nu)$.

By applying space inverse Fourier transform to Eq. (3.2), we can obtain the normal mode coordinate of each vibrational mode

$$X(\vec{k},\ \nu;\ t) = \frac{1}{N^{1/2}} \sum_{jl} m_j^{1/2} \exp(-i\vec{k}\vec{r}(jl))\vec{e}^*(j,\ \vec{k},\ \nu)\vec{u}(jl,\ t) \tag{3.3}$$

where N is the total number of unit cells and $\vec{e}$ is the mode eigenvector , which can be obtained by diagonalizing the dynamic matrix $\mathrm{D}(\vec{k})$.

After that, based on Fourier transform, the displacement of each atom can be written using the normal mode coordinate $X(\vec{k},\ \nu;\ t)$ as

$$\vec{u}(jl,\ t) = \frac{1}{(Nm_j)^{1/2}} \sum_{\vec{k},\ \nu} \vec{e}(j,\ \vec{k},\ \nu) \exp(i\vec{k}\vec{r}(jl))X(\vec{k},\ \nu;\ t) \tag{3.4}$$

Since E_j and $\mathbf{S}_j$ in Eq. (3.1) are related to the displacement of atom j (Chalopin et al., 2014; Chalopin and Volz, 2013; Sääskilahti et al., 2015), their space Fourier transform, denoted by $\tilde{E}$ and $\tilde{\mathbf{S}}$, respectively, can be defined as

$$\tilde{E}(\vec{k},\nu;t) = \frac{1}{N^{1/2}} \sum_{jl} \vec{\xi}_1(j,\vec{k},\nu) \exp(i\vec{k}\vec{r}(jl))E(jl,t) \tag{3.5}$$

and

$$\tilde{\mathbf{S}}(\vec{k},\nu;t) = \frac{1}{N^{1/2}} \sum_{jl} \vec{\xi}_2(j,\vec{k},\nu) \exp(i\vec{k}\vec{r}(jl))\mathbf{S}(jl,t) \tag{3.6}$$

where the $\vec{\xi}_1$ and $\vec{\xi}_2$ represents the polarization vector of E and $\mathbf{S}$, respectively. Then, E_j and $\mathbf{S}_j$ can be rewritten as

$$E(jl,t) = \frac{1}{N^{1/2}} \sum_{jl} \vec{\xi}_1^*(j,\vec{k},\nu) \exp(-i\vec{k}\vec{r}(jl))\tilde{E}(\vec{k},\nu;t) \tag{3.7}$$

and

$$\mathbf{S}(jl,t) = \frac{1}{N^{1/2}} \sum_{jl} \vec{\xi}_2^*(\vec{j},k,\nu) \exp(-i\vec{k}\vec{r}(jl))\tilde{\mathbf{S}}(\vec{k},\nu;t) \tag{3.8}$$

Using Eq. (3.1), Eq. (3.4), Eq. (3.7) and Eq. (3.8), we can write the heat current contributed by each atom, $\vec{q}(jl)$, in the wave-vector reciprocal space as

$$\begin{aligned}
\vec{q}(jl) &= \langle (E(jl) - \mathbf{S}(jl))\vec{v}(jl) \rangle \\
&= \Bigg\langle \frac{1}{N^{1/2}} \Bigg\{ \sum_{\vec{k},\nu} \vec{\xi}_1^*(j,\vec{k},\nu) \exp(-i\vec{k}\vec{r}(jl))\tilde{E}(\vec{k},\nu) - \\
&\quad \sum_{k,\nu} \vec{\xi}_2^*(j,\vec{k},\nu) \exp(-i\vec{k}\vec{r}(jl))\tilde{\mathbf{S}}(\vec{k},\nu) \Bigg\} \cdot \\
&\quad \frac{1}{(Nm_j)^{1/2}} \sum_{\vec{k},\nu} \vec{e}(j,\vec{k},\nu) \exp(i\vec{k}\vec{r}(jl))\dot{X}(\vec{k},\nu) \Bigg\rangle
\end{aligned} \tag{3.9}$$

Here, we define the contribution of an individual phonon mode $(\vec{k},\ \nu)$ to the heat current of an individual atom (jl) as

$$\begin{aligned}
\vec{q}(jl,\vec{k},\nu) &= \Bigg\langle \frac{1}{N^{1/2}} \Bigg\{ \sum_{\vec{k},\nu} \vec{\xi}_1^*(j,\vec{k},\nu) \exp(-i\vec{k}\vec{r}(jl))\tilde{E}(\vec{k},\nu) - \\
&\quad \sum_{k,\nu} \vec{\xi}_2^*(j,\vec{k},\nu) \exp(-i\vec{k}\vec{r}(jl))\tilde{\mathbf{S}}(\vec{k},\nu) \Bigg\} \cdot \\
&\quad \frac{1}{(Nm_j)^{1/2}} \vec{e}(j,\vec{k},\nu) \exp(i\vec{k}\vec{r}(jl))\dot{X}(\vec{k},\nu) \Bigg\rangle
\end{aligned} \tag{3.10}$$

Thus, the heat current of each phonon mode $\vec{Q}(\vec{k},\nu)$ can be described as

$$\begin{aligned}
\vec{Q}(\vec{k},\nu) &= \Bigg\langle \frac{1}{N^{1/2}} \Bigg\{ \sum_{\vec{k},\nu} \vec{\xi}_1^*(j,\vec{k},\nu) \exp(-i\vec{k}\vec{r}(jl))\tilde{E}(\vec{k},\nu) - \\
&\quad \sum_{k,\nu} \vec{\xi}_2^*(j,\vec{k},\nu) \exp(-i\vec{k}\vec{r}(jl))\tilde{\mathbf{S}}(\vec{k},\nu) \Bigg\} \cdot \\
&\quad \frac{1}{(Nm_j)^{1/2}} \vec{e}(j,\vec{k},\nu) \exp(i\vec{k}\vec{r}(jl))\dot{X}(\vec{k},\nu) \Bigg\rangle \\
&= \sum_{jl} \Bigg\langle (E(jl,t) - \mathrm{S}(jl,t)) \frac{1}{(Nm_j)^{1/2}} \vec{e}(j,\vec{k},\nu) \exp(i\vec{k}\vec{r}(jl))\dot{X}(\vec{k},\nu) \Bigg\rangle
\end{aligned} \tag{3.11}$$

Finally, by assuming the same temperature gradient for all phonon modes, the

contribution of an individual phonon mode $(\vec{k},\ \nu)$ to the overall thermal conductivity can be calculated by Fourier's law

$$\kappa_{TDDDM}(\vec{k},\ \nu) = -\frac{1}{V_c}\frac{\vec{Q}(\vec{k},\ \nu)}{\nabla T} \tag{3.12}$$

where V_c is the volume of control box in a NEMD simulation [see Figure 3.1 for details]. Here, the direct results from TDDDM are the decomposed heat current. We should combine Eq. (3.12) and Eq. (3.13) if we want to know more information about phonons, such as relaxation time and MFP.

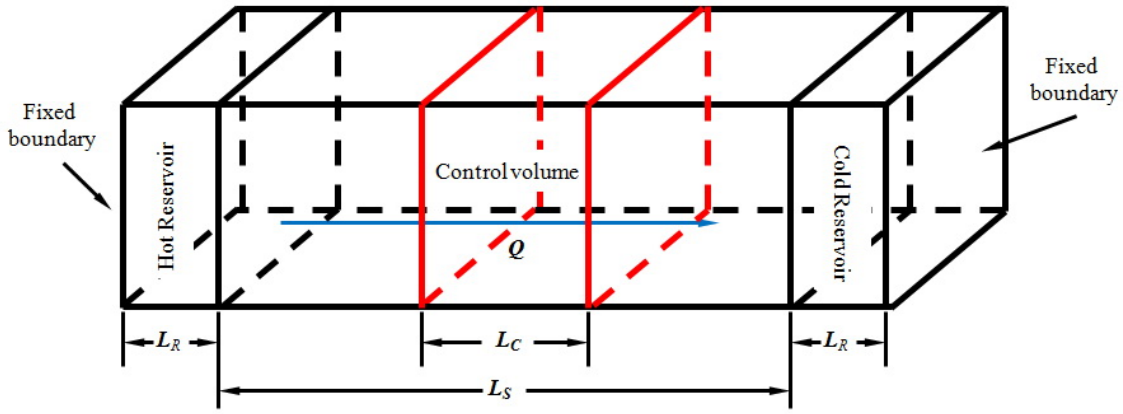


FIGURE 3.1: (Color online) Schematic of simulation cell used in TDDDM (NEMD) simulation. $\vec{Q}$ represents the heat current in the system. L_S, L_C and L_R is the total length of the system, the length of the control volume, and the length of thermostats, respectively.

Using the relaxation time approximation (Turney et al., 2009) to solve BTE yields an expression of thermal conductivity $\kappa_{BTE}(\vec{k},\ \nu)$ (Ashcroft and Stroud, 1978)

$$\kappa_{BTE}(\vec{k},\ \nu) = c_{ph}(\vec{k},\ \nu)\tau(\vec{k},\ \nu)\ v_g(\vec{k},\ \nu) \otimes v_g(\vec{k},\ \nu) \tag{3.13}$$

where the phonon mode $(\vec{k},\ \nu)$ has group velocity $\vec{v}_g(\vec{k},\ \nu)$, volume specific heat $c_{ph}(\vec{k},\ \nu)$, and phonon lifetime $\tau(\vec{k},\ \nu)$. In classical molecular dynamics simulation, the volumetric specific heat can been obtained by $c_{ph}(\vec{k},\ \nu) = k_B/V$, where k_B and $V$is the Boltzmann's constant and system volume, respectively. The phonon lifetime can be obtained by TDNMA or SED in MD simulations.

In contrast, in the framework of frequency domain (also run in EMD), a spectral energy density (SED), $\Phi(\vec{k},\ \nu)$, can be calculated by [84]

$$\Phi(\vec{k},\nu) = 2\lim_{t_0\to\infty}\frac{1}{2t_0}\left|\frac{1}{\sqrt{2\pi}}\int_0^{t_0} X(\vec{k},\nu;t)\exp(-i\omega t)dt\right|^2 \tag{3.14}$$

Fitting the SED using the Lorentzian function with center at $\omega_0(\vec{k},\ \nu)$ and line width equal to $\Gamma(\vec{k},\ \nu)$, one can obtain

$$\Phi(\vec{k},\ \nu) = C_0(\vec{k},\ \nu)\frac{\Gamma(\vec{k},\ \nu)/\pi}{\left[\omega_0(\vec{k},\ \nu) - \omega\right]^2 + \Gamma^2(\vec{k},\ \nu)} \tag{3.15}$$

where $C_0(\vec{k},\ \nu)$ is a mode dependent constant. The lifetime of the phonon mode $\tau_{SED}(\vec{k},\ \nu)$ is then given by [84]

$$\tau_{SED}(\vec{k},\ \nu) = \frac{1}{2\Gamma(\vec{k},\ \nu)} \tag{3.16}$$

Finally, the thermal conductivity contributed by each phonon mode can be calculated from Eq. (3.13). Here, it is worth noting that the thermal conductivity computed by Eq. (3.12) and Eq. (3.13) is a tensor. In our calculation we only calculated the thermal conductivity along the concerned direction.

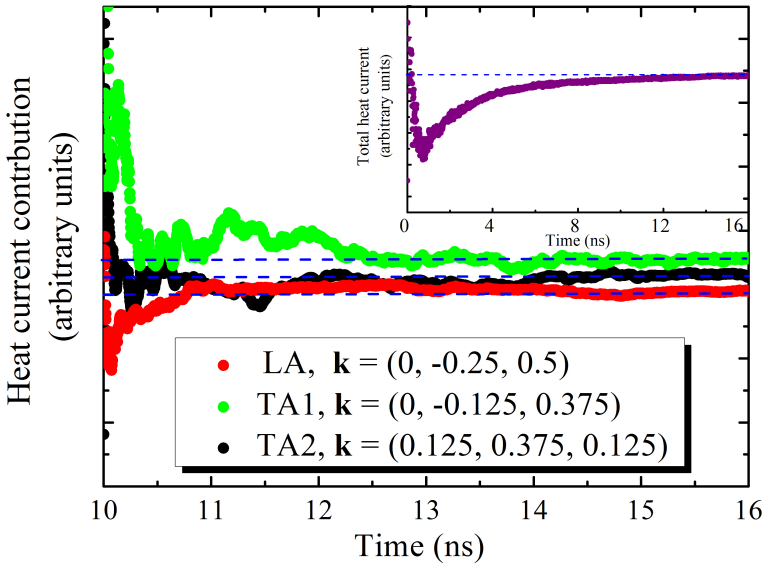


FIGURE 3.2: (Color online) Heat current contributions of three typical individual phonon modes of LJ Argon, normalized by total predicted heat current. (Inset) Time development of total predicted heat current of the system. The dashed lines are guide for the eyes.

3.2.2 Validation of time domain direct decomposition method

Heat current fluctuation of individual phonon mode: Since the heat current of each phonon mode in principle is the decomposition of the total heat current, it should also reach the steady state finally as total heat current does. As formulized in Sec. 3.2.1, we start the validation of our TDDDM approach with the investigation of the time development of heat current contributed by individual phonon modes. Here, the heat current contributions of three typical individual phonon modes for LJ Argon are used as examples for analysis [Figure 3.2]. It can be clearly seen from Figure

3.2 that, the heat current of the individual phonon mode converges after averaging over about 3 ns. In addition, it is interesting to find that the longitudinal phonon mode (red line) is more stable than the other two transverse phonon modes (green and black line). Using TDNMA/SED, we can find that the relaxation time of phonon modes corresponding to red line, green line and black line are 6.27, 20.78 and 17.38 ps, respectively. The longitudinal phonon mode (red line) has smaller relaxation time, which means during the statistic window it appears and disappears more frequently than the other two phonon modes (green and black line). Therefore, the heat current corresponding to this longitudinal phonon mode (red line) is averaged by more times during the same time period, which makes the fluctuation smaller. Furthermore, it is found that the total heat current of the system reaches steady state more quickly. This is understandable considering that the total heat current of the system is the sum of the heat current from all the phonons. The fluctuations of each individual phonon modes may be cancelled out with each other, so the fluctuation of total heat current is much smaller than those of a single phonon mode.

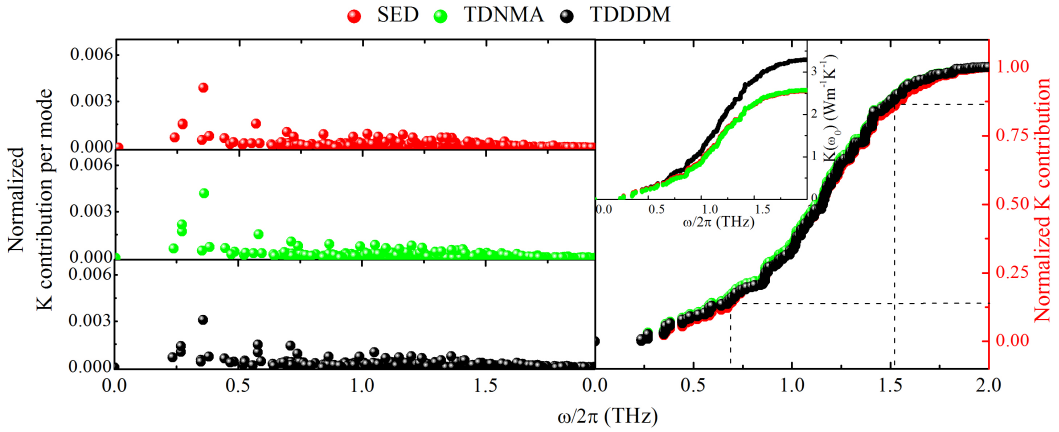


FIGURE 3.3: (Color online) Mode dependent thermal conductivity contribution (left) and accumulative thermal conductivity as a function of mode frequency (right) for the case of LJ Argon calculated using SED, TDNMA, and TDDDM methods. The mode dependent thermal conductivity and accumulative thermal conductivity is normalized by the overall thermal conductivity predicted by each respective method. The dashed lines are guide for the eyes.

For SW Si, the contribution to the heat current from each phonon mode possesses similar properties. We did not show the results for brevity. Using TDNMA/SED, we can know that the relaxation time of SW Si is larger than that of LJ Argon. It means that the total run time, that is needed to make the heat current of those low frequency phonon modes to be stable in TDDDM, should be quite long. For some cases a total run time of 28 ns is needed for SW Si in our TDDDM simulation. Generally speaking, the lower intrinsic relaxation time a phonon mode has, the shorter run time the corresponding heat current to reach a steady state takes. In addition, since our TDDDM scheme is established on decomposing the atomic velocity in the heat

current formula onto each phonon mode, our heat current computed using TDDDM should in principal be equal to the value calculated by Eq. (3.1), which has been proved using MD simulations.

Contribution of individual phonon modes to overall thermal conductivity: In this section, the thermal conductivity contribution from each individual phonon modes is predicted by TDDDM and the results are compared with that obtained by SED and TDNMA. The size of the TDDDM models discussed in this section is chosen as 8aAr $\times$ 8aAr $\times$ 500aAr for LJ Argon and 4aSi $\times$ 4aSi $\times$ 4000aSi for SW Si. Isotropic approximation is used by Henry and Chen (Henry and Chen, 2008) and McGaughey and Kaviany (McGaughey and Kaviany, 2004a) for SW Si and LJ Argon to compute the thermal conductivity contribution of individual phonon modes. However, Turney *et. al.* (Turney et al., 2009) and Larkin *et. al.* (Larkin and McGaughey, 2013) found that the predicted thermal conductivity by an isotropic approximation is lower than that predicted using the full Brillouin zone. Therefore, the full Brillouin zone should be used to calculate the thermal conductivity contributions. To improve the computational efficiency, in this paper the crystal lattice's irreducible Brillouin zone is used to compute the contribution of each phonon mode, which has been shown to predict the same thermal conductivity of the material with respect to use the full Brillouin zone (Larkin and McGaughey, 2013). The results are reported in Figure 3.3 (LJ Argon) and Figure 3.4 (SW Si). Both figures show that the TDDDM approach predicts identical thermal conductivity contribution of each phonon mode and the accumulative thermal conductivity with respect to mode frequency as well, where the accumulative thermal conductivity is calculated by

$$\kappa(\omega_0) = \sum_{\omega<\omega_0} \kappa(\omega) \tag{3.17}$$

These results prove that our TDDDM approach yields the same correct results as SED and TDNMA and captures the phonon properties accurately in NEMD runs. From the left panel of Figure 3.3 it is also interesting to see that some phonon modes in the low frequency range of LJ Argon ($<$ 0.5 THz) contribute much more than those in higher frequency region. This phenomenon may lead to the common assumption that low frequency phonon modes dominate the thermal transport (Bergman et al., 2011; Lienhard, 2013). However, from the right panel of Figure 3.3, we know that the phonon modes in the medium frequency range (0.7$\sim$1.5 THz) contribute as much as 70% of the total thermal conductivity. Thus, this common assumption should be considered cautiously (at least invalid for LJ Argon).

For SW Si at 300 K, the acoustic phonon modes contribute over 90% of the predicted thermal conductivity (Figure 3.4). It is often assumed that the optical modes (τ_∞ for SW Si) do not contribute thermal conductivity considerably, due to their short relaxation time. Here, in our simulations, we find that the optical phonon modes contribute only $\sim$6% to the predicted thermal conductivity, which is in accordance with the previous results reported by Sellan *et. al.* (Sellan et al., 2010a)

and Goicochea *et. al.* (Goicochea, Madrid, and Amon, 2010). Thus, it is reasonable to neglect their contribution to the overall thermal conductivity. Once again, we find that in SW Si some low frequency phonon modes contribute extremely large portion to the overall thermal conductivity as compared to other higher frequency phonon modes. In addition, the accumulative thermal conductivity of the predicted thermal conductivity in the low frequency region (0∼8 THz) reaches 90%. Therefore, we can conclude that the low frequency phonon modes dominate the thermal transport in bulk Si at room temperature. What is also worth noting is the absolute value of thermal conductivity. For LJ Argon the absolute thermal conductivity calculated by TDDDM and SED/TDNMA is 3.29 and 2.55 W/mK (McGaughey and Kaviany, 2004a), respectively, while GK-MD shows the result of such system is 4.00 W/mK and about 2.50 W/mK (Larkin and McGaughey, 2013). For SW Si the thermal conductivity calculated by TDDDM and SED/TDNMA is 381.24 W/mK and 355.32 W/mK (379.66 W/mK in Ref. (Goicochea, Madrid, and Amon, 2010)), respectively. It is obvious that the absolute values of thermal conductivity calculated by TDDDM and TDNMA/SED are different. The reason for this discrepancy could come from the inherent difference between EMD and NEMD and the finite extractable phonon modes in TDNMA/SED.

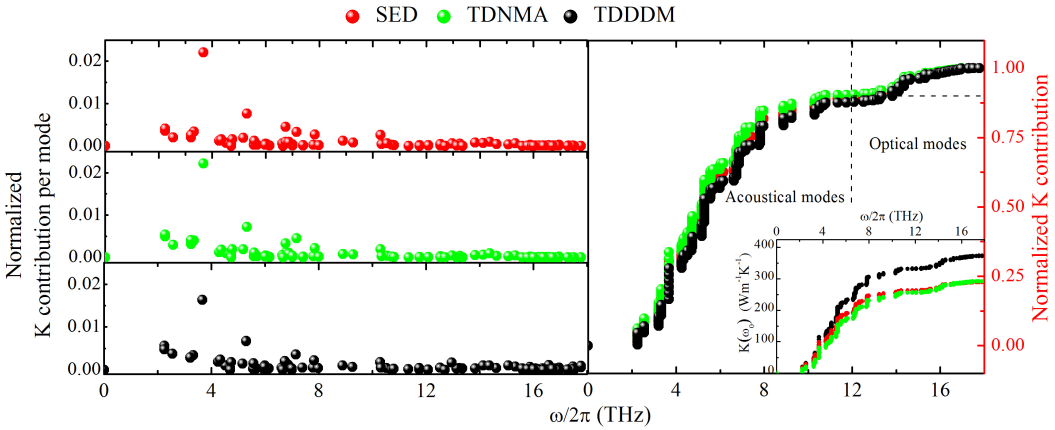


FIGURE 3.4: (Color online) The same as Figure 3.3 for the case of SW Si. The dashed lines are guide for the eyes.

3.2.3 Applications of time domain direct decomposition method

Size effect of thermal conductivity contribution of individual phonon modes: It is well known that, for many materials there exists size effect in thermal conductivity predictions when the NEMD method is used. Since TDDDM is based on the NEMD method, there is also size effect in the phonon mode contribution to the overall thermal conductivity. For LJ Argon, the largest MFP in our model system extracted by SED/TDNMA is about 65 nm. It means that all the intact phonon modes predicted by SED/TDNMA can only appear when the length in z direction is larger than 65 nm. When the system size is smaller than 65 nm, the phonons with MFP larger than

65 nm will be truncated and then become incomplete phonons. It should be noted that the truncation of the long MFP phonons is different from the non-existing of phonons. Here, the dimension in the concerned direction in our models for LJ Argon is chosen to be about 34 ∼158 nm. The results of TDDDM for different total length of the system are compared in the left panel of Figure 3.5. We find that all the extractable phonon modes contribute to thermal conductivity for the systems with total size in z direction larger than 65 nm. When the system size in z direction is smaller than 65 nm, only phonon modes with MFP smaller than the system size can contribute to the overall thermal conductivity.

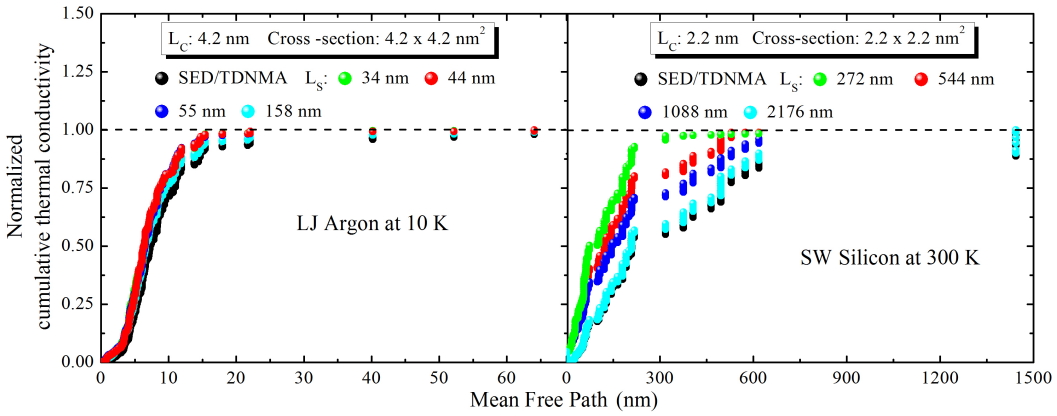


FIGURE 3.5: (Color online) Comparison of the accumulative thermal conductivity as a function of frequency for the case of LJ Argon (left) and SW Si (right) with different total length in TDDDM. The results of SED and TDNMA are also shown for comparison with sample size of 4.2 × 4.2 × 4.2 nm^3 (LJ Argon) and 2.2 × 2.2 × 2.2 nm^3 (SW Si).

For SW Si, previous studies have demonstrated that the thermal conductivity computed using NEMD can be seriously affected by the size of the model (Schelling, Phillpot, and Keblinski, 2002a; Volz and Chen, 2000). The difference in thermal conductivity between NEMD and EMD method can be as large as a few times (Sellan et al., 2010b; Volz and Chen, 2000). In our SED/TDNMA simulations, the largest phonon MFP of SW Si reaches 1420 nm, which is already a quite large size for NEMD simulations. In our TDDDM (NEMD) simulation models, the system size in z direction ranges from 272 to 2176 nm. Therefore, the longest simulation size should accommodate the largest MFP phonons. The results are reported in the right panel of Figure 3.5. It clearly shows that all the phonon modes contribute to the thermal conductivity when the length in z direction is 2176 nm. For the model with length of 1088 nm in z direction, phonon modes with MFP larger than about 1 μm are truncated and therefore contribute little to the overall thermal conductivity. The corresponding critical MFP for models with 544 nm in z direction is found to be about 500 nm. When the size in z direction is decreased to 272 nm (by one order of magnitude smaller than the longest length of 2176 nm), it is interesting to find that the phonon modes with MFP larger than 260 nm (more or less equal to the system size of 272

nm) contribute very little to the overall thermal conductivity, i.e. the corresponding heat current contribution is quite small for these phonon modes. With total length increasing, phonon modes with MFP longer than the system length are present and then they are able to contribute to the heat conduction. Our TDDDM approach provides direct evidence that, the phenomenon that the thermal conductivity of NEMD simulations increases with length increasing is solely resulted from the truncation of long MFP phonons induced by the finite length of the system. Although general understanding to the size effect in NEMD simulation has been established for a long time, it is the first time that physically meaningful and direct evidence is presented and the length dependence of thermal conductivity in NEMD simulation is *quantified* by our TDDDM approach. Certainly, it should be noted that, when TDDDM is implemented to analyze systems with thermal conductivity dominated by very long MFP phonons, both system length and run time should be very long.

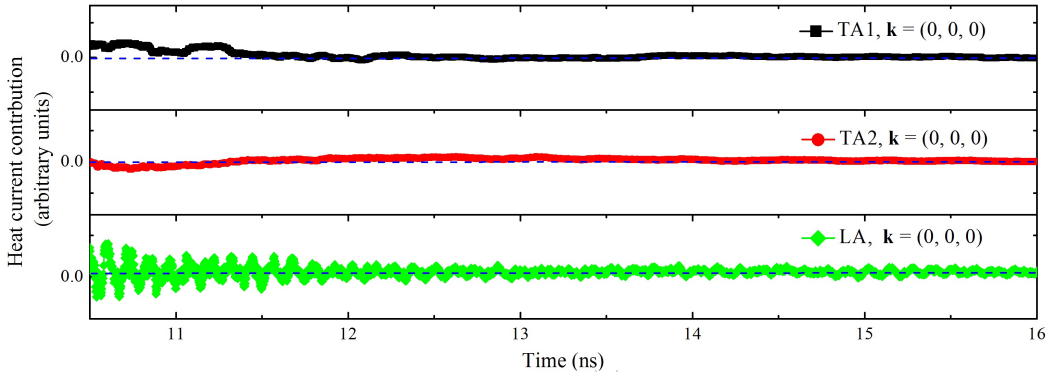


FIGURE 3.6: (Color online) Time development of heat current contributed by the Gamma point for the case of LJ Argon predicted by the TDDDM. Dashed lines denote zero heat current and are guide for the eyes.

Thermal conductivity contribution of Gamma point: Another interested point in phonon mode specific thermal conductivity is the contribution of Gamma point. The Gamma point corresponds to the bulk translational movement and therefore should not contribute to the thermal conductivity (McGaughey and Larkin, 2014). However, neither SED nor TDNMA can prove this directly. Instead, both methods just assume that the Gamma point's contribution is zero. In TDDDM, the heat current of phonon modes corresponding to the Gamma point, i.e. $\vec{k} = (0,\ 0,\ 0)$, can be explicitly written as [Eq. (3.9)]

$$\vec{Q}(\vec{k}=\mathbf{0},\nu) = \sum_{jl} \langle (E(jl,t) - \mathbf{S}(jl,t)) \cdot \frac{1}{(Nm_j)^{1/2}} \vec{e}(j,\vec{k},\nu) \frac{1}{N^{1/2}} \sum_{jl} m_j^{1/2}\, \vec{e}^{*}(j,\vec{k},\nu) \vec{u}(jl,t) \Big\rangle \tag{3.18}$$

For Gamma point of a phonon mode, different basis atoms have the same eigenvector. Therefore,

$$\vec{Q}(\vec{k}=\mathbf{0},\nu)=\sum_{jl}\left\langle (E(jl,t)-\mathrm{S}(jl,t))\frac{1}{(m_j)^{1/2}}\frac{1}{N}\sum_{jl}(m_j)^{1/2}\,\vec{u}(jl,t)\right\rangle \tag{3.19}$$

Based on Eq. (3.18), we can know that the heat current of phonon modes contributed by Gamma point is related to the momentum of the system, $\sum_{jl}(m_j)^{1/2}\,\vec{u}(jl,t)$, which is zero in the NEMD system as shown in Figure 3.1, since the two ends of the system are fixed. Thus, the thermal conductivity contribution of phonon modes by the Gamma point should be zero in a steady NEMD simulation. To verify this, the heat current contribution from the Gamma point for the case of LJ Argon is shown in Figure 3.6. It is clearly seen that the contribution is equal to zero, when the heat current reaches steady state.

3.3 Frequency Domain Direct Decomposed Method

In this section, another method named frequency domain direct decomposition method, which is still based on NEMD simulations, is proposed from the atomistic heat current formula to calculate the spectrum contribution to thermal conductivity. The effects of all level phonon scattering processes are included in our method, since we do not neglect the higher-order phonon scattering in simulations. Using our approach, it is straightforward to find that the number of phonons in the low frequency range, or equivalently with long MFP, increases with system size increasing. It is also straightforward to identify that the high temperature enhances the anharmonic energy transfer in the system, which is well known and proves that our FDDDM reveals the correct physical picture of phonon-phonon scattering. Furthermore, the most striking feature of this new method is to characterize the phonon properties of complicated systems, such as amorphous or alloyed materials. Unlike the method in Ref. (Sääskilahti et al., 2015) which only considers the first order anharmonic interactions between two atoms, our new FDDDM approach includes all orders of anharmonicity in the interatomic interaction.

3.3.1 Framework of frequency domain direct decomposed method

It is well known that, NEMD simulations explicitly rely on launching a steady heat flux flowing through the system. The atomistic heat current $\vec{q}_{ij}$ between two atoms i and $j$can be written as (Chalopin and Volz, 2013; Sääskilahti et al., 2015; Chalopin et al., 2012)

$$\vec{q}_{ij}=\frac{1}{2}\left\langle \vec{F}_{ij}(\vec{v}_i+\vec{v}_j)\right\rangle \tag{3.20}$$

where $\vec{F}_{ij}$ is the force between two atoms and $\vec{v}$ is the velocity of atoms, $\langle\rangle$ denotes the time average. Meanwhile, it has been proved that the spectrum decomposition

of heat current is related to the correlation time between force and velocity (Chalopin and Volz, 2013; Sääskilahti et al., 2015). Therefore, we can write the auxiliary correlation term $\vec{C}_{ij}(\tau)$ as

$$\vec{C}_{ij}(t_2 - t_1) = \frac{1}{2}\left\langle \vec{F}_{ij}(t_1)(\vec{v}_i(t_2) + \vec{v}_j(t_2))\right\rangle \tag{3.21}$$

where $\vec{C}_{ij}$ only depends on the time difference due to the stable state and ensemble average of the system. By defining characteristic time τ as $\tau = t_2 - t_1$, we can re-write the atomistic heat current in the form of

$$\begin{aligned} \vec{q}_{ij} &= \frac{1}{2}\lim_{t_2 \to t_1}\left\langle \vec{F}_{ij}(t_2)\cdot(\vec{v}_i(t_1) + \vec{v}_j(t_1))\right\rangle \\ &= \frac{1}{2}\lim_{\tau \to 0}\left\langle \vec{F}_{ij}(\tau)\cdot(\vec{v}_i(0) + \vec{v}_j(0))\right\rangle \\ &= \frac{1}{2}\lim_{\tau \to 0}\vec{C}_{ij}(\tau) \end{aligned} \tag{3.22}$$

As usual, we can define the time Fourier transform

$$\vec{\tilde{C}}_{ij}(\omega) = \int_{-\infty}^{+\infty}\vec{C}_{ij}(\tau)\, e^{i\omega\tau}d\tau \tag{3.23}$$

and

$$\vec{C}_{ij}(\tau) = \int_{-\infty}^{+\infty}\vec{\tilde{C}}_{ij}(\omega)\, e^{-i\omega\tau}d\tau \tag{3.24}$$

Here, the ω represents the angular frequency. Thus, $\vec{q}_{ij}$ can be further given by

$$\begin{aligned} q_{ij} &= \frac{1}{2}\lim_{\tau \to 0}\int_{-\infty}^{+\infty}\vec{\tilde{C}}_{ij}(\omega)\, e^{-i\omega\tau}\frac{d\omega}{2\pi} \\ &= \frac{1}{2}\int_{-\infty}^{+\infty}\vec{\tilde{C}}_{ij}(\omega)\frac{d\omega}{2\pi} \\ &= \frac{1}{2}\int_{-\infty}^{+\infty}\int_{-\infty}^{+\infty}C_{ij}(\tau)\, e^{i\omega\tau}d\tau\frac{d\omega}{2\pi} \end{aligned} \tag{3.25}$$

Since $\vec{C}_{ij}(\tau)$is a real number, the real and imaginary part of $\vec{\tilde{C}}_{ij}(\omega)$ should be an even and odd function. Combining with Eq. (3.22), the spectrum of atomistic heat current can be obtained by

$$\vec{q}_{ij}(\omega) = \frac{1}{2}\int_{-\infty}^{+\infty}\vec{C}_{ij}(\tau)e^{i\omega\tau}d\tau = \mathrm{Re}[\int_{0}^{+\infty}\vec{C}_{ij}(\tau)e^{i\omega\tau}d\tau] \tag{3.26}$$

On the other hand, the molecular dynamics expression of the heat current, which was first derived by Irving and Kirkwood (Irving and Kirkwood, 1950), and later on

extended by Daichi *et. al.* (Torii, Nakano, and Ohara, 2008), can be written as

$$\vec{Q} = \sum_i E_i \vec{v}_i + \sum_n \sum_{S_1} \sum_{S_1<S_2} \cdots \sum_{S_{n-1}<S_n} \left[\sum_{\alpha=1}^{n-1} \sum_{\beta=\alpha+1}^{n} \vec{F}_{S_\alpha S_\beta} \cdot (P^n_{S_\alpha} \vec{v}_{S_\alpha} + P^n_{S_\beta} \vec{v}_{S_\beta}) \cdot (\vec{r}_{S_\alpha} - \vec{r}_{S_\beta}) \right] \tag{3.27}$$

where $\vec{Q}$ is the heat current, the sum is taken over all atoms which are described by n-body potential in the control volume, S_i denotes the atoms, E_i and $\vec{r}_i$ are the energy and position of atoms, respectively. P stands for the distribution of the interaction potential and satisfies (Torii, Nakano, and Ohara, 2008).

$$\sum_n P_i = 1 \tag{3.28}$$

In the classical systems, equal partition of potential energy between atoms $P_i = {}^1/_n$ is usually assumed (Torii, Nakano, and Ohara, 2008). Since the small fluctuations in the atomic coordinates cannot cause energy transfer over macroscopic distance and time, there is negligible macroscopic atom diffusion in a solid material (Ladd, Moran, and Hoover, 1986). Then, for solid materials the Eq. (3.27) can be simplified as

$$\vec{Q} \approx \sum_n \sum_{S_1} \sum_{S_1<S_2} \cdots \sum_{S_{n-1}<S_n} \left[\sum_{\alpha=1}^{n-1} \sum_{\beta=\alpha+1}^{n} \vec{F}_{S_\alpha S_\beta} \cdot (P^n_{S_\alpha} \vec{v}_{S_\alpha} + P^n_{S_\beta} \vec{v}_{S_\beta}) \cdot (\vec{r}_{S_\alpha} - \vec{r}_{S_\beta}) \right] \tag{3.29}$$

Furthermore, since for a stable system

$$(\vec{r}^{\,0}_{s_\alpha} - \vec{r}^{\,0}_{s_\beta}) \gg (\vec{u}_{s_\alpha} - \vec{u}_{s_\beta}) \tag{3.30}$$

which has already been proved by MD simulations, the position difference of the two atoms ω 12 THz can be assumed as

$$(\vec{r}_{s_\alpha} - \vec{r}_{s_\beta}) = (\vec{r}^{\,0}_{s_\alpha} - \vec{r}^{\,0}_{s_\beta}) + (\vec{u}_{s_\alpha} - \vec{u}_{s_\beta}) \approx (\vec{r}^{\,0}_{s_\alpha} - \vec{r}^{\,0}_{s_\beta}) \tag{3.31}$$

where $\vec{r}^{\,0}_i$ and $\vec{u}_i$ represents the equilibrium position and displacement of atom i.Using Eq. (3.22), Eq. (3.25), Eq. (3.27), Eq. (3.29) and Eq. (3.31), the heat current can be written as

$$\begin{aligned} \vec{Q} &= \sum_n \sum_{S_1} \sum_{S_1<S_2} \cdots \sum_{S_{n-1}<S_n} \left[\sum_{\alpha=1}^{n-1} \sum_{\beta=\alpha+1}^{n} \frac{1}{n} \vec{q}_{S_\alpha S_\beta} \cdot (\vec{r}^{\,0}_{s_\alpha} - \vec{r}^{\,0}_{s_\beta}) \right] \\ &= \sum_n \sum_{S_1} \sum_{S_1<S_2} \cdots \sum_{S_{n-1}<S_n} \left[\sum_{\alpha=1}^{n-1} \sum_{\beta=\alpha+1}^{n} \frac{1}{2n} \int_{-\infty}^{+\infty} \int_{-\infty}^{+\infty} C_{ij}(\tau)\, e^{i\omega\tau} d\tau \frac{d\omega}{2\pi} (\vec{r}^{\,0}_{s_\alpha} - \vec{r}^{\,0}_{s_\beta}) \right] \end{aligned} \tag{3.32}$$

and the spectrum of heat current in a control volume can be obtained as

$$\vec{Q}(\omega)=\sum_{n}\sum_{S_1}\sum_{S_1<S_2}\cdots\sum_{S_{n-1}<S_n}\left[\sum_{\alpha=1}^{n-1}\sum_{\beta=\alpha+1}^{n}\frac{1}{n}\,\mathrm{Re}\left[\int_{-\infty}^{+\infty}C_{ij}\left(\tau\right)e^{i\omega\tau}d\tau\right]\left(\vec{r}^{\,0}_{s_\alpha}-\vec{r}^{\,0}_{s_\beta}\right)\right] \tag{3.33}$$

Finally, by assuming the same temperature gradient for all phonon modes, the contribution of phonon mode with a specific frequency to the overall thermal conductivity can be calculated by Fourier's law

$$\kappa_{FDDDM}(\omega)=-\frac{1}{V_c}\frac{\vec{Q}(\omega)}{\nabla T} \tag{3.34}$$

where V_c is the volume of control box in a NEMD simulation (see Figure 3.1 for details). Note that $\kappa\left(\omega\right)$ is a 3×3 tensor, since is a spatial gradient and can be either along or perpendicular to the direction of the heat flux $\vec{Q}(\omega)$. Using the relaxation time approximation (Srivastava, 1990) to solve Boltzmann transport equation yields an expression of modal thermal conductivity $\kappa_{BTE}(\vec{k},\nu)$ (Turney et al., 2009). It is well known that for each frequency ω, there are typically multiple phonon modes with different polarizations and vectors $(\vec{k},\nu)$. In order to compare the results between FDDDM and TDNMA directly, we compute thermal conductivity contributed by each frequency in TDNMA using

$$\kappa_{BTE}(\omega)=\sum_{\vec{k},\,\nu}\kappa_{BTE}(\omega;\ \vec{k},\ \nu) \tag{3.35}$$

where the thermal conductivity of a specific frequency is taken over different branches (e.g. LA, TA, TO and LO) for the same frequency without using broadening functions. Meanwhile, we also generated the modal thermal conductivity from the space Fourier transform which is called TDDDM in our first paper in the series. Here we give some comparisons of these two methods from the theory aspect. For FDDDM we start from the auxiliary correlation between atomic force ($\vec{F}$) and velocity ($\vec{v}$) and then obtain the heat current spectrum. For TDDDM we directly get the heat current of each mode from $\vec{F}$ and the decomposed $\vec{v}$. Although these two approaches are fundamentally different (the FDDDM is based on the Fourier transform of time and the TDDDM is from the Fourier transform of space), we speculate that there might be some relations between the time and space Fourier transform. However, it is beyond the authors' knowledge to prove this theoretically. Although it is natural to obtain similar results using these two methods, so far no one can prove these formulas are equivalent.

3.3.2 Validation of frequency domain direct decomposed method

In this section, the frequency dependent thermal conductivity contribution is predicted by FDDDM and the result is compared with that obtained by TDNMA. Meanwhile, based on our discussion above, the size of the FDDDM models mentioned here should be at least 8aAr $\times$ 8aAr $\times$ ($>$ 123aAr) for LJ Argon and 8aSi $\times$ 8aSi $\times$ ($>$ 3676aSi) for SW Si. Here, due to the computational efficiency, we choose the size of FDDDM models as 8aAr $\times$ 8aAr $\times$ 200aAr for LJ Argon and 8aSi $\times$ 8aSi $\times$ 2000aSi for SW Si. Thus, for LJ Argon all extractable phonon modes in TDNMA can be included in FDDDM simulations, while for SW Si about 10% of phonon modes that can be extracted in TDNMA are truncated (ignored) in the FDDDM simulations. Furthermore, the full Brillouin zone, which has been proved to be more appropriate than the isotropic approximation, is used to predict the thermal conductivity in TDNMA. In this paper, in order to improve the computational efficiency, the crystal lattice's irreducible Brillouin zone is used to compute the contribution of each phonon mode, which has been shown to predict the same thermal conductivity of a material with respect to use the full Brillouin zone. Figure 3.7 shows the results predicted by FDDDM and TDNMA.

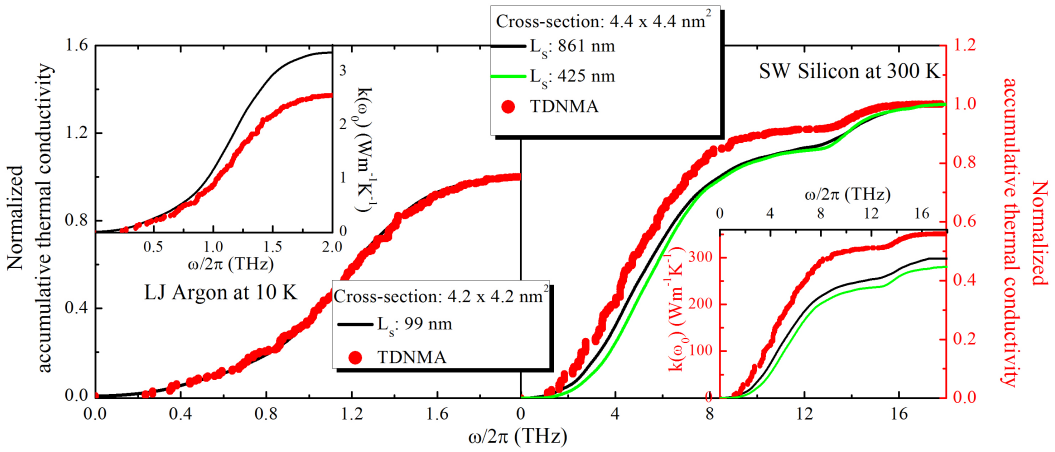


FIGURE 3.7: (Color online) Accumulative thermal conductivity as a function of mode frequency for the case of (left) LJ Argon and (right) SW Si calculated using TDNMA and FDDDM methods. The accumulative thermal conductivity is normalized by the overall thermal conductivity predicted by the respective method. (Inset) The actual accumulative thermal conductivity vs. frequency.

For both LJ Argon and SW Si, the results obtained by FDDDM show similar trends with that calculated by using TDNMA. For LJ Argon at 10K [left panel of Figure 3.7], the results show that our FDDDM approach yields the similar results with TDNMA. It is not surprising to see this phenomenon, since the largest MFP appearing in our TDNMA simulations is smaller than the size of the system in FDDDM. Therefore, all the extractable phonon modes in TDNMA are present and extracted in our FDDDM simulation. Meanwhile, the phonon modes in the medium frequency

region (0.7 $\sim$ 1.6 THz) are found to dominate the phonon transport (contribute more than 90% of the total thermal conductivity). The phonon modes in the low frequency region ($<$ 0.7 THz) and high frequency region ($>$ 1.6 THz) contribute very little to the total thermal conductivity. All our findings are consistent with that observed in Ref. (Turney, McGaughey, and Amon, 2010). For SW Si at 300 K [right panel of Figure 3.7], the predictions of our FDDDM method is slightly different from that of TDNMA. We attribute the difference to the size effects in FDDDM, since it is based on NEMD. To further prove this, the size along z (heat flux) direction in the system is reduced to be 425 nm. It is clearly seen that the results of FDDDM for the longer system is much closer to the predictions of TDNMA, in particular the accumulative thermal conductivity in the low frequency range has a slight augment. Therefore, we anticipate that the results calculated by FDDDM will be in accordance with the prediction of TDNMA when the largest extractable MFP in TDNMA can be included in the system of FDDDM simulations. Furthermore, from Figure 3.7 we can see that the acoustic phonon modes ($\omega < 12\,\mathrm{THz}$ for SW Si) contribute about 90% of the predicted thermal conductivity. Thus, it is reasonable to conclude that the optical phonon modes ($\omega < 12\,\mathrm{THz}$ for SW Si) do not contribute much to the overall thermal conductivity (Sellan et al., 2010a; Turney, McGaughey, and Amon, 2010). In addition, phonon modes in low frequency region ($<$ 8 THz) are found to dominate the thermal conductivity (the accumulative thermal conductivity reaches about 80% for frequency up to 8 THz). Both previous work (Sellan et al., 2010a) and this work have shown that, the common assumption that low frequency phonon modes dominate the thermal transport (Bergman et al., 2011; Lienhard, 2013) should be considered cautiously (invalid for LJ Argon, while valid for SW Si).

Although the relative contribution of each phonon mode should be the same when there is no size effect in the system, since the same phonon should have the same effect in the same system, the actual thermal conductivities calculated using TDNMA/SED (EMD) and FDDDM (NEMD) are different [insets in Figure 3.7]. The discrepancy may come from the size effect [such as SW Si in Figure 3.7] and more importantly the inherent difference between EMD and NEMD. Thus, it is difficult to directly compare the actual thermal conductivity between FDDDM and SED/TDNMA.

3.3.3 Applications of frequency domain direct decomposed method

Size effect on frequency dependent thermal conductivity contribution: It is well known that the size effect cannot be avoided when NEMD method is used to calculate the thermal conductivity of materials. As analyzed above, size effect is inherent in our FDDDM simulations since it is based on the NEMD method. In our results shown above, we have proved that the size effect for LJ Argon in the NEMD simulations can be ignored when the size of the system reaches about several hundreds of nanometers. Here the SW Si is chosen as the example to analyze the size effect

in FDDDM. For SW Si, it has been demonstrated in literature that the thermal conductivity computed using NEMD can be strongly affected by the size of the model (Sellan et al., 2010b; Schelling, Phillpot, and Keblinski, 2002a; Sellan et al., 2010a; Volz and Chen, 2000). The difference in thermal conductivity between NEMD and EMD method, which usually has small size effect, can be as large as a few times (Sellan et al., 2010b; Volz and Chen, 2000; Zhang et al., 2014; Khadem and Wemhoff, 2013). The results of FDDDM for different total length of system are plotted in Figure 3.8. From the left panel of Figure 3.8, we can find that in low frequency region ($\omega < 6$ THz), the frequency dependent thermal conductivity is found to be proportional to the excited transverse and longitude acoustic phonon modes, i.e. increasing as ω^2. This phenomenon is also observed in Ref. (Sääskilahti et al., 2015). In the frequency region from 6 to 12 THz, the contribution to the overall thermal conductivity decreases because the number of phonon modes is much less than that in the low frequency region (only longitude acoustic phonon mode in this range) (Goicochea, Madrid, and Amon, 2010). In the high frequency region ($\omega < 12$ THz), all phonons are optic. It is usually believed that the contribution of optic phonons can be ignored for SW Si. Here, in our simulations, the optic phonons contribute as little as 10% of the total thermal conductivity [right panel of Figure 3.8,], which is accordance with the common sense. It is also worth noting that more phonons in the low frequency region ($\omega < 6$ THz), or equivalently phonons with longer MFP, appear in the FDDDM simulations with system size increasing [left panel of Figure 3.8,]. Therefore, the contribution of the low frequency phonon modes rises with the increase of system size [right panel of Figure 3.8]. Furthermore, as discussed in the TDDDM, the phonons in the low frequency region or with long MFP are truncated and then contribute little to the thermal conductivity. The similar phenomenon can be found here as well. However, it should be noted that the truncation of long MFP phonons does not mean that these phonons do not exist. Here, we recommend using the TDDDM to investigate the size effect in NEMD simulations, since we can observe the truncation of long MFP phonons clearly when using TDDDM. We also calculate the actual thermal conductivity using FDDDM [inset in Figure 3.8]. The value of our largest system shown in Figure 3.8 is 275 W/mK. However, Goicochea *et. al.* (Goicochea, Madrid, and Amon, 2010) show the thermal conductivity of bulk Si is 380 W/mK using EMD with the same original SW potential. The large difference between our result and that of the reference should come from the size effect in NEMD simulations. To this end, we increase the length along the concerned direction to about 870 nm and the thermal conductivity increases to 300 W/mK. Using the linear extrapolation between $1/\kappa$ and $1/L$, we obtain the thermal conductivity of bulk Si to be 385 W/mK, which is in very good agreement with the result from Ref. (Goicochea, Madrid, and Amon, 2010). One should also keep in mind that the length along the concerned direction used to do the linear extrapolation should be comparable to or longer than the dominant MFP in the system. One thing we have to mention here is

that using the large samples (the four samples used to extrapolate the thermal conductivity of SW Silicon at 300 K is from ∼115 nm to ∼700 nm in our simulations) is necessary to obtain the accurate result.

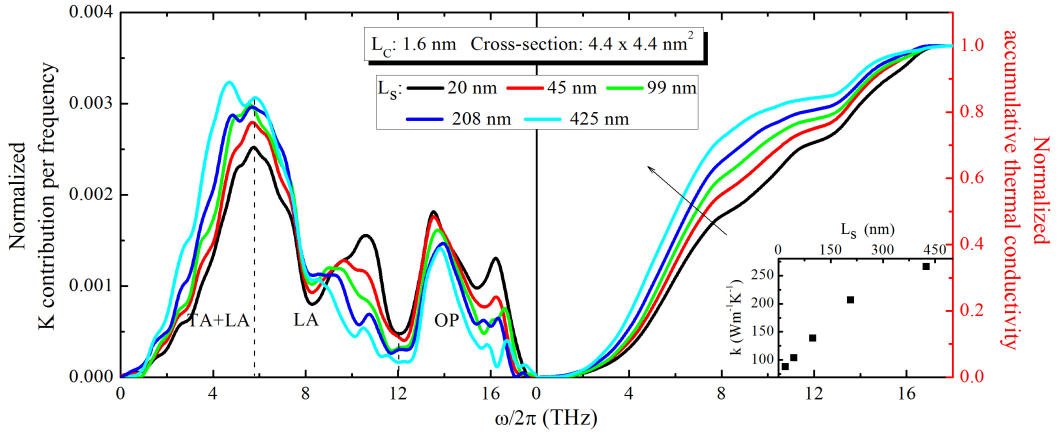


FIGURE 3.8: (Color online) (Left) Normalized spectral contribution to thermal conductivity and (right) corresponding normalized accumulative thermal conductivity as a function of mode frequency for the case of SW Si with different system size computed using FDDDM. The dashed lines and the arrow are guide for the eyes. (Inset) Actual thermal conductivity of SW Si vs. system length.

It is worth pointing out that, the heat flux spectrum obtained by FDDDM is "continuous" with respect to frequency. The total heat flux flowing in the system, which is fixed for given computational parameters in the thermostats in NEMD simulation, is the entire area (integral) of the spectrum with respect to frequency. All frequencies predicted by FDDDM are real. If a specific frequency has no contribution to overall thermal transport, the corresponding heat flux spectrum is zero. This can be clearly seen from Figure 3.8, 3.10 and 3.11 that, the thermal conductivity contribution goes to zero for frequencies higher than the cutoff frequency of the material. Furthermore, a material system of a finite size does not necessarily mean that the total number of phonon frequencies available in the system is also limited, due to the anharmonicity (such that each eigenfrequency actually has a spanning width), and also considering periodic boundary conditions are used in the lateral directions in our simulation.

Temperature effect on spectral contribution to thermal conductivity: Another important issue is the temperature effect on the thermal conductivity. Four different system temperatures are used to investigate the temperature effects. The results of both LJ Argon Figure 3.9 and SW Si Figure 3.10 show that the anharmonic energy transfer, which is caused by the anharmonic phonon scattering, is enhanced with the increase of the temperature.

For LJ Argon at 10K the phonon modes around 1.2 THz (the peak region in left panel of Figure 3.9) can carry energy farther before scattering, as compared with the system at relatively higher temperatures such as 20 K, 30 K and 40K, because the anharmonic effect is weak at such low temperature. For the systems at temperature

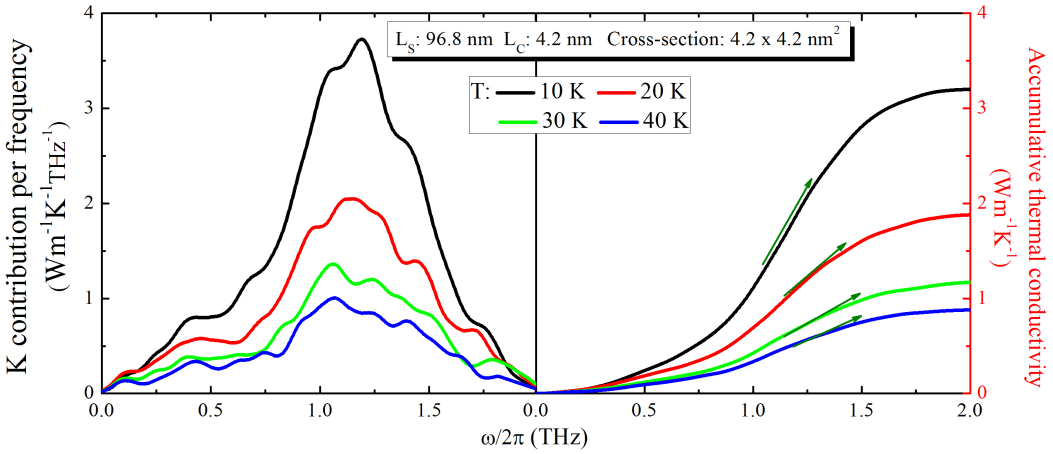


FIGURE 3.9: (Color online) (Left) Spectral contribution to thermal conductivity and (right) corresponding accumulative thermal conductivity as a function of mode frequency for the cases of LJ Argon with different system temperature. The arrows are guide for the eyes.

of 20 K, 30 K and 40 K, the above phonons still carry energy farther before scattering than other phonons. However, their contribution is decreased considerably with respect to that for 10 K. With the increase of temperature, the difference of thermal conductivity contribution between each phonon modes decreases. At relatively high temperature (40 K in our cases), the contribution of phonon modes is even almost equal to each other, i.e. the frequency dependent thermal conductivity contribution is very broad throughout the entire frequency range. It is also easy to find that, in high frequency region ($\omega < 1.7$ THz) the contribution of phonon modes almost remains unchanged at different temperatures. Phonons in this region can appear and annihilate easily, since these phonons usually have an extremely short lifetime. The reduction or improvement of relaxation time caused by the system temperature in this region is quite small, and therefore, leads to the constant contribution of phonons in this region. In addition, it is interesting to find that the thermal conductivity decreasing with temperature is nonlinear (right panel of Figure 3.9), which is also observed in Ref. (Sääskilahti et al., 2015). What is more, the actual thermal conductivity calculated using FDDDM for LJ Argon is 3.2 W/mK (10 K), 1.88 W/mK (20 K), 1.17 W/mK (30 K) and 0.88 W/mK (40 K). The four corresponding values are 4.0, 1.57, 0.903 and 0.574 W/mK computed using GK-EMD (McGaughey and Kaviany, 2004b). The difference here should come from two aspects. Firstly, our FDDDM result is obtained by one simulation run. Using more simulation runs, we can obtain a more accurate result with an error bar. Secondly, there is still a weak size effect in our systems.

For SW Si, the profile of the thermal conductivity spectrum is scaled down for the entire frequency range with temperature increasing [left panel of Figure 3.10]. We

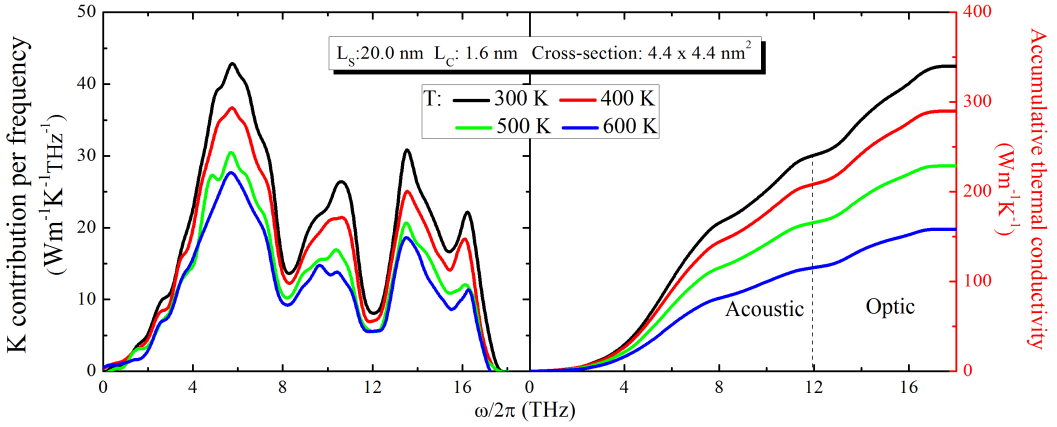


FIGURE 3.10: (Color online) Same figure as Figure 3.9 for the case of SW Si. The dashed line is guide for the eyes.

can also see that the range of frequency decreases from 17.8 to 17.0 THz with temperature increasing, due to the well-known phonon softening effect at high temperatures. Since temperature has pronounced effect on both acoustic and optic phonons (Goicochea, Madrid, and Amon, 2010), it can be observed that the slope of the accumulative thermal conductivity with respect to frequency has significant change in both acoustic and optic phonon region with temperature increasing. It is also worth noting that, the reduction of the actual accumulative thermal conductivity for optic phonons due to the increase of the temperature is larger than that for acoustic phonons. In addition, we should mention that the actual thermal conductivity may be quite different from the bulk (infinite length) thermal conductivity at the same temperature conditions, since the length used in our model is quite short.

Frequency dependent thermal conductivity of amorphous Si: The unique advantage of FDDDM prior to previous methods is the ability to deal with disordered systems. Other methods, e.g. SED and TDNMA, can only deal with the amorphous materials with assumptions, since one of the foundations involved in all of them is lattice dynamics. To certify this, in this section we perform FDDDM analysis to amorphous Si (a-Si). The method in Ref. (France-Lanord et al., 2014) is used to generate the amorphous Si samples. It should be noticed that the amorphous material may have many different atomic configurations with nearly equivalent potential energies, and therefore, leading to the potential meta-stability during the MD simulations (Larkin and McGaughey, 2014). To overcome the meta-stability, all samples are annealed at a temperature of 3000 K for 5 ns. Moreover, the result discussed below is averaged by four independent runs. In order to verify the result of our new method, the phonon properties of a-Si are also computed by the Allen-Feldman (AF) theory, where the isotropic modal thermal conductivity which is a scalar can be calculated as (Allen and Feldman, 1993)

$$\kappa_{AF}(\omega) = k_B D(\omega) \tag{3.36}$$

where $D(\omega)$ is the AF diffuson diffusivity and can be calculated from (Allen and Feldman, 1993)

$$D(\omega) = \frac{\pi V^2}{\hbar^2 \omega^2} \sum_{\omega \neq \omega'} |S_{\omega\omega'}|^2 \delta(\omega - \omega') \tag{3.37}$$

where δ is the Dirac delta function. The heat current operator $S_{\omega\omega'}$ measures the thermal coupling between vibrational modes ω and ω'. The computing details of $S_{\omega\omega'}$ can be found in Ref. [103]. Finally, using Eq. (3.36) and (3.37), the AF thermal conductivity per frequency can be obtained.

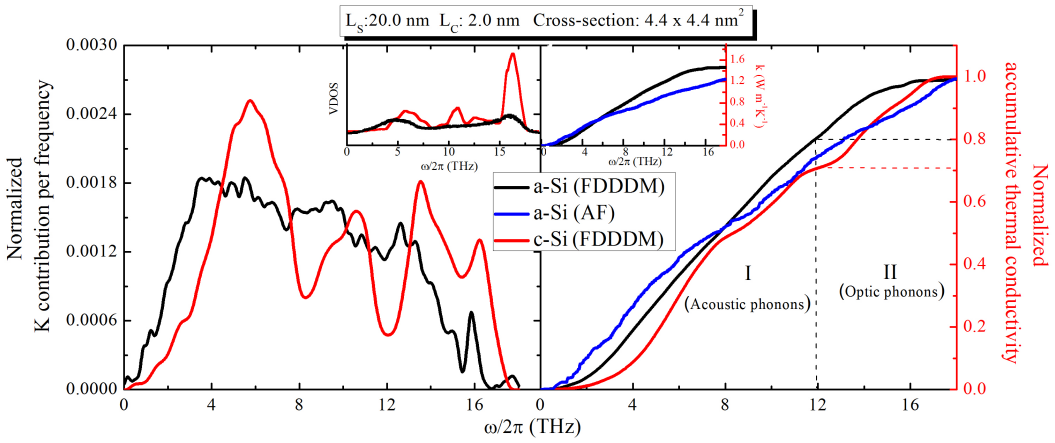


FIGURE 3.11: (Color online) (Left) Normalized spectral contribution to thermal conductivity and (right) corresponding normalized accumulative thermal conductivity as a function of mode frequency for amorphous Si computed using FDDDM and AF theory. The dashed lines are guide for the eyes. (Left inset) Comparison of VDOS between amorphous Si and crystalline Si. (Right inset) The actual accumulative thermal conductivity of c-Si and a-Si vs. frequency.

The results calculated using FDDDM and AF theory are compared in Figure 3.11. Here, we also give the result of crystalline Si (c-Si) for comparison. General consistency is found between the results calculating with FDDDM and that of AF theory. Comparing with the results of FDDDM, the AF-predicted phonons have relatively high thermal conductivity contribution in the low-frequency region ($\omega < 8$ THz). The reason is the broadening of the Dirac delta function, which can lead to the decreasing of diffusivities at intermediate and high frequencies (Larkin and McGaughey, 2014). In disordered materials, Larkin et al. (Larkin and McGaughey, 2014) find that the relaxation time of each phonon in the middle frequency region (4∼12 THz) is nearly in the same magnitude (Figure 3.4 in Ref. (Larkin and McGaughey, 2014)), which means the scattering of phonons in such materials is quite strong. Furthermore, we also plot the vibrational density of states (VDOS) of a-Si and c-Si, which shows that the distribution of phonons in a-Si is more uniform with respect to that of c-Si [inset of Figure 3.11]. Therefore, it is not surprising to find that the contribution of middle frequency phonons in a-Si is more uniform than that in c-Si [left panel of Figure 3.11]. We also observe that the phonons of a-Si in high

frequency region contribute less than that of c-Si in the same region, or equivalently, phonons of a-Si in this region is more likely to scatter. Generally speaking, in the disordered materials, diffusons are the main heat carriers (Larkin and McGaughey, 2014; Sosso et al., 2012). Therefore, it is usual to treat the disordered materials as homogenous materials when the thermal conductivity of such material is concerned. Once again, we plot the actual thermal conductivity of the a-Si computed using FDDDM and AF theory. The results are 1.45 W/mK for FDDDM and 1.21 W/mK for AF theory. We think the difference should come from the fact that the propagating phonon mode which is not considered by AF theory can contribute to the total thermal conductivity to some extent. At the same time, Larkin *et al*. (Larkin and McGaughey, 2014) give the thermal conductivity of a-Si as 2.0 W/mK using GK-MD and 1.2 W/mK using AF theory. The result obtained using GK-MD is larger than that by FDDDM and AF theory. This may be related to the propagating phonon modes, which deserves further study in the future.

3.4 Extension based on Frequency Domain Direct Decomposed Method

In this section, we derive frequency dependent thermal conductance caused by the three-phonon scattering at the interface by extending the derivation of Sääskilahti *et. al*. (Sääskilahti et al., 2015) and FDDDM. All possible three-phonon scattering channels at the interface are included in our expression by considering the full third order force constants field. Using our approach, it is straightforward to observe the importance of three-phonon scattering process at interface. Furthermore, by knowing the contribution to a specific vibration frequency from all possible atoms, we can explicitly know the contributions of different types of three-phonon scattering process.

3.4.1 Framework of the methodology

For a classical atomic system, we can construct its potential energy P by performing Taylor expansion up to the third order using the atomic displacement of atom i (u_i) with respect to its equilibrium position (Maradudin and Fein, 1962)

$$P \approx P_0 + \sum_{\alpha}\sum_{i}\Phi_i^{\alpha}u_i^{\alpha} + \frac{1}{2!}\sum_{\alpha\beta}\sum_{ij}\Phi_{ij}^{\alpha\beta}u_i^{\alpha}u_j^{\beta} + \frac{1}{3!}\sum_{\alpha\beta\gamma}\sum_{ijk}\Phi_{ijk}^{\alpha\beta\gamma}u_i^{\alpha}u_j^{\beta}u_k^{\gamma} \tag{3.38}$$

where P_0 is the potential energy of the atom at the equilibrium position, Φ_i, Φ_{ij} and Φ_{ijk} are the first, second (harmonic) and third (cubic) force constants, respectively. $\Phi_i = 0$ since the displacements u_i are always around the equilibrium positions in

solid materials. The harmonic and cubic force constants can be obtained using

$$\Phi_{ij}^{\alpha\beta} = \left.\frac{\partial^2 V}{\partial u_i^\alpha \partial u_j^\beta}\right|_{\vec{u}=0} \tag{3.39}$$

and

$$\Phi_{ijk}^{\alpha\beta\gamma} = \left.\frac{\partial^3 V}{\partial u_i^\alpha \partial u_j^\beta \partial u_k^\gamma}\right|_{\vec{u}=0} \tag{3.40}$$

Meanwhile, it is well known that, NEMD simulations explicitly rely on launching a steady state heat flux to flow through the system. The interparticle energy exchange rate (EER) ξ_{ij} between two atoms i and j can be written as (Torii, Nakano, and Ohara, 2008; Dobson, 2013)

$$\xi_{ij} = \frac{1}{2}\left\langle \sum_\alpha F_{ji}^\alpha \cdot v_i^\alpha - \sum_\beta F_{ij}^\beta \cdot v_j^\beta \right\rangle \tag{3.41}$$

where the bracket represents the time average, α] and β stands for the direction (x, y, or z), v_i and v_j are the velocities of atom i and j, respectively, $\vec{F}_{ij}$ is the interparticle force on atom j due to atom i. Based on the potential displayed in Eq. (3.38) , one can extract the expression for the force required in MD simulation (Sääskilahti et al., 2014)

$$F_{ji}^\alpha = -\sum_\beta \Phi_{ij}^{\alpha\beta} u_j^\beta - \frac{1}{3}\sum_{\beta\gamma}\sum_k \Phi_{ijk}^{\alpha\beta\gamma} u_j^\beta u_k^\gamma \tag{3.42}$$

Thus, the interparticle force on atom j due to atom i, $\vec{F}_{ij}$, can be written as (Sääskilahti et al., 2014)

$$F_{ji}^\alpha = -\sum_\beta \Phi_{ij}^{\alpha\beta} u_j^\beta - \frac{1}{3}\sum_{\beta\gamma}\sum_k \Phi_{ijk}^{\alpha\beta\gamma} u_j^\beta u_k^\gamma \tag{3.43}$$

Here, we regard the contribution of the harmonic and cubic term of potential energy to EER as ξ_{ij}^{Two} and ξ_{ij}^{Three} respectively. Then, with the help of Eq. (3.38), the detailed expression of ξ_{ij}^{Two} can be shown as

$$\xi_{ij}^{Two} = -\frac{1}{2}\left\langle \sum_{\alpha\beta} u_j^\beta \Phi_{ij}^{\alpha\beta} \cdot v_i^\alpha + \sum_{\alpha\beta} u_i^\alpha \Phi_{ij}^{\alpha\beta} \cdot v_j^\beta \right\rangle \tag{3.44}$$

and the ξ_{ij}^{Three} has the form of

$$\xi_{ij}^{Three} = -\frac{1}{6}\left\langle \sum_{\alpha\beta\gamma}\sum_k u_j^\beta u_k^\gamma \Phi_{ijk}^{\alpha\beta\gamma} \cdot v_i^\alpha + \sum_{\alpha\beta\gamma}\sum_k u_i^\alpha u_k^\gamma \Phi_{ijk}^{\alpha\beta\gamma} \cdot v_j^\beta \right\rangle \tag{3.45}$$

Furthermore, it has been proved that the spectral decomposition of EER is related to the correlation time between interparticle force and velocity (Chalopin and Volz, 2013; Sääskilahti et al., 2015). Therefore, we can write the auxiliary correlation term

C_{ij} as

$$C_{ij} = \frac{1}{2}\left\langle \sum_{\alpha} F_{ji}^{\alpha}(t_2)\cdot v_i^{\alpha}(t_1) - \sum_{\beta} F_{ij}^{\beta}(t_2)\cdot v_j^{\beta}(t_1)\right\rangle \tag{3.46}$$

Based on Eq. (3.43) - (3.46), we can find that

$$C_{ij} \approx C_{ij}^{Two} + C_{ij}^{Three} \tag{3.47}$$

and the expression can be written as

$$C_{ij}^{Two} = \frac{1}{2}\left\langle \sum_{\alpha\beta} u_j^{\beta}(t_2)\Phi_{ij}^{\alpha\beta}\cdot v_i^{\alpha}(t_1) + \sum_{\beta} u_i^{\alpha}(t_2)\Phi_{ij}^{\alpha\beta}\cdot v_j^{\beta}(t_1)\right\rangle \tag{3.48}$$

and

$$C_{ij}^{Three} = \frac{1}{6}\left\langle \sum_{\alpha\beta\gamma}\sum_{k} u_j^{\beta}(t_2)u_k^{\gamma}(t_2)\Phi_{ijk}^{\alpha\beta\gamma}\cdot v_i^{\alpha}(t_1) + \sum_{\alpha\beta\gamma}\sum_{k} u_i^{\alpha}(t_2)u_k^{\gamma}(t_2)\Phi_{ijk}^{\alpha\beta\gamma}\cdot v_j^{\beta}(t_1)\right\rangle \tag{3.49}$$

When we define the characteristic time $\tau = t_2 - t_1$, the interparticle EER can be written as

$$\xi_{ij} = -\lim_{\tau\to 0}\left[C_{ij}^{Two}(\tau) + C_{ij}^{Three}(\tau)\right] \tag{3.50}$$

As generated by Sääskilahti *et. al.* (Sääskilahti et al., 2015), we can define the Fourier transform

$$\tilde{C}_{ij}^{Two}(\omega) = \int_{-\infty}^{+\infty} C_{ij}^{Two}(\tau)\, e^{i\omega\tau} d\tau \tag{3.51}$$

$$\tilde{C}_{ij}^{Three}(\omega) = \int_{-\infty}^{+\infty} C_{ij}^{Three}(\tau)\, e^{i\omega\tau} d\tau \tag{3.52}$$

Then, $C_{ij}^{Two}(\tau)$ and $C_{ij}^{Three}(\tau)$ can be obtained using the inverse Fourier transform of $\tilde{C}_{ij}^{Two}(\omega)$ and $\tilde{C}_{ij}^{Three}(\omega)$, respectively. Then, the detailed expressions of $C_{ij}^{Two}(\tau)$ and $C_{ij}^{Three}(\tau)$ can be shown as

$$C_{ij}^{Two}(\tau) = \int_{-\infty}^{+\infty} \tilde{C}_{ij}^{Two}(\omega)\, e^{-i\omega\tau}\frac{d\omega}{2\pi} \tag{3.53}$$

and

$$C_{ij}^{Three}(\tau) = \int_{-\infty}^{+\infty} \tilde{C}_{ij}^{Three}(\omega)\, e^{-i\omega\tau}\frac{d\omega}{2\pi} \tag{3.54}$$

Therefore, using Eq. (3.50) - (3.54) the EER can be recast in the form of

$$\begin{aligned}\xi_{ij} &= -\lim_{\tau\to 0}\left[\int_{-\infty}^{+\infty} \tilde{C}_{ij}^{Two}(\omega)\, e^{-i\omega\tau}\frac{d\omega}{2\pi} + \int_{-\infty}^{+\infty} \tilde{C}_{ij}^{Three}(\omega)\, e^{-i\omega\tau}\frac{d\omega}{2\pi}\right] \\ &= -\int_{-\infty}^{+\infty} \tilde{C}_{ij}^{Two}(\omega)\frac{d\omega}{2\pi} - \int_{-\infty}^{+\infty} \tilde{C}_{ij}^{Three}(\omega)\frac{d\omega}{2\pi}\end{aligned} \tag{3.55}$$

From Eq. (3.48), (3.53), and

$$\tilde{v}_i^{\alpha}(\omega) = -i\omega\tilde{u}_i^{\alpha}(\omega) \tag{3.56}$$

Then, we can know that

$$\begin{aligned}
\tilde{C}_{ij}^{Two}(\omega) =& \int_{-\infty}^{+\infty} \left\{ \frac{1}{2} \left\langle \sum_{\alpha\beta} u_j^{\beta}(\tau)\Phi_{ij}^{\alpha\beta} v_i^{\alpha}(0) + \sum_{\alpha\beta} u_i^{\alpha}(\tau)\Phi_{ij}^{\alpha\beta} v_j^{\beta}(0) \right\rangle \right\} e^{i\omega\tau} d\tau \\
=& \frac{1}{2} \left\{ \sum_{\alpha\beta} \Phi_{ij}^{\alpha\beta} \int_{-\infty}^{+\infty} \left\langle u_j^{\beta}(\tau) v_i^{\alpha}(0) \right\rangle e^{i\omega\tau} d\tau + \sum_{\alpha\beta} \Phi_{ij}^{\alpha\beta} \int_{-\infty}^{+\infty} \left\langle u_i^{\alpha}(\tau) v_j^{\beta}(0) \right\rangle e^{i\omega\tau} d\tau \right\} \\
=& \frac{1}{2} \left\{ \sum_{\alpha\beta} \Phi_{ij}^{\alpha\beta} \left\langle \tilde{u}_j^{\beta}(\omega) \tilde{v}_i^{\alpha *}(\omega) \right\rangle + \sum_{\alpha\beta} \Phi_{ij}^{\alpha\beta} \left\langle \tilde{u}_i^{\alpha}(\omega) \tilde{v}_j^{\beta *}(\omega) \right\rangle \right\} \\
=& \frac{i}{\omega} \left[\sum_{\alpha\beta} \Phi_{ij}^{\alpha\beta} \left\langle \tilde{v}_j^{\beta}(\omega) \tilde{v}_i^{\alpha *}(\omega) \right\rangle \right]
\end{aligned} \tag{3.57}$$

Based on Eq. (3.49) and (3.54), in the same way, we can write $\tilde{C}_{ij}^{Three}(\omega)$as

$$\begin{aligned}
\tilde{C}_{ij}^{Three}(\omega) =& \int_{-\infty}^{+\infty} \left\{ \frac{1}{6} \left\langle \sum_{\alpha\beta\gamma} \sum_{k} u_j^{\beta}(\tau) u_k^{\gamma}(\tau) \Phi_{ijk}^{\alpha\beta\gamma} \cdot v_i^{\alpha}(0) \right.\right. \\
& \left.\left. + \sum_{\alpha\beta\gamma} \sum_{k} u_i^{\alpha}(\tau) u_k^{\gamma}(\tau) \Phi_{ijk}^{\alpha\beta\gamma} \cdot v_j^{\beta}(0) \right\rangle \right\} e^{i\omega\tau} d\tau \\
=& \frac{1}{6} \sum_{\alpha\beta\gamma} \sum_{k} \Phi_{ijk}^{\alpha\beta\gamma} \int_{-\infty}^{+\infty} \left\langle u_j^{\beta}(\tau) u_k^{\gamma}(\tau) v_i^{\alpha}(0) \right\rangle e^{i\omega\tau} d\tau + \\
& \frac{1}{6} \sum_{\alpha\beta\gamma} \sum_{k} \Phi_{ijk}^{\alpha\beta\gamma} \int_{-\infty}^{+\infty} \left\langle u_i^{\alpha}(\tau) u_k^{\gamma}(\tau) v_j^{\beta}(0) \right\rangle e^{i\omega\tau} d\tau
\end{aligned} \tag{3.58}$$

In order to obtain the final expression of $\tilde{C}_{ij}^{Three}(\omega)$, we define

$$D(\tau) = u_j^{\beta}(\tau) u_k^{\gamma}(\tau) \tag{3.59}$$

Then, we can find that

$$\begin{aligned}\tilde{D}(\omega) &= \int_{+\infty}^{+\infty} D(\tau)e^{i\omega\tau}d\tau \\ &= \int_{+\infty}^{+\infty} u_j^{\beta}(\tau)u_k^{\gamma}(\tau)e^{i\omega\tau}d\tau \\ &= \int_{+\infty}^{+\infty} u_j^{\beta}(\tau)e^{i\omega\tau}\int_{-\infty}^{+\infty}\tilde{u}_k^{\gamma}(\omega')e^{-i\omega'\tau}\frac{d\omega'}{2\pi}d\tau \\ &= \int_{-\infty}^{+\infty}\tilde{u}_k^{\gamma}(\omega')\int_{+\infty}^{+\infty} u_j^{\beta}(\tau)e^{i(\omega-\omega')\tau}d\tau\frac{d\omega'}{2\pi} \\ &= \int_{-\infty}^{+\infty}\tilde{u}_j^{\beta}(\omega-\omega')\tilde{u}_k^{\gamma}(\omega')\frac{d\omega'}{2\pi}\end{aligned} \tag{3.60}$$

Furthermore, $\int_{-\infty}^{+\infty}\left\langle u_j^{\beta}(\tau)u_k^{\gamma}(\tau)v_i^{\alpha}(0)\right\rangle e^{i\omega\tau}d\tau$ can be written in the form of

$$\int_{-\infty}^{+\infty}\left\langle u_j^{\beta}(\tau)u_k^{\gamma}(\tau)v_i^{\alpha}(0)\right\rangle e^{i\omega\tau}d\tau = \int_{-\infty}^{+\infty}\langle D(\tau)v_i^{\alpha}(0)\rangle e^{i\omega\tau}d\tau = \left\langle\tilde{D}(\omega)\tilde{v}_i^{\alpha*}(\omega)\right\rangle \tag{3.61}$$

Combining Eq. (3.56), Eq. (3.59) and Eq. (3.60), we can rewrite the expression of Eq. (3.58) as

$$\begin{aligned}\tilde{C}_{ij}^{Three}(\omega) =& \frac{1}{6}\sum_{\alpha\beta\gamma}\sum_{k}\Phi_{ijk}^{\alpha\beta\gamma}\int_{-\infty}^{+\infty}\left\langle\tilde{v}_i^{\alpha*}(\omega)\tilde{u}_j^{\beta}(\omega-\omega')\tilde{u}_k^{\gamma}(\omega')\right\rangle\frac{d\omega'}{2\pi} + \\ & \frac{1}{6}\sum_{\alpha\beta\gamma}\sum_{k}\Phi_{ijk}^{\alpha\beta\gamma}\int_{-\infty}^{+\infty}\left\langle\tilde{v}_j^{\beta*}(\omega)\tilde{u}_i^{\alpha}(\omega-\omega')\tilde{u}_k^{\gamma}(\omega')\right\rangle\frac{d\omega'}{2\pi} \\ =& -\frac{1}{6}\sum_{\alpha\beta\gamma}\sum_{k}\Phi_{ijk}^{\alpha\beta\gamma}\int_{-\infty}^{+\infty}\frac{\left\langle\tilde{v}_i^{\alpha*}(\omega)\tilde{u}_j^{\beta}(\omega-\omega')\tilde{u}_k^{\gamma}(\omega')\right\rangle}{(\omega-\omega')\omega'}\frac{d\omega'}{2\pi} \\ & -\frac{1}{6}\sum_{\alpha\beta\gamma}\sum_{k}\Phi_{ijk}^{\alpha\beta\gamma}\int_{-\infty}^{+\infty}\frac{\left\langle\tilde{v}_j^{\beta*}(\omega)\tilde{u}_i^{\alpha}(\omega-\omega')\tilde{u}_k^{\gamma}(\omega')\right\rangle}{(\omega-\omega')\omega'}\frac{d\omega'}{2\pi}\end{aligned} \tag{3.62}$$

Since the real and imaginary part of $\tilde{C}_{ij}^{Two}(\omega)$ and $\tilde{C}_{ij}^{Three}(\omega)$ should be even and odd functions, respectively (Sääskilahti et al., 2015), by combining Eq. (3.55), (3.56),

(3.57), and (3.62), the EER spectrum can be shown as

$$\begin{aligned}\tilde{\xi}_{ij}(\omega) = \mathrm{Re}\Bigg\{ & -\frac{2i}{\omega}\left[\sum_{\alpha\beta}\Phi_{ij}^{\alpha\beta}\left\langle\tilde{v}_j^{\beta}(\omega)\tilde{v}_i^{\alpha*}(\omega)\right\rangle\right] \\ & + \frac{1}{6}\sum_{\alpha\beta\gamma}\sum_{k}\Phi_{ijk}^{\alpha\beta\gamma}\int_{-\infty}^{+\infty}\frac{\left\langle\tilde{v}_i^{\alpha*}(\omega)\tilde{u}_j^{\beta}(\omega-\omega')\tilde{u}_k^{\gamma}(\omega')\right\rangle}{(\omega-\omega')\omega'}\frac{d\omega'}{2\pi} \\ & + \frac{1}{6}\sum_{\alpha\beta\gamma}\sum_{k}\Phi_{ijk}^{\alpha\beta\gamma}\int_{-\infty}^{+\infty}\frac{\left\langle\tilde{v}_j^{\beta*}(\omega)\tilde{u}_i^{\alpha}(\omega-\omega')\tilde{u}_k^{\gamma}(\omega')\right\rangle}{(\omega-\omega')\omega'}\frac{d\omega'}{2\pi} \\ & - \frac{1}{6}\sum_{\alpha\beta\gamma}\sum_{k}\Phi_{ijk}^{\alpha\beta\gamma}\int_{-\infty}^{+\infty}\frac{\left\langle\tilde{v}_i^{\alpha*}(\omega)\tilde{u}_j^{\beta*}(\omega+\omega')\tilde{u}_k^{\gamma}(\omega')\right\rangle}{(\omega+\omega')\omega'}\frac{d\omega'}{2\pi} \\ & - \frac{1}{6}\sum_{\alpha\beta\gamma}\sum_{k}\Phi_{ijk}^{\alpha\beta\gamma}\int_{-\infty}^{+\infty}\frac{\left\langle\tilde{v}_j^{\beta*}(\omega)\tilde{u}_i^{\alpha*}(\omega+\omega')\tilde{u}_k^{\gamma}(\omega')\right\rangle}{(\omega+\omega')\omega'}\frac{d\omega'}{2\pi}\Bigg\}\end{aligned} \tag{3.63}$$

The first term on the right-hand-side of Eq. (3.63) indicates that the heat flux across the interface carried by a specific vibrational mode is only related to the same vibrational frequency of atom i and j (the vibration of each atom can be decomposed into the contribution from many vibrational modes). In other words, a vibrational mode with frequency ω on the left side of the interface can only exchange energy with a vibrational mode with the same frequency ω on the right side of the interface. Since the energy exchange between the vibrational modes corresponds to "phonon scattering", the first term on the right-hand-side of Eq. (3.63) can then be regarded as the two-phonon scattering process. Based on the analysis above, the heat flux spectrum calculated here should be in accordance with that using AGF for low temperature system (only at low temperatures the vibrations of atoms can be regarded as harmonic, or rigorously speaking harmonic dominated, see Sec. below for details), which has been proved in Ref. (Sääskilahti et al., 2015). The rest terms on the right-hand-side of Eq. (3.63) (here the second term is chosen as an example for analysis) show that, a vibrational mode of atom i with frequency ω can exchange energy with the vibrational mode $(\omega-\omega')$ of atom j and the vibrational mode (ω') of atom k. Therefore, the first term on the right-hand-side of Eq. (3.63) is related to a two-phonon (elastic) process and the rest terms correspond to the three-phonon (inelastic) scattering process.The EER across any cross-section separating disjointed atom sets (denoted as "L" and "R", which can be regarded as the left and right side

of an interface, respectively) can be obtained as

$$\begin{aligned}
\tilde{\xi}(\omega) &= \sum_{i\in L,\, j\in R} \tilde{\xi}_{ij}(\omega) \\
&\approx \sum_{i\in L,\, j\in R} \mathrm{Re}\left\{ -\frac{2i}{\omega}\left[\sum_{\alpha\beta}\Phi_{ij}^{\alpha\beta}\left\langle \tilde{v}_j^{\beta}(\omega)\tilde{v}_i^{\alpha *}(\omega)\right\rangle\right]\right. \\
&\quad + \frac{1}{6}\sum_{\alpha\beta\gamma}\sum_{k}\Phi_{ijk}^{\alpha\beta\gamma}\int_{-\infty}^{+\infty}\frac{\left\langle \tilde{v}_i^{\alpha *}(\omega)\tilde{u}_j^{\beta}(\omega-\omega')\tilde{u}_k^{\gamma}(\omega')\right\rangle}{(\omega-\omega')\omega'}\frac{d\omega'}{2\pi} \\
&\quad + \frac{1}{6}\sum_{\alpha\beta\gamma}\sum_{k}\Phi_{ijk}^{\alpha\beta\gamma}\int_{-\infty}^{+\infty}\frac{\left\langle \tilde{v}_j^{\beta *}(\omega)\tilde{u}_i^{\alpha}(\omega-\omega')\tilde{u}_k^{\gamma}(\omega')\right\rangle}{(\omega-\omega')\omega'}\frac{d\omega'}{2\pi} \\
&\quad - \frac{1}{6}\sum_{\alpha\beta\gamma}\sum_{k}\Phi_{ijk}^{\alpha\beta\gamma}\int_{-\infty}^{+\infty}\frac{\left\langle \tilde{v}_i^{\alpha *}(\omega)\tilde{u}_j^{\beta *}(\omega+\omega')\tilde{u}_k^{\gamma}(\omega')\right\rangle}{(\omega+\omega')\omega'}\frac{d\omega'}{2\pi} \\
&\quad \left. - \frac{1}{6}\sum_{\alpha\beta\gamma}\sum_{k}\Phi_{ijk}^{\alpha\beta\gamma}\int_{-\infty}^{+\infty}\frac{\left\langle \tilde{v}_j^{\beta *}(\omega)\tilde{u}_i^{\alpha *}(\omega+\omega')\tilde{u}_k^{\gamma}(\omega')\right\rangle}{(\omega+\omega')\omega'}\frac{d\omega'}{2\pi}\right\}
\end{aligned} \tag{3.64}$$

Here, we can find that the harmonic term, i.e. first term on the right-hand-side of Eq. (3.64), of the EER spectrum yields the same expression as in Ref. (Sääskilahti et al., 2015) (defined as the heat current spectrum in the reference), and the three-phonon scattering contribution can be written as

$$\begin{aligned}
\tilde{\xi}^{Three}(\omega) &= \sum_{i\in L,\, j\in R} \tilde{\xi}_{ij}^{Three}(\omega) \\
&= \sum_{i\in L,\, j\in R} \mathrm{Re}\left\{ \frac{1}{6}\sum_{\alpha\beta\gamma}\sum_{k}\Phi_{ijk}^{\alpha\beta\gamma}\int_{-\infty}^{+\infty}\frac{\left\langle \tilde{v}_i^{\alpha *}(\omega)\tilde{u}_j^{\beta}(\omega-\omega')\tilde{u}_k^{\gamma}(\omega')\right\rangle}{(\omega-\omega')\omega'}\frac{d\omega'}{2\pi}\right. \\
&\quad + \frac{1}{6}\sum_{\alpha\beta\gamma}\sum_{k}\Phi_{ijk}^{\alpha\beta\gamma}\int_{-\infty}^{+\infty}\frac{\left\langle \tilde{v}_j^{\beta *}(\omega)\tilde{u}_i^{\alpha}(\omega-\omega')\tilde{u}_k^{\gamma}(\omega')\right\rangle}{(\omega-\omega')\omega'}\frac{d\omega'}{2\pi} \\
&\quad - \frac{1}{6}\sum_{\alpha\beta\gamma}\sum_{k}\Phi_{ijk}^{\alpha\beta\gamma}\int_{-\infty}^{+\infty}\frac{\left\langle \tilde{v}_i^{\alpha *}(\omega)\tilde{u}_j^{\beta *}(\omega+\omega')\tilde{u}_k^{\gamma}(\omega')\right\rangle}{(\omega+\omega')\omega'}\frac{d\omega'}{2\pi} \\
&\quad \left. - \frac{1}{6}\sum_{\alpha\beta\gamma}\sum_{k}\Phi_{ijk}^{\alpha\beta\gamma}\int_{-\infty}^{+\infty}\frac{\left\langle \tilde{v}_j^{\beta *}(\omega)\tilde{u}_i^{\alpha *}(\omega+\omega')\tilde{u}_k^{\gamma}(\omega')\right\rangle}{(\omega+\omega')\omega'}\frac{d\omega'}{2\pi}\right\}
\end{aligned} \tag{3.65}$$

From the expression above, we can easily find that the energy conservation among the three-phonon scattering process is satisfied through

$$\omega = (\omega-\omega') + \omega' \tag{3.66}$$

and

$$\omega + \omega' = (\omega+\omega') \tag{3.67}$$

The EER of a specific phonon mode is resulted from all the possible three-phonon

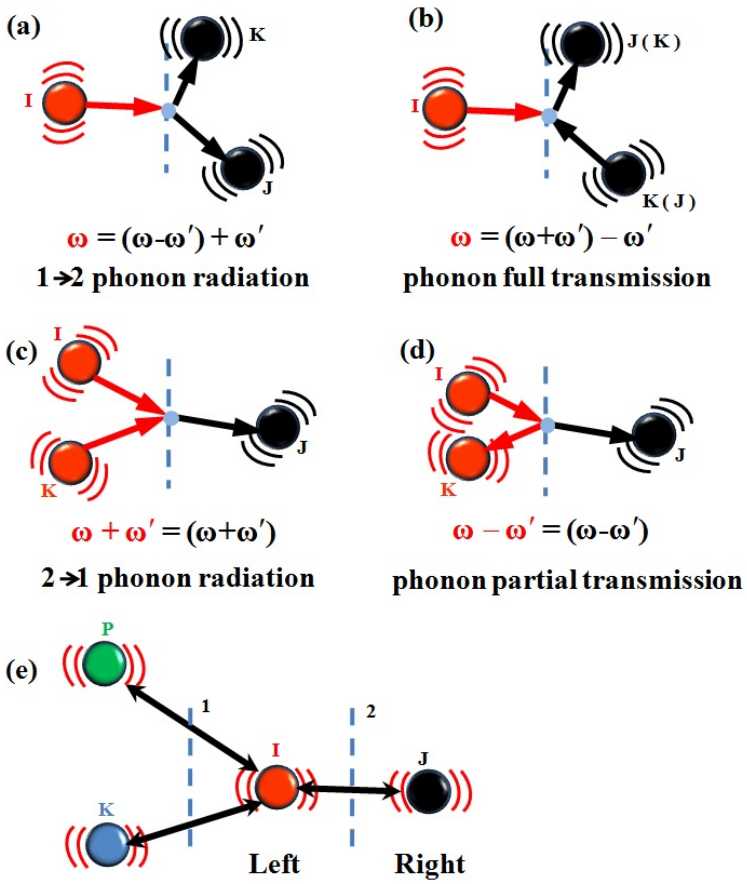


FIGURE 3.12: (Color online) Schematic of four different types of three-phonon scattering process at the interface (a-d). The situation in bulk materials (e). The blue dashed line represents the interface separating two different materials (a-d) or an imaginary interface in a bulk material (e).

scattering process which satisfies the energy conservation. Here, we have to emphasize that our results are frequency dependent rather than mode dependent. To further distinguish the phonon mode level, the space Fourier transform of the atomic velocity could be implemented, which will be studied in our future work. Then, we can know that the three-phonon process in our paper actually include all the mode level three-phonon scattering process involving ω, ω' and $\omega + \omega'$. If one wants to calculate the thermal conductance of frequency ω, all the possible mode-level three phonon process should be included, which means the results will be identical to the one we compute using our theory. Thus, here, the three-phonon contributed thermal conductance of frequency ω are truly from all the possible three-phonon process, which should satisfy the energy conservation. Based on the vibration of an atom k belonging to the left or right side of the interface [Eq. (3.65)], we can define four different types of three-phonon process similar to that in Ref. (Hohensee, Wilson, and

Cahill, 2015), namely, 1 to 2 phonon radiation, phonon full transmission, 2 to 1 radiation and phonon partial transmission [Figure 3.12]. Regarding all phonon modes hold the same temperature change at the interface or temperature gradient as we did above, we can write the contribution of a phonon mode with specific frequency to the overall thermal conductance $G(\omega)$ in the form of

$$G(\omega) = \frac{\tilde{\xi}(\omega)}{A\Delta T} \approx \frac{\tilde{\xi}^{Two}(\omega) + \tilde{\xi}^{Three}(\omega)}{A\Delta T} \tag{3.68}$$

where A is the area of the cross-section in a NEMD simulation (blue dashed line in Figure 3.12), ∇T is the temperature drop at the interface. Both the second- and third-order inter-atomic force constants are computed using a real-space finite displacement difference method. For practical purpose, a cutoff radius is defined such that the atoms farther than the cutoff distance are not considered for interaction. Here, in our simulations, we choose the cutoff distance in the interatomic potential as our cutoff radius to calculate the inter-atomic force constants, which is 8.5 Å and 3 Å for the Ar-heavy Ar and Si-Ge systems, respectively.

3.4.2 Validation and application of the methodology

Benchmark of bulk Ar: Before we investigate the thermal transport across the interface, we calibrate our theoretical framework by studying the heat flux of bulk Ar, since in principle we can assume an imaginary interface in the bulk system and then apply our method for analysis. Results obtained using the theory presented in Sec. IIA are compared to those calculated using FDDDM which *automatically* includes all the higher-order phonon scattering process (Zhou and Hu, 2015). Here, we have to note that the two- and three-phonon processes are only valid for the imaginary interface we set, not for the entire bulk system (see details below). Next, we use the heat flux rather than thermal conductivity to characterize the two- and three-phonon process in bulk Ar, since the heat flux in our theory is the quantity related to the imaginary interface. All the two- and three-phonon process mentioned in this Section are referring to the imaginary interface. In Figure 3.13 we show the results of bulk Ar. It is evident to find that, only considering the two-phonon process (elastic) is not enough [Figure 3.13], even at low temperature (as low as 10 K for bulk Ar), where anharmonic phonon scattering is usually thought to be not strong. If three-phonon process are taken into consideration, both the frequency dependent heat flux [left panel of Figure 3.13] and the accumulative heat flux [right panel of Figure 3.13] are close to the real values (results from FDDDM), when the system temperature is relatively low, e.g. lower than 30 K. With system temperature increasing (above 30 K), the heat flux, when only considering two- and three-phonon process, becomes lower than the real value obviously (only reaches 85% and 77% of total heat flux for 40 K and 50 K, respectively) [right panel of Figure 3.13]. This implies that, in such cases even higher order phonon process, such as four phonon process (only valid for the imaginary interface), should be considered as well. It should be noticed that the

results calculated using the theory mentioned above are different from those computed by FDDDM at a certain extent. Such discrepancy is anticipated to originate from the inherent fluctuation of the heat flux across the interface (the current theoretical framework) and the heat current calculated in a control volume in FDDDM. Nevertheless, the results shown in Figure 3.13 confirm the validity of our theoretical framework.

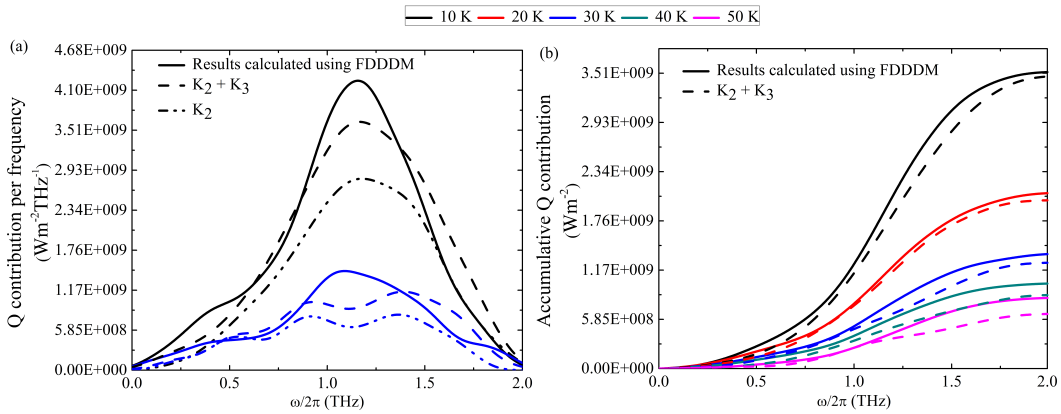


FIGURE 3.13: (Color online) (a) Spectral contribution to overall heat flux of bulk Ar calculated using two-phonon process (double-dashed line), two- and three-phonon process (dashed line) and FDDDM (solid line). (b) Accumulative heat flux as a function of frequency computed using two- and three-phonon process and FDDDM. Here, the two- and three-phonon processes are only valid for the imaginary interface.

Analysis of Ar-heavy Ar interface: We now apply our theoretical framework to analyze the thermal transport process across the Ar-heavy Ar interface. Since the importance of three-phonon process to interfacial thermal conductance is the main topic of this paper, five different system temperatures (from 10 K to 50 K) are used to investigate the contribution of two- and three-phonon process with respect to the total interfacial thermal conductance. Firstly, if only two-phonon process is taken into consideration, phonons with frequency larger than 1.0 THz contribute a little to the overall thermal conductance [Figure 3.14a and 3.14c], because these high frequency phonons cannot propagate in the heavy Ar, due to the absence of overlap between the vibrational density of states (VDOS) of Ar and heavy Ar [Figure 3.15a]. Meanwhile, the nonlinearities which increase with temperature in the potential enable the inelastic atomic interactions in the bulk near the interface (such effect is reflected by the velocity in Eq. (3.64) (see Sec. below for details), and therefore, phonons above 1.0 THz can transmit their energy across the interface (but it is still the two-phonon process) (Sääskilahti et al., 2015). When the three-phonon process is included, the computed total thermal conductance becomes very close to the actual thermal conductance (more than 95% of the total thermal conductance) for these systems with temperature lower than 30 K. Once again, we find that the higher order phonon process should be included when system temperature is above 30 K. Ignoring the

higher order phonon process can result in an error as high as 23% in our simulation results [Figure 3.15c]. Since the phonons transport from the normal Ar lead to heavy Ar lead in our simulation, it is possible to use the phonon properties of bulk Ar to describe the thermal conductance. The low frequency phonons in bulk Ar, which normally have long mean free path, can be scattered by the interface and then contribute little to the thermal conductance. The high frequency phonons can only contribute a little to the thermal conductance due to the low energy carried by these phonons (small group velocity). Therefore, the phenomena that the contribution of these three-phonon process are mainly related to the phonons in the middle frequency region (0.75 ∼1.5 THz), are because of their moderate mean free path and relative large group velocity in bulk Ar. It should be noted that the three-phonon process is important even in the low temperature system. Duda *et. al.* (Duda et al., 2011)found that the inelastic phonon process can contribute as large as 50% of the thermal conductance at 10 K, which is in reasonable accordance with our results (33%). The difference should come from the different mass ration between Ar and heavy Ar used in their work and our system.

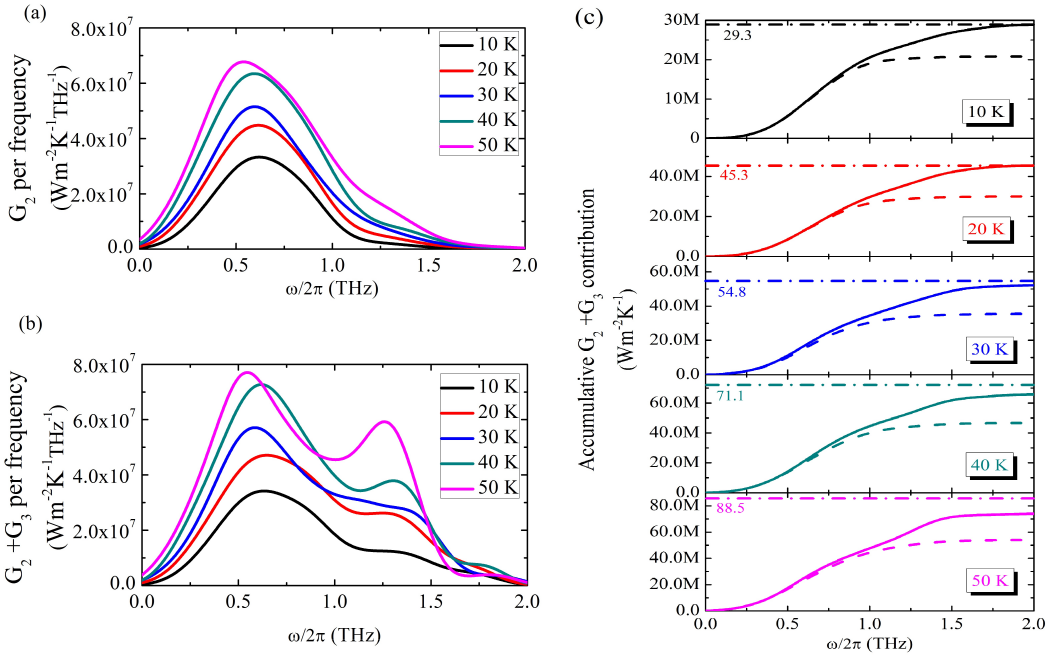


FIGURE 3.14: (Color online) (a) Spectral thermal conductance of Ar-heavy Ar interface contributed only by the two-phonon process at different temperatures. (b) The corresponding spectral thermal conductance contributed by the two- and three-phonon process. (c) The comparison of accumulative thermal conductance contributed by only two-phonon process (dashed line), two- and three-phonon process (solid line).

Next, we pay our attention to the contribution of different types of three-phonon scattering process as we defined in above [Figure 3.12]. From Figure 3.16, we can find that in the low temperature system, the 2 to 1 phonon radiation [Figure 3.12c]

and the phonon partial transmission [Figure 3.12d] can carry more energy in a fixed period than the other three process including 1 to 2 phonon radiation [Figure 3.121] and phonon full transmission [Figure 3.12b]. In our systems with low temperature, three-phonon process, which involves one high frequency phonon at the Ar side [>1.5 THz as shown in Figure 3.15] and the rest two-phonons at the heavy Ar side, contributes a little to the thermal conductance. However, with system temperature increasing, such three-phonon process can contribute to the thermal conductance significantly. Consequently, the contribution of these four types of three-phonon process becomes similar [Figure 3.16]. Very recently, Hohensee *et. al.* (Hohensee, Wilson, and Cahill, 2015) find that the phonon partial transmission (equal to the summation of the phonon partial transmission and 2 to 1 phonon radiation in our case) plays major role in the energy exchange across the metal/diamond interface. They explain this phenomenon in the sense that the mismatch of the frequency range between metal and diamond is very large, and therefore, the phase space for the phonon partial transmission is quite large. In our case, the difference of the frequency between Ar and heavy Ar is not too large. Thus, such mechanism does not play a dominant role.

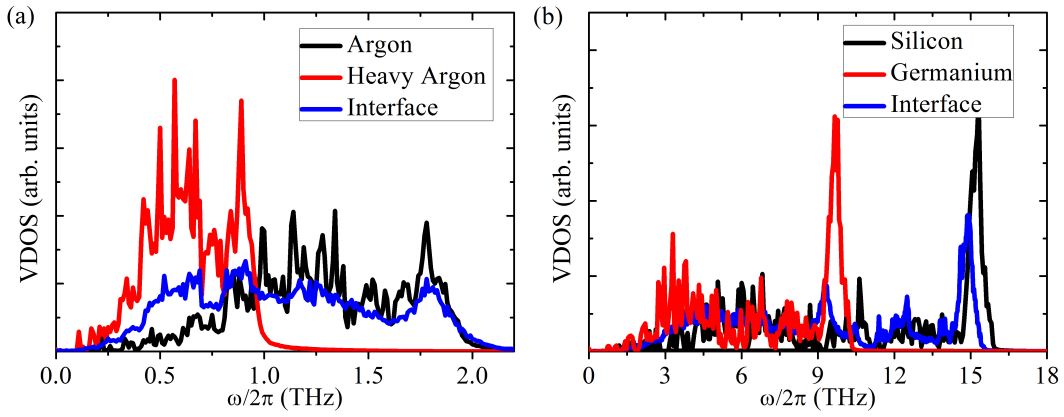


FIGURE 3.15: (Color online) (a) The vibrational density of states (VDOS) of Ar, heavy Ar and interface (defined as the structure within the cut-off distance away from the interface). (b) Same figure as (a) for the case of Si-Ge interface.

Si-Ge interface: In this Section, we study a more realistic structure: Si-Ge interface which has wide applications such as thermoelectrics (Joshi et al., 2008; Wang et al., 2008b; Chalopin et al., 2012; Dobson, 2013; Tian, Esfarjani, and Chen, 2012). Similarly, we design systems with five different temperatures (300 - 700 K). It is not surprising to find that only considering the two-phonon process is far not enough for these finite temperature systems [Figure 3.17c], since the inelastic phonon process can be activated for the systems with temperature equal or above room temperature. As we discussed above, phonons above the cut-off frequency of Ge (about 10 THz) can also carry heat across the interface through the two-phonon process due to the inelastic atomic interactions near the interface (mainly located in the frequency

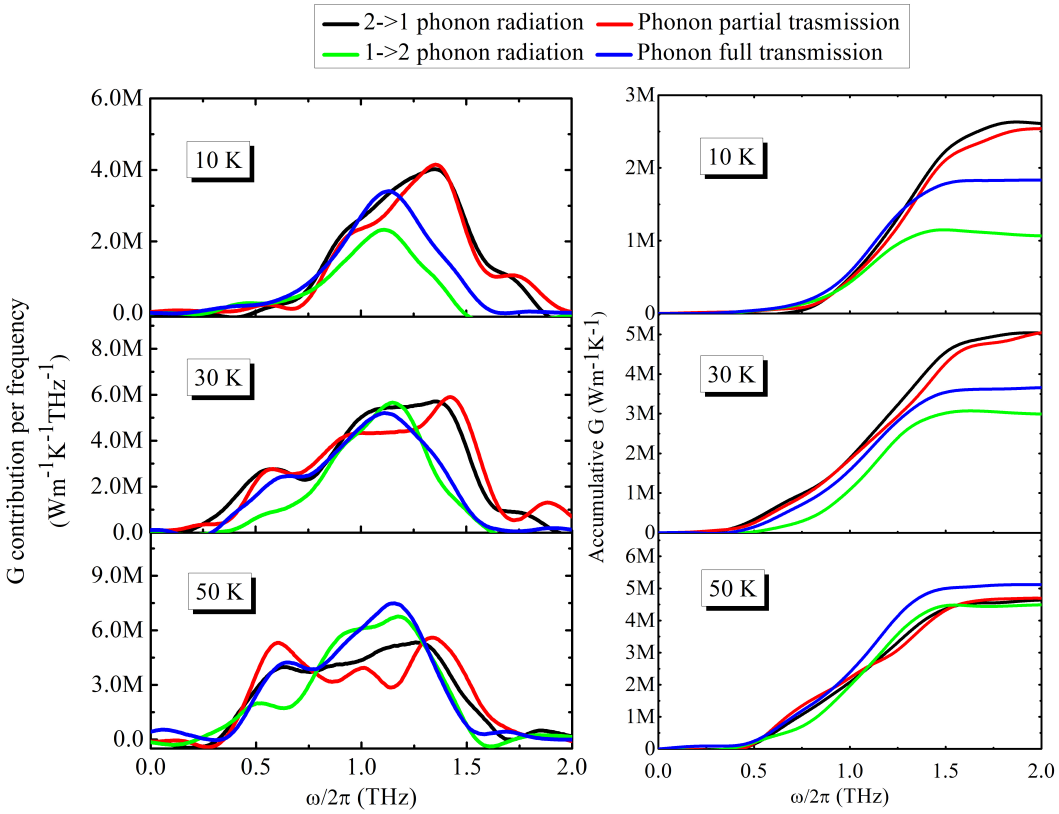


FIGURE 3.16: (Color online) The spectral thermal conductance of different types of three-phonon process (left panel) for Ar-heavy Ar interface. The accumulative thermal conductance contributed by the individual three-phonon process (right panel).

region around 12 THz, detailed discussion can be found below). Even considering the two- and three-phonon process is not enough for all the cases demonstrated here [Figure 3.17c]. For these situations, the higher order (larger than 3) phonon-process can take as large as 17% of the total thermal conductance in our systems, and therefore, further development of computational method is needed to take such higher order phonon-process into consideration. Furthermore, from Figure 3.17a and 3.17b, it is easy to find that the three-phonon process is mainly located in the frequency region of 1.5 - 9.5 and 11 - 15 THz. This is mainly because the vibrational frequency of the interfacial phonons is located in these two regions [see the VDOS of interfacial atoms in Figure 3.15b]. We would like to point out that our theoretical framework cannot distinguish thermal conductance contributed by the interfacial modes, since we do not calculate the mode level thermal conductance as Gordiz and Henry (Gordiz and Henry, 2016) did. However, based on Gordiz and Henry's work, we can know the non-intuitively large thermal conductance contributed by the phonons around 12-13 THz is mainly comprised of interfacial modes. Such small ratio of phonon modes (only < 0.1% of all the modes) can contribute around 15% of the total thermal conductance. Meanwhile, it is also found that the contribution to

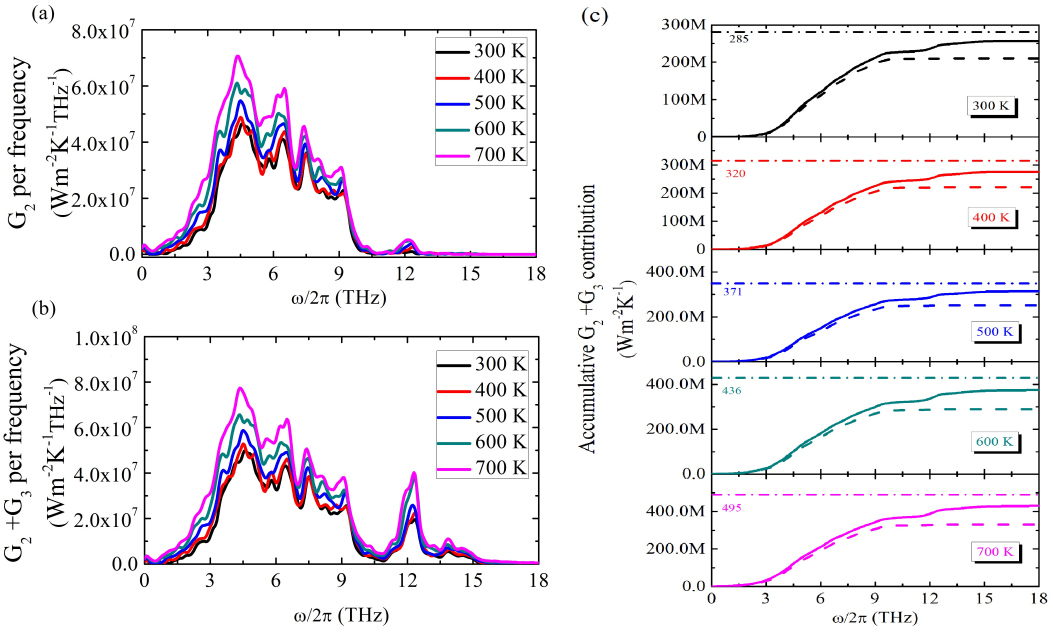


FIGURE 3.17: (Color online) Same figure as Figure 3.14 for the case of Si-Ge interface.

the thermal conductance from the small group of phonons around 12 THz is relatively large (around 11%) in our results [Figure 3.17], which is in accordance with Gordiz and Henry's work. The new frequency phonons (12 THz) in the Ge side near the interface, based on the Landry and McGaughey's study (Landry and McGaughey, 2010), are mainly due to the thin thickness of the Ge (the thickness of the Ge side near the interface can be regarded as a quite thin layer that is different from bulk counterpart). We also study the respective contribution to the overall thermal conductance from the four types of three-phonon process [Figure 3.18] as we did for the Ar-heavy Ar systems before. It is interesting to find that these four different types of three-phonon scattering process have similar heat carrier ability across the interface for systems with temperature ranging from 300 to 700 K [Figure 3.18]. Furthermore, it is also interesting to find that the phonons located in the frequency region around 4.5 and 12 THz contribute quite high thermal conductance with respect to those in other region. It may be due to the fact that these middle frequency phonons have high energy and also have stronger relations with other phonons as Gordiz and Henry found before (Gordiz and Henry, 2016).

3.4.3 Inherent inclusion of anharmonicity in the methodology

Firstly, we would like to state that our theory is not suitable to extract the two- and three-phonon process in bulk materials. From Figure 3.12(e) in our paper, it is easy to know that the vibration mode ω of atom i can transport energy to the vibration mode ω of atom j, which means a two-phonon process for the interface 2 as defined in our paper. At the same time, we can also regard the vibration mode ω of atom i is

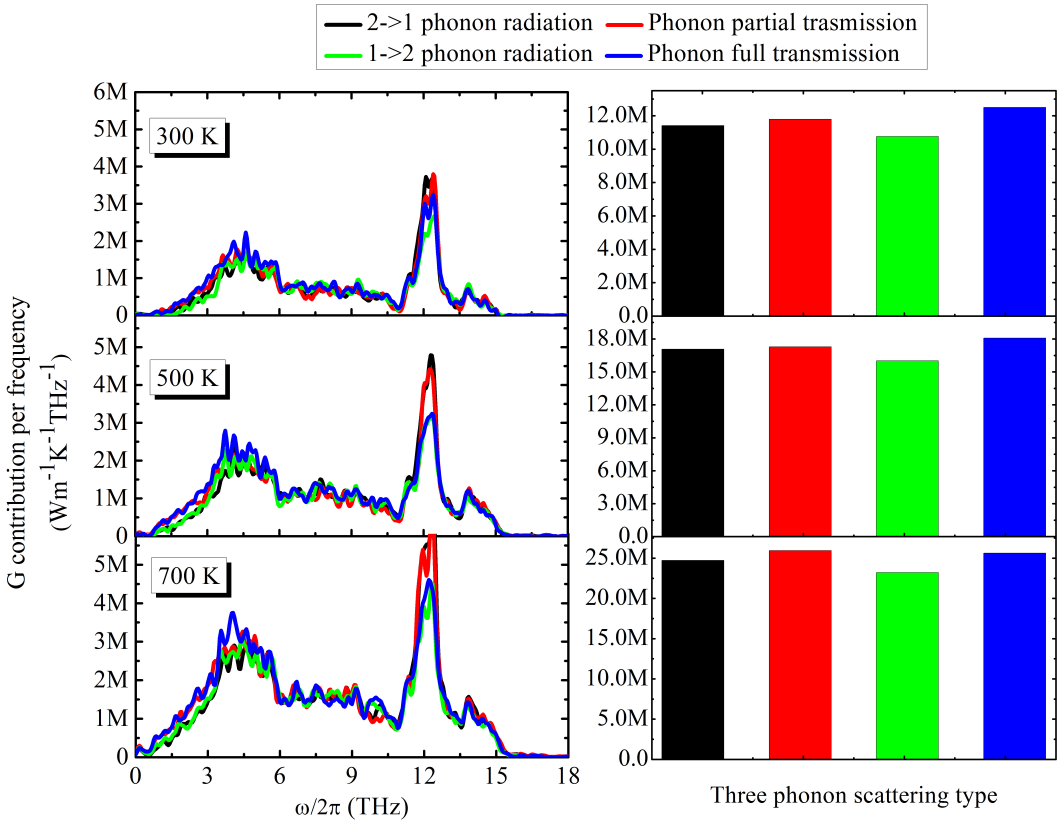


FIGURE 3.18: (Color online) The spectral thermal conductance of different types of three-phonon process for Si-Ge interface (left panel). Comparison of thermal conductance contributed by individual three-phonon process (right panel). The different type of phonon process is defined in Figure 3.12.

generated by the vibration mode ω' of atom k and vibration mode $\omega \pm \omega'$ of atom p, which indicates a three-phonon process for the interface 1 as defined in our formula [see also schematic in Figure 3.12(e)]. For bulk materials, we can imagine that there are infinite interfaces, and therefore, our theory here is invalid for bulk materials. However, for the real interface, such problem does not exist anymore. For instance, if the interface 2 is the real interface in the system, obviously, the vibration mode ω of atom i can transport energy to the vibration mode ω of atom j only through the two-phonon process. Next, we emphasize that both the two- and three-phonon process as defined in our theory are actually anharmonic. At the beginning, let us assume that there is no energy transport across the interface. The equilibrium position of the vibration of atoms near the interface (atom i and atom j) is different from that of the bulk atoms due to the different interaction from the neighbor sides with respect to the bulk counterpart. Then, this new equilibrium position is not the equilibrium position as assumed in the potential anymore. Therefore, there are some vibration modes with frequency larger than the cut-off frequency can also appear in the right side of the interface since the potential used in our simulations includes the nonlinearities. These vibrational modes are generated by the nonlinearities of

potential used in our simulation, rather than the three-phonon process as defined in our theory. At the same time, the velocity of atoms for the specific frequency should be written as

$$v_i(\omega) = v_{i-har}(\omega) + \rho v_{i-anhar}(\omega) \tag{3.69}$$

where v_{i-har} and $v_{i-anhar}$ are the velocity contributed from the harmonic and anharmonic interactions of the potential, respectively, and ρ is just a random coefficient. Then, if there is heat transport, the two-phonon process [Eq. (3.63)] as defined in our manuscript can be shown

$$\xi^{Two}(\omega) = \sum_{i\in L,\ j\in R} \tilde{\xi}_{ij}^{Two}(\omega) = -\frac{2i}{\omega} \sum_{i\in L,\ j\in R} \sum_{\alpha\beta} \Big[\Phi_{ij}^{\alpha\beta} \Big\langle \tilde{v}_{j,\ har}^{\beta}(\omega) \tilde{v}_{i,\ har}^{\alpha *}(\omega) + \rho_1 \tilde{v}_{j,\ har}^{\beta}(\omega) \tilde{v}_{i,\ anhar}^{\alpha *}(\omega) + \rho_2 \tilde{v}_{j,\ anhar}^{\beta}(\omega) \tilde{v}_{i,\ har}^{\alpha *}(\omega) + \rho_1 \rho_2 \tilde{v}_{j,\ anhar}^{\beta}(\omega) \tilde{v}_{i,\ anhar}^{\alpha *}(\omega) \Big\rangle \Big] \tag{3.70}$$

where ρ_1 and ρ_2 are random coefficients. From the equation above, it is easy to find that the heat current contributed from the harmonic interactions of the potential can be written in the form of

$$\xi^{Two}(\omega) = -\frac{2i}{\omega} \sum_{i\in L,\ j\in R} \sum_{\alpha\beta} \Big[\Phi_{ij}^{\alpha\beta} \Big\langle \tilde{v}_{j,\ har}^{\beta}(\omega\ \ ) \tilde{v}_{i,\ har}^{\alpha *}(\omega) \Big\rangle \Big] \tag{3.71}$$

The above formula is exactly the two-phonon process in AGF (pure harmonic), which has been proved by Sääskilahti *et. al.* (Sääskilahti et al., 2015) The rest terms in Eq. (3.71) are due to the nonlinearities of potential. Most recently, Hellman *et. al.* (Romero et al., 2015; Hellman, Abrikosov, and Simak, 2011; Hellman et al., 2013) find that the third term on the right of Eq. (3.37), which is generally thought to be only related to harmonic vibration, should include the anharmonic effect, which is actually in accordance with our theory. The anharmonic character of this term (the atomic velocity is not harmonic) is the main reason that leads to our conclusion: the two-phonon process in NEMD is actually anharmonic. Therefore, some vibrational modes with frequency larger than cut-off frequency can also transport energy by two-phonon process [Figure 3.14(a) and 3.17(a)] and all these two-phonon process is anharmonic (such effect is reflected by the velocity) due to anharmonic vibration of atoms near the interface (it is caused by the nonlinearities in the potential rather than the three-phonon process). In addition, it is a common sense that the three-phonon process is definitely an anharmonic process. Therefore, we do not discuss it in detail here.

3.5 Conclusion

In this chapter, we firstly developed a computational framework named time domain direct decomposition method, which is directly based on non-equilibrium molecular dynamics simulation and lattice dynamics theory, to characterize thermal conductivity contribution from individual phonon modes. The new TDDDM approach is validated by studying the cases of bulk LJ Argon and SW Si and comparing the results to that by SED and TDNMA from equilibrium molecular dynamics simulation. Some important parameters involved in TDDDM simulation are explicitly considered and fully discussed. The TDDDM approach inherently possesses the nature of both NEMD simulation and lattice dynamics. Comparing to EMD methods (SED and TDNMA), TDDDM has some distinct features and power in three aspects: (1) It provides direct evidence and quantitative analysis for the length dependence of thermal conductivity in NEMD simulation. We investigated the size effect of individual phonon mode contribution to the overall thermal conductivity in the TDDDM framework. We observe that the phonon modes with mean free path larger than the system size are truncated in TDDDM (NEMD) simulations, and therefore contribute little to the thermal conductivity. With system length increasing, phonons with mean free path longer than the system length are presented and then they are able to contribute to the thermal conductivity. (2) Using TDDDM, we prove that the thermal conductivity contributed from Gamma point is related to the momentum of the system, which is equal to zero for a stable system. Thereby the well-known common sense of the zero contribution of Gamma point can be rigorously proved using TDDDM. (3) We anticipate that TDDDM can be effectively used for studying phonon behaviors in nanostructures or under confined conditions, in particular when the structure size is significantly smaller than the characteristic MFP of the dominant phonons, which also cannot be realized by EMD methods.

We next propose a new approach named frequency domain direct decomposition method based on non-equilibrium molecular dynamics simulation and time Fourier transform of atomistic heat current to quantitatively characterize frequency dependent thermal conductivity in solid materials. The validity of our new FDDDM is assessed by comparing the results of bulk LJ Argon and SW Si to TDNMA, which is based on the equilibrium molecular dynamics simulation. Some important parameters in FDDDM implementation and calculation are discussed explicitly. Comparing with previous methods such as SED, TDNMA, and TDDDM, the new FDDDM approach has unique features and power in the following aspects: (1) Due to the inherent nature that FDDDM is based on NEMD, we can use FDDDM to explicitly investigate the size effect of frequency dependent thermal conductivity. Generally speaking, more phonons in the low frequency region, or equivalently phonons with long MFP, are present when the system size increases. (2) There is no assumption of the system temperature in our theoretic model, therefore, in principle the FDDDM can be used to observe the temperature effect of phonon mode thermal conductivity

directly. Anharmonic energy transfer is found to increase with temperature increasing, which is well known but proves that our FDDDM reveals the correct physical picture of the phonon-phonon scattering. (3) The FDDDM can be directly used to study the phonon behavior of disordered systems. The amorphous Si is chosen as a benchmark system to prove the unique advantage of our FDDDM method. The contribution of phonons are found to be quite uniform, since the relaxation time of phonons in amorphous materials is substantially short and therefore the scattering is strong as compared with the crystalline materials.

Finally, based on FDDDM, a rigorous and direct method to evaluate the two- and three-phonon scattering process at the interface within the framework of non-equilibrium molecular dynamics simulation has been developed. All possible three-phonon scattering process are taken into consideration by explicitly incorporating the three-body interaction force constants. By investigating the bulk Ar, Ar-heavy Ar and Si-Ge systems, we have validated our methodology and also revealed that combining two- and three-phonon scattering process is enough for some cases at low temperatures (Ar-heavy Ar interface). Higher order phonon scattering process should be included when the system temperature is higher. However, for Si-Ge interface, only considering two- and three-phonon scattering is far not enough even at room temperature. The higher order phonon scattering process at such interfaces can contribute more than 10% of the total thermal conductance. We also emphasize that, the three-phonon scattering process can enhance the heat transport ability through interaction with larger frequency phonons than the cut-off frequency at the interface. Four different types of three-phonon scattering process at interface, namely 1 to 2 phonon radiation, phonon full transmission, 2 to 1 radiation and phonon partial transmission, are described and their respective contribution to the overall phonon transport are explicitly assessed and compared. The 2 to 1 radiation and phonon partial transmission are found to be more important than the other two three-phonon scattering process at low temperature (lower than 30 K for Ar-heavy Ar interface). With temperature increasing, the contribution of all four three-phonon scattering process is found to be comparable. However, for Si-Ge interface, the four three-phonon process are found to have similar contribution in the entire temperature range studied, since 300 K may be already high enough to activate the phonon with frequency above the cut-off frequency of Ge in the region near the interface of Ge side. It is also observed that there is a small group of phonons around 12 THz contributes a relatively large thermal conductance, which mainly stems from the contribution of three-phonon scattering process at interface. Our method for determining the contributions of different vibrational frequencies to the overall heat flux or thermal conductance caused by two- and three-phonon scattering process is beneficial for the insight of the phonon process at interfaces, and therefore can provide guidance for relevant emerging applications involving interfacial thermal transport.

Chapter 4

Modulating Thermal Transport via Nanostructuring

4.1 Adjusting Thermal Conductivity in Nanowires via Surface Orientation

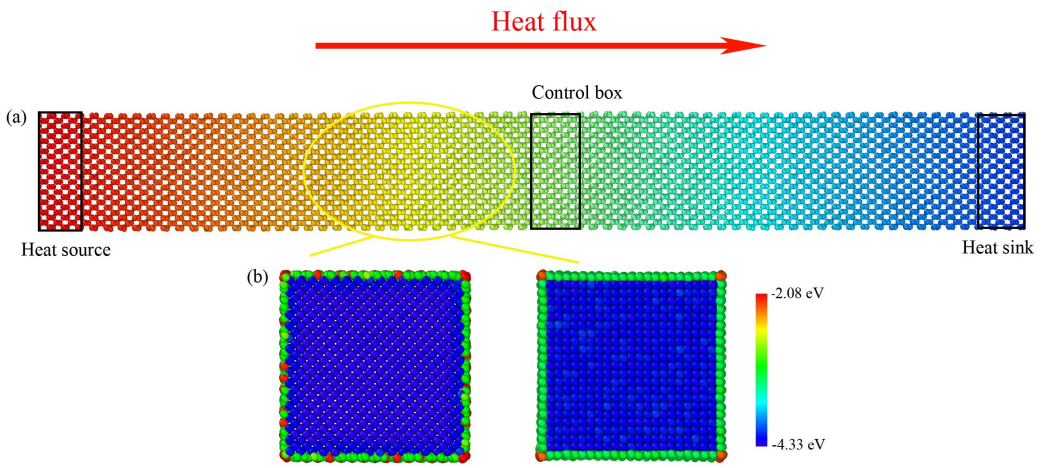


FIGURE 4.1: (a) Schematic of NEMD simulation domain. The heat source, heat sink, and the control volume used for our FDDDM analysis are highlighted by the rectangular box. The heat flux is along the (100) direction. (b) The cross-sectional view of two typical Si nanowires with (100) and (110) surface orientation. The atoms are colored by their atomic potential energy.

In this section, using atomistic simulations and theory predictions, we examine the impact of surface orientation on the thermal conductivity of Si NWs along the [001] direction (see schematic in Figure 4.1). Effects of length and diameter on the thermal conductivity with various oriented surfaces are systematically investigated. Our study shows that the surface orientation can alter the thermal conductivity of Si NWs by as large as 2.7 $\sim$ 4.2 times. Detailed analysis of vibrational density of states (VDOS) and spectral thermal conductivity, which was proposed by us recently, are used to reveal the underlying mechanism responsible for this huge difference. The

coupling between the surface atoms and the interior (core) atoms, which is the so-called phonon-boundary scattering, is found to be the governing mechanism of the different thermal conductivity of the NWs with various orientation. In addition, we find that only the phonons in the medium frequency region (1.5 $\sim$ 10 THz) are affected by surface strongly.

4.1.1 Theory and computational methods

Theory of full spectrum: By using the RTA to solve the BTE, one can obtain the relaxation time of a phonon mode $(\vec{k},\nu)$ as (Tian, Esfarjani, and Chen, 2012)

$$\tau(\vec{k},\nu)=\frac{n_0(\vec{k},\nu)[n_0(\vec{k},\nu)+1]}{D(\vec{k},\nu)} \tag{4.1}$$

where $n_0(\vec{k},\nu)$ is the Bose-Einstein distribution function of phonons and $D(\vec{k},\nu)$ is the diagonal part of the three phonon-phonon, phonon-impurity and phonon-boundary operator collision, ν and $\vec{k}$ are the branch index and phonon wave vector, respectively. Here, one should note that the Bose-Einstein distribution can be an approximate to Boltzmann distribution, which is usually used to depict the classic system when temperature of system is moderate and high (above 300 K in our cases). The detail expression of $D(\vec{k},\nu)$ can be written as (Fugallo et al., 2013)

$$D(\vec{k},\nu)=\sum_{(\vec{k}'',\nu'')(\vec{k}',\nu')}\left(\Gamma^{+}_{(\vec{k},\nu)(\vec{k}'',\nu'')(\vec{k}',\nu')}+\frac{1}{2}\Gamma^{-}_{(\vec{k},\nu)(\vec{k}'',\nu'')(\vec{k}',\nu')}\right)+\sum_{(\vec{k}'',\nu'')}\Gamma^{I}_{(\vec{k},\nu)(\vec{k}',\nu')}+\Gamma^{B}_{(\vec{k},\nu)} \tag{4.2}$$

Here, $\Gamma^{\pm}_{(\vec{k},\nu)(\vec{k}'',\nu'')(\vec{k}',\nu')}$ are the scattering rates for three-phonon process. $\Gamma^{I}_{(\vec{k},\nu)(\vec{k}',\nu')}$ and $\Gamma^{B}_{(\vec{k},\nu)}$ are the scattering rates for phonon-impurity and phonon-boundary, respectively. As we know, the first summation in Eq. 4.2 includes two processes: one is the *N process* which must satisfy the momentum and energy conservation simultaneously; and the other is the *U process* which only needs to satisfy the energy conservation. Then, the $D(\vec{k},\nu)$ can be written in the form of

$$D(\vec{k},\nu)=D^{N}(\vec{k},\nu)+D^{U}(\vec{k},\nu)+D^{I}(\vec{k},\nu)+D^{B}(\vec{k},\nu) \tag{4.3}$$

Combining with Eq. 4.1, we can know the total relaxation time $\tau(\vec{k},\nu)$ reflects the Matthiessen's rule as

$$\frac{1}{\tau(\vec{k},\nu)}=\frac{1}{\tau^{N}(\vec{k},\nu)}+\frac{1}{\tau^{U}(\vec{k},\nu)}+\frac{1}{\tau^{I}(\vec{k},\nu)}+\frac{1}{\tau^{B}(\vec{k},\nu)} \tag{4.4}$$

Meanwhile, the total thermal conductivity κ can be regarded as the summation of the contribution of all phonon modes

$$\kappa=\frac{1}{3}\frac{1}{(2\pi)^3}\int C(\vec{k},\nu)\vec{v}^{2}(\vec{k},\nu)\tau(\vec{k},\nu)d\vec{k}d\nu \tag{4.5}$$

where the mode specific heat capacity has

$$C(\vec{k},\nu) = k_B[\hbar\omega(\vec{k},\nu)]^2 n_0(\vec{k},\nu)[n_0(\vec{k},\nu)+1] \tag{4.6}$$

and $\vec{v}(\vec{k},\nu)$ is the group velocity of the phonon mode $(\vec{k},\nu)$. Meanwhile, it is well known that the relaxation time of *N* and *U processes* is dependent on both frequency and temperature

$$\tau^{N\ or\ U}(\vec{k},\nu;\ T) = \frac{1}{f^{N\ or\ U}[\omega(\vec{k},\nu)]\cdot f^{N\ or\ U}(T)} \tag{4.7}$$

where $f^{N\ or\ U}[\omega(\vec{k},\nu)]$ and $f^{N\ or\ U}(T)$ are the functions of frequency and temperature. Using the *ab initio* approach, Ward and Broido (Ward and Broido, 2010) give the detailed expression for acoustic phonons as

$$\frac{1}{\tau^N_{TA\ or\ LA}(\vec{k},\nu;\ T)} = A^N_{TA\ or\ LA}\hbar^2\omega^2(\vec{k},\nu)T[1-exp(-3T/\theta_D)] \tag{4.8}$$

and

$$\frac{1}{\tau^U_{TA\ or\ LA}(\vec{k},\nu;\ T)} = A^U_{TA\ or\ LA}\hbar^4\omega^4(\vec{k},\nu)T[1-exp(-3T/\theta_D)] \tag{4.9}$$

where θ_D is the Debye temperature. For Si $\theta_D = 654$ K, $A^N_{TA} = 253322\ (\mathrm{meV}^2K\cdot s)^{-1}$, $A^N_{TA} = 253322\ (\mathrm{meV}^2K\cdot s)^{-1}$, $A^N_{LA} = 163921\ (\mathrm{meV}^2K\cdot s)^{-1}$, $A^U_{TA} = 2012\ (\mathrm{meV}^4K\cdot s)^{-1}$ and $A^U_{LA} = 507\ (\mathrm{meV}^4K\cdot s)^{-1}$. For the contribution of optic phonons, we take the form of relaxation time of *N* and *U processes* from the Callaway model (Callaway, 1959)

$$\frac{1}{\tau^O(\vec{k},\nu;\ T)} = (B_1+B_2)\omega^2(\vec{k},\nu)T^3 \tag{4.10}$$

where B_1 and B_2 are the constants related to the three phonon-phonon scattering, $i=1$ stands for the *N process* and $i=2$ is the *U process* scattering. For Si Callaway obtained the parameters $B_1+B_2 = 3.8\times10^{-24}(s\cdot deg^{-1})$ via fitting the theoretical results to experiments (Callaway, 1959). Point defect scattering from atoms with different mass is one of the most common cases of impurity scattering in materials. For such case, Klemens (Klemens, 1955) gives the relaxation time in the form of

$$\frac{1}{\tau^I(\vec{k},\nu;\ T)} = A\omega^4, A = \frac{gV}{4\pi {v_s}^3} \tag{4.11}$$

with the constant A containing the mass variance (g), the atomistic volume (V) and the averaged sound velocity (v_s). The boundary scattering is found to be related to the roughness and the orientation of the boundary (Aksamija and Knezevic, 2010). The expression can be written as

$$\frac{1}{\tau^B(\vec{k},\nu)} = \left[\frac{1-p(\vec{k},\nu)}{1+p(\vec{k},\nu)}\right]\frac{\vec{v}(\vec{k},\nu)\cdot\vec{n}}{d} \tag{4.12}$$

where d is the distance between the boundaries, $p(\vec{k},\nu)$ and $\vec{n}$ are the momentum dependent specularity parameter and direction vector of the boundary, respectively. Thus, for $p(\vec{k},\nu) = 0$ which means a very rough surface, it can be regarded as the fully diffusive boundary scattering. The ideal smooth surface will have $p(\vec{k},\nu) = 1$. For boundary with root mean square (RMS) height of Δ, the parameter $p(\vec{k},\nu)$ is calculated as (Haile, 2014; Aksamija and Knezevic, 2010)

$$p(\vec{k},\nu) = \exp(-4\vec{k}^2\Delta^2 cos^2\phi) \tag{4.13}$$

where ϕ is the angle between the phonon wave vector and the direction vector of the boundary surface. Moreover, for NW with square-like cross-section, the relaxation time of phonon-boundary scattering is direction dependent, since the length of the system is usually finite. For the length of the system (L) and the lateral width (W) such terms should be in the form of

$$\frac{1}{\tau^B(\vec{k},\nu)} = \begin{cases} \left[\frac{1-p(\vec{k},\nu)}{1+p(\vec{k},\nu)}\right] \frac{\vec{v}(\vec{k},\nu)\cdot\vec{n}_L}{L}, & \frac{\vec{v}(\vec{k},\nu)\cdot\vec{n}_L}{L} > \frac{\vec{v}(\vec{k},\nu)\cdot\vec{n}_W}{W} \\ \left[\frac{1-p(\vec{k},\nu)}{1+p(\vec{k},\nu)}\right] \frac{\vec{v}(\vec{k},\nu)\cdot\vec{n}_W}{W}, & \frac{\vec{v}(\vec{k},\nu)\cdot\vec{n}_L}{L} <= \frac{\vec{v}(\vec{k},\nu)\cdot\vec{n}_W}{W} \end{cases} \tag{4.14}$$

where $L/\vec{v}(\vec{k},\nu)\cdot\vec{n}_L$ and $W/\vec{v}(\vec{k},\nu)\cdot\vec{n}_W$ are the time that a phonon needs to travel ballistically before hitting the boundary.

Computational details of NEMD simulations: Our large-scale nonequilibrium molecular dynamic simulations, performed with LAMMPS package (Plimpton, 1995) and the Tersoff potential (Tersoff, 1989), consider the Si NW systems with different surface orientation. Based on the previous experiments (Wu et al., 2004a; Holmes et al., 2000), the Si NWs can be aligned along the [100], [110] and [111] direction with longitudinal dimension ranging from 1 to 100 nm. In our study, we focus on the [100] longitudinally oriented Si NWs with diverse surface orientations, such as (100), (110), and (890) (28 different surface orientations in total). The size of the cross-section ranges from 2.18 to 6.52 nm and the NW length ranges from 54.3 to 162.9 nm. Figure 4.1(a) shows the schematic of the simulation model. Non-periodic boundary condition is applied in all three directions. All the simulations in this paper are performed with 1.02 $\times$107 NEMD steps with timestep of 1 fs, i.e. the total running time of MD simulation is 10.2 ns. The first 200 ps running with NPT (constant particles, volume, and temperature) ensemble is used to obtain the equilibrium state and the relaxed structure of Si NWs. Following the equilibrium, we run 7 ns to make sure that a steady heat flux is established in the system. To generate the heat current through the systems, the atoms located in the distance from the left and right ends of the system [see Figure 4.1(a)] are coupled to hot and cold Langevin thermostats with constant temperature of $T + \Delta T/2$ and $T - \Delta T/2$, respectively. The left-most and right-most layers are maintained at fixed positions to prevent large deformations and the translational movement of the system. The average system temperature in

all our simulations is fixed at $T = 300$K and the temperature difference between the cold and hot thermostats is $\Delta T = 60$ K. Once the heat flux reaches steady state, we apply the frequency domain direct decomposition method (FDDDM) in the last 3 ns for the system and then obtain the heat current spectrum. The computational details of FDDDM can be found in our previous paper (Zhou and Hu, 2015). Finally, the thermal conductivity is obtained using the Fourier's law. The group velocity and frequency of phonons used in our theoretical model are calculated by ab initio, which can provide the accurate phonon dispersion of bulk Si.

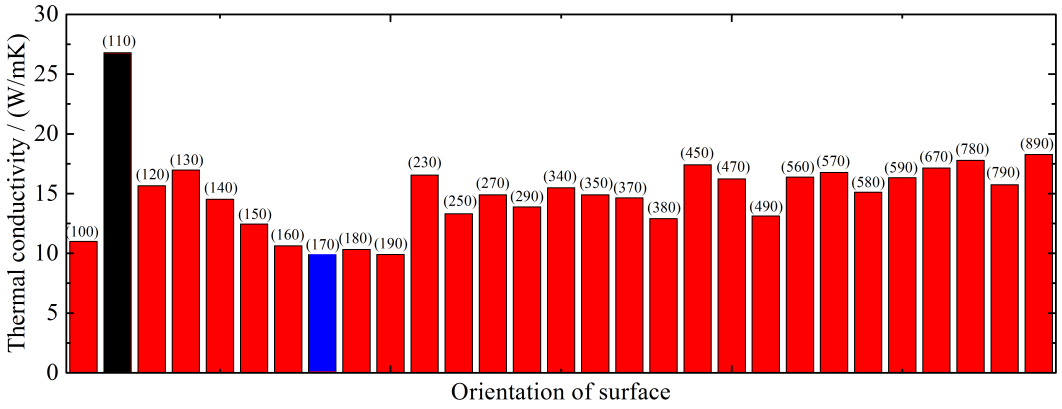


FIGURE 4.2: Thermal conductivity of Si nanowires with different surface orientations. The highest and lowest thermal conductivity is colored in black and blue, respectively.

4.1.2 Simulation and theory results

The thermal conductivity of Si NWs with 28 different surface orientations is collected and compared in Figure 4.2. It is interesting to find that the difference in the thermal conductivity between diverse oriented surfaces can be as large as about 2.7 times (even 4.2 times for Si NWs with smaller cross-section, details will be shown later). Since the only difference between different models is the surface orientation, then it is intuitive to see that the surface orientation should be responsible for the immense difference shown in Figure 4.2. Based on Eq. (4.9) in the theory part, the relaxation time for a specific phonon boundary scattering can be affected by $\vec{n}$, φ and Δ, which means the direction vector of the boundary, the angle between the phonon wave vector and the direction vector of the boundary surface, and the roughness of the surface, respectively. Since the second parameter φ is only related to $\vec{n}$, then the Eq. (4.4) is only affected by $\vec{n}$ and Δ. Thus, the orientation of the surface can affect the thermal conductivity of Si NWs through two ways: (1) surface orientation can change the angle between the phonon wave vector and the direction vector of the boundary surface (ϕ), then alter the modal specularity and the time that a phonon needs to travel ballistically before hitting the boundary, and therefore, lead to the

change of thermal conductivity; (2) different surface orientation corresponds to different distribution of atoms on the surface, and then changes the roughness of the surface, and thus, varies the thermal conductivity of NWs. To assess the relative contribution of these two effects on the overall thermal transport in Si NWs, we choose two typical models with (100) and (110) surfaces as examples. Using our theoretical model, we can obtain the thermal conductivity of these two models with different RMS height of roughness (Δ). The results are presented in Figure 4.3. We find that the largest difference between the two models which have the same is only about 4 W/mK, which is about 5% of the average thermal conductivity of the two mentioned NWs. On the other hand, we notice that a small difference between the Δ of the two NWs can lead to a big change of thermal conductivity [see point A and B in Figure 4.3]. Therefore, we conclude that the main reason for the large difference of the thermal conductivity of NWs with different surface orientation [Figure 4.2] should be the second effect as we discussed above. Meanwhile, it is well known that the results of NEMD simulations are strongly length dependent along the heat current direction (Sellan et al., 2010b; Schelling, Phillpot, and Keblinski, 2002a). Furthermore, the thermal conductivity of NWs is also affected by the size of cross-section intensively (Lim et al., 2012; Li et al., 2003; Chen et al., 2008). We now discuss how these two effects couple with the surface orientation in sequence.

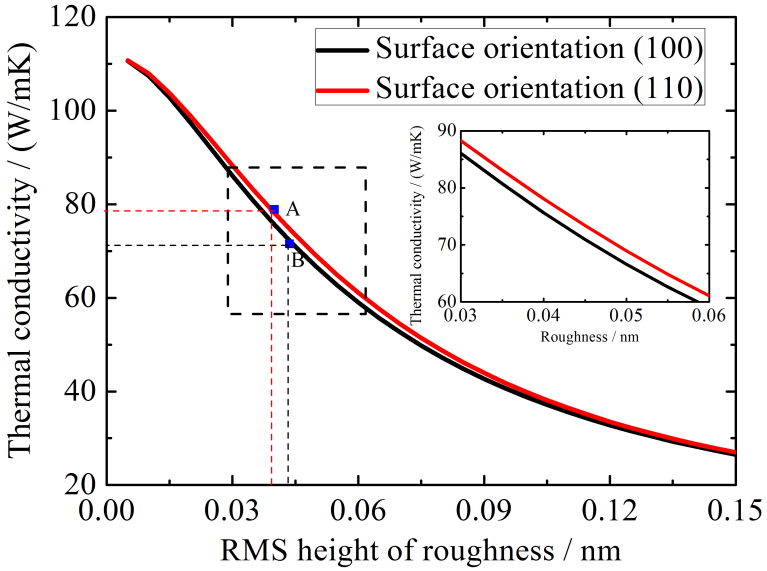


FIGURE 4.3: Thermal conductivity of Si nanowires as a function of RMS height of roughness for the cases of (100) and (110) surface orientation. (Inset) The dashed region is zoomed in.

Length dependence of thermal conductivity of Si NWs: Generally speaking, there is always length effect in NEMD simulations, since the long mean free path phonons are truncated by the length boundaries and contribute little to the overall thermal conductivity (Zhou, Zhang, and Hu, 2015). For NWs with cross-sections

of a few nanometers, the MFP is only several nanometers (Wang et al., 2009). Furthermore, using the method generated by Schelling *et. al.* (Schelling, Phillpot, and Keblinski, 2002a), we also obtain the MFP to be 13.5 nm (300K), 10.8 nm (500K) and 9.4 nm (800K) for the NW with (110) surface orientation, and to be 7.30 nm (300 K), 8.38 nm (500K) and 5.56 nm (800K) for the NW with (100) surface orientation. Thus, the linear extrapolation between the reciprocal of thermal conductivity ($1/\kappa$) and the reciprocal of length ($1/L$) can be used to obtain the thermal conductivity of infinitely long NWs ( ) in our simulations, which is the popular method to eliminate the length effect in NEMD simulations (Sellan et al., 2010b; Schelling and Phillpot, 2003a). Here, the system with cross-section of 4.35 $\times$ 4.35 nm2 is used as a representative to analyze the length effect of Si NWs. The results are reported in Figure 4.4. We find that κ_∞ of Si NW with (100) surface orientation is 16.86 W/mK (300 K), 14.39 W/mK (500 K) and 10.25 W/mK (800 K). Wang *et. al.* (Wang et al., 2009) report the κ_∞ of Si NW with same surface orientation is 6.86 W/mK (400 K). The difference between their results and ours can be attributed to the different potentials used (Stillinger-Weber potential in their work and Tersoff potential in this work), the lattice parameter and the system temperature. Furthermore, in Wang's (Wang et al., 2009) work quantum corrections are used for their results. However, Turney *et. al.* (Turney, McGaughey, and Amon, 2009) prove that the classical thermal conductivity should not be quantum corrected based on the mode dependence of phonon properties. For NW with (110) surface, κ_∞ is 45.55 W/mK (300 K), 32.26 W/mK (500 K) and 20.83 W/mK (800 K). It can be found that for NWs with infinite length, there is still large difference in thermal conductivity between different surface orientations. In addition, our simulation results are much higher than that of experiments (Li et al., 2003; Chen et al., 2008), since the NWs in our model are perfect (no impurities, defects, and grain boundaries) and the RMS height of roughness is much smoother than that in experiments.

Cross-section dependence of thermal conductivity of Si NWs: It is obvious that for the same orientations/roughness the NW with larger cross-section has higher thermal conductivity, since phonons scatter with boundary less intensively in the case of larger cross-section. All the results of the NWs with different cross-section in this paper are found to be consistent with the common knowledge [Figure 4.5]. Furthermore, as discussed before, the roughness for the NWs with the same size of cross-section is the key point that leads to the different thermal conductivity. However, it is quite difficult to measure the RMS height of roughness, since the surfaces are already atomically smooth in some cases. Thus, it is necessary to define a parameter which is related to the roughness to describe the roughness dependent thermal conductivity. The surface energy is a quite popular parameter to depict the mechanical properties of NWs with different surface orientation (Yang, Lu, and Zhao, 2009; Zhou, Yang, and Lu, 2014; Yang et al., 2014; Zhou et al., 2016). Unfortunately, we do not find any clear relationship between the thermal conductivity and the surface energy.

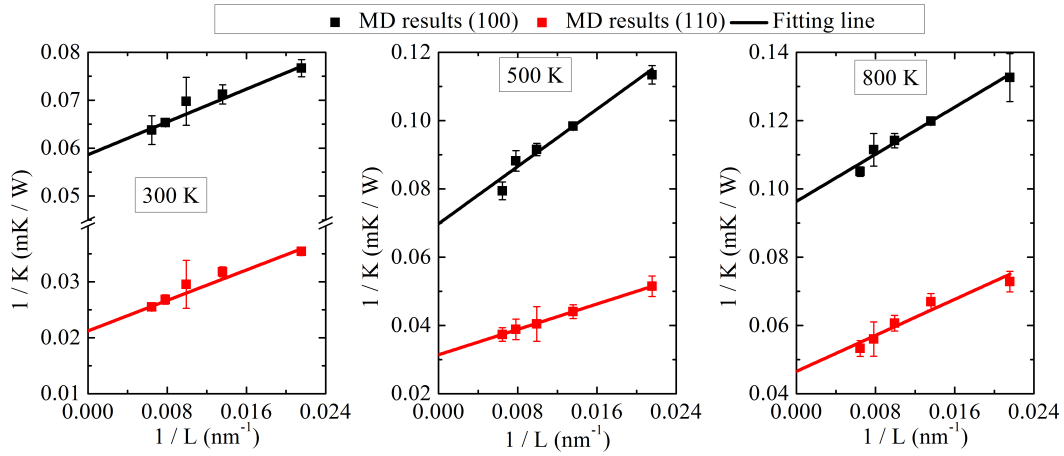


FIGURE 4.4: Length dependence of thermal conductivity of Si nanowires with two typical (100) and (110) surface orientations. Three different temperatures of 200 K, 500 K, and 800 K are considered.

Since the roughness characterizes the local atom arrangement or structure on the surface region of NWs, we define the average surface atom energy which uses the surface energy divided by the number of atoms in the surface region. Here, we regard the atoms with energy 0.45 eV larger than that of the bulk counterpart as surface region. We find that the thermal conductivity of NWs decreases with the average surface atom energy, since the smaller the average surface atom energy, the more stable the surface structure, which means the boundary scattering decreases in this case. In addition, we can obtain that the thickness of the surface region is about $0.1 \sim 0.5$ nm, which means the RMS height of roughness should fall in this range as well. From Figure 4.1(b), it can be also found that the roughness of the NWs in our simulations should be roughly $1 \sim 2$ atomic layers. Then, using our theoretical model, we can plot the thermal conductivity of NWs vs. RMS height of roughness [Figure 4.5]. We find that the theoretical predictions are in good agreement with the MD results. Both our theoretical predictions and MD results show that the difference in the thermal conductivity between different surface orientations can be as large as about 3 folders. It should be noted that the phonon dispersion will change when the cross-section of nanowires (NWs) is quite small (Zou and Balandin, 2001; Neogi et al., 2015), which is also well known due to the phonon confinement effect. However, this phonon confinement effect is not easy to consider in the theoretical model due to the large computational cost. We calculated the phonon dispersion of Si NWs with cross-section of 4×4 u.c. and 6×6 u.c. for (100) surface orientation (results not shown for brevity), and we find that the small diameter NWs have very crowded and complex phonon band structures. In addition, it is well known that there are two methods to calculate the thermal conductivity of NWs with no impurities in the theoretical processes: 1) Using the bulk phonon dispersions, the total phonon scattering process includes phonon-phonon scattering, phonon-boundary scattering et al., and

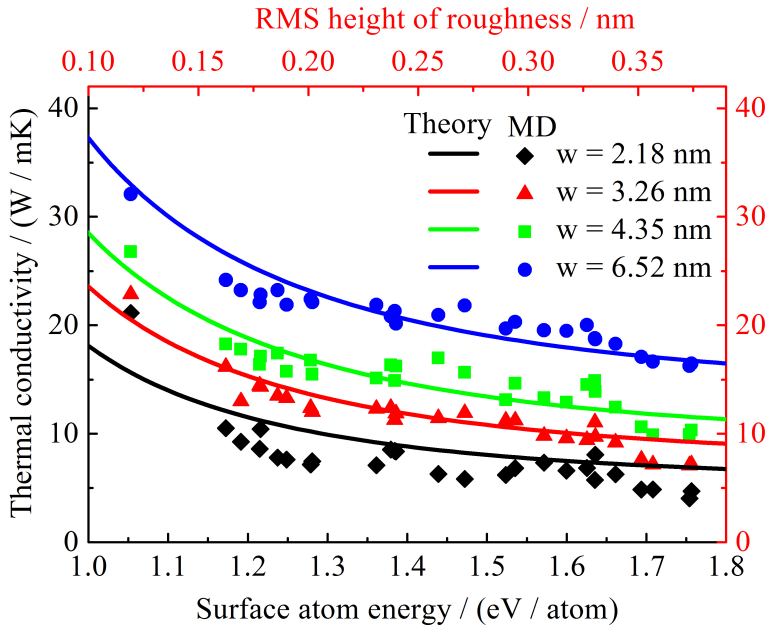


FIGURE 4.5: Thermal conductivity of Si nanowires with different cross-section vs. average surface atom energy. The symbols and solid lines are NEMD simulation results and theoretical predictions, respectively.

then the phonon relaxation time can be obtained using the Matthiessen's rule (Callaway, 1959; Aksamija and Knezevic, 2010; McGaughey and Jain, 2012; Aksamija and Knezevic, 2011). 2) Using the full phonon dispersions of NWs, the total phonon relaxation time can be obtained by only considering phonon-phonon scattering in the materials (Mingo et al., 2003; Mingo, 2003). Here, we choose the first method to deal with the problem in our cases, because we want to investigate the effect of boundary (induced by the surface orientation) on the phonon transport. What is more, it is worth pointing out that, the NWs in our simulations are perfect. The mass variance (g) will be zero if there is no defect in our models, and then the defect scattering will have no effect on the results. Here, we consider the defect scattering in our theoretical model, so that the results predicted by the theoretical model can be more general. Furthermore, the size effects of NWs were discussed systematically using theories based on the relaxation approximation of BTE as well. F. Alvarez *et. al.* (Alvarez and Jou, 2008) considered the size effect via doing the moment expansion of linearized Boltzmann transport equation in the relaxation time approximation, and found that the effective thermal conductivity will increase and then converge with the effective length. In the system with small effective length (dozens of nanometers in our paper), the thermal conductivity will be size dependent due to the fact that the phonons with MFP larger than the system will be truncated and have no contribution to the total thermal conductivity (Zhou, Zhang, and Hu, 2015). Recently, Hua and Cao (Hua and Cao, 2016) generated a theory based on the phonon BTE to study the influence of boundary constraints on thermal conductivity of NWs. Apart

from the phonon boundary scattering mechanism, they found that, the phonon ballistic transport, which usually exists in the system with length shorter or comparable to the phonon MFP, can cause temperature jump at the boundaries in contact with phonon baths. However, in our study we do not consider such effect, since the length of the models is the length that excludes the phonon baths. Both F. Alvarez *et. al.* (Alvarez and Jou, 2008) and Hua's (Hua and Cao, 2016) work show that the thermal conductivity of NWs increases firstly and converges finally with the effective length (including both the longitudinal and lateral directions), which is in accordance with our findings. Furthermore, the converged thermal conductivity of NWs can be obtained through linear extrapolation, since the MFPs of Si NWs in our simulations are only several tens of nanometers.

4.1.3 Phonon transport mechanism

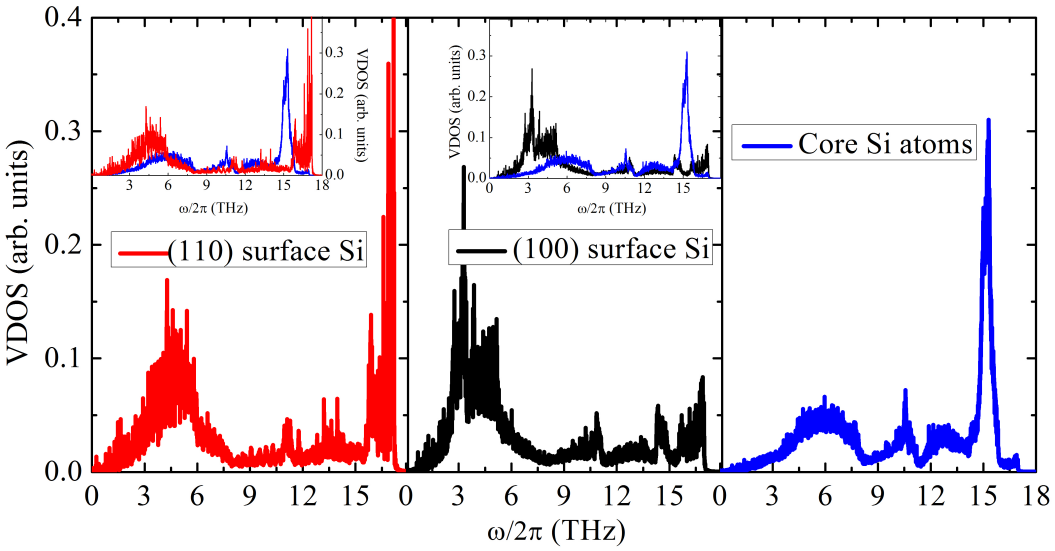


FIGURE 4.6: Vibrational density of states (VDOS) of surface and core atoms in Si nanowires with two typical (100) and (110) surface orientations. (Inset) Comparison of VDOS between the surface and core atoms.

Vibrational density of states analysis: To understand the mechanism of large difference between the NWs with diverse surface orientations, firstly we calculate the VDOS via Fourier transform of the autocorrelation function of atomic velocity. We compare the VDOS of Si atoms in the surface region and in the interior region (we call them core atoms in this paper) in [Figure 4.6]. The atomic velocities of the surface and core atoms are sampled every 2 fs during the total output time of 100 ps. It can be seen that the VDOS of the atoms in the surface region have similar shapes with that in the interior region for the medium frequency range (6 $\sim$ 14 THz), but quite different geometries in the low and high frequency range (0 $\sim$ 6 and 15 $\sim$ 18 THz). For the cases of both (100) and (110) surface orientation, the low frequency

VDOS of the surface atoms moves leftward (redshift) and is enhanced as compared with that of the core atoms. For the core atoms, there are four typical peaks in the VDOS, which corresponds to the transverse acoustic, longitudinal acoustic, transverse optic and longitudinal optic phonon modes, respectively. Phonons of Si atoms in the (110) surface region are mainly concentrated in the low frequency region (0 $\sim$ 7.5 THz) and a few high frequency peaks occur in the range from 9 to 18 THz. In contrast, the low frequency VDOS of Si atoms in the (100) surface region have a further left shift (redshift) as compared to that of the core atoms and the Si atoms in the (110) surface. Furthermore, the extremely high frequency VDOS (15 $\sim$ 18 THz) for the case of (100) surface decreases largely and a new peak appears in the low frequency region (0 $\sim$ 6 THz) with respect to in the case of (110) surface, which means the degenerated transverse acoustic phonon modes are split. Meanwhile, it can be found the overlap area of VDOS between the atoms in the (110) surface and the core atoms is larger than that between the atoms in the (100) surface and the core atoms (see insets in Figure 4.6), and the overlap area mainly resides in the low frequency region (0 $\sim$ 10 THz). In other words, the vibrational mismatch between the atoms in the (110) surface region and the core atoms is smaller with respect to other NWs considered in this paper, or equivalently, the phonon-boundary scattering for the case of (110) surface orientation is weaker, which naturally leads to the significantly higher thermal conductivity than other cases of surface orientations, as presented in Figure 4.2.

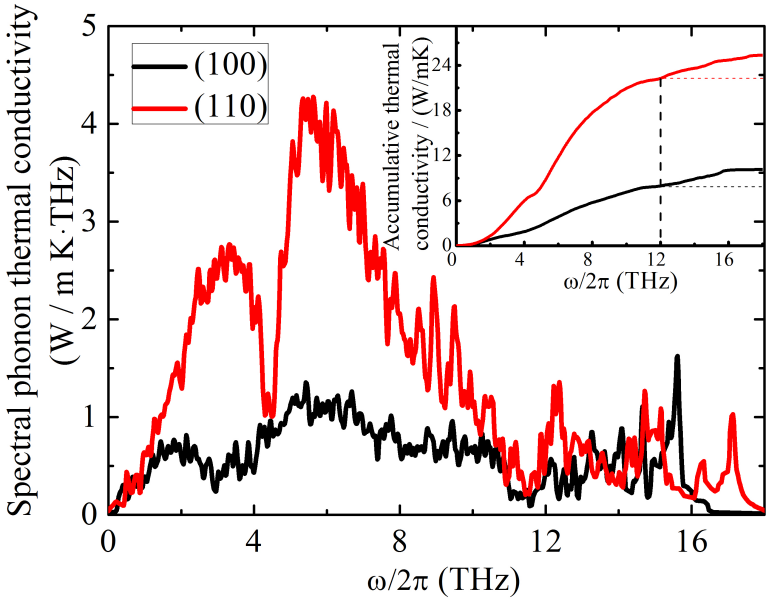


FIGURE 4.7: Vibrational density of states (VDOS) of surface and core atoms in Si nanowires with two typical (100) and (110) surface orientations. (Inset) Comparison of VDOS between the surface and core atoms.

Spectral thermal conductivity: Figure 4.7 shows the spectral (frequency dependent) thermal conductivity of Si NWs with (100) and (110) surface orientations at

300 K. It can be easily found that the difference in the frequency dependent thermal conductivity resides in the medium frequency range (1.5 $\sim$ 10 THz), which should be responsible for the large difference in the overall thermal conductivity as shown in Figure 4.2. Furthermore, the low frequency phonons (0 $\sim$ 2 THz), or equivalently, the phonons with long MFP, contribute little to the total thermal conductivity. The medium frequency phonons (2 $\sim$ 12 THz) contribute more than 85% of the total thermal conductivity [see inset in Figure 4.7], and therefore, it proves the common sense that the phonons in the high frequency range (optic phonons) contribute little to the thermal conductivity, as discussed above. Meanwhile, we find that the contribution of phonons in the NW with (100) surface is more or less uniform in the dominant frequency range of 2 to 10 THz, in contrast to the two major peaks for NW with (110) surface, since the phonon-boundary scattering is stronger in the former case, which is caused by the rougher surface [see the structure in Figure 4.1(b)]. We can also see that the maximum (cutoff) frequency is about 17.8 THz for NW with (110) orientation and 16.5 THz for the NW with (100) orientation, which means the NW with (110) surface is stiffer. Same conclusion has been drawn by Yang *et. al.* (Yang, Lu, and Zhao, 2009) using MD simulations.

4.2 Reducing Interfacial Thermal Resistance: Mass Gradient Interface

In this section, we uncover an excellent candidate, namely mass graded interface (MGI) to dramatically decrease the interfacial thermal resistance (ITR), which has already been shown to effectively tune the interfacial electronic properties (Wu et al., 1994). We found that the mass graded structure can easily reduce the overall ITR by 6 folders with respect to the perfectly abrupt interface (we call it "PI" hereafter). At the same time, the commonly used rough (alloyed) interface (RI) structure is also studied and the ITR of such interfaces is increased by 5 times larger. By decomposing the heat flux (Chalopin and Volz, 2013; Sääskilahti et al., 2015; Zhou, Yang, and Lu, 2014), the underlying mechanism is explained clearly. The result of frequency dependent transmission coefficient shows that the ability of effective phonons to pass through is: mass graded interface $>$ perfectly abrupt interface $>$ rough interface. At the same time, the mechanisms of how the high frequency phonons evolve in the interfacial region are found to be distinct for these three types of interfaces. In addition, with the help of phonon wave packet method (Schelling and Phillpot, 2003b), the underlying mechanism for the frequency dependent transmission coefficient changing with different interfacial structure is interpreted in detail.

4.2.1 Structure and simulation details

Our large-scale nonequilibrium molecular dynamic (NEMD) simulations, performed with LAMMPS package (Plimpton, 1995) and the standard 12-6 Lennard-Jones (LJ)

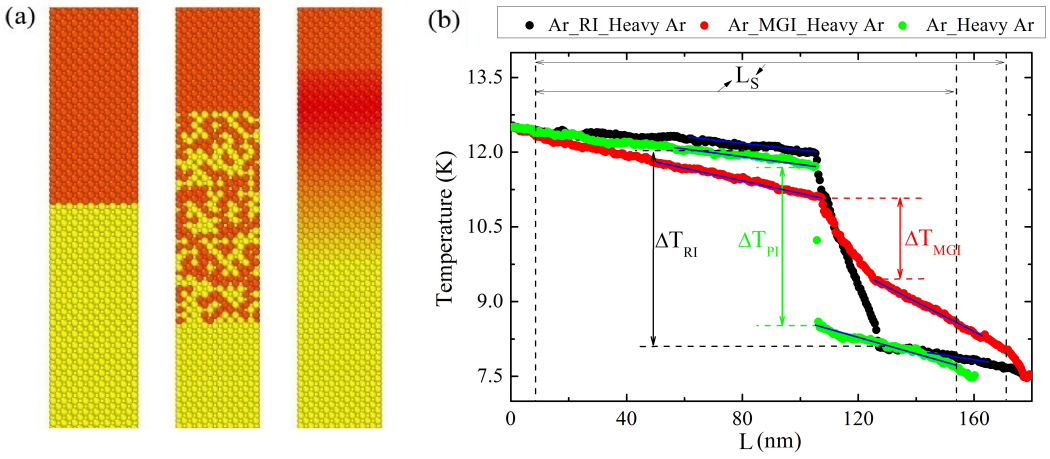


FIGURE 4.8: (a) Side view of three interface structures studied in this work. From left to right: perfectly abrupt interface, rough interface, mass graded interface. (b) Steady state temperature profile for the three kinds of interface structures shown in (a) calculated by nonequilibrium molecular dynamics simulation with average system temperature $T = 10\ K$.

potential, considered Ar-heavy Ar crystalline lattice systems with the lattice constant of 0.529 nm. The ratio between heavy Ar and regular Ar is 10. Three different types of interfaces are studied: the perfectly abrupt interface, rough alloyed interfaces with different thickness (1.1 $\sim$ 63.5 nm) and volume concentration of heavy Ar (0.13 $\sim$ 0.90), and mass graded interfaces with thickness ranging from 4.23 to 423 nm. In our simulations, we construct the mass graded layer through gradually increasing the mass in the interface region from the regular argon to the heavy argon. Then, there are two parameters we can control in the mass graded layer: the number of added mass and the thickness of each layer. In our simulations, the number of mass ranges from 8 to 100 and the thickness of each layer ranges from 0.529 nm to 4.232 nm. Detailed structures of the interfaces are shown in Figure 4.8(a). The cross-sectional area of all models in our simulations is 4.232 $\times$ 4.232 nm2. Periodic boundary conditions are applied in lateral directions, while non-periodic boundary condition is implemented in the heat flux direction, which is perpendicular to the interfaces. To generate steady heat current flowing through the systems, the atoms locate in the distance L_{bath} from the left and right ends of the system are coupled to hot and cold Nose-Hoover thermostats at temperatures $T + \Delta T/2$ and $T - \Delta T/2$, respectively. Two left and right-most layer atoms are maintained at fixed positions to prevent large deformations and translational movement of the systems. The mean temperature of the entire system is fixed at $T = 10$ K and the temperature difference between the two thermostats is $\Delta T = 5$ K. It has already been proved in previous study that the non-linear effect caused by the temperature difference of 5 K in the Ar system with system temperature of 10 K can be ignored (Sääskilahti et al., 2015). We

perform $8.4 \times 10_6$ NEMD steps with a time step of 5 fs, corresponding to total running time of 42 ns. In all of our simulations, the first 20 ns is used to obtain the steady temperature gradient and heat flux, and then the following 20 ns is used to calculate the average temperature gradient and heat flux, which are used to compute the interfacial thermal resistance. We have verified that the system temperature, the total energy of the system and the heat flux reach steady state after running 20 ns. A typical averaged temperature profile obtained from the NEMD simulation is shown in Fig. 4.8b. The temperature drop ΔT at the interface is estimated from the difference between the linear temperature profiles extrapolated to the interface as illustrated in Figure 4.8(b), where ΔT_{PI},ΔT_{RI} and ΔT_{MGI} represents the temperature drop at the perfectly abrupt interface, rough interface, and mass graded interface, respectively. Then, the ITR can be obtained by $R_{\text{int}} = A\Delta T/q$ and $G = 1/R_{\text{int}}$, where are the cross-sectional area and heat current, and G is the overall interfacial thermal conductance. It is well known that, ITR depends on the length of the two materials in contact, which originates from the truncation of long MFP phonons at finite length. In order to guarantee all possible phonons can appear in our models, the length of Ar and heavy Ar parts should be long enough to accommodate phonons with the largest MFP. Here, using the TDNMA (Ladd, Moran, and Hoover, 1986; Zhou, Zhang, and Hu, 2015) with a $8 \times 8 \times 8$ unit cell systems, we obtain the largest MFPs of Ar and heavy Ar to be 65 nm and 24 nm, respectively. Therefore, in all our models we choose the length of Ar lead as 100 nm and the heavy Ar lead as 50 nm. In this way, the ITR can be regarded as independent of the length of two leads. Meanwhile, we also calculate the ITR of the abrupt interface system with different lengths and cross-sectional areas. The results (not shown for brevity) demonstrate that the size effects in our models can be ignored.

4.2.2 Results and discussions

The ITR results obtained for the three interfaces are summarized in Figure 4.9. We first notice that almost all rough interfaces have a larger ITR with respect to the perfectly abrupt interface case. It is quite understandable and well documented that making interface rough is a quite efficient way to increase the ITR (English et al., 2012; Hopkins et al., 2011; Hopkins et al., 2010). Here, our results show that the value of ITR can be enhanced by as large as about 5 times when the alloyed material is used as an additive layer. Such a huge improvement of ITR implies that the method of making the interface rough has immense potential in the field of thermal insulation, but not beneficial for heat dissipation in electronic cooling. Such interfacial structures have already been manufactured in experiments (Hopkins et al., 2011). Using atomistic Green's function method, Li *et. al.* (Li and Yang, 2012) and Gu *et. al.* (Gu, Li, and Yang, 2015) also find that adding a disordered layer in the interface region can enhance the ITR dramatically. Moreover, both Li's work (Li and Yang, 2012) and our paper (Figure 4.10) find that the high frequency phonons scatter quite strongly. It is also worth noting that, when the thickness of the rough additive

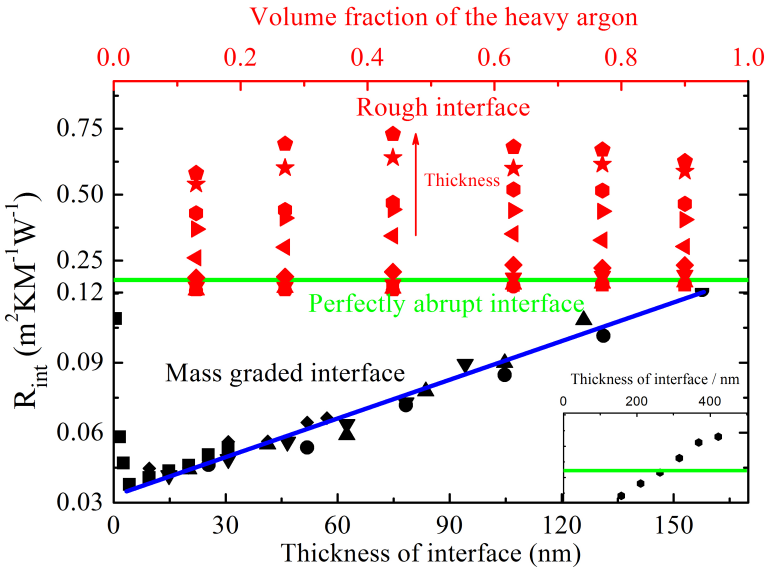


FIGURE 4.9: The overall interfacial thermal resistance across the entire interface region calculated by the Fourier's law. The black (red) symbols represent the results of mass graded (rough) interface with various thickness (volume fraction). The arrow indicates the direction of thickness increasing. The green line is the interfacial thermal resistance of the perfectly abrupt interface. The blue line is a fitting line. (Inset) The ITR of mass graded interface goes beyond that for the perfectly abrupt interface, when the mass graded interface is thick enough (at least 300 nm). For the rough interface, the different symbols represent different thickness of the interface layer. For the mass graded interface, the different symbols mean different number of atom mass added in the mass graded layer.

layer decreases to a few atomic layers, the ITR can even surpass that for perfectly abrupt interface. However, based on our current result and others' work, such way to reduce the ITR is not efficient, since the largest reduction percentage achieved so far is only in the range of 20% 50% (Tian, Esfarjani, and Chen, 2012; English et al., 2012), i.e. by up to 2 folders. In addition, manufacturing a structure with only a few atomic layers is not an easy task, meaning this method is impractical in realistic applications.

Surprisingly, for mass graded additive layers the ITR can be suppressed by as large as about 6 folders as compared with that for perfectly abrupt interface. Such finding shows that the mass graded structures have great promise in thermal management of electronic cooling. It is also interesting to find that the ITR linearly increases with thickness. Actually, the ITR of such structure is even larger than that of perfectly abrupt interface when the thickness is large enough [the inset of Figure 4.9]. It is not surprising to find this phenomenon because, as the thickness increasing the thermal resistance induced by the mass graded layer itself increases as well and eventually dominates the ITR across the entire interface region. What is more, the ITR of the mass graded interface approaches the ITR of the abrupt interface, when the additive layer is thin enough, e.g. the ITR of the mass graded interface with the

smallest possible thickness of 0.529 nm (1 unit cell of Ar lattice) reaches 62% of that for the abrupt interface [Figure 4.9]. Now we analyze the underlying mechanism of the thermal transport across different interfacial additive layers by analyzing the phonon process in NEMD simulations. The expression for the heat current q_{ij} between atoms i and j can be given by (Sääskilahti et al., 2015; Zhou and Hu, 2015)

$$q_{ij} = \frac{1}{2}\left\langle \vec{F}_{ij} \cdot (\vec{v}_i + \vec{v}_j) \right\rangle \tag{4.15}$$

where $\vec{F}_{ij}$ is the force between two atoms and $\vec{v}$ is the velocity of atoms, $\langle\ \rangle$ denotes the steady-state nonequilibrium ensemble average. Meanwhile, it has been proved that the spectrum decomposition of heat current is related to the correlation time between force and velocity (Chalopin and Volz, 2013; Sääskilahti et al., 2015; Chalopin et al., 2012). Therefore, q_{ij} can be further given in the expression below after mathematical operations (details can be found in Refs. (Sääskilahti et al., 2015; Zhou, Yang, and Lu, 2014))

$$q_{ij} = \frac{1}{2}\int_{-\infty}^{+\infty}\int_{-\infty}^{+\infty} C_{ij}(\tau)e^{i\omega\tau}d\tau\frac{d\omega}{2\pi} \tag{4.16}$$

where C_{ij} is the auxiliary correlation term with the expression of

$$C_{ij}(\tau) = \left\langle \vec{F}_{ij}(\tau) \cdot (\vec{v}_i(0) + \vec{v}_j(0)) \right\rangle \tag{4.17}$$

In addition, it is usual to assume that $F_{ij}^{\alpha} \approx \sum_{\beta} u_i^{\beta} K_{ij}^{\alpha\beta}$ in the low temperature system, where $K_{ij}^{\alpha\beta}$ is the second order interatomic forces constants. Then, Eq. (4.16) can be rewritten as (details can be found in Refs. (Chalopin et al., 2014; Chalopin and Volz, 2013))

$$q_{ij} = \int_0^{+\infty}\left(-\frac{2}{t_{simu}\omega}\sum_{\alpha,\beta\in\{x,y,z\}}\mathrm{Im}\left\langle \tilde{v}_i^{\alpha}(\omega)^* K_{ij}^{\alpha\beta}\tilde{v}_j^{\beta}(\omega)\right\rangle\right)\frac{d\omega}{2\pi} \tag{4.18}$$

Finally, we can write the frequency dependent thermal conductance across an individual interface as

$$G(\omega) = -\frac{2}{t_{simu}\omega A\Delta T}\sum_{i\in L,j\in R}\sum_{\alpha,\beta\in\{x,y,z\}}\mathrm{Im}\left\langle \tilde{v}_i^{\alpha}(\omega)^* K_{ij}^{\alpha\beta}\tilde{v}_j^{\beta}(\omega)\right\rangle \tag{4.19}$$

where t_{simu} is the simulation time, "L" and "R" means the left and right region separated by the interface. In order to compare our results consistently, all the temperature drops used in Eq. (4.19) are the interfacial temperature drops. Using Eq. (4.19), we can obtain the frequency dependent thermal conductance as illustrated in Figure 4.10. We notice that the first panel of all three systems is not exactly the same, even if they have the same crystal structure. In our three models, the temperature gradient in the regular Ar part is different [Figure 4.8] despite of the same crystal structure. However, we can easily find that the shape of these three pictures is similar except the different noise in it. Such noise is inevitable when one uses Eq. (4.18)

to obtain the frequency dependent heat flux. It seems that the only method to reduce the noise is to enlarge the temperature gradient in the system, which will certainly increase the non-linear effect in the system as well. Therefore, there is somehow a compromise between the small noise in the frequency dependent heat flux and the large non-linear effect from the thermostats. On the one hand, we know that for any kind of interfaces only phonons with frequency below the cutoff frequency of the second material, i.e. $\omega_c^{heavy\ argon} = 0.68$ THz, can carry heat across the interface, because higher frequency modes cannot propagate in the heavy Ar, which is determined by its lowered phonon dispersion curves [inset of Figure 4.12]. On the other hand, for low temperature systems, it is widely regarded that the transmission coefficient can be written as $\Gamma(\omega) = G(\omega)/k_b$ (Sääskilahti et al., 2014; Sääskilahti et al., 2015), which means we can simply regard the G as Γ. Then, it is easy to observe that the transmission coefficient of phonons that can pass through the rough interface has a lower value than that for the perfectly abrupt interface [comparing Figure 4.10(a) and 4.10(b)]. While for the mass graded interface, the transmission coefficient of phonons is substantially higher than that for the perfectly abrupt interface [comparing Figure 4.10(a) and 4.10(c)]. However, when the size of the rough interface decreases to several atomic layers, the transmission coefficient of phonons has a larger value than that for perfectly abrupt interface (results not shown for brevity). Consequently, it results in the incremental drop in the ITR [about $20\% \sim 40\%$ in our work, see Figure 4.10].

We now turn to the mechanism of how the phonons with frequency larger than the cutoff frequency of heavy Ar evolve in the interface region. For the perfectly abrupt interface [Figure 4.10(a)], phonons with frequency below the cutoff frequency have the possibility to pass through the interface. All the phonons with frequency beyond cutoff frequency are reflected by the interface. When the interface becomes rough, high frequency phonons ($\omega > \omega_c^{heavy\ argon}$) are presented in the interface region [see the 2nd to 5th pictures in Figure 4.10(b)], due to the possibility of the population of full frequency range phonons for the alloyed interface. We also observe that the heat energy carried by these high frequency phonons decreases gradually from left to right and almost annihilates at the right interface between the alloyed layer and the heavy Ar [the 5th picture in Figure 4.10(b)]. Thus, we can conclude that for sandwiched rough layers, the main mechanism for the disappearance of the high frequency phonons in the right lead is phonon scattering in the course of traveling. However, it is worth pointing out that, when the thickness of rough interface decreases to a few atomic layers, the dominant mechanism becomes to the phonon reflection at the interface, since there is no enough space for such phonons to scatter. Therefore, for rough interface there are two different regimes of interfacial heat transfer, which originates from the competition between phonon scattering and the thickness of the rough interface. When a mass graded material is added into the interface region [Figure 4.10(c)], phonons with frequency higher than 0.68

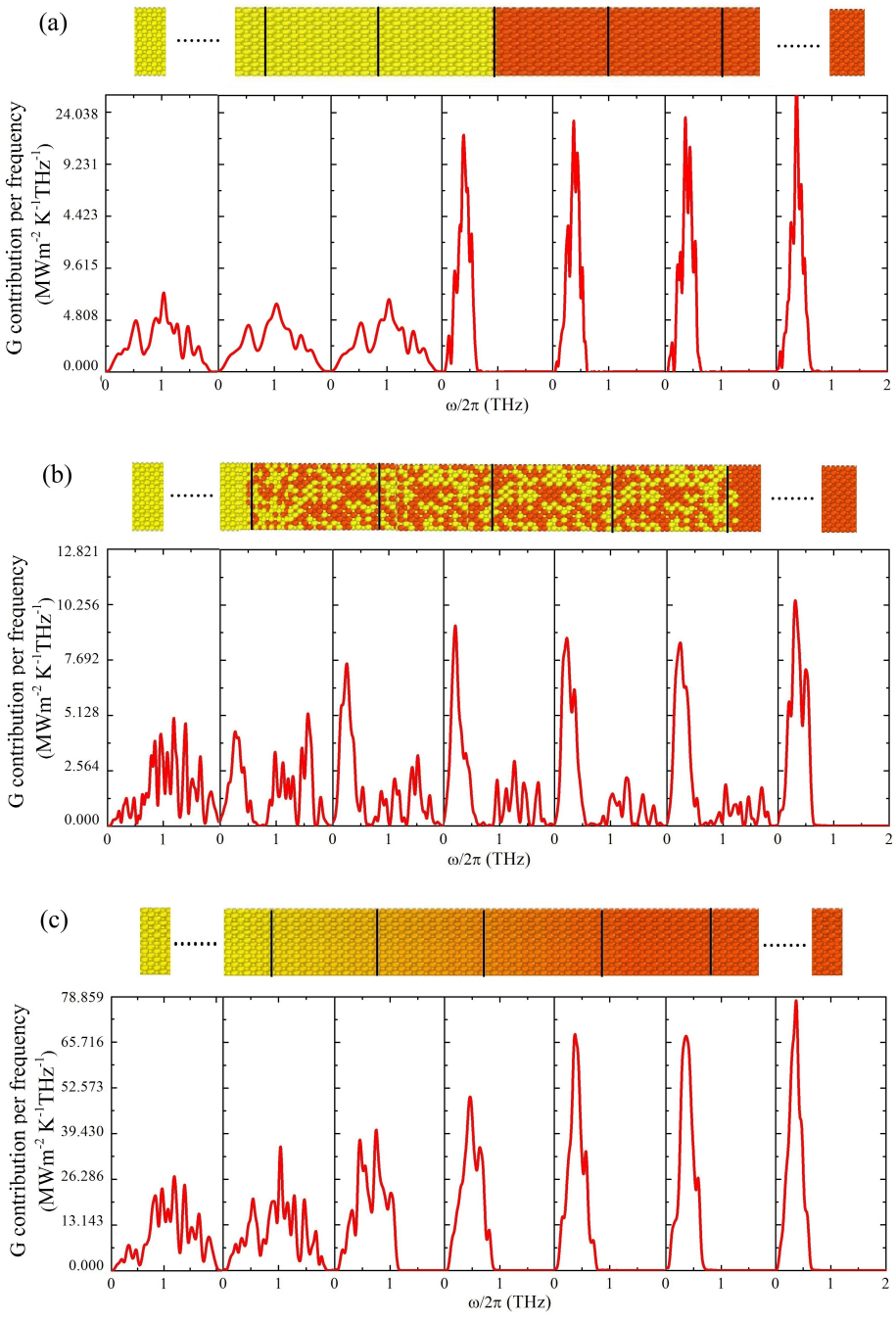


FIGURE 4.10: Frequency dependent interfacial thermal conductance (FDITC) for (a) perfectly abrupt interface, (b) rough interface, and (c) mass graded interface. The first and last panel in (a) to (c) represent the FDITC in the middle of the left and right leads, respectively. The second to fifth panel is the FDITC at the positions indicated by the black lines in the corresponding structure models. The temperature at the interface is used to obtain the FDITC results.

THz are truncated gradually, due to the gradually increasing transmission coefficient with number of layers increasing (each layer and its adjacent layer with slight mass difference can be regarded as an interface), as we will see later. Thereby, we see from Figure 4.10(c) that the peak of the frequency dependent thermal conductance around 0.38 THz becomes sharper as phonons travel across the mass graded region, meaning that the majority of the thermal energy is transmitted by these medium frequency phonons. This can be understood in terms of their relatively high transmission coefficient [as we will see later in Figure 4.5] and decent phonon group velocities as compared with low frequency phonons.

In order to gain more insight into the mechanism of phonon transport across these three typical interfaces, we perform the wave packet dynamics simulation (Schelling, Phillpot, and Keblinski, 2002b; Sinha et al., 2005) to compute the frequency dependent transmission coefficient. This method has been successfully used to analyze phonon transport across various interfaces (Schelling, Phillpot, and Keblinski, 2002b). The phonon wave packets are generated from linear combinations of vibrational eigenstates of bulk Ar, which are obtained from harmonic lattice dynamics calculations using PHONOPY software (Togo, Oba, and Tanaka, 2008). To generate a wave packet centered in wave vector space at $\vec{k}_0$ and in geometrical space at $\vec{z}_0$, we displace the atoms according to (Schelling, Phillpot, and Keblinski, 2002b)

$$\vec{u}_{il\mu} = A_m \vec{\varepsilon}_{i\mu\lambda}(\vec{k}_0) \exp[i\vec{k}_0(\vec{z}_l - \vec{z}_0)] \exp[-\eta^2(\vec{z}_l - \vec{z}_0)^2] \tag{4.20}$$

where $\vec{z}_l$ is the position of the l^{th} unit cell, $\vec{u}_{il\mu}$ the th component of displacement for the atom i in the l^{th} unit cell, A_m the amplitude of the wave, $\vec{\varepsilon}_{i\mu\lambda}(\vec{k}_0)$ the eigenvector for the λ^{th}th phonon branch at $\vec{k}_0$. The value of η is selected to keep the wave packet extent to be about 100 unit cells. The initial atomic velocities are set according to the formula given in Ref. (Schelling, Phillpot, and Keblinski, 2002b). Here, we choose one typical longitudinal acoustic phonon in the medium frequency region ($\omega/2\pi = 0.23$ THz) among all effective phonons as an example. For the perfectly abrupt interface, the most of the incoming energy carried by the wave packet can transfer across the interface and the remaining part is reflected by the interface directly [Figure 4.11(a)]. In contrast, for the structure with rough interface, the majority of the incident energy is quite difficult to go through the interface region, due to the strong scattering between atoms with different mass in this region [Figure 4.11(b)]. Only a small portion of phonon's energy can transport across the interface, resulting in a much lower transmission coefficient than that of perfectly abrupt interface. In the case of mass graded interface, the major energy reflection (but note that the transmission coefficient is rather high) occurs at the first interface position [Figure 4.11(c)], i.e. when the phonon traveling in the regular Ar lead suddenly encounters the mass graded structure. After that, very little phonon energy is reflected as the phonon continues to travel across the mass graded region, although each two adjacent mass graded layers can be regarded as an interface. This is mainly because

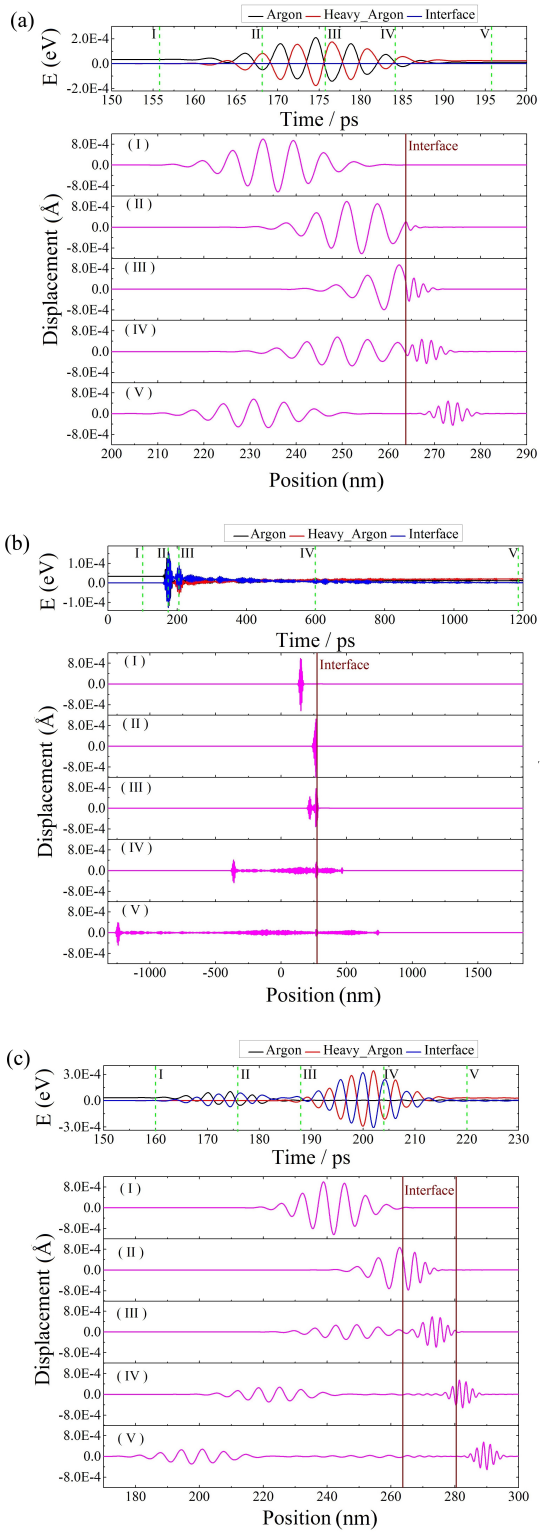


FIGURE 4.11: (Top) Phonon energy evolvement as a function of time by wave packet simulation and (Bottom) snapshots of displacements for a longitudinal acoustic wave packet with frequency of 0.23 THz at some typical timesteps indicated by the Roman numerals for (a) perfectly abrupt interface, (b) rough interface, and (c) mass graded interface. Color coding: black, Argon; red, heavy Argon; blue, interface. The brown vertical lines in the bottom panel indicate the position of interfaces.

the acoustic impedance at each mass graded interface decreases with layer number increasing. The details are explained below.

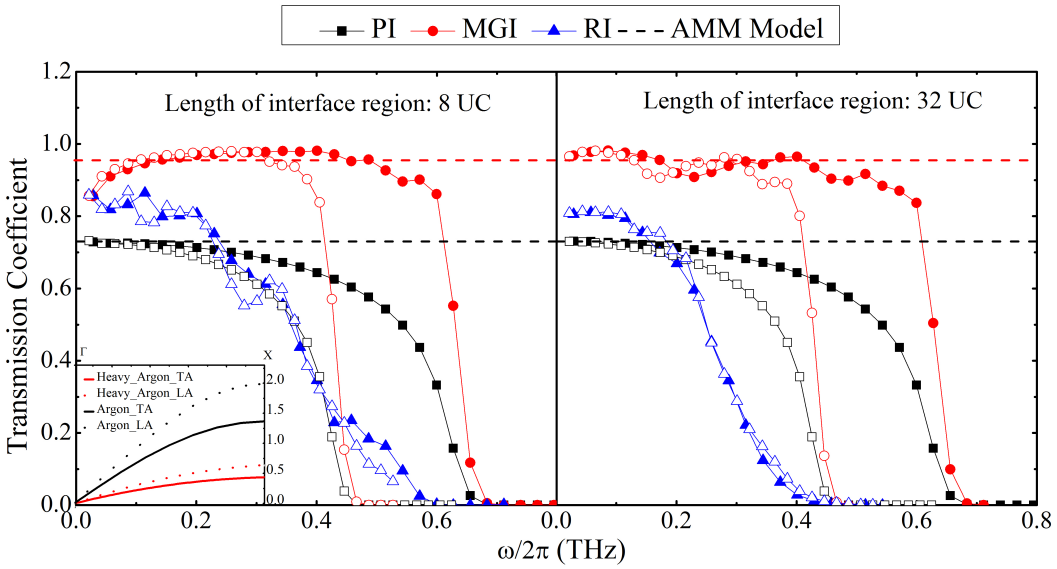


FIGURE 4.12: Phonon frequency dependent transmission coefficients for perfectly abrupt interface (black symbols), mass graded interface (red symbols) and rough interface (blue symbols) with interface thickness of (left) 8 unit cells and (right) 32 unit cells. The black and red dashed line denotes the transmission coefficient at long-wavelength limit using acoustic mismatch model for perfectly abrupt interface and mass graded interface, respectively. The filled and open symbols denote the longitude acoustic (LA) and transverse acoustic (TA) branch, respectively. (Inset) Phonon dispersion curves of regular Ar (black lines) and heavy Ar (red lines).

In Figure 4.12 we compare the frequency dependent transmission coefficient for the three types of interfaces with two typical interface thicknesses. Due to the fact that the long MFP phonons (with respect to the thickness of interface) can pass the thin layer with small interference, the transmission coefficient of these phonons is relatively higher than that for high frequency phonons [see low frequency region in Figure 4.12]. As can be seen from Figure 4.12, for rough interface, with interface thickness increasing, the frequency dependent transmission coefficient has a downward and leftward shift, indicating that the number of phonons with lower transmission coefficient than that of perfectly abrupt interface increases, which leads to an increased ITR [Figure 4.9 and Figure 4.10(b)]. When the thickness of rough interface region is reduced to several atomic layers [8 unit cells, left panel of Figure 4.12], the transmission coefficient of almost all phonons below the cutoff frequency increases as compared with that for thicker rough interface, especially for the medium frequency range (0.15 $\sim$ 0.58 THz), leading to the ITR even lower than that of perfectly abrupt interface [Figure 4.9]. For the mass graded interface we find that almost all the effective phonons have substantially high transmission coefficient (between 0.85 and 1) as compared with both perfectly abrupt interface and rough interface.

The transmission coefficient sharply drops down to zero as phonon frequency approaches the cutoff frequency (0.51 and 0.68 THz for longitudinal acoustic and transverse acoustic phonon, respectively). As a result, the ITR of mass graded interface decreases largely [by 6 folders at the most as shown in Figure 4.9 and Figure 4.10(c)]. Before closing, we use the AMM model to predict the transmission coefficient of the perfectly abrupt interface and the mass graded interface. For perfectly abrupt interface, the AMM formula says (Swartz and Pohl, 1989)

$$\alpha_{1\to 2} = \frac{4Z_1Z_2}{(Z_1+Z_2)^2} \tag{4.21}$$

where $Z_i = \rho_i c_i$ is the acoustic impedance of the regular Ar and heavy Ar lead, which is equal to the product of mass density and sound velocity. In the case of same interatomic interaction strength, the acoustic impedance is proportional to the square root of atomic mass. Then we predict the AMM transmission coefficient of the perfectly abrupt interface is 0.73 for $\omega \to 0$, which is consistent with the wave packet results shown in Figure 4.12. For mass graded interface, we first calculated the transmission coefficient of each interface composed of two adjacent mass graded structures using the AMM model. We found that these transmission coefficient values are very close to 1, due to extremely low mass mismatch in the mass graded interface structure. Then we calculated the overall transmission coefficient according to the following equations (Schelling and Phillpot, 2003b)

$$\alpha_{1\to 3} = \alpha_{1\to 2}\alpha_{2\to 3}\sum_{m=1}^{\infty}(1-\alpha_{1\to 2})^m(1-\alpha_{2\to 3})^m \tag{4.22}$$

and

$$\alpha_{1\to N+1} = \alpha_{1\to N}\alpha_{N\to N+1}\sum_{m=1}^{\infty}(1-\alpha_{1\to N})^m(1-\alpha_{N\to N+1})^m \tag{4.23}$$

In this way, the final overall transmission coefficient across the entire mass graded interface is calculated to be 0.948, which is again consistent with the wave packet results shown in Figure 4.5 and this value is much higher than that of perfectly abrupt interface (0.73). Also, we calculated the transmission coefficient of the directly transmitted wave, i.e. only counting the phonon energy that transmits across each mass graded interface with a gradually increasing transmission coefficient and neglecting the energy that goes back-and-forth across the multi-layers, by

$$\alpha_{1\to N+1} = \prod_{n=1}^{N}\alpha_{n\to n+1} \tag{4.24}$$

The obtained directly transmitted transmission coefficient is 0.947, which is very close to the above overall transmission coefficient of the mass graded interface, indicating that the enhanced transmission coefficient of the mass graded interface compared to that of the perfectly abrupt interface is purely due to the reduced mass

mismatch and the phonon process in the mass graded interface region is dominated by the simple direct transmission of phonons without observable reflection and go-back-and-forth inside the mass graded interface region. Actually, this can be clearly seen from the wave packet results as shown in Figure 4.11(c). Note that the AMM model reproduces the transmission coefficient of the low frequency phonons but does not agree very well with the high frequency phonons [Figure 4.12], due to the fact that the AMM model is based on the acoustic impedance and only valid for the long-wavelength limit. The results of both the decomposed interfacial thermal conductance and transmission coefficient computed using wave packet method show that the main reason for the reduction of ITR for mass graded interface is the enhancement of the transmission coefficient of phonons, which comes from the small mass mismatch between two neighboring layers in the mass graded interface region [Figure 4.10 and Figure 4.12].

4.3 Thermal Transport in Ultra-thin NWs

In this section, we resolve the existing controversy on κ of extremely thin Si NWs using GK-EMD method with different interatomic potentials, and we demonstrate that the κ of Si NWs varies nonmonotonically as the NW diameter (D) decreases, with minima occurring at diameter of $2 \sim 3$ nm. The κ of the thinnest possible Si NWs does not diverge, but converges to a super-high value instead (can be more than one order of magnitude higher than their bulk value), which enforces us to re-examine the previous viewpoint of divergence of κ at the extremely thin limit. Furthermore, we identified two competing mechanisms governing the thermal transport in the ultra-thin Si NWs, responsible for the nonmonotonic behavior: the normal (N) three-phonon scattering process in the low frequency region, forming hydrodynamic phonon flow (Cepellotti et al., 2015; Lee et al., 2015) in the extremely thin NWs, results in the negative $d\kappa/dD$ relationship, while the traditionally well-known phonon-boundary scattering dominates the phonon transport in wider Si NWs, leading to $d\kappa/dD > 0$.

4.3.1 Simulation and model details

As proved by both experiments (Wu et al., 2004a; Holmes et al., 2000) and simulations (Chadi, 1979; Alerhand et al., 1988), the (100) surface of diamond-like Si will reconstruct, and thus the structure is not stable. Here, the model structures of all Si NWs are built along the [100] direction with (110) surface in the lateral directions. The lattice parameters along the [100] ($a_{[100]}$) and [110] ($a_{[110]}$) directions are 0.5442 and $\sqrt{2} \times 0.5442$ nm, respectively. All models in our paper are $100a_{[100]}$ long (Zhou et al., 2016) and the cross-sectional size ranges from $0.9a_{[110]}$ to $5a_{[110]}$. Hereafter, for simplicity we call the NW cross-sectional size as "diameter", although the cross-sectional shape is not perfectly circle-like. The diameter in our paper is simply taken as the width of the NWs. Three most popular empirical potentials, namely Tersoff

(Tersoff, 1989), environment dependent interatomic potential (Bazant, Kaxiras, and Justo, 1997) (EDIP) and SW (Stillinger and Weber, 1985), are used to depict the interactions between the Si atoms. Here, unless stated otherwise, we refer to the results of Tersoff potential. Periodic boundary condition is applied in the axial (longitudinal) direction and free boundary conditions are applied in the two lateral directions. A timestep of 1 fs is used for all systems. Firstly, 500 ps run with NPT (constant particles, constant pressure and constant temperature) ensemble is implemented to relax the structure. Following equilibrium, 500 ps to 80 ns run is carried out with NVE (constant particles, constant volume without thermostat) ensemble. The heat flux is calculated using (Torii, Nakano, and Ohara, 2008)

$$\vec{Q} = \frac{1}{V}\left[\sum_{i}^{N} e_i\vec{v}_i + \frac{1}{2}\sum_{i,\,j;\,i\neq j}^{N}(\vec{F}_{ij}\cdot\vec{v}_i)\vec{r}_{ij} + \sum_{i,\,j,\,k;\,i\neq j\neq k}^{N}(\vec{F}_{ijk}\cdot\vec{v}_i)(\vec{r}_{ij}+\vec{r}_{ik})\right] \tag{4.25}$$

in which e_i is the energy of atoms, $\vec{v}_i$ is the velocity of atoms, $\vec{r}_{ij}$ is the distance between two atoms i and j, $\vec{F}_{ij}$ and $\vec{F}_{ijk}$ are the two-body and three-body force, respectively. Finally, the κ can be derived using Green-Kubo formula (Kubo, 1966)

$$\kappa = \frac{V}{k_B T^2}\int_0^\infty \langle Q_z(\tau)Q_z(0)\rangle\, d\tau \tag{4.26}$$

where k_B is Boltzmann constant, V is system volume, $T$is system temperature and τ is auto-correlation time. The angular bracket means the ensemble average. For each case 50 independent runs are performed in order to obtain a stable averaged κ. The correlation time considered in our simulation for extremely thin Si NWs can be up to 80 ns, which is much longer than that used in most of materials (McGaughey and Kaviany, 2004a; McGaughey and Kaviany, 2004b; Schelling, Phillpot, and Keblinski, 2002a; Volz and Chen, 2000; Yang, Yang, and Li, 2014) (usually less than 500 ps). Figure 4.13 shows the κ of some representative ultra-thin Si NWs with different diameters. All cases calculated using Tersoff potential are presented here, while for the other two potentials only the Si NWs with diameter of 0.96 nm (EDIP) and 1.5 nm (SW) are presented as typical examples. It is clearly seen that, it takes quite a long time (∼30 ns for Tersoff, 10 ns for EDIP and 4 ns for SW potential) for the thermal conductivity of the extremely thin Si NWs to converge [Figure 4.13 (a), (e) and (f)], since the hydrodynamic heat flow is formed in such thin Si NWs (see discussion below). With NW diameter increasing, the correlation time for the GK-EMD simulation becomes smaller, since the phonon boundary scattering becomes more important. Nevertheless, the κ of all thermodynamically stable ultra-thin Si NWs can converge to a finite value, when a sufficiently long correlation time is adopted for postprocessing of GK-EMD simulation.

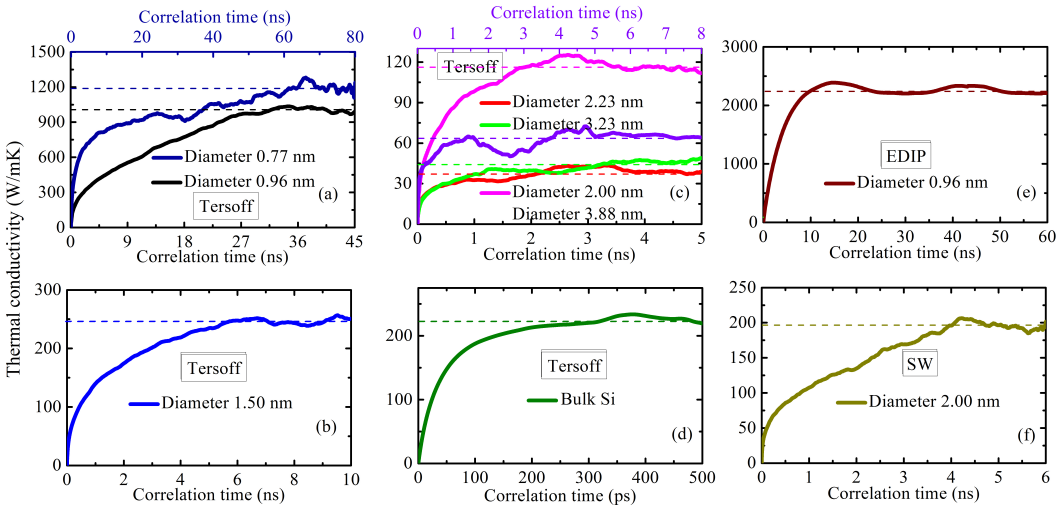


FIGURE 4.13: (a-c) Thermal conductivity of ultra-thin Si NWs with different diameter calculated using Tersoff potential. For comparison thermal conductivity of bulk Si with Tersoff potential (d) and thermal conductivity of the thinnest possible Si NWs using EDIP (e) and SW (f) potential are also shown. The dashed lines denote the finally converged value.

4.3.2 Results and discussions

The κ of Si NWs as a function of diameter is plotted in Figure 4.14. The three different potentials yield consistently that, the κ first decreases with diameter decreasing, reaching the lowest value at the critical point at diameter of 2.3 nm (,2.0 nm and 3.23 nm for EDIP and SW potential, respectively), and then steeply increases when the diameter is decreased further. The κ for the smallest NW diameter can be as large as 13 and 79 times of their bulk value and the minima, respectively. This is counterintuitive since in the common sense the κ is reduced with diameter decreasing (Ramayya et al., 2012), considering that the fraction of the core atoms that can be affected by the surface becomes larger (or equivalently stronger surface effect) for thinner NWs. Then a spontaneous question should be addressed: will the κ of the thinnest Si NWs diverge or converge? Here, based on our GK-EMD results, although the κ of the thinnest possible Si NWs (0.77, 0.96, and 2.0 nm for Tersoff, EDIP, and SW potential, Appendix A) is quite large, it unambiguously converges to a specific value. Recent experiment (Yu et al., 2016) also shows that the NW will become unstable when the diameter is smaller than 1 nm, which is in accordance with our results here. Therefore, the upper limit of the thermal conductivity here is the possible maximum thermal conductivity for the numerically or experimentally thinnest possible Si NWs. It is also worth noting that, it is possible to consider smaller diameter NW or even single atom chain by theory. However, no matter how thin the Si NW is, the thermal conductivity should converge rather than diverge. As we discuss below, the thermal conductivity will diverge only when the system is a strict momentum conservation system, e. g., pure N system, which is also theoretically

proved by Liu *et. al.* (Liu et al., 2014). Obviously, even for single atom chain limit, it is easy to find there should be some Umklapp (U, definition can be found below) process based on the phonon dispersion (two transverse acoustic and one longitude acoustic branches). Therefore, even for the theoretically thinnest Si NW, the thermal conductivity should converge. Meanwhile, as we discuss below, the optical phonon branches will shift downwards with diameter increasing and provide more U scattering channels. That means decreasing the diameter of Si NW will strength the importance of the dominant N process in the low frequency region. Therefore, the thermal conductivity should increase with the reduction of diameter, which is in accordance with our conclusion. Here, we would like to emphasize that in this paper we are proving the thermal conductivity for the extremely thin NWs will increase with the reduction of the diameter and converge rather than aiming to calculate the exact upper limit of the thermal conductivity. All the Si NWs in our paper satisfy the rules of both statically and thermodynamically stable. It is worth noting the following factors if one desires to obtain an accurate κ for extremely thin NWs using GK-EMD: (1) the atomic systems run in the MD simulations should have both static and thermodynamic stability, e.g. temperature is stable and system energy is conserved in NVE run; (2) the total number of independent MD runs used to obtain average κ should be as many as possible (Yang et al., 2014); (3) the autocorrelation time should be long enough (as long as 50 ns for some cases), since some phonons cannot be scattered easily [Figure 4.15]. Actually, the factors (2) and (3) guarantee that the phase space is large enough to satisfy the ergodicity, which is the foundation of the linear response theory. While using NEMD to calculate the length independent κ of extremely thin Si NWs as Hu *et. al.* (Hu and Poulikakos, 2012) and Yang *et. al.* (Yang, Zhang, and Li, 2010) did, one should notice: (1) the system should hold both the static and thermodynamic stability; (2) the model length should be long enough to include the maximum mean free path (MFP) of phonons (Sellan et al., 2010b). Therefore, there are two main reasons that may cause the divergence of κ reported in Ref. (Yang, Zhang, and Li, 2010): (1) the system in their study (Si NW with (100) surface and SW potential) might be unstable; (2) although the largest length of the model reaches 1 μm, it is still too short as we prove that the effective mean free path (EMFP) of phonons in extremely thin Si NWs can be as large as 0.5 cm [Figure 4.15]. Generally speaking, the Fourier's law fails and then the κ can diverge when (1) there is significantly ballistic heat transport in the system (Zhou, Zhang, and Hu, 2015; Mu et al., 2014); (2) the system is a momentum conservation system strictly (Liu et al., 2014). It is obvious that both conditions do not apply to our GK-EMD systems. For example, although most of scattering process in the low frequency range satisfy the momentum conservation, our systems are not strictly momentum conserved, since there are also plenty of scattering process that break the momentum conservation (see discussion below for details).

Now, we analyze the underlying mechanism that leads to the super-high κ of the extremely thin Si NWs using Boltzmann transport equation (BTE) (Ward et al.,

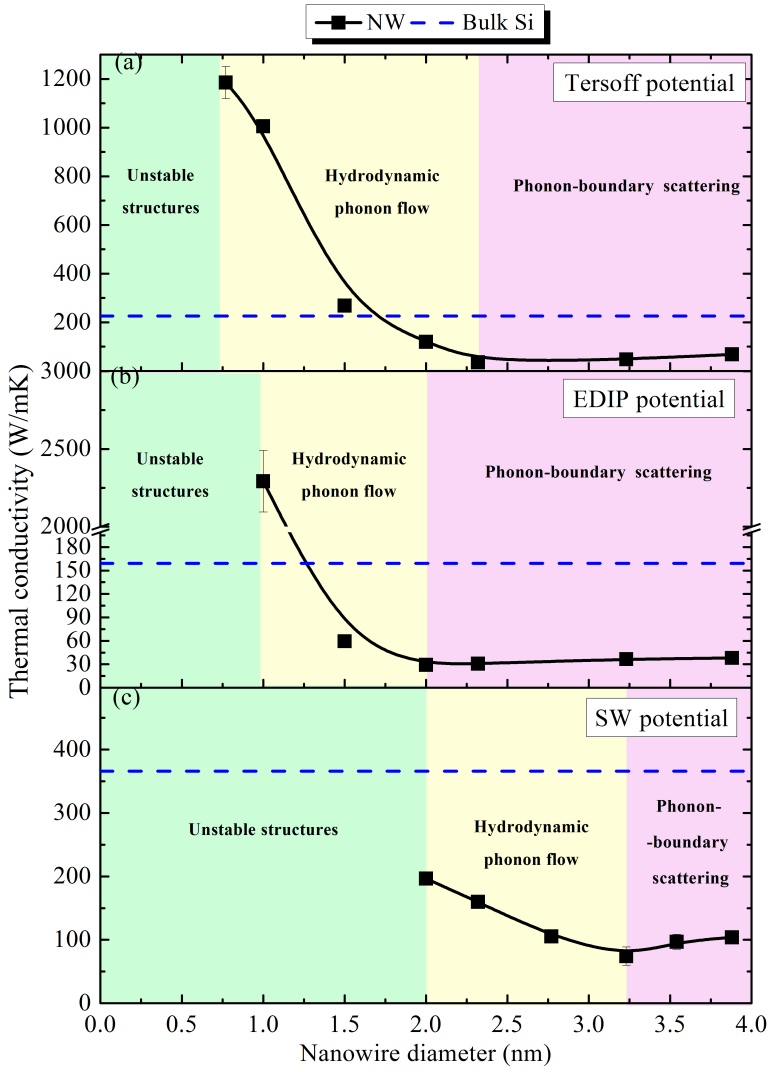


FIGURE 4.14: Diameter dependent thermal conductivity of Si NWs calculated by GK-EMD with different interatomic potentials: (a) Tersoff, (b) EDIP and (c) SW. The dashed lines denote the thermal conductivity of bulk Si. The spline lines are guide for the eyes. Different shading color represents different heat conduction regime.

2009). The BTE, which is formulated by Peierls (Peierls, 1955), can be solved by assuming the scattering term expanded to its first-order perturbation f^1. Then, without considering the impurities and boundaries, the linearized BTE can be recast into (Fugallo et al., 2013; Ward et al., 2009)

$$-c(\vec{k},\nu)\left(\frac{\partial n_0(\vec{k},\nu)}{\partial T}\right) = \sum_{(\vec{k}',\nu'),\,(\vec{k}'',\nu'')} \Big[\Gamma^{(\vec{k},\nu)}_{(\vec{k}',\nu'),\,(\vec{k}'',\nu'')}\left(f^1_{(\vec{k},\nu)} + f^1_{(\vec{k}',\nu')} - f^1_{(\vec{k}'',\nu'')}\right) + \frac{1}{2}\,\Gamma^{(\vec{k}',\nu'),\,(\vec{k}'',\nu'')}_{(\vec{k},\nu)}\left(f^1_{(\vec{k},\nu)} - f^1_{(\vec{k}',\nu')} - f^1_{(\vec{k}'',\nu'')}\right)\Big] \tag{4.27}$$

where $(\vec{k},\nu)$ is the phonon mode with wave vector $\vec{k}$ and branch ν. $c(\vec{k},\nu)$, n_0 and T

are the specific heat capacity, equilibrium phonon population and system temperature, respectively. Γ is the scattering rate at equilibrium of a process where a phonon mode is scattered by absorbing another phonon to generate the third phonon or decayed to two different phonons. The scattering rate matrix can be obtained based on the Fermi's golden rule. Moreover, following the Bose-Einstein distribution of phonons, $n_0(\vec{k},\nu) = (e^{\hbar\omega(\vec{k},\nu)/k_bT} - 1)^{-1}$, where $\hbar$ and $\omega(\vec{k},\nu)$ are the reduced Planck constant and phonon frequency, respectively. With the help of recently released ShengBTE package (Li et al., 2014), the Eq. (4.27) can be solved with the input of 2nd and 3rd interatomic force constants (IFCs), both of which are calculated using the empirical Tersoff potential. In addition, based on the definition of N and U process, we can split them in the three-phonon scattering process by judging whether the momentum conservation is obeyed, i.e. $\vec{k} + \vec{k'} - \vec{k''} = 0$ (N) or $\vec{k} - \vec{k'} - \vec{k''} = 0$ (U).

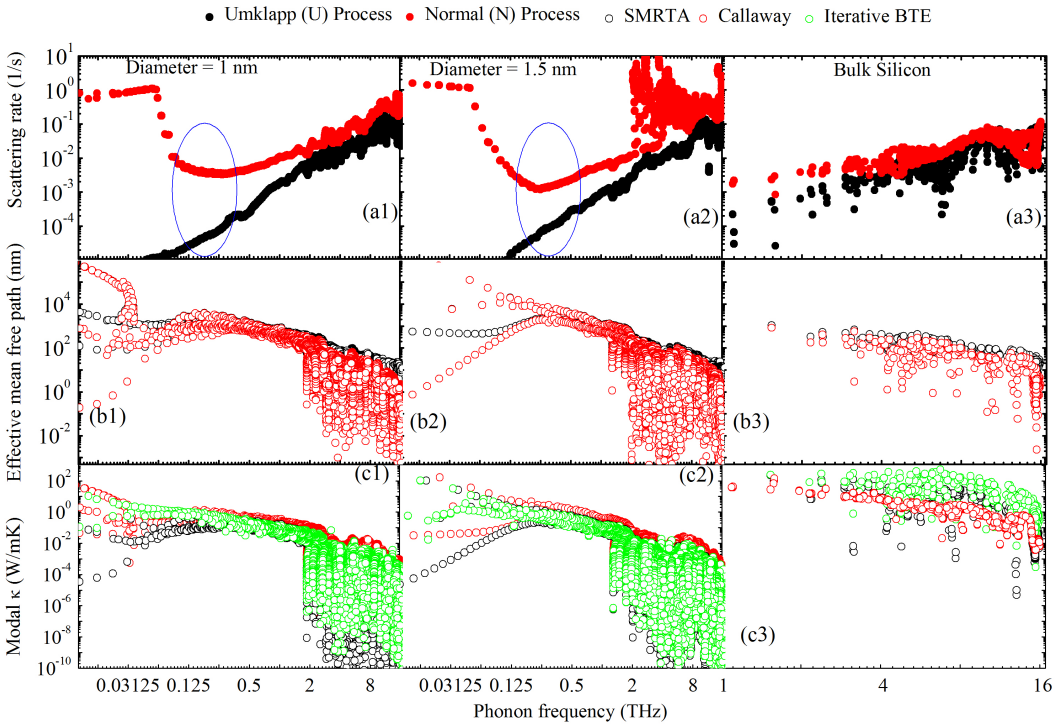


FIGURE 4.15: (Top panels) Three-phonon scattering rates for Si NWs with diameter of (a1) 1 nm, (a2) 1.5 nm and (a3) bulk Si. The blue circle is a guide for eyes. (Middle panels) The corresponding effective mean free path calculated by the single mode relaxation time approximation (SMRTA) and the Callaway model. (Bottom panels) Comparison of the corresponding modal thermal conductivity calculated by SMRTA, Callaway model and iterative Boltzmann transport equation (BTE) method.

It is well known that only U process can be treated as resistive scattering, where the phonon modes will be relaxed to the stationary equilibrium Bose-Einstein distribution, and therefore the momentum of the phonon mode will be relaxed to zero. However, for N process, phonons will formulate the group and the momentum

will be exchanged among these phonons, and thus all the phonons exhibit the same drift velocity, which means the momentum of the system will not be able to relax to zero. Therefore, if N process is dominant in the three-phonon scattering, the out-of-equilibrium distributions can be redistributed by strong N process with quite a small reduction by U process, such that these corresponding phonon modes will have the same drift velocity and form a hydrodynamic phonon "fluid" flow (Cepellotti et al., 2015; Lee et al., 2015). In the ultimate case, if the phonon scattering process are totally N process, the out-of-equilibrium distributions will never decay to the equilibrium state, and thus will lead to an infinite κ (divergence). Meanwhile, as theoretical studies proved by Alvarez *et. al.* (Alvarez, Jou, and Sellitto, 2009) and Dong *et. al.* (Dong, Cao, and Guo, 2014), only considering hydrodynamic phonon "fluid" flow will yield wrong diameter dependence of thermal conductivity of Si NWs. This indicates that even in the hydrodynamic phonon "fluid" flow dominant system, the effect of U process should be considered. Therefore, as we discussed above, for the thinnest Si NWs in our paper, their thermal conductivity should converge. To address such property of N process, Callaway (Callaway, 1959) introduces a drift distribution function $n(\vec{k},\nu)^{drift} = \left(e^{(\hbar\omega(\vec{k},\nu)-k\cdot\Delta)/k_BT}-1\right)^{-1}$ (Δ is the Lagrange multiplier), which is proved by Klemens to be the most probable distribution in a system where the momentum is conserved (Klemens, 1958). Then, one can regard the N process is relaxed from $n(\vec{k},\nu)$ to $n(\vec{k},\nu)^{drift}$, and obtain

$$\begin{aligned} -\vec{v}(\vec{k},\nu)\cdot\nabla T\left(\frac{\partial\bar{n}(\vec{k},\nu)}{\partial T}\right) =& \Gamma(\vec{k},\nu)^{U}\left[n(\vec{k},\nu)-\bar{n}(\vec{k},\nu)\right]+ \\ & \Gamma(\vec{k},\nu)^{N}\left[n(\vec{k},\nu)-n(\vec{k},\nu)^{drift}\right] \end{aligned} \tag{4.28}$$

From Eq. (4.28), we can find that an out-of-equilibrium distribution will mostly relax to the drift distribution firstly when the N process $\Gamma(\vec{k},\nu)^{N}$ dominates, and then from this state decays to the static equilibrium. Figure. (4.15)(a1 - a3) shows the scattering rate of N and U process for Si NWs with diameter of 1 nm and 1.5 nm, and bulk Si for comparison. Due to the computational capacity, we cannot calculate the Si NW with diameter larger than 1.5 nm. We clearly observe that for extremely thin Si NWs the N process are much stronger than the U process by as large as five orders of magnitude in the low frequency range ($<$ 2 THz). In contrast, the N process in bulk Si are found to be on the same order of magnitude with the U process over the almost entire frequency range, which is in accordance with the results of Ref. (Ma, Li, and Luo, 2014). Therefore, in the extremely thin Si NWs the out-of-equilibrium distribution in the low frequency range can be redistributed to the drift state with only small reduction due to the significantly strong N process. On the other hand, if the phase space is large enough, such out-of-equilibrium distribution will be scattered to the static equilibrium finally by these weak U process [Eq. (4.28)]. Thus, the κ of extremely thin Si NWs converges. With diameter increasing, the difference of the scattering rates between the N and U process becomes smaller [blue circle in Figure.

(4.15)(a)]. Then, the κ of Si NW with diameter of 1.5 nm is decreased with respect to that for diameter of 0.96 nm. In order to depict the above phenomenon more straightforwardly, we define EMFP and the thermal conductivity for each phonon mode based on the Callaway model (Appendix B)), similar to the definition in the single mode relaxation time approximation (SMRTA).

$$\Lambda_z^{effective}(\vec{k},\nu) = \frac{1}{\Gamma(\vec{k},\nu)^U + \Gamma(\vec{k},\nu)^N}\left\{v_z(\vec{k},\nu) + \frac{k_z\Gamma(\vec{k},\nu)^N\left\{\sum\limits_{(\vec{k}',\nu')}\frac{\Gamma(\vec{k}',\nu')^N\hbar\omega(\vec{k}',\nu')v_z(\vec{k}',\nu')k'_z\bar{n}(\vec{k}',\nu')\left[1+\bar{n}(\vec{k}',\nu')\right]}{\Gamma(\vec{k}',\nu')^U+\Gamma(\vec{k}',\nu')^N}\right\}}{\hbar\omega(\vec{k},\nu)\sum\limits_{(\vec{k}',\nu')}\frac{\Gamma(\vec{k}',\nu')^U\Gamma(\vec{k}',\nu')^N k'_z k'_z\bar{n}(\vec{k}',\nu')\left[1+\bar{n}(\vec{k}',\nu')\right]}{\Gamma(\vec{k}',\nu')^U+\Gamma(\vec{k}',\nu')^N}}\right\} \tag{4.29}$$

and

$$k_{zz} = \frac{1}{k_B T^2 NV}\sum_{(\vec{k},\nu)}\left(\hbar\omega(\vec{k},\nu)\right)^2 v_z(\vec{k},\nu)\Lambda_z^{effective}(\vec{k},\nu)\bar{n}(\vec{k},\nu)\left[1+\bar{n}(\vec{k},\nu)\right] \tag{4.30}$$

It is not surprising to find that, the EMFP for these phonon modes [Figure. 4.15(b1) and (b2)] is incredibly large in the extremely thin Si NWs, which even reaches 0.5 cm and 0.1 cm for diameter of 0.96 nm and 1.5 nm, respectively, due to the fact that the N process have no decay. Moreover, the EMFP calculated by the Callaway model is quite different from those computed using SMRTA, since phonons cannot be treated independently when N process are dominant. Therefore, the significant strong N process in the low frequency range should be responsible for the ultra-high κ of extremely thin Si NWs. Meanwhile, we calculate the EMFP of bulk Si for comparison. From Figure. 4.15(b3) we find that the EMFP predicted by the Callaway model is almost the same as that by SMRTA, which indicates that the phonon modes in bulk Si can be treated as independent and they can decay to the static equilibrium state completely. Furthermore, we calculate the modal and total thermal conductivity using SMRTA, Callaway model and iterative BTE [Figure. 4.15(c1), (c2) and Figure. 4.16]. The results of the Callaway model fit very well with those of iterative BTE, which confirms that the Callaway model can well reflect the scattering process in such extremely thin Si NWs. The mode dependent thermal conductivity in the low frequency range ($<$ 2 THz) computed by both Callaway model and iterative BTE is much higher than that using SMRTA, which again confirms that the low frequency phonons in the extremely thin NWs can hardly relax to the static equilibrium. For bulk Si, once again we find that both modal and total κ [Figure. 4.16(c)] calculated using these three methods are almost the same, since the contribution of the N and U process to a specific phonon mode is similar and the out-of-equilibrium distribution can decay to the static equilibrium easily. We also consider the effect of isotope, and find that the collective phonons, which are defined by Tomas *et. al.* (De Tomas

et al., 2015) using the definition analog to the kinetic phonons to describe the hydrodynamic "fluid" flow, will be largely weakened by the phonon impurity scattering. Such phenomena is also found in the results of Tomas *et. al.* (De Tomas et al., 2015). However, the results show that the thinner NW has the higher κ, which means there is still hydrodynamic phonon flow in the extremely thin Si NWs with isotopes.

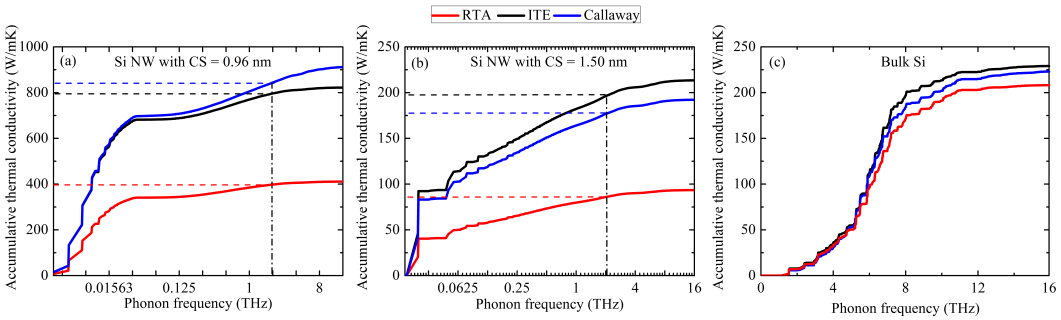


FIGURE 4.16: Accumulative thermal conductivity calculated using the Callaway model, the relaxation time approximation (RTA) and the iterative BTE method for Si NWs with diameter of (a) 0.96 nm and (b) 1.50 nm and (c) bulk Si. The dashed lines indicate the contribution of the low frequency phonon modes ($<$ 2 THz) to the total thermal conductivity.

Before closing, we explain why the thermal conductivity of Si NWs reaches minima at critical diameter equal to 2.3 nm. To this end, we compare the phonon dispersion of Si NWs with diameter of 0.96 nm, 1.5 nm and 2.0 nm in Figure. 4.17. Considering the vast amount of phonon branches in Si NWs, we only show the phonon dispersion below 3 THz, which is the dominant part to the overall thermal transport for extremely thin Si NWs. The optical phonon branches caused by the surface atoms (surface optical phonon branches were defined in Refs. (Gupta et al., 2003; Evans and Mills, 1972)) shift downward when the NW diameter increases. This activates a vast of new phonon scattering channels such as acoustic + acoustic $\rightarrow$ surface optical in the low frequency region. For diameter of 2.0 nm the low frequency phonons (ω_1 and ω_2 less than 0.75 THz), which are the major part for the hydrodynamic phonon flow, can scatter with the surface optical phonons [Figure. 4.17(c)]. Furthermore, these scattering channels prefer U scattering process, since N scattering process needs to satisfy additional momentum conservation condition. To confirm our discussion above, we calculate the modal phase space of these three NWs, which considers all the possible scattering channels in the systems, by (Lindsay and Broido, 2008)

$$P(\vec{k},\nu)^{N\ or\ U} = \frac{\Omega}{(6\pi n)^3}\left[\omega(\vec{k},\nu)\pm\omega(\vec{k'},\nu')-\omega(\vec{k''},\nu'')\right]\begin{Bmatrix}\delta(\vec{k}+\vec{k'}-\vec{k''})\\ \delta(\vec{k}+\vec{k'}-\vec{k''}-G)\end{Bmatrix} \tag{4.31}$$

where n and Ω are the braches and volume of the unit cell. It can be easily found that the relative contribution of N process in the low frequency range ($<$ 2 THz) is

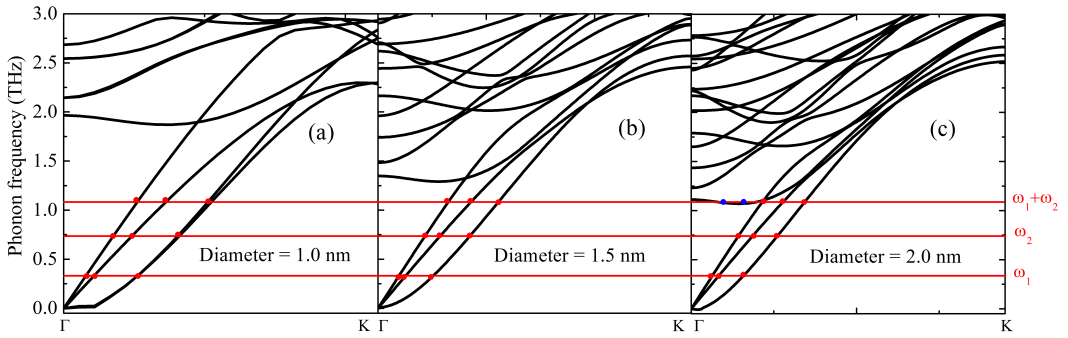


FIGURE 4.17: Phonon dispersion curves of the ultra-thin Si NWs with diameter of (a) 1 nm, (b) 1.5 nm and (c) 2.0 nm. For brevity only the dispersion curves below 3 THz are presented. The blue and red dots in the dispersion curves are schematic of low frequency modes for phonon scattering. The red horizontal lines are the guide for the eyes.

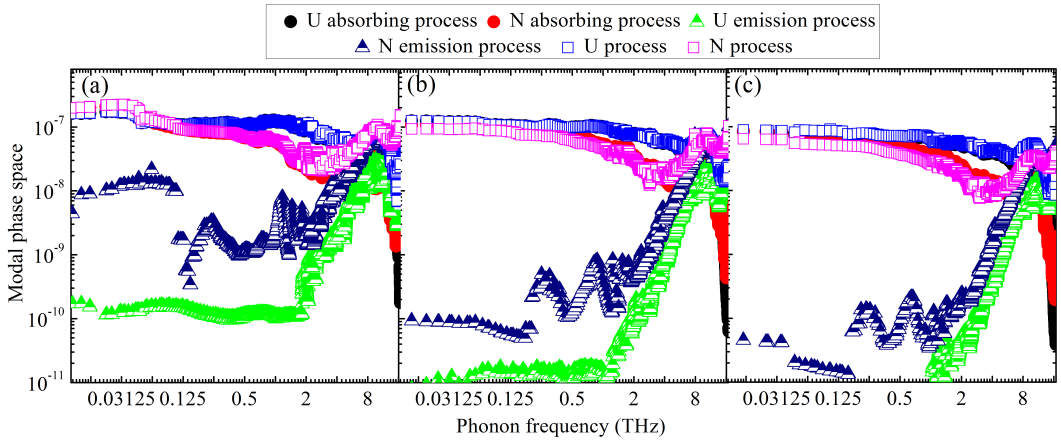


FIGURE 4.18: The modal phase space of ultra-thin Si NWs with diameter of (a) 1 nm, (b) 1.5 nm and (c) 2.0 nm. The different colors represent different phonon process (N/U, absorbing, emission, etc.).

decreased with NW diameter increasing [Figure. 4.18], i.e. the contribution of U process increases with NW diameter increasing, which confirms that the additional three-phonon scattering process are U process. Then, the out-of-equilibrium distributions can decay to the static equilibrium state more easily, and therefore the heat transported by hydrodynamic phonon flow due to the N process becomes smaller and is not the dominant thermal transport mechanism anymore. On the other hand, the phonon-boundary scattering, which is the well-known mechanism for the κ reduction of NWs, becomes dominant for larger NW diameter (Zhou and Hu, 2016; Zhou, Chen, and Hu, 2016; Zhou, Yao, and Hu, 2016). Since the proportion of the surface atoms in the NWs decreases with NW diameter increasing, leading to weaker phonon boundary scattering, the κ of Si NWs undoubtedly increases with diameter increasing. The above two competing mechanisms finally drive the minimum κ of the ultra-thin Si NWs.

4.4 Conclusion

In this chapter, we have calculated the thermal conductivity of Si NWs with diverse surface orientations using NEMD simulations and the full spectrum theory. The difference of the thermal conductivity among all the NWs considered can be as large as about 2.7 4.2 times. The physics responsible for this phenomenon originates from two effects: (1) different surface orientation can change the angle between the phonon wave vector and the normal vector of the surface, then alter the modal specularity, and therefore, leads to the change of thermal conductivity; (2) surface roughness changes due to the different surface structure, and thus, the thermal conductivity varies remarkably. The latter effect is found to be the main mechanism for the large difference in the thermal conductivity. Furthermore, the thermal conductivity of Si NWs is found to decrease with surface atom energy, or RMS height of roughness. Size effects, which include both the cross-section and length, are considered. The large difference among the NWs with diverse surface orientation is also found to exist for infinitely long NWs. We explain the underlying mechanism from phonon level using the vibrational density of states and spectral thermal conductivity. We find that, in the case of (110) orientation the mismatch of the VDOS between the surface atoms and the bulk atoms is smaller than that in other models, which means the stronger coupling between the surface and core atoms, and therefore, it leads to the highest thermal conductivity for (110) orientation among all the NWs studied. Meanwhile, with the help of our newly developed frequency domain direct decomposition method, we investigate the frequency dependent contribution of thermal conductivity. The largely scattered thermal conductivity among the NWs with various surface orientation is found to mainly stems from the medium frequency phonons (1.5 10 THz). The results presented herein are expected to be quite useful in thermal engineering applications, such as realizing high efficiency thermoelectrics by reducing thermal conductivity with engineered surface orientation.

Next, by using a model structure of regular Ar and heavy Ar in contact, we have presented the superiority of largely decreasing the interfacial thermal resistance by sandwiching a mass graded layer. While the widely adopted alloyed interface usually increases the overall interfacial thermal resistance by several times as compared with perfectly abrupt interface, except for atomically thin layers, the mass graded structure substantially reduces the overall resistance by 6 folders. Using atomic heat flux spectrum theory, the governing mechanisms are well explained. There are two different regimes of interfacial heat transfer across the rough interface, which originates from the competition between phonon scattering and the interface thickness. When the thickness is large enough, there is enough space for high frequency phonons to scatter then the interfacial thermal resistance will increase, while when the thickness is reduced to only a few atomic layers, there is no enough space for phonon scattering and thus the interfacial thermal resistance decreases to some

extent. Moreover, the detailed phonon process for high frequency phonons across three types of interfaces ($\omega > \omega_c^{heavy\ argon}$) are studied using wave packet method and acoustic mismatch model. For the perfectly abrupt interface, all the phonons with frequency above the cutoff frequency of heavy Ar are reflected and for the alloyed interface, the high frequency phonons gradually disappear through phonon scattering in the alloyed region. In contrast, for the mass graded interface the minor phonon reflection occurs when the phonons first reach the mass graded area. After that, the phonons can easily transmit across the subsequent multi-layers with gradually increasing transmission coefficient and hardly reflect. Consequently the major thermal energy transport turns out to be carried by medium frequency phonons. Wave packet simulation also show that, for rough interface the short and medium mean free path (corresponding to medium and high frequency) phonons have lower transmission coefficient with respect to those in perfectly abrupt interface due to the strong phonon scattering, while the long mean free path (corresponding to low frequency) phonons have the opposite trend, since they can transport across the thin layer with small interference. For the mass graded interface, almost all the phonons with frequency below the cutoff frequency of heavy Ar have significantly higher transmission coefficients, primarily due to the small mass mismatch between the adjacent layers in the interface region, and therefore, the interfacial thermal resistance is dramatically reduced. Although the present results are based on simple lattice models, our findings shed light on the field of interfacial heat transfer in terms of improving the heat dissipation efficiency in electronic cooling.

Finally, by performing GK-EMD simulations, we show the nonmonotonic dependence of the thermal conductivity of extremely thin Si NWs on the NW diameter. By analyzing the relative contribution of the two different three-phonon scattering process (N and U) using the BTE, we identify that, the nonmonotonic diameter dependence stems from two competing mechanisms governing the heat conduction in thin Si NWs. For Si NWs with diameter smaller than a critical value, the N process which cannot destroy their momentum are the dominant three-phonon scattering process for the low frequency phonons. Therefore, the excess momentum of these phonons gained from a temperature gradient will be redistributed by the super-strong N process with small reduction, and therefore all of these phonons will transport heat with the same drift velocity (hydrodynamic phonon flow). Consequently, the thermal conductivity of extremely thin Si NWs converges to a very high value, which can be as large as 13 folders of its bulk value for the thinnest but still thermodynamically stable Si NWs. When the NW diameter is larger than the critical value, new U scattering channels for the low frequency phonons are triggered due to the downward-shift of the surface optical phonons, and therefore breaking the dominant role of N scattering. As a result, the thermal conductivity of ultra-thin Si NWs, which is dominated by the phonon boundary scattering rather than the hydrodynamic phonon flow, increases with NW diameter increasing. Our results solve the contradictory problem (convergence vs. divergence) in the literature for the thermal

conductivity of extremely thin Si NWs, and for the first time we provide an exact explanation for the mechanism underlying the converged thermal conductivity even for the thinnest possible Si NWs. Our study is expected to offer useful guidance for the rational design of Si NW based structures for advanced nanoelectronics.

Chapter 5

Enhancing Thermoelectric Performance via Nanostruturing

5.1 Introduction

Thermoelectric (TE) devices enable solid-state cooling to replace cumbersome vapor-compression cycle technologies as well as electricity generation from a variety of waste heat sources such as industries and vehicles (Klemens, 1951; Tritt, Böttner, and Chen, 2008; Tritt, 2000; Snyder and Toberer, 2008b). The performance of the TE materials is characterized by a dimensionless figure-of-merit (ZT) which can be written as $ZT = S^2\sigma T/(\kappa_{el} + \kappa_{ph})$, where S, σ, κ_{el} and κ_{ph} are the thermoelectric power (Seebeck coefficient), electrical conductivity, electronic thermal conductivity and lattice (phonon) thermal conductivity, respectively. An ideal TE should be electrical conductor [high power factor (PF) $S^2\sigma$], but thermal insulator [low thermal conductivity $(\kappa_{electron} + \kappa_{phonon})$]. This conflicting requirement poses a material challenge, due to the strong coupling between the electronic and phononic transport. In general, development schemes to improve TE conversion efficiency in the past decades were guided by the concept of "phonon glass – electron crystal" (Hsu et al., 2004b; Biswas et al., 2012; Zhang and Zhao, 2015), i.e., reducing the lattice contribution to the thermal conductivity as closely as possible to an amorphous state, while keeping relatively high electrical conductivity and Seebeck coefficient (Zheng et al., 2014). Nanostructuring the existing bulk TE materials has been proved to be a quite efficient way to obtain decent thermoelectric performance (Lan et al., 2010; Minnich et al., 2009b; Snyder and Toberer, 2008b; Vineis et al., 2010; Minnich et al., 2009a; Zhou et al., 2010).

5.2 Significantly Decreasing Thermal Conductivity via Polycrystallization

In this section, by performing non-equilibrium and Green-Kubo equilibrium molecular dynamics simulations we report that the thermal conductivity of Si NWs in polycrystalline form can reach a record low value substantially below the Casimir limit, a theory of diffusive boundary limit that regards the direction-averaged mean

free path is limited by the characteristic size of the nanostructures. The astonishingly low thermal conductivity of polycrystalline Si NW is 269 and 77 times lower with respect to that of bulk Si and pristine Si NW, respectively, and is even only about 1/3 of the value of the purely amorphous Si NW at room temperature. By examining the mode level phonon behaviors including phonon group velocities, lifetime etc., we identify the mechanism of breaking the Casimir limit as the strong localization of the middle and high frequency phonon modes, which leads to a prominent decrease of effective mean free path of the heat carriers including both propagons and diffusons. The contribution of the propagons to the overall thermal transport is further quantitatively characterized and is found to be dramatically suppressed in polycrystalline Si NW form as compared with bulk Si, perfect Si NW and pure amorphous Si NW. Consequently, the diffusons, which transport the heat through overlap with other vibrations, carry the majority of the heat in polycrystalline Si NWs. We also proposed approach of introducing "disorder" in the polycrystalline Si NWs that could eradicate the contribution of propagons to achieve an even lower thermal conductivity than that ever thought possible. Our investigation provides a deep insight into the thermal transport in polycrystalline NWs and offers a promising strategy to construct a new kind of semiconducting thermoelectric NW with high figure of merit.

5.2.1 Simulation details and model generation

As indicated by He and Galli (He and Galli, 2012), introducing grain boundaries in NWs might be more efficient than modulating the surface morphology of NWs in terms of thermal conductivity reduction. Motivated by this, we construct polycrystalline NWs that approach realistic situations [Figure 5.1c] using the Voronoi algorithm (Fritzen, Böhlke, and Schnack, 2008). The grain size of polycrystalline Si NWs in this letter ranges from ∼1 to 3.5 nm. Based on the development of nanotechnology (Feser et al., 2013; Yu et al., 2016; Wang et al., 2008a; Wu et al., 2004b; Singh et al., 2006; Wu, 2004), such small grain size polycrystalline NWs should be feasibly fabricated in experiments right now. Meanwhile, the bulk Si, perfect Si NWs [Figure 5.1a] and amorphous Si NWs [Figure 5.1b] are constructed as comparison as well.. All the NWs have the same cross-section of 10 $\times$ 10 unit cells, corresponding to 5.442 $\times$ 5.442 nm^2, and all the simulations reported below are run with interatomic interaction of Tersoff potential (Tersoff, 1989). Here, we have to notice that using the semi-empirical potential will bring some inaccuracy in results. However, depicting the system with semi-empirical potential has been proved to obtain the same trend with experiments and be in good agreement with density function theory (DFT) calculations in many aspects (Yang et al., 2014; Stoffers et al., 2015; Brenner and Garrison, 1988; Conrad, Scheerschmidt, and Gösele, 1996; Wingert et al., 2015; Losego et al., 2012; Yasaei et al., 2015). It is also worth noting that, the parameterization of semi-empirical potentials usually take the surface or interface situation into account. The reliability of Tersoff potential used for capturing surface effect is well justified

in lots of literatures (Yan, Hu, and Jónsson, 1994; Bolding and Andersen, 1990; Hara et al., 2005). Furthermore, describing different structures with same potential is a standard procedure in simulations (Hu and Poulikakos, 2012; Sansoz, 2011; Yang, Yang, and Li, 2014; Qiu et al., 2012; Cartoixà et al., 2016b), and therefore, it is fair to compare all results computed using the same method and potential.

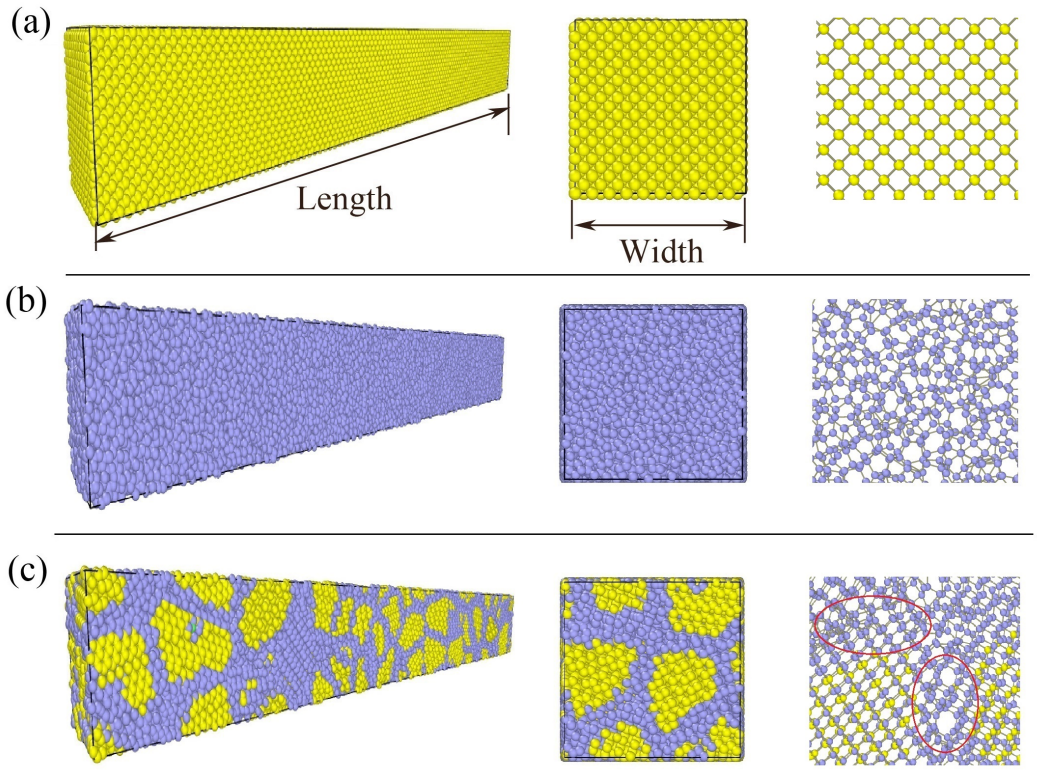


FIGURE 5.1: Snapshot of (a) perfect Si NW, (b) amorphous Si NW and (c) polycrystalline Si NW used in our NEMD simulations. (Left panel) Overview and (middle panel) cross-sectional view of the structures. (Right panel) Zoom-in picture of the atomic structures. Atoms are colored using coordinate number analysis (blue and yellow atoms denote the disordered structure and the original perfect diamond structure, respectively). The red circles indicate the discontinuity (defects) between nanograins.

After obtaining the optimized structures of these three types of NWs, NEMD and GKEMD (Kubo, 1957) simulations, which are based on the Fourier's law and linear response theory, respectively, are applied to calculate the thermal conductivity of the NWs. To generate steady heat current flowing through the system in NEMD simulation, the atoms located in the distance L_{bath} (3.2 nm in all our cases) from the left and right ends of the system are coupled to hot and cold Nose-Hoover thermostats at temperatures $T + \Delta T/2$ and $T - \Delta T/2$, respectively, to mimic the future plausible experiments. We set two atom layers at both ends as "rigid walls" to prevent large deformations and translational movement of the systems. The mean temperature

of the system T and the temperature difference between two thermostats ΔT are fixed as 300 K and 60 K, respectively. The temperature difference has been carefully checked to be able to obtain stable thermal conductivity. Once the steady state is reached, which usually takes 2-6 ns in our systems, the thermal conductivity can be obtained in the following 5 ns using the Fourier's law $\kappa = -Q/(A\nabla T)$, in which the Q, A and ΔT are the heat flux, cross-sectional area and temperature gradient, respectively. The length of NWs used in the GK-EMD simulations are 100 unit cells, which has been proved to be long enough to obtain the converged thermal conductivity (Donadio and Galli, 2009).

5.2.2 Record low thermal conductivity

The thermal conductivity of bulk Si is then found to be 226.07±2.86 W/mK by GK-EMD, while Hu and Pulikakos (Hu and Poulikakos, 2012) predicted a value of 243±11 W/mK using the same Tersoff potential and NEMD technique. The slight difference between GK-EMD and NEMD can be attributed to the not long enough length of the samples used in previous NEMD to extrapolate the infinite thermal conductivity (Hu and Poulikakos, 2012), since the mean free path (MFP) of phonons in bulk Si can reach several micrometers, and therefore the relation between $1/\kappa$ and $1/L$ cannot be simplified into a linear form (Sellan et al., 2010b). By applying the same Tersoff potential, Hayat *et. al.* (Zaoui et al., 2016) find the thermal conductivity of bulk Si is about 230 W/mK using approach-to-equilibrium molecular dynamics (AEMD), and He and Galli (He and Galli, 2012) obtain the value to be 196.80±33.28 W/mK using GK-EMD. Henry *et. al.* (Henry and Chen, 2008) and Yang *et. al.* (Yang, Yang, and Li, 2014) reported GK-EMD results of 160 W/mK and 170±16 W/mK, respectively, which are different to our result, since different potentials are applied in their work. It is also worth noting that the experimental thermal conductivity of bulk Si at 300 K is about 156 W/mK (Glassbrenner and Slack, 1964), which means our computed results are overestimated. Such discrepancy could come from the inaccuracy of the semi-empirical potential in our simulations and phonon Boltzmann distribution inherent in classical MD simulation (Boltzmann distribution vs. the real Bose-Einstein distribution in experiments). Another reason, although in common sense, is the defects inevitable in the experimental samples as compared with the pristine structure used in our computational model. However, it may not be an important factor, since the BTE coupled with first-principles (without defects considered) already gives consistent result with experiments (Jain and McGaughey, 2015). Here, all of our results are calculated using the same methods and the same interatomic potential, and therefore this overestimation is believed to have no impact on our comparison and conclusion. We also perform the cross-check with different potentials (see results below). In order to confirm the accuracy of our simulations, we calculate the thermal conductivity of NWs using both NEMD and GK-EMD. Based on the results of GK-EMD, we find the thermal conductivity of perfect and amorphous Si NWs is 64.5±4.5 W/mK and 2.4±0.25 W/mK, respectively [Figure 5.2a]. It

is also easy to find from Figure 5.2a that thermal conductivity of perfect and amorphous Si NWs calculated by NEMD gradually saturates to the GK-EMD results at the length of about 310 nm and 130 nm for perfect Si NW and amorphous Si NW, respectively, which is due to the fact that the long mean free path phonons are not truncated and then contribute to the thermal conductivity (Zhou, Zhang, and Hu, 2015) (see the MFP distribution of effective phonons below). For the polycrystalline Si NWs, only NEMD simulation is enough to obtain the thermal conductivity, since there is no noticeable size effect along the length direction [see results in Figure 5.3a below] (**205**). We also prove that the thermal conductivity of polycrystalline Si NW increases and approaches that of the perfect Si NW with increase of the grain size (results not shown for brevity). Using the same potential as in our work, Donadio and Galli (Donadio and Galli, 2009) find that the thermal conductivity of perfect Si NWs with a 3 $\times$ 3 nm^2 cross-section is about 43$\pm$10 W/mK with the framework of GK-EMD. Hu and Pulikakos (Hu and Poulikakos, 2012) report that the thermal conductivity of perfect Si NWs with a cross-section of 3.06 $\times$ 3.06 nm2 is 45.5$\pm$1.9 W/mK using the same Tersoff potential and the same NEMD method as we did in this paper. There is no surprise to find our thermal conductivity of the perfect Si NW is much larger than these two previous studies, since the cross-section of the NWs in our work is 5.442 $\times$ 5.442 nm^2, which is far larger than that of the references (Hu and Poulikakos, 2012; Donadio and Galli, 2009). It is worth noticing that our result of perfect Si NW with even smaller diameter is much larger than experimental values (Li et al., 2003; Chen et al., 2008). There are several reasons responsible for this: (1) The thermal conductivity of crystalline Si NWs strongly depends on the surface structure. For instance, the thermal conductivity of the Si NW with a diameter of 56 nm can reach about 30 W/mK when the root mean square (RMS) roughness height (Δ) is about 0.1 nm, i.e. the surface roughness is on the atomic scale level (ultra-smooth), while the thermal conductivity drops down to about only 2 W/mK when is equal to 3 nm [211]. More recently, the authors also find that the surface orientation can affect the thermal conductivity of Si NWs strongly (the difference can be as large as about 3 times) (Zhou, Chen, and Hu, 2016). The surface orientation of perfect Si NW ((110) surface) used in this letter is quite smooth, and therefore will lead to a high thermal conductivity (Zhou, Chen, and Hu, 2016). (2) Our simulation models are perfect (pristine) and have no defects or isotopes, grains, dislocations, voids, etc., all of which are usually inevitable in experiments. It is well known that such defects also bring a significant reduction to the thermal transport of Si NWs. Therefore, if considered in our MD simulation, the absolute value of thermal conductivity from MD will definitely be reduced dramatically. (3) The quantum effect in MD simulations, in which the phonon distribution follows Boltzmann distribution rather than Bose-Einstein distribution, may also lead to a high thermal conductivity with respect to the real value. However, we use a full spectrum model (Zhou, Chen, and Hu, 2016) with the correct Bose-Einstein distribution of phonons and find that the quantum effects on the results of MD simulations at 300 K can be actually

ignored. Furthermore, Turney *et. al.* (Turney, McGaughey, and Amon, 2009) prove that, for bulk Si, applying the quantum corrections to the classical predictions does not bring them into better agreement with the quantum predictions as compared with the uncorrected classical values above temperature of 200 K, which also shows that the quantum effect for Si can be ignored when the system temperature is 300 K. (4) The empirical potential used in our paper is still not perfect yet, which demands for further improvement.

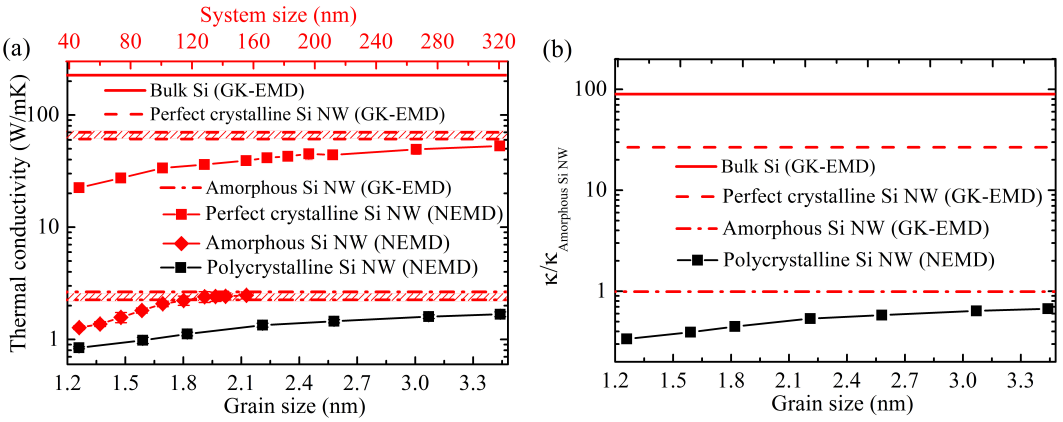


FIGURE 5.2: (a) The thermal conductivity of bulk Si, perfect Si NWs, amorphous Si NWs and polycrystalline NWs. The perfect crystalline Si NW and amorphous Si NW use the left-upper axes and the polycrystalline Si NW uses the left-bottom axes. The length of the polycrystalline Si NWs is 45 nm. (b) Comparison of thermal conductivity between bulk Si, perfect Si NWs, polycrystalline Si NWs and amorphous Si NWs. The thermal conductivity is normalized by the value of thermal conductivity of amorphous Si NWs (2.4 W/mK). All the NWs have the same cross-sectional size of 5.442 $\times$ 5.442 nm^2.

The comparison of the thermal conductivity among bulk Si, pristine Si NW, amorphous Si NW and polycrystalline Si NW is reported in Figure 5.2a. We find that the polycrystalline Si NWs, which introduce a large amount of grain boundaries inside the NWs, have the lowest thermal conductivity among these four kinds of structures. Meanwhile, it is astonished to find from Figure 5.2b that the thermal conductivity of the polycrystalline Si NWs, which is 0.843$\pm$0.018 W/mK by NEMD for grain size of 1.26 nm with cross-section of 5.442 $\times$ 5.442 nm^2 and length of 45 nm, as compared with GK-EMD result of 0.88$\pm$0.12 W/mK, can be reduced by as much as 269 and 77 times with respect to bulk Si (226.07$\pm$2.86 W/mK by GK-EMD) and perfect Si NW (64.5$\pm$4.5W/mK by GK-EMD), respectively, and is even only about 1/3 of that of amorphous Si NW (2.4$\pm$0.25 W/mK by GK-EMD). This is actually counter-intuitive to our usual thought that the purely amorphous structure without impurities and porosity should possess the lowest possible thermal conductivity. We also check that thermal conductivity of polycrystalline Si NW will be close to that of the perfect Si NW when the number of grain boundaries in polycrystalline Si

NWs decreases, which is in accordance with the common sense. Furthermore, previous experimental study on polycrystalline CdSe thin films (Feser et al., 2013) and Si nanocrystals with amorphous layer (Nakamura et al., 2015) also shows that the thermal conductivity of polycrystalline structure is much lower than that for amorphous structure, which confirms our results are reliable. Regarding the thermal conductivity of amorphous Si NW, Hu *et. al.* (Hu and Poulikakos, 2012) obtain the value of 1.23 W/mK for cross-section of 3.07 $\times$ 3.07 nm^2. Here, our amorphous Si NW has a much larger thermal conductivity, also primarily due to the much larger cross-section, since the MFP of propagon in it can be quite large (as large as 100 nm). For the amorphous structure, we know that the thermal conductivity is strongly dependent on the detailed structure. The thermal conductivity of bulk amorphous Si has been shown to range from 1.5 to 6 W/mK for different experimental preparation conditions (He, Donadio, and Galli, 2011). In that paper, using the same Tersoff potential, the thermal conductivity of bulk amorphous Si (obtained by melting-annealing method) is found to be about 3.0 W/mK and 2.8$\pm$0.5 W/mK for extrapolated NEMD and GK-EMD simulation, respectively. Furthermore, in our previous work (Hu and Poulikakos, 2012), only four data points are used to do the extrapolation of NEMD, which may cause a large error in the final thermal conductivity for infinite length. Meanwhile, as we show in this letter, the MFP of phonons in amorphous Si NW can be as large as 100 nm, which means the size effects in amorphous Si NWs is strong. Such conclusion can be also found in Ref. (He, Donadio, and Galli, 2011). Moreover, we also calculate the thermal conductivity of our amorphous Si NW using GK-EMD, and find that the results of NEMD simulation gradually saturate to GK-EMD result (2.4$\pm$0.25 W/mK) at the length of about 130 nm since almost all phonons can contribute to thermal conductivity. Unfortunately, to the best of our knowledge, there are no other studies on the thermal conductivity of amorphous Si NWs available in literature, thus direct comparison with other groups is not possible at this moment. Furthermore, from Figure 5.2a it is also easy to find that the thermal conductivity of polycrystalline Si NW slowly increases with the grain size increasing from 1.2 nm to 3.5 nm. This is because the boundary scattering becomes weaker when the grain size increases from 1.2 nm to 3.5 nm, and then results in an increase of thermal conductivity. It means that, as grain size increasing, the phonons with possible longer wavelength (normally corresponding to low frequency phonons) can be accommodated inside the grains. Another common question concerned with classical MD simulation is to check if the phenomenon reported is independent of the empirical potential used. To this end, we compare the results using different potentials and ab initio calculations for a typical case of perfect Si NW. It is easy to find that the MD results depend on the interatomic potential strongly. However, we find that the thermal conductivity computed using Tersoff potential agrees very well with that calculated by the full spectrum model, which uses the phonon dispersion inputs from ab initio calculations. This indicates that the Tersoff potential we used is rather accurate to describe the phonon transport process in Si NWs. To prove our conclusion

TABLE 5.1: Comparison of thermal conductivity of amorphous Si NW (length of 100 unit cells) and polycrystalline Si NW (grain size of 1.26 nm) by NEMD simulations with different interatomic potentials.

Potential	Amorphous Si NW (W/mK)	Polycrystalline Si NW (W/mK)
Tersoff	1.27±0.02	0.84±0.02
SW	1.18±0.06	0.94±0.03
EDIP	1.09±0.04	0.90±0.04

further, we also calculate our polycrystalline (grain size of 1.26 nm) and amorphous Si NWs with a length of 100 unit cells using SW potential and environment dependent interatomic potential (EDIP). The results are compared in Table 5.1. It can be found that, all three interatomic potentials consistently yield that the thermal conductivity of polycrystalline Si NW is lower than that for the amorphous Si NW with length of 100 unit cells. Note that the thermal conductivity value reported here for amorphous Si NW with finite length should be much lower than that for infinitely long amorphous Si NW, since there is size effect in phonon transport in amorphous Si NW (Larkin and McGaughey, 2014; He, Donadio, and Galli, 2011). These results verify that different interatomic potentials will not change the main conclusion of this manuscript.

Next, we investigate the length and cross-section dependence of the polycrystalline Si NWs. As expected, the thermal conductivity of polycrystalline Si NWs is independent of the system length (Figure 5.3a). This is understandable considering that, due to the presence of different crystallites, the effective MFP of the phonons is limited to the grain size (see details below), which is much smaller than the system length, and therefore the heat transport is completely diffusive in polycrystalline Si NWs. However, it is unexpected to find that there is a weak dependence of the thermal conductivity of polycrystalline Si NWs on the size of the NW cross-section. This is because when constructing the polycrystalline NWs, the size of some grains is comparable to the cross-section size along the lateral direction, and thus sometimes the lateral surface itself is the grain boundary. Increasing the size of cross-section (Figure 5.2b) or decreasing the size of grains will relieve such effects somehow.

5.2.3 Underlying mechanism for low thermal conductivity

We now focus on the underlying mechanism that leads to the huge reduction of thermal conductivity of polycrystalline Si NWs as compared with pristine Si NWs and bulk Si. First, we calculate the modal participation ratio $P(\vec{k},\nu)$, which can be used to quantitatively characterize the mode localization. The detailed expression of $P(\vec{k},\nu)$ can be written as (Donadio and Galli, 2009)

$$P(\vec{k},\nu)=\frac{1}{N_b\sum_1^{N_b}\left(\sum_\alpha^3 e^*_{i,\,\alpha}(\vec{k},\nu)e_{i,\,\alpha}(\vec{k},\nu)\right)^2} \tag{5.1}$$

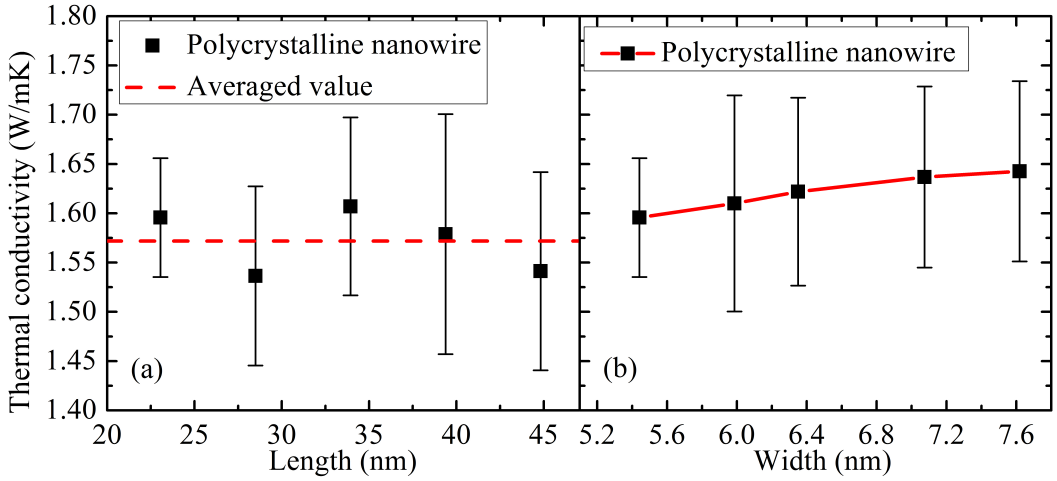


FIGURE 5.3: Length (a) and cross-sectional width (b) dependence of thermal conductivity of polycrystalline Si NWs. All the results are for the average grain size of 3.07 nm. The length used for the cross-sectional width dependence calculation is 45 nm.

in which N_b is the total number of the unit cell and $e_{i,\,\alpha}(\vec{k},\nu)$ is the component of the eigenmode $(\vec{k},\nu)$ relative to the coordinate α of atom i. Each mode considers the contribution from all the atoms in the unit cell. The less atoms participating in the motion of a specific mode, the smaller the $P(\vec{k},\nu)$. In other words, when all the atoms participate in a specific modal motion, $P(\vec{k},\nu)$ is equal to unity. $P(\vec{k},\nu)$ will be $1/N_b$ when only one atom contributes to a mode. Results of the frequency dependent participation ratio are shown in Figure 5.4. For bulk Si all the $P(\vec{k},\nu)$ are located in the range between 0.5 and 1, which means there are only extended vibrational modes in bulk Si (Bodapati et al., 2006). Our results for bulk Si fit very well with that obtained by Yang *et. al.* (Yang, Yang, and Li, 2014). It is interesting to find that the $P(\vec{k},\nu)$ for the perfect Si NW is more scattered over the entire frequency range and the $P(\vec{k},\nu)$ for some vibrational modes can be even smaller than that for the amorphous and polycrystalline Si NW. The reason is that the surface and core atoms in the perfect Si NW have quite different vibrational states, and therefore the surface phonons which are mainly contributed from the surface atoms are strongly localized and hold very small $P(\vec{k},\nu)$. In contrast, for amorphous Si NW due to its disordered structure the difference in the vibration between surface atoms and core atoms becomes smaller, and therefore the $P(\vec{k},\nu)$ of the amorphous Si NW appears a little more well distributed. For polycrystalline Si NWs a vast of grain boundaries are introduced in the structures, and then the localization of phonon modes becomes stronger (corresponding to smaller $P(\vec{k},\nu)$) with respect to the amorphous Si NW, in particular for phonon modes with frequency lager than ~1.5 THz. It is also interesting to find that, unlike the pristine Si NW, for both amorphous and polycrystalline Si NWs the low frequency vibrational modes (below 1.5 THz) which are considered as

the major contributor to the total thermal conductivity, do not undergo significant localization, while the vibrational modes in the middle and high frequency range have a quite strong localization. This phenomenon seems to conflict with the fact that the calculated thermal conductivity of these two kinds of NWs is quite low. Here, we have to emphasize that the vibrational modes in the low frequency region (below 2 THz), which usually have effective MFP larger than the average interatomic distance (AVD) and then can be defined as propagons (Larkin and McGaughey, 2014; Allen and Feldman, 1993; He, Donadio, and Galli, 2011), only contribute a small portion of the total thermal conductivity (detailed quantitative analysis can be found below) in the amorphous and polycrystalline Si NWs. The rest part of the thermal conductivity originates from the vibrational modes with propagation distance smaller than the AVD, named diffusons (Allen and Feldman, 1993), which contribute to the thermal conductivity by harmonic coupling with other modes. These diffusons are unusually located in the middle and high frequency range in bulk Si (He, Donadio, and Galli, 2011). Therefore, the strong localization of the vibrational modes in the middle and high frequency region of amorphous and polycrystalline Si NWs will lead to a large reduction of thermal conductivity [Figure 5.2]. Also, because of the even stronger localization of the vibrational modes (smaller $P(\vec{k}, \nu)$) in polycrystalline Si NWs as compared with amorphous Si NW, the much lower thermal conductivity of polycrystalline Si NWs can be understood.

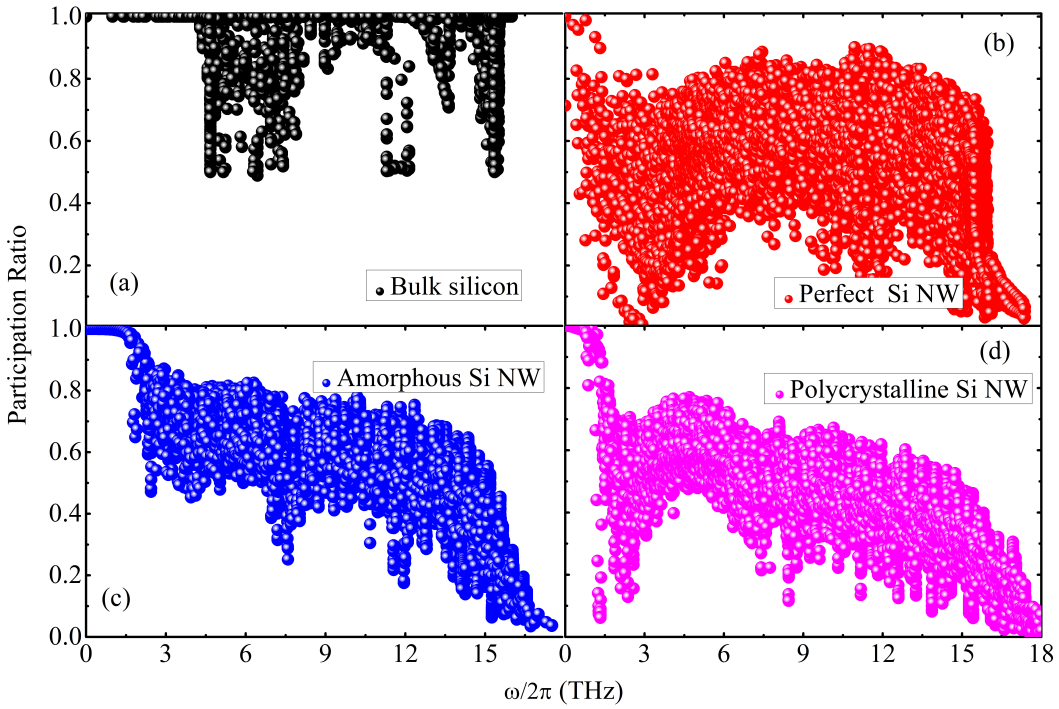


FIGURE 5.4: Comparison of the participation ratio among (a) bulk Si, (b) perfect Si NW, (c) amorphous Si NW and (d) polycrystalline Si NW. The cross-sectional size of all NWs is 5.442×5.442 nm^2 and the average grain size of the polycrystalline NW is 3.07 nm.

In order to understand the phonon transport mechanism in polycrystalline Si NWs more deeply, we calculate a more quantitative parameter: the effective mean free path of the heat carriers. We define effective MFP of a vibrational mode $(\vec{k}, \nu)$, as He *et. al.* (He, Donadio, and Galli, 2011) did before, by $\Lambda(\vec{k}, \nu) = \left|\vec{v}_g(\vec{k}, \nu)\right| \tau(\vec{k}, \nu)/3$, where $v_g(\vec{k}, \nu)$ and $\tau(\vec{k}, \nu)$ are the effective group velocity and lifetime of this vibrational mode. The effective group velocity $\vec{v}_g(\vec{k}, \nu)$ is computed by diagonalizing the dynamical matrix of the system and the lifetime $\tau(\vec{k}, \nu)$ is obtained using the time domain normal mode analysis (Zhou and Hu, 2015)

$$\tau(\vec{k}, \nu) = \int_0^{t^*} \left(\frac{\left\langle E(\vec{k}, \nu;\ t) E(\vec{k}, \nu;\ 0) \right\rangle}{\left\langle E(\vec{k}, \nu;\ 0) E(\vec{k}, \nu;\ 0) \right\rangle} \right) dt \tag{5.2}$$

where the upper integration limit t^* should be much longer than the lifetime of a specific phonon. The detailed method to calculate the total energy of each vibrational mode, $E(\vec{k}, \nu)$, can be found in Ref. (Zhou and Hu, 2015).

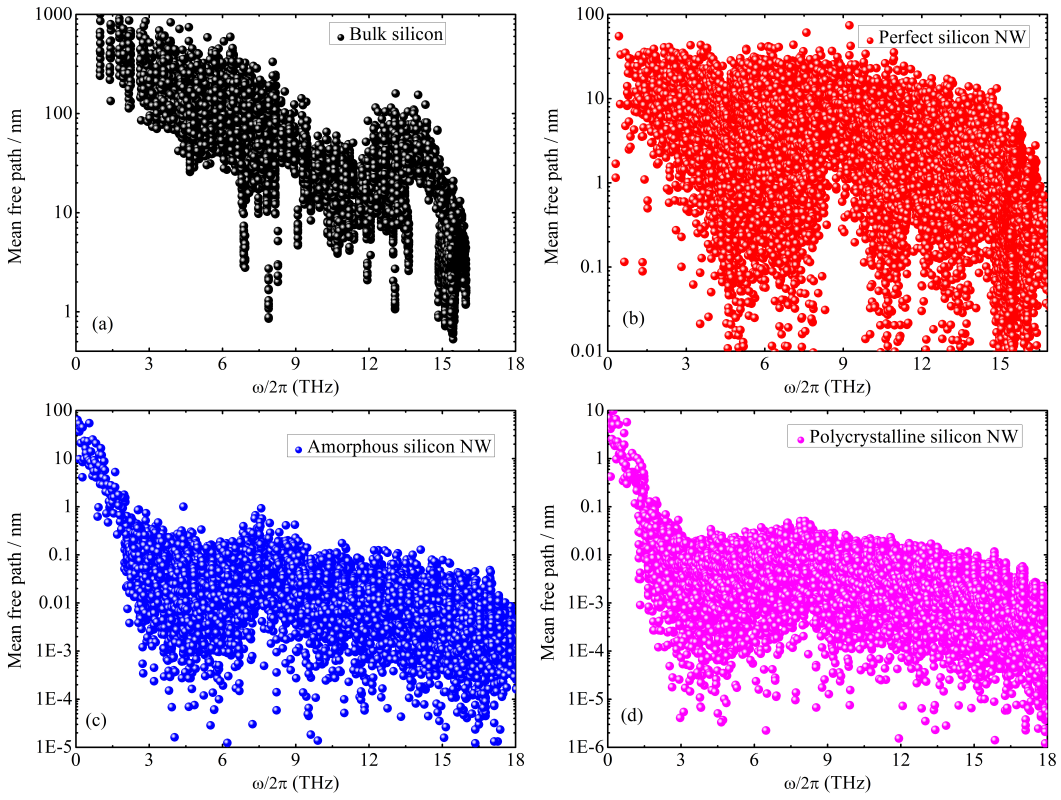


FIGURE 5.5: Comparison of the effective mean free path among (a) bulk Si, (b) perfect Si NW, (c) amorphous Si NW and (d) polycrystalline Si NW. The cross-sectional size of all NWs is 5.442 × 5.442 nm^2 and the average grain size of the polycrystalline NW is 3.07 nm.

From Figure 5.5a it is clearly observed that the effective MFP of the vibrational modes in bulk Si can be as large as 1 μm, while the extremely long MFP phonons (larger than 100 nm) will disappear in the perfect Si NW due to the phonon-nanowire

surface scattering [Figure 5.5b]. For amorphous Si NW [Figure 5.5c], although there are still a part of vibrational modes that can hold a relatively large effective MFP ($>$ 10 nm), the majority of the vibrational modes possess very small effective MFP (smaller than 0.1 nm) due to the strong inherent disorder of the amorphous structure. As for polycrystalline Si NW [Figure 5.5d], it is overjoyed to discover that the effective MFP of almost all vibrational modes (from 10^{-6} to 6.1 nm) approaches or is even smaller than the average grain size, which is about 3.07 nm for the case presented in Figure 5.5d. Here, we have to note that for the diffusons, the group velocity cannot be obtained by solving the dynamic matrix in which all the vibrations are assumed to be phonons (propagons). Therefore, the dramatic decrease of effective MFP around 3 THz should come from the fact that the group velocity is only accurate for the propagons [Figure 5.5]. For the diffusons with frequency larger than 3 THz, the method used in this letter to calculate the group velocity is questionable. Based on the definition of diffusons (He et al., 2011), it is feasible to choose the critical value (AVD here) to distinguish the diffusons and propagons. For the contribution of diffusons, we use the total thermal conductivity minus the contribution of propagons rather than obtain it directly. In addition, using the same method as in our paper, it is also found that the MFP is substantially lower than 0.5 nm when frequency is above 3 THz for bulk amorphous Si with the same Tersoff potential (Bodapati et al., 2006). Based on the above discussions, we know the thermal conductivity of polycrystalline Si NWs contributed by the propagons (detailed definition can be seen below, and the average MFP value of propagons is only 1.03 nm which is much shorter than the average grain size) can be well below the Casimir limit (Casimir, 1938). Here, if we assume all the vibrations are propagons, we can calculate the thermal conductivity of the Casimir limit and MD (contributed by propagons) roughly using (Zhou, Chen, and Hu, 2016)

$$\kappa_{Casimir\ limit\ or\ propagons\ in\ MD} = \frac{3}{(2\pi)^3}\int C_{ph} v_{sound} \Lambda_{grain_size\ or\ AMFP\ in\ MD} d\vec{k} \tag{5.3}$$

in which the C_{ph}, $\vec{k}$ and v_{sound} are the phonon specific capacity, phonon wave vector and sound velocity, respectively. Therefore, we can find the thermal conductivity of Casimir limit and propagons from MD simulation are 3.28 W/mK and 1.10 W/mK without considering the thermal resistance of grain boundaries, respectively. Furthermore, there is no surprise to find that thermal conductivity of MD simulation contributed by vibrations is much higher than the value calculated using the definition of propagons (see below for details), since we treat all the vibrations as phonons there. In Casimir model the direction-averaged MFP is $\lambda_{Casimir} = D$, where D is the wire diameter. Here, the boundary is assumed to be purely diffusive. This approach was then extended by Ziman (Ziman, 1960) who considered the effect of partly specular surfaces and yielded $\lambda_{Casimir} = D(1+P)/(1-P)$, in which P is the coefficient of specularity, ranging from 0 (diffusive) to 1 (mirror-like reflection). Here, we use the approximation formula of Casimir model and assume the grain boundaries are

purely diffusive. It is easy to find that this assumption will lead to a lower limit of the modified Casimir model ($P = 0$), which may underestimate the real value of Casimir limit. Meanwhile, it is reasonable to assume a purely diffusive phonon-boundary scattering in our polycrystalline NWs, since the grain boundaries here are quite disordered (see Figure 5.1c). Then, once our average MFP is lower than this lower bound of Casimir limit, we can safely conclude that our results are lower than the Casimir limit. Furthermore, the $\lambda_{Casimir}$ in this letter is taken as the average grain size rather than the diameter of NWs, and there is no defect inside the grain [Figure 5.1]. This means we compare the average MFP of phonons to the average grain size rather than the diameter of NWs. However, in our polycrystalline NWs, apart from the rough grain boundaries, which can be regarded as discontinuity caused by the different orientations of the grains and defects in the grain boundaries, phonon confinement and phonon backward scattering can be also introduced, since the grain size in our simulations is at the nano-scale and the grain boundaries can reflect the phonons somehow. Furthermore, unlike the single grain materials with boundary, the thermal conductivity of polycrystalline materials should be $\kappa = (1/\kappa_{grain} + R_{grain_boundary}/d)^{-1}$ (Yang et al., 2002), where κ_{grain}, $R_{grain_boundary}$ and d are the thermal conductivity of grain, thermal resistance at the grain boundary and the grain size, respectively. Therefore, the combined phonon-grain boundary scattering, phonon-nanowire surface scattering, phonon confinement and phonon backward scattering should be responsible for the phenomenon of the large thermal conductivity reduction mentioned above. Furthermore, as we know, the effective MFP is related to the effective group velocity and lifetime of a vibrational mode. Comparing with amorphous Si NWs, we find that the main reason for the decrease in the effective MFP for polycrystalline Si NWs resides in the large reduction of the phonon relaxation time, instead of the difference in phonon group velocity, which again indicates that there is extremely strong phonon scattering in the polycrystalline Si NWs. In addition, based on the single relaxation time approximation of Boltzmann transport equation (BTE), the lattice thermal conductivity κ_{BTE} can be calculated by

$$\kappa_{BTE} = \sum\nolimits_{(\vec{k},\ \nu)} c(\vec{k},\ \nu) v_{g,\ x}(\vec{k},\ \nu) \Lambda(\vec{k},\ \nu) \tag{5.4}$$

where $c(\vec{k}, \nu)$ is the specific heat per unit volume of a vibrational mode. According to the definition of $c(\vec{k}, \nu)$, one can know that the k_{BTE} only accounts for the propagating vibrational modes (propagons), whose effective MFP is substantially larger than the AVD. Here, we regard the AVD as 0.22 nm from the radial distribution function (RDF) of the structures. Then, we can define the contribution to the total thermal conductivity (κ_{total}) from the propagons as

$$\kappa_{propagons} = \sum_{\Lambda(\mathrm{k},\ \nu)\ >\ 0.22\ nm} c(\vec{k},\ \nu) v_{g,\ x}(\vec{k},\ \nu) \Lambda(\vec{k},\ \nu) \tag{5.5}$$

and the rest part of the thermal conductivity, which should originate from diffusons, can be computed by $\kappa_{total} - \kappa_{propagons}$. The total thermal conductivity is the value calculated using NEMD (polycrystalline Si NW) and GK-EMD (bulk Si, perfect and amorphous Si NWs) as plotted in Figure 5.2. In Figure 5.6, we draw the thermal conductivity as a function of effective mean free path. It is clearly seen that the contribution from theses vibrations with effective MFP smaller than 0.22 nm can be ignored if we assume these vibrations as phonons. The effective MFP dependent thermal conductivity curve shifts leftwards noticeably from bulk Si to pristine Si NW to amorphous Si NW and polycrystalline Si NW. The distinct difference between amorphous Si NW and polycrystalline Si NW resides in the effective MFP range of $\sim$0.2 nm – 3 nm. Recalling that the average grain size of the polycrystalline Si NW shown in Figure 6 is about 3.07 nm, it is safe to believe that the grain induced severe phonon scattering results in tremendous reduction in thermal conductivity of polycrystalline NW as compared with pure amorphous form. Figure 6 also indicates that for polycrystalline Si NW the phonon modes with effective MFP larger than the average grain size (or equivalently low frequency phonons) have higher modal thermal conductivity than those with shorter effective MFP, which is consistent with the analysis to the previous results [Figure 5.4]. We also compare the relative contribution to the total thermal conductivity from the propagons and diffusions among the four types of systems we studied [inset of Figure 5.6]. It can be found that, for bulk Si all the thermal conductivity are contributed by the propagons. For perfect Si NWs almost all of the thermal conductivity (as large as 99%) come from the propagons and the diffusons only contribute 1% of the total thermal conductivity. In amorphous Si NWs, the diffusons can contribute as large as 60% of the total thermal conductivity, which is in accordance with the conclusion of He *et. al.* (He, Donadio, and Galli, 2011) for bulk amorphous Si. More interestingly, we discover that the diffusions largely dominate the thermal transport in polycrystalline Si NWs (contribute 81% of total thermal conductivity) and the effect of propagons is strongly weakened.

Moreover, for amorphous Si depicted by Tersoff potential, He *et. al.* (He, Donadio, and Galli, 2011) find that the contribution of diffusons is about half of the total value (about 1.4-1.5 W/mK), which is in accordance with our result (around 1.4 W/mK) as well. We also calculate the thermal conductivity of bulk amorphous Si using GK-EMD and find that the thermal conductivity is 2.9$\pm$0.3 W/mK, which is also in accordance with He's result (He, Donadio, and Galli, 2011). Furthermore, using the same Tersoff potential, Donadio and Galli (Donadio and Galli, 2010) find that the contribution of diffusons in Si NW with amorphous layer is about 0.7 W/mK using the Allen-Feldman (AF) theory, which is in accordance with our result of polycrystalline Si NW (about 0.72 W/mK). It seems strange that the contribution of diffusons in Si NWs with amorphous layer and polycrystalline Si NWs is much lower than that in the pure amorphous structure. However, in our opinion, this difference should come from the fact that there are defects in the Si NWs with amorphous layer (in the region between the amorphous layer and crystalline Si NW) and polycrystalline

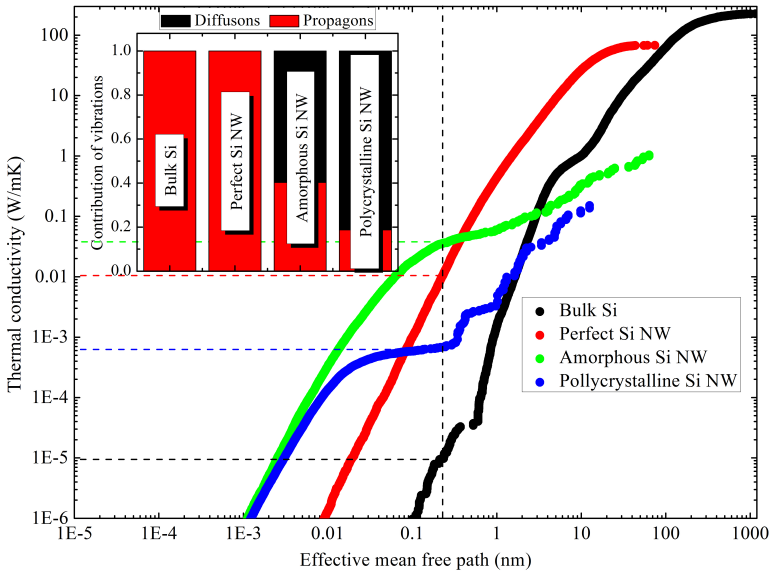


FIGURE 5.6: The thermal conductivity as a function of effective mean free path for bulk Si, perfect Si NW, amorphous Si NW and polycrystalline Si NW. The dashed line indicates the contribution from the vibrations with effective mean free path smaller than AVD (0.22 nm), below which we regard the vibration as diffusons. The cross-sectional size of the perfect crystalline NW, amorphous NW and polycrystalline NW is 5.442 $\times$ 5.442 nm^2 and the average grain size of the polycrystalline NW is 3.07 nm. (Inset) Comparison of the relative contribution to the total thermal conductivity of propagons and diffusions.

Si NW as pointed out earlier, which are quite efficient to decrease the contribution of both diffusons and propagons. Therefore, it is understandable that our results of thermal conductivity of polycrystalline Si NWs is lower than the diffuson part in the pure amorphous Si NW.

Now, an intuitive question that can be raised is, why is the polycrystalline structure so effective to suppress the propagation of propagons? It has been found that the amorphous Si is composed by a continuous network of strongly bonded tetrahedral structures (Larkin and McGaughey, 2014) [right panel of Figure 5.1b], and therefore the low frequency phonon-like vibrations (propagons) can transport easily. However, the structure of the grain boundary in polycrystalline Si is an interface between two grains and is discontinued [see red circles in the right panel of Figure 5.1c]. Then, the propagons can be easily "blocked" by the grain boundaries. Moreover, the backward scattering among propagons can be introduced by the grain boundaries as well. Thus, the propagons in the polycrystalline Si will be scattered quite strongly due to the incorporation of the grain boundaries.

Another intuitive question is: what is the lowest possible thermal conductivity of Si NWs? The only way to further reduce the thermal conductivity of these two kinds of disordered Si NWs (amorphous and polycrystalline) is through completely

eliminating the contribution of propagons, since diffusons are caused by the inherent structural disorder and thus cannot be eliminated. It has been proved that the propagons that can appear in the disordered Si are primarily due to the strong interatomic interactions among Si atoms (Larkin and McGaughey, 2014). Therefore, alleviating the interaction strength of the Si-Si bonds in amorphous Si is helpful for decreasing the thermal conductivity of amorphous Si further. For instance, Lakin *et. al.* (Larkin and McGaughey, 2014) find the contribution of propagons to thermal conductivity in silica is only 6% due to the weaken bond that exists between the SiO4 tetrahedra with respect to that in the diamond-like bulk Si. In contrast, for polycrystalline Si NWs there are some other possibilities to further suppress or even totally eliminate the contribution of propagons, e.g. by introducing "disorder" inside the grains. If we assume the contribution of diffusons will not be affected when dealing with propagons, the thermal conductivity of amorphous and polycrystalline Si NW can be further reduced to about 60% and 81% of their original value [Figure 5.6], respectively. This means that the thermal conductivity of such kind of polycrystalline Si NW contributed by propagons can be markedly lower than the Casimir limit after some internal treatment for the grains, such as incorporating nanotwinned structures inside the grains. This method could be more effective than the approach of digging deep cavities on the NW's surface proposed by Carrete *et. al.* (Carrete et al., 2011). It is also worth mentioning that such longing nanotwinned structures have already been realized in experiments (Huang et al., 2014) recently.

Before closing, we would like to emphasize that the strength of scattering of propagons depends on the continuity of structures rather than disorderedness. Actually, for bulk amorphous Si, the MFP of propagons can be as large as 1 μm (He, Donadio, and Galli, 2011), which means the scattering in bulk amorphous Si is not so strong. In fact, for the amorphous structures, the structure disorder will determine whether the propagons can appear in such structures, since the propagons need to satisfy the requirement of plane wave (such as wavelength). For instance, when the strength of interatomic bonding is weak (such as SiO2), there will be no propagons since it is difficult to satisfy the wavelength of propagons (the vibrations of one atom cannot transport energy to another atom which holds a distance of half wavelength from it). For the polycrystalline structure of Si, the propagons in the entire frequency range can appear, and will be scattered by the grain boundaries due to the discontinuity between perfect crystals and grain boundaries. Thus, the mechanism of decreasing the contribution of propagons in polycrystalline Si NW and amorphous Si NW is inherently different. In addition, it is worth pointing out that, even without considering the contribution of propagons, the thermal conductivity of polycrystalline Si NWs (0.69 W/mK) is still evidently lower than that for the amorphous counterpart (1.81 W/mK). This is because there are some defects [Figure 5.1c] existing in the grain boundaries due to the discontinuity of the neighboring grains, which can also affect the thermal transport of diffusons. It is also worth noting that, when the grain size is extremely small (e.g. less than $\sim$2 nm), the polycrystalline

structure can be regarded as small crystallites embedded in an amorphous matrix as well, while for large grain sizes the structures are well-defined polycrystalline structures. It is well known that the ZT coefficient largely depends on the electrical conductivity and Seebeck coefficient. For polycrystalline Si NWs, the electrical conductivity should depend on the two competitive mechanisms, since both crystalline filler and amorphous "matrix" exist in the polycrystalline Si NWs. According to the recent experimental results (Hochbaum et al., 2008), introducing the amorphous structure in Si NW (such as shell) may have a more strong impact on thermal conductivity than electrical conductivity. Therefore, polycrystalline Si NWs may be a good candidate for thermoelectric material. Moreover, Y. Nakamura *et. al.* (Nakamura et al., 2015) experimentally find that the electrical properties of Si nanocrystals with oriented crystals separated by amorphous layer will not change with respect to bulk Si when the amorphous layer (analog with grain boundaries in our paper) is thin for the crystals embedded in the amorphous matrix. Certainly, enhancement of ZT coefficient of thermoelectrics requires synergetic optimization of both electrical and phononic transport properties.

5.3 Improving the Thermoelectric Performance via Decreasing the Thermal Conductivity

It is popularly known that Si based materials are promising candidates for thermoelectrics due to their low-cost, environmentally friendly and wide usage in the semiconductor industries (Venkatasubramanian et al., 2001; Poudel et al., 2008b). However, the ZT of bulk crystalline Si is quite low: only about 0.004 (Mangold, Neogi, and Donadio, 2016). Nanostructuring Si using the form of NW (Hochbaum et al., 2008; Boukai et al., 2008; Vo et al., 2008), membrane (Mangold, Neogi, and Donadio, 2016), alloy (Yu et al., 2012; Wang et al., 2008b; Minnich et al., 2009a; Bera et al., 2010) and SL (Koga et al., 2000; Hinsche, Mertig, and Zahn, 2011), poly-crystallization (Nakamura et al., 2015; Valalaki, Vouroutzis, and Nassiopoulou, 2016) can increase the ZT to as large as $0.03 \sim 0.6$ at room temperature. The huge enhancement of ZT coefficient of these nanostructures is mainly benefited from the significant reduction of lattice thermal conductivity which is caused by the strong phonon-boundary scattering. However, in all of these nanostructures, the lattice thermal conductivity is still higher than the amorphous limit, which is generally regarded as the lowest thermal conductivity of a material in common sense. Most recently, we found that the thermal conductivity of polycrystalline structure can break the amorphous limit when the grain size is small, e.g., below 3 nm (Zhou and Hu, 2016). At the same time, the electrical transport properties can be modulated via nanostructuring as well. It indicates that it may be possible to decrease the lattice thermal conductivity to an extremely low value while keep the power factor at the bulk comparable level. Therefore, it may still have some space to further increase the ZT of Si-based materials.

Motivated by this idea, in this section, we design two new advanced structures: SiGe superlattice and anti-superlattice nanocrystalline heterostructures (SL-NC HS and ASL-NC HS) based on the polycrystalline and superlattice structure, both of which have already been fabricated in experiments (Schuberth et al., 1991; People et al., 1984; Ismail et al., 1993). With the help of such strategy, we can then obtain much lower thermal conductivity of such heterostructures than that of polycrystalline Si with same grain size (only 50 %), and gain an extremely low thermal conductivity for these Si based SL (ASL) nanostructures with a relative large grain size due to the significant strong phonon-boundary and phonon Si-Ge interface scattering. For instance, the thermal conductivity of the poly-structures with SiGe-ASL inside the grains (grain size is around 8 nm) can be as low as about 1.3 W/mK (only 43% of the amorphous limit). Meanwhile, the PF of such nanostructures can be comparable to that of the bulk crystalline Si by modulating the periodic length (λ) of the SL or ASL structure inside the grains. As a result, for the limit grain size (around 1 nm) that is achievable in experiments (Zhou et al., 2012), the ZT coefficient of such NC HSs can be as large as around 0.5 at room temperature, which is the highest value in Si-based bulk structures. Even for the medium grain size (above 5 nm) which is quite easy to fabricate in experiments (Schuberth et al., 1991; People et al., 1984; Ismail et al., 1993), the ZT value is still as large as around 2 time of thermoelectric performance of the existing bulk Si-based nanostructures.

5.3.1 Computational details and theory framework

Computational details: The SL- and ASL-NC HS [Figure 5.7] are constructed by using Voronoi algorithm (details can be found in our previous paper [31]). The nanocrystalline (NC) Si [Figure 5.7a] is used as comparison and studied in this paper as well. The grain size of all the Si based nanostructures in this paper ranges from $\sim$3 to 8 nm, which can be fabricated in experiments easily right now (Feser et al., 2013; Yu et al., 2016; Wang et al., 2008a; Wu et al., 2004b; Singh et al., 2006; Wu, 2004; Sumiya and Irifune, 2007). All the models have the same length (31 nm) and width (31 nm), and the various thickness ranging from 1.2 nm to 5.0 nm. Periodic boundary conditions are applied along the length and width direction, while free boundary conditions are used along the thickness direction. It indicates that the model used in our study is actually a membrane. All the simulations on thermal transport properties reported below are run with interatomic interaction of Tersoff potential (Tersoff, 1989) and the thermal conductivity is calculated using GK-EMD simulations (details can be found in Ref. (Zhou and Hu, 2016)). It is worth noting that, using the Tersoff potential will overestimate the thermal conductivity of bulk crystalline Si: around 200 W/mK calculated by Tersoff potential at room temperature compared to experimental value of 156 W/mK (Glassbrenner and Slack, 1964). Such overestimation is mainly caused by the distortion of the acoustic phonon branches calculated using Tersoff potential. However, for the nanostructures, the phonon-boundary or surface scattering will become the dominant scattering mechanism that determines

the total thermal conductivity, and therefore, the thermal conductivity computed using semi-empirical (Tersoff potential) will not lead to a big error since the group velocity calculated by Tersoff potential is similar to the real values. Another point we need to pay attention to is that the phonon follows the Boltzmann distribution in classical MD simulations rather than Bose-Einstein distribution (the real distribution in experiments). However, we use a full spectrum model (Zhou, Chen, and Hu, 2016) with the correct Bose-Einstein distribution of phonons and find that the quantum effects on the results of MD simulations above 300 K can be actually ignored. Furthermore, Turney *et. al.* (Turney, McGaughey, and Amon, 2009) prove that, for Si materials, applying the quantum corrections to the classical predictions does not bring them into better agreement with the quantum predictions as compared with the uncorrected classical values above temperature of 200 K, which also shows that the quantum effect for Si can be ignored when the system temperature is higher than 300 K. In order to calculate the electrical transport properties, we assume that the band structure of the nanostructure is the same as that of its perfect grain, and the grain boundary only affects the relaxation time of carrier (details will be discussed below). Such an assumption is quite popular when the electrical properties of nanostructures are calculated (Minnich et al., 2009a; Zhou et al., 2010). The band structures of the bulk Si, SiGe SL and ASL [Figure 5.7c-d] are calculated using the Vienna ab-initio simulation package (VASP) based on the DFT (Kresse and Furthmüller, 1996). The pseudopotentials contain s^2p^2 as valence states with the LDA in the Project-Augmented-Wave (PAW) exchange-correlation function are used to describe the Si and Ge atoms, respectively. A plane-wave basis is employed with kinetic energy cutoff of 320 eV for Si and Ge. The lattice constant and the geometry of the systems are first optimized until the energy difference and the Hellman-Feynman force are converged within eV eV and 5 $\times 10^{-3}$ eV/Å respectively, using a 4 $\times$ 4 $\times$ 4 to 10 $\times$ 10 $\times$ 10 shifted Monkhorst-Pack mesh of points to sample the first Brillouin zone. Then, the electrical transport properties of the bulk Si, SiGe SL and ASL are calculated using the BoltzTrap code (Madsen and Singh, 2006) based on the semi-classical Boltzmann transport equation (BTE). In order to ensure the accuracy of the Kohn-Sham eigenvalues which are used as input in the BoltzTrap code, we employ a very dense points mesh of 15 $\times$ 15 $\times$ 15. Then, the electrical transport of the NC HSs can be obtained based on BTE (see details below).

Theory framework: Solving phonon BTE using the relaxation time approximation (Srivastava, 1990) yields the expression of modal thermal conductivity $\kappa_{phonon}(\vec{k},\ \nu)$ (Turney et al., 2009)

$$\kappa_{phonon}(\vec{k},\ \nu) = c_{phonon}(\vec{k},\ \nu)\left|\vec{v}_{phonon,\ x}(\vec{k},\ \nu)\right|^2 \tau^{phonon}_{tot,\ membrane\ or\ bulk}(\vec{k},\ \nu) \tag{5.6}$$

The phonon group velocity $\vec{v}_{phonon}(\vec{k},\ \nu)$ can be obtained from lattice dynamics and the volume specific heat $c_{phonon}(\vec{k},\ \nu)$ can be calculated by $c_{phonon}(\vec{k},\ \nu) = k_b/\mathrm{V}$, in which k_b and V is the Boltzmann constant and system volume, respectively. The

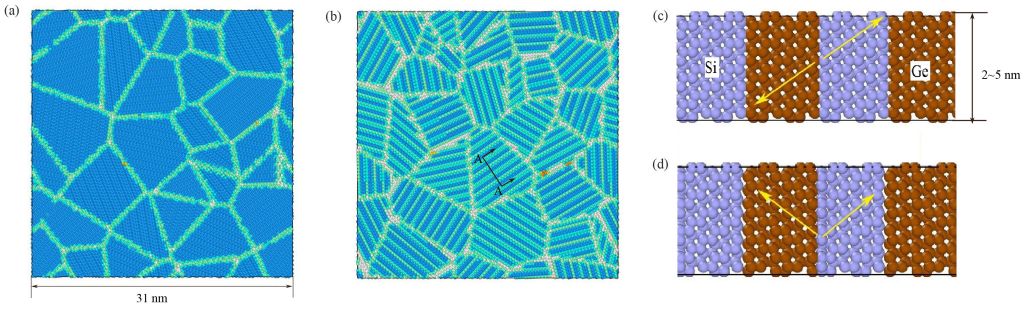


FIGURE 5.7: Snapshot of (a) polycrystalline Si and (b) SiGe superlattice or SiGe anti-superlattice nanostructures. The schematic of SiGe superlattice (c) and SiGe anti-superlattice (d), where Si and Ge atoms are shown in different color.

modal relaxation time can be calculated using the Matthiessen's rule

$$\frac{1}{\tau^{phonon}_{tot,\,membrane}(\vec{k},\,\nu)} = \frac{1}{\tau^{phonon}_{in}(\vec{k},\,\nu)} + \frac{1}{\tau^{phonon}_{surf}(\vec{k},\,\nu)} + \frac{1}{\tau^{phonon}_{GB}(\vec{k},\,\nu)} \tag{5.7}$$

and

$$\frac{1}{\tau^{phonon}_{tot,\,bulk}(\vec{k},\,\nu)} = \frac{1}{\tau^{phonon}_{in}(\vec{k},\,\nu)} + \frac{1}{\tau^{phonon}_{GB}(\vec{k},\,\nu)} \tag{5.8}$$

in which $\tau^{phonon}_{tot}(\vec{k},\,\nu)$ is the total relaxation time of the specific phonon $(\vec{k},\,\nu)$, $\tau^{phonon}_{in}(\vec{k},\,\nu)$, $\tau^{phonon}_{surf}(\vec{k},\,\nu)$ and $\tau^{phonon}_{GB}(\vec{k},\,\nu)$ are the relaxation time induced by inherent phonon-phonon scattering, phonon-surface and phonon-grain boundary scattering, respectively. Here, the inherent phonon relaxation time $\tau^{phonon}_{in}(\vec{k},\,\nu)$ is calculated by the time domain normal mode analysis (TDNMA) (Zhou and Hu, 2015; Zhou, Zhang, and Hu, 2015)

$$\tau^{phonon}_{in}(\vec{k},\,\nu) = \int_0^{t^*} \left(\frac{\left\langle E(\vec{k},\,\nu;\,t)E(\vec{k},\,\nu;\,0) \right\rangle}{\left\langle E(\vec{k},\,\nu;\,0)E(\vec{k},\,\nu;\,0) \right\rangle} \right) dt \tag{5.9}$$

where the upper integration limit t^* should be much longer than the lifetime of the specific phonon. The total energy of each phonon mode, $E(\vec{k},\,\nu)$, is calculated from

$$E(\vec{k},\,\nu;\,t) = \frac{1}{2}\omega^2(\vec{k},\,\nu)Q(\vec{k},\,\nu;\,t)Q^*(\vec{k},\,\nu;\,t) + \frac{1}{2}\dot{Q}(\vec{k},\,\nu;\,t)\dot{Q}^*(\vec{k},\,\nu;\,t) \tag{5.10}$$

where $Q(\vec{k},\,\nu)$, $\dot{Q}(\vec{k},\,\nu)$ and $\omega(\vec{k},\,\nu)$ are the normal mode coordinate, velocity and frequency of the specific phonon $(\vec{k},\,\nu)$, respectively. More details about TDNMA can be found in Ref. (Zhou, Zhang, and Hu, 2015).

Using the momentum-dependent specularity $P(\vec{k})$ with considering the surface

or grain boundary roughness, we can find modal relaxation time due to phonon-surface and phonon-grain boundary as

$$\tau_{surf}^{phonon}(\vec{k},\ \nu) = \left[\frac{1+P_{surf}(\vec{k})}{1-P_{surf}(\vec{k})}\right]\frac{L}{v_{phonon}^{\perp}(\vec{k},\ \nu)} \tag{5.11}$$

$$\tau_{GB}^{phonon}(\vec{k},\ \nu) = \left[\frac{1+P_{GB}(\vec{k})}{1-P_{GB}(\vec{k})}\right]\frac{D}{v_{phonon}^{\parallel}(\vec{k},\ \nu)\ or\ v_{phonon}(\vec{k},\ \nu)} \tag{5.12}$$

in which, $v_{phonon}^{\perp}(\vec{k},\ \nu)$ and $v_{phonon}^{\parallel}(\vec{k},\ \nu)$ are the component of phonon group velocity $\vec{v}_{phonon}(\vec{k},\ \nu)$ normal and parallel to the surface, respectively. L and D are the thickness of the membrane and average size of grain. Based on the expression of relaxation time of phonon (carrier)-surface (grain boundary), we can know that, $P(\vec{k}) = 0$ means a very rough surface and can be regarded as the fully diffusive boundary scattering. The ideal smooth surface will have $P(\vec{k}) = 1$. For boundary with root mean square (RMS) height of roughness Δ, the parameter $P(\vec{k})$ is calculated as (Haile, 2014; Aksamija and Knezevic, 2010)

$$P(\vec{k},\ \nu) = \exp(-4|\vec{k}|^2\Delta^2 cos^2\phi) \tag{5.13}$$

where ϕ is the angle between the carrier (phonon) wave vector and the direction vector of the surface or grain boundary. On the other side, all the models used in our simulations have the (110) surface, the root mean square of surface roughness is 0.125 nm in our theoretical model, which is determined by various different orientation surface of Si NWs [Figure 5 in Ref. (Zhou, Chen, and Hu, 2016)]. For the grain boundary, we assume it is a very rough surface, i.e. $P(\vec{k}) = 0$, which has been proved to be a quite good approximation (see results below).

To calculate the electronic transport properties, the most popular approach assumes that the electronic band structure is unchanged with doping and only the Fermi level is shifted. Based on the electronic BTE theory, we have

$$\sigma_{\alpha\beta}(T;\ \mu) = \frac{1}{\Omega}\int \Pi_{\alpha\beta}(\xi)\left[-\frac{\partial N_0^{F-D}(T;\ \mu)}{\partial\xi}\right]d\xi \tag{5.14}$$

$$\kappa_{\alpha\beta}^{electron}(T;\ \mu) = \frac{1}{e^2T\Omega}\int \Pi_{\alpha\beta}(\xi)(\xi-\mu)^2\left[-\frac{\partial N_0^{F-D}(T;\ \mu)}{\partial\xi}\right]d\xi \tag{5.15}$$

$$S_{\alpha\beta} = \frac{1}{eT\Omega\sigma_{\alpha\beta}(T;\ \mu)}\int \Pi_{\alpha\beta}(\xi)(\xi-\mu)\left[-\frac{\partial N_0^{F-D}(T;\ \mu)}{\partial\xi}\right]d\xi \tag{5.16}$$

where α and β are the Cartesian indices, Ω, e, μ, T and N_0^{F-D} are the volume of the unit cell, electron charge, the Fermi level, the temperature and the Fermi-Dirac distribution function of electrons, respectively. $\Pi_{\alpha\beta}(\xi)$ is the transport distribution

function and can be written as

$$\Pi_{\alpha\beta}(\xi) = \frac{1}{N}\sum_{i,\,\vec{k}} e^2 \tau^{carrier}_{total,\,membrane\ or\ bulk} v_\alpha(\vec{k},\,i) v_\beta(\,\vec{k},\,i) \left[-\frac{\delta(\xi - \xi_{\vec{k},\,i})}{d\xi}\right] \tag{5.17}$$

in which, N is the number of k-points sampling, i is the band index. ν and $\tau^{carrier}_{total}$ are group velocity which can be calculated from the band structure and the total relaxation time of electrons, respectively. It is usually assumed that the band structure of the grain is the same as its bulk counterpart (Minnich et al., 2009a; Zhou et al., 2010). Then, the total relaxation time can be obtained using the Matthiessen's rule which assumes that the scattering events are independent with each other

$$\frac{1}{\tau^{carrier}_{tot,\,membrane}} = \frac{1}{\tau^{carrier}_{in}} + \frac{1}{\tau^{carrier}_{surf}} + \frac{1}{\tau^{carrier}_{GB}} \tag{5.18}$$

and

$$\frac{1}{\tau^{carrier}_{tot,\,membrane}} = \frac{1}{\tau^{carrier}_{in}} + \frac{1}{\tau^{carrier}_{GB}} \tag{5.19}$$

where $\tau^{carrier}_{in}$, $\tau^{carrier}_{surf}$ and $\tau^{carrier}_{GB}$ are the carrier (hole or electron) relaxation time due to inherent carrier scattering, carrier-surface and carrier-grain boundary scattering, respectively. The inherent relaxation time of carrier should include effect of several scattering mechanisms: the carrier-impurity scattering, carrier-longitude polar optical phonon scattering, carrier-deformation acoustic and optical phonon scattering. Here, we obtain the inherent relaxation time of carrier by fitting the experimental results (Appendix C)) rather than calculating it directly. For the carrier-surface and phonon-grain boundary relaxation time, we apply the same method as we did above for the phonons, and we have

$$\tau^{carrier}_{surf}(\vec{k},\,i) = \left[\frac{1 + P_{surf}(\vec{k})}{1 - P_{surf}(\vec{k})}\right] \frac{L}{v^{\perp}_{carrier}(\vec{k},\,i)} \tag{5.20}$$

$$\tau^{carrier}_{GB}(\vec{k},\,i) = \left[\frac{1 + P_{GB}(\vec{k})}{1 - P_{GB}(\vec{k})}\right] \frac{D}{v^{||}_{carrier}(\vec{k},\,i)\ or\ v^{||}_{carrier}(\vec{k},\,i)} \tag{5.21}$$

in which, $v^{\perp}_{carrier}(\vec{k},\,i)$ and $v^{||}_{carrier}(\vec{k},\,i)$ are the component of carrier group velocity normal and parallel to the surface, respectively. Then, the carrier-surface and carrier-grain boundary relaxation time are obtained by averaging over all carrier momenta

$$\tau^{carrier}_{surf} = \frac{\int \tau^{carrier}_{surf}(\vec{k},\,i) N_0^{F-D}\left[\xi(\vec{k},\,i)\right] d^3\vec{k}di}{\int N_0^{F-D}\left[\xi(\vec{k},\,i)\right] d^3\vec{k}di} \tag{5.22}$$

$$\tau^{carrier}_{GB} = \frac{\int \tau^{carrier}_{GB}(\vec{k},\,i) N_0^{F-D}\left[\xi(\vec{k},\,i)\right] d^3\vec{k}di}{\int N_0^{F-D}\left[\xi(\vec{k},\,i)\right] d^3\vec{k}di} \tag{5.23}$$

Finally, the thermal conductivity, power factor and ZT coefficient for the nanostructured Si based on SLs and ASLs can be obtained from Eq. 5.6, Eq. 5.14-5.16.

5.3.2 Results and discussions

Understanding the bulk comparable power factor of the Si heterostructures: It is easy to know that the computed electrical transport properties (Seebeck coefficient, electrical conductivity and electronic thermal conductivity) should be direction dependent for the SL and ASL NC HSs [Figure. 5.8a-c] because of the un-equivalent crystal orientations along the three directions. However, for the nanostructure we studied here, it is appropriate to regard it as a homogenous material in the in-plane directions. Thus, the results are the average of the electrical transport properties along two in-plane directions. Figure. 5.8 shows the calculated S, σ, $\kappa_{electron}$ and the PF ($S^2\sigma$) of the bulk crystalline Si, NC Si, SiGe SL-NC and ASL-NC HSs as a function of carrier density. Here, we only plot the case of N-doping (or hole doping), as P-doping can be analyzed in the similar way. It is well-known that the Seebeck coefficient can be increased by the SL structures due to the quantum confinement effect which is caused by band converge (Hicks and Dresselhaus, 1993a; Hicks and Dresselhaus, 1993b; Broido and Reinecke, 2000; Broido and Reinecke, 1995). On the other hand, the reduced band gap caused by the lattice mismatch between Si and Ge compared to its bulk counterpart will decrease the Seebeck coefficient. Therefore, the Seebeck coefficient S of the SL based nanostructures studied here is actually determined by two competing mechanisms: the confinement effect and the reduction of band gap. Then, it is not surprising to observe an enhancement of S for SiGe SL-NC HS [Figure. 5.8a] with short λ, for example, $\lambda = 3.9$nm inside the grains (denoted as SiGe SL-NC HS-1) compared to the bulk Si due to the large band converge number. For the large periodic length SiGe SL nanostructures with $\lambda = 7.8$nm (denoted as SiGe SL-NC HS-2), we can find the S is decreased with respect to the bulk counterpart [Figure. 5.8a], which indicates the reduction of band gap is the dominant reason for the Seebeck coefficient. For the nanostructures with SiGe ASL inside grains (denoted as SiGe ASL-NC HS-1 and SiGe ASL-NC HS-2), the Seebeck coefficient of both cases decreases with respect to the bulk crystalline Si [Figure. 5.8a]. This indicates that the reduction of band gap is the dominant mechanism that affects the Seebeck coefficient in these systems. Furthermore, when the periodic length of SiGe SL or SiGe ASL is larger than 7.9 nm, it is interesting to find the valence and conduction band cross each other around the Gamma point, which indicates the SiGe SL and SiGe ASL with large λ will become metallic. Such phenomenon is in accordance with Riccardo et. al.'s finding (Amato and Rurali, 2015): the residual strain will change the band gap strongly, and then make the semiconductor become metallic. Here, we only focus on the cases when the band gap is larger than zero, since the PF of the cases with band gap smaller than zero is quite small and leads to a quite low thermoelectric power and a low figure of merit. At the relatively low carrier density (below about $3.2 \times 10^{19} cm^{-3}$ for SiGe SL-NC HSs and smaller than around

$1.6 \times 10^{19} cm^{-3}$ for SiGe ASL-NC HSs), the SL nanostructures with longer periodic length have higher electrical conductivity due to the narrower band gap [Figure. 5.8b]. When the carrier density increases, which indicates that more activated electron state can exist in the system, the electrical conductivity of the SL nanostructures with shorter periodic length is larger than that with longer periodic length, because of the larger Seebeck coefficient which indicates the average energy of electrical carriers is higher (Minnich et al., 2009a). Following the Wiedemann-Franz law (Jonson and Mahan, 1980), the electronic thermal conductivity should have the similar trend with electric conductivity [Figure. 5.8c]. It is worth noting that the $\kappa_{electron}$ which is popular to be ignored for the Si-based NC HSs should be taken into consideration, since the value of $\kappa_{electron}$ is at the same level with κ_{phonon} (the detailed value can be found below). Due to the combined effect of Seebeck coefficient and electrical conductivity, the maximum PF of NC Si, SiGe SL-NC and SiGe ASL-NC HSs will reach around 0.8, 0.6 and 0.57 of the optimal PF of the bulk Si [Figure. 5.8d].

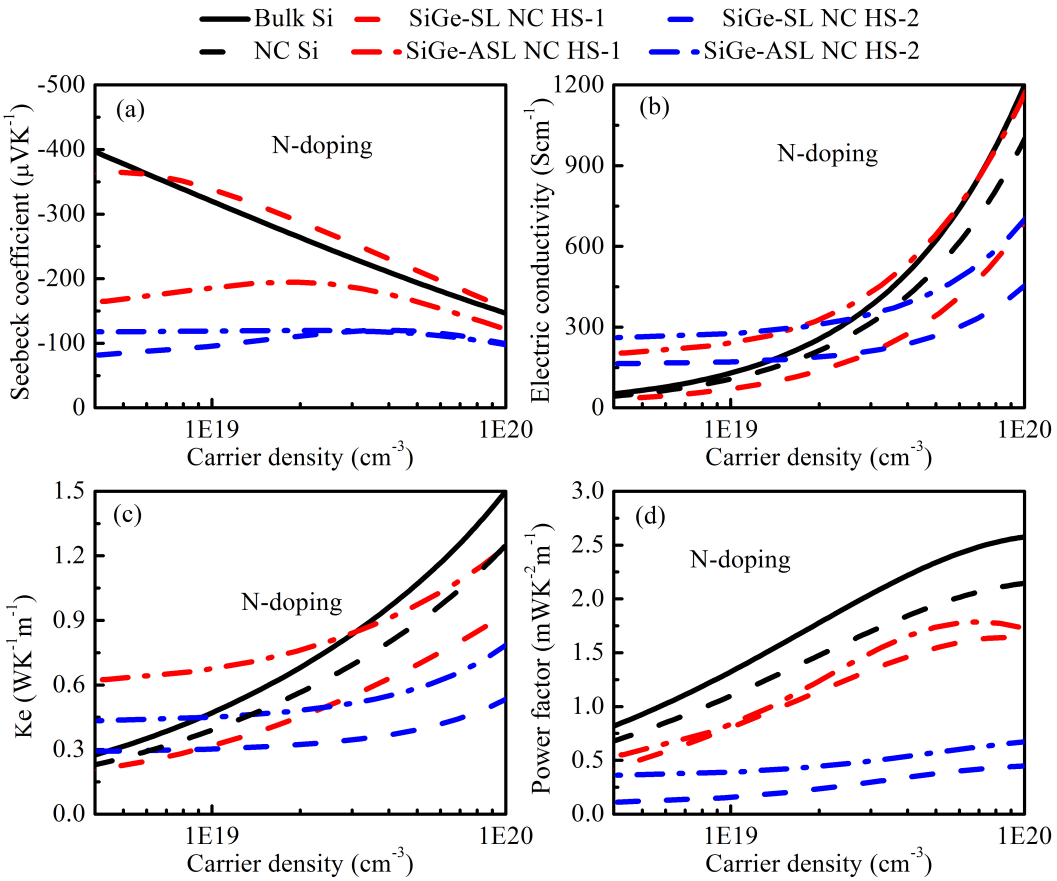


FIGURE 5.8: (a) Seebeck coefficient, (b) electric conductivity, (c) electronic contribution to the thermal conductivity, and (d) the power factor, as a function of the carrier density at room temperature.

Next, we turn our attention to the influence of grain size on the electrical transport properties [Figure. 5.9]. It is easy to find the Seebeck coefficient (Eq. 5.16) is independent on the carrier relaxation time, since $\tau_{total}^{carrier}$ is only related to the Fermi

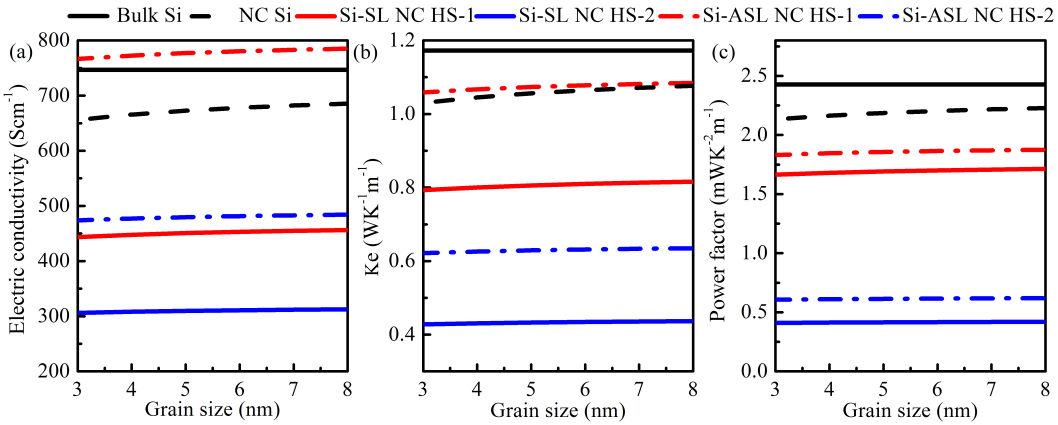


FIGURE 5.9: (a) Electric conductivity, (b) electronic contribution to the thermal conductivity, and (c) the power factor at room temperature, as a function of the grain size with a fixed carrier density of $6 \times 10^{19} cm^{-3}$ and a fixed layer thickness of around 3 nm.

level μ and then the $\tau_{total}^{carrier}$ in Eq. 5.16 can be removed. Here, in order to study the grain size independently, we fix the layer thickness of our models at 3 nm and the carrier density at $6 \times 10^{19} cm^{-3}$. From the results [Figure. 5.9a and 5.9b], we can know the grain size has a stronger influence on NC Si than that on other cases. From the band structures, we know the electron group velocity of Si at middle location of the valence band will be much larger than that of nanostructures with SiGe SL and ASL due to the much larger slope of band dispersion. It is also worth noting that σ, $\kappa_{electron}$ and PF are affected by the grain size weakly. From our computational results, we find that the carrier relaxation time and the carrier group velocity is on the order of 0.01 ps and 100 nm/ps, respectively. It indicates the mean free path (MFP) of carrier will be on the order of 1 nm which is much smaller than the grain size. Therefore, the carrier-boundary or carrier surface scattering is not so important for the cases here. The similar phenomena are found for the effect of layer thickness.

Analyzing the ultra-low lattice thermal conductivity of the Si heterostructures: In order to investigate the grain size effect on lattice thermal conductivity, again we fix the thickness of membrane at 3 nm. For the polycrystalline Si, we find the lattice thermal conductivity by both the MD results and theoretical predictions is comparable or smaller than the amorphous limit of Si [Figure. 5.10], which are generally thought to be the lowest thermal conductivity of Si, when the grain size is smaller than 4.5 nm due to the extremely strong phonon boundary scattering (see discussion below). Such phenomenon is in accordance with our pervious theoretical study (Zhou and Hu, 2016) and experiment (Feser et al., 2013): the strong phonon boundary scattering will lead the thermal conductivity of a material breaks its amorphous limit. With the grain size further increasing (larger than 5 nm), the lattice thermal conductivity becomes higher than the amorphous limit and increases to a relatively large value (around 5 W/mK for the grain size of around 8 nm) due to the weakened

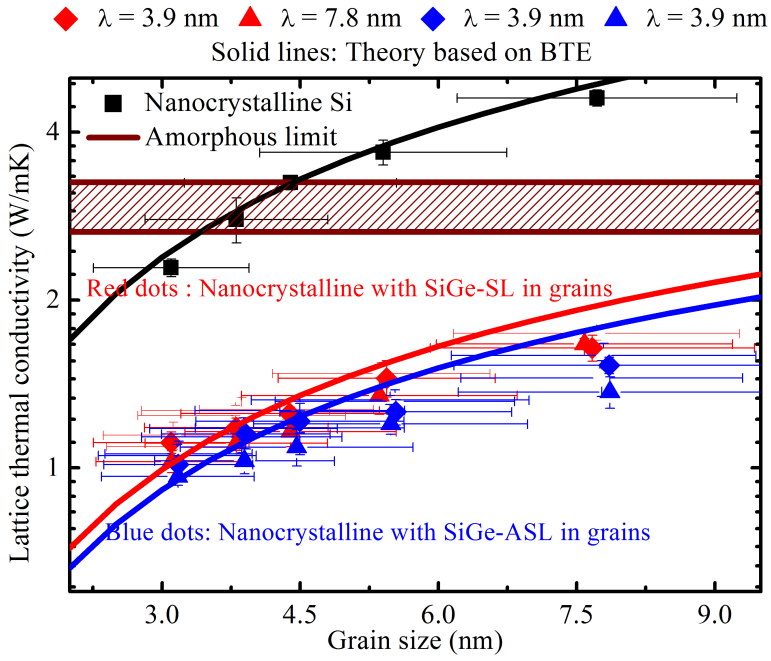


FIGURE 5.10: The lattice thermal conductivity calculated by MD simulations and predicted by theory based on phonon BTE.

effect of phonon boundary scattering. Such large thermal conductivity has a negative effect on gaining high ZT values. However, for the nanostructures with SiGe SL and ASL in grains, the thermal conductivity will be further strongly decreased with respect to the polycrystalline Si due to the further phonon boundary scattering at the Si-Ge interfaces inside the grain. Assuming the grain size is 1 nm which is thought to be limit grain size in experiments (Yu et al., 2016), from our theoretical predictions, the thermal conductivity of polycrystalline Si and nanostructures with SiGe SL or SiGe ASL is only around 1.5, 0.5 and 0.45 W/mK, respectively. In addition, based on our theory, it is easy to find the thermal conductivity of the nanostructures with SiGe SL or ASL in grains can be smaller than the amorphous limit even when the grain size is around 10 nm, which is quite easy to be fabricated in experiments (Feser et al., 2013; Yu et al., 2016; Wang et al., 2008a; Wu et al., 2004b; Singh et al., 2006; Wu, 2004; Sumiya and Irifune, 2007).

Next, we choose two grain sizes (3.8 nm and 5.5nm) to study the effect of thickness of the membrane on the lattice thermal conductivity. It is easy to find the thermal conductivity of NC Si will increase a little with the membrane thickness increasing [Figure. 5.11]. For the larger grain size (5.5 nm), the thickness dependence will be stronger due to the decrease of phonon boundary scattering. However, for the nanostructures with SiGe SL or SiGe ASL in grains, it is not surprising to find that the thermal conductivity is independent on the thickness due to the additional strong phonon scattering at the Si-Ge interfaces. In the following, the MFP of phonons has been calculated based on our theoretical model. From Figure. 5.12a, because of the significant strong phonon boundary scattering in the NC Si, it is easy

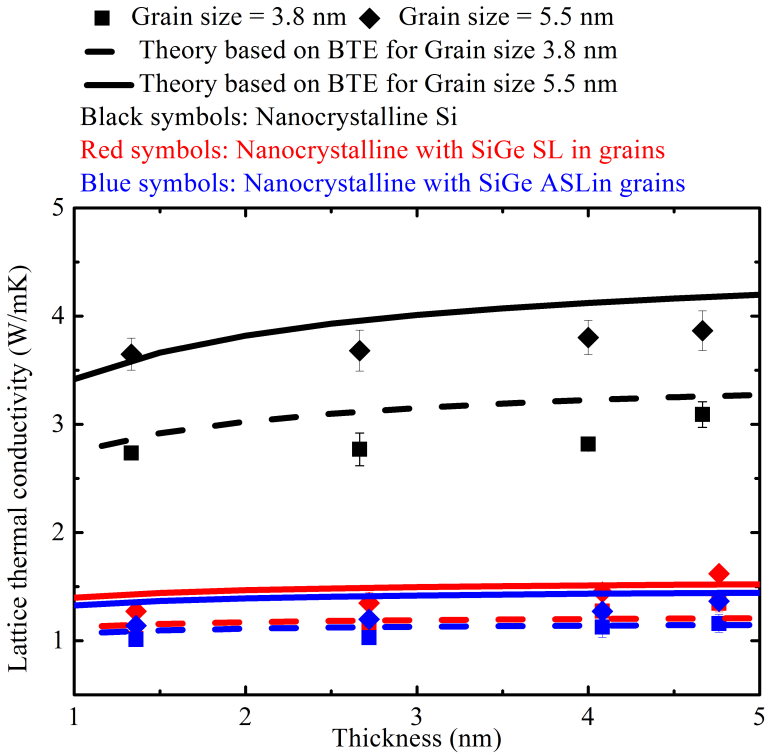


FIGURE 5.11: The lattice thermal conductivity from MD simulations and theoretical predictions as a function of membrane thickness. The square and diamond symbols represent the thermal conductivity of nanocrystalline structures with grain size of 3.8 and 5.5 nm, respectively. The black, red and blue color represent the results for the traditional nanocrystalline Si, SiGe superlattice nanocrystalline and SiGe anti-superlattice nanocrystalline, respectively.

to find the thermal conductivity of NC Si will break the Casimir limit, in which the phonon MFP is assume to be the average grain size, since the maximum phonon MFP is much smaller than average grain size. For instance, for the NC Si with grain size of around 8 nm, the maximum phonon MFP is only about 4 nm and the MFP of the dominant phonons is in the range of 1 to 4 nm. With the grain size decreasing, the maximum MFP can be as small as only 1.5 nm, which is not surprising to be observed since the phonon boundary scattering becomes extremely strong. With the layer thickness increasing, more relatively long MFP phonons can exist in the system and the contribution of these phonons becomes larger. For example, the phonons with MFP of 0.8 nm to 1.6 nm contribute about 80% of the total thermal conductivity when the thickness is about 5 nm, and only 60% of the thermal conductivity in the system with layer thickness of around 1.4 nm. For the nanostructures with SiGe SL or ASL in grains [Figure. 5.12b and 5.12c], the phonons can be further scattered by the Si-Ge interfaces inside the grains, leading to a smaller thermal conductivity with respect to the NC Si: the maximum phonon MFP in the SL/ASL-NC HS systems is only 3 nm (compared to 4 nm for the NC Si) and the dominant phonons are in range of 0.5 to 3 nm (compared to 1 to 4 nm for the NC Si) even for the system with grain

size of around 8 nm. Once again, decreasing the grain size will certainly decrease the MFP of phonons, and then, the thermal conductivity will be reduced. Moreover, the layer thickness has been found to be a negligible factor for the SiGe SL and ASL HSs. This can be understood in terms of the quite intense phonon scattering caused by the normal grain boundaries and the additional Si-Ge interfaces.

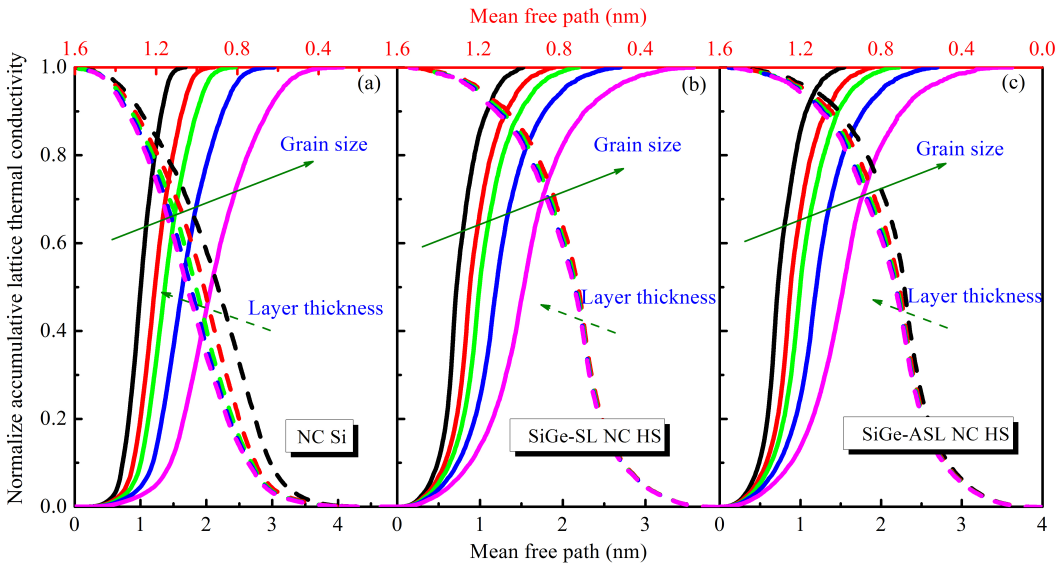


FIGURE 5.12: The phonon mean free path vs. grain size and layer thickness for polycrystalline Si (a), SiGe superlattice nanocrystalline (b) and SiGe superlattice nanocrystalline (c). The solid lines use the black bottom-left axes and the dashed lines use the red up-left axes.

The maximum possible ZT value of Si-based superlattice nanocrystalline heterostructures at room temperature: With the known electric and thermal properties, we can calculate the figure-of-merit for the nanostructured silicon-based superlattice systems. Firstly, we study the grain size effect on the thermoelectric properties which means the layer thickness is set as a constant [Figure. 5.13a]. For the NC Si, the ZT value is around 0.18 when the grain size is around 3 nm and the ZT value will be reduced with increase of the grain size due to the rise of lattice thermal conductivity. The ZT value is only 0.125 when the grain size is increased to about 8 nm. By introducing the SiGe SL or ASL into the grains, the thermal conductivity will be reduced strongly due to the additional phonon scattering at the Si-Ge interfaces. The ZT value of the nanostructures with SiGe SL or ASL can be as large as 0.3 when the grain size is around 3 nm. However, because of the degeneration of electric properties when the periodic length of SL or ASL becomes large which means PF of such systems decreases [Fig. 5.8], the ZT value will be decreased to around 0.1 when the periodic length of SL or ASL is around 7.8 nm. In addition, the ZT will be decreased with increase of the grain size due to the increase of lattice thermal conductivity. Next, the ZT value dependence of layer thickness is took into consideration [Figure. 5.13b]. The ZT of all these systems can be increased a little bit: 0.26 (0.24), 0.23 (0.23) and 0.18 (0.14) for the nanostructures of SiGe SL NC, SiGe ASL NC and pure NC Si

with grain size of 3.8 nm (5.5 nm), respectively, when the layer thickness is reduced to about 1.4 nm due to the small reduction of lattice thermal conductivity caused by the enhancement of phonon-surface scattering.

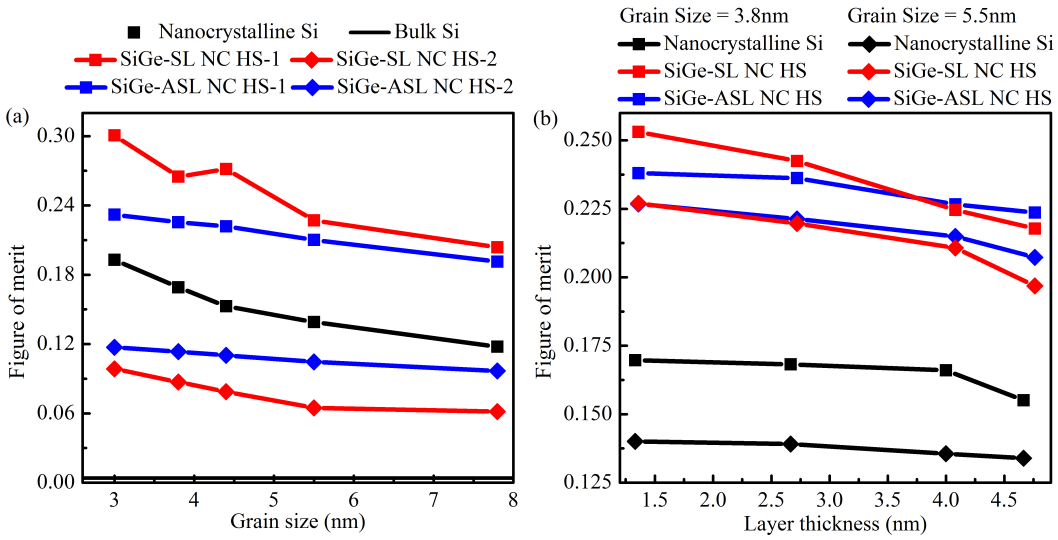


FIGURE 5.13: The figure of merit as a function of grain size (a) and layer thickness (b).

Now, an intuitive question that can be raised is, what is the maximum possible ZT value of the Si-based SL-NC HSs? The way to further improve the ZT is to increase the PF and decrease the thermal conductivity as far as possible. Here, the average PF can be improved once we also consider the out-of-plane direction (Appendix D)) meaning bulk Si-based SL nanocrystallines. Meanwhile, the thermal conductivity can be reduced as well due to the increased phonon boundary scattering along the out-of-plane direction in the bulk Si-based SL nanocrystallines. Figure. 5.14 shows that considering the out-of-plane direction, the lattice thermal conductivity can be further reduced compared to the nanostructured membranes and the lowest lattice thermal conductivity can be only 0.9, 0.45 and 0.37 for pure polycrystalline Si, bulk SiGe SL-NC HSs and bulk SiGe ASL-NC HSs, respectively. In the meantime the PF for bulk SiGe SL-NC HSs and bulk SiGe ASL-NC HSs is improved with respect to the nanostructured membrane counterparts. Therefore, for the limit grain size (around 1 nm) in experiments (Yu et al., 2016), the maximum ZT can reach 0.5 for SiGe SL-NC HSs, 0.42 for SiGe ASL-NC HSs and 0.32 for the NC Si at room temperature. It indicates that the new structures proposed in this paper are quite competitive for the Si-based TE materials: the ZT value can be improved by two orders of magnitude compared to bulk crystalline Si. The ZT value predicted here is also super among all the bulk Si-based nanostructures, including polycrystalline Si with grain size of 100 nm (ZT value is around 0.033) (Valalaki, Vouroutzis, and Nassiopoulou, 2016) and bulk SiGe alloy (the maximum ZT value is 0.08) (Yu et al., 2012), nanostructured SiGe alloy with a maximum ZT of around 0.16 (Wang et al., 2008b; Minnich et al., 2009a; Bera et al., 2010).

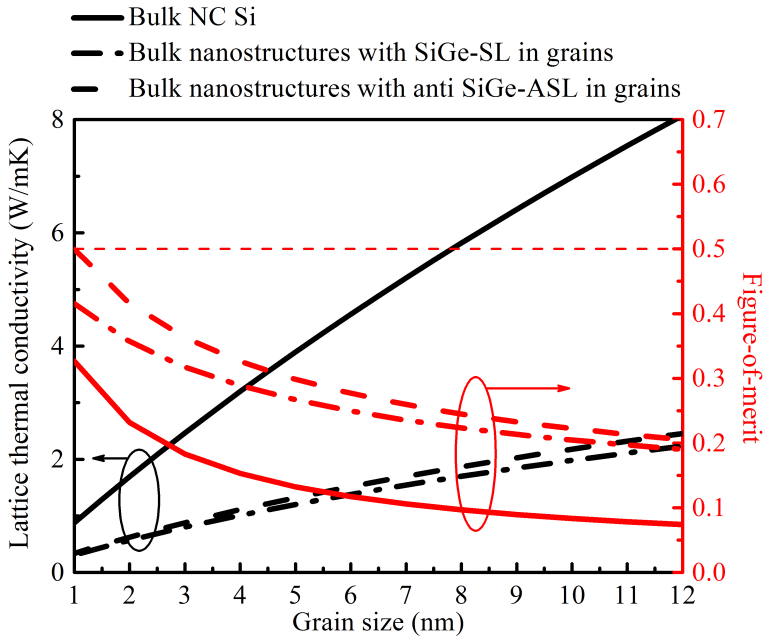


FIGURE 5.14: The lattice thermal conductivity (left axis) and figure of merit (right axis) of the bulk polycrystalline Si, bulk SiGe superlattice nanocrystallines and bulk SiGe anti-superlattice nanocrystallines.

5.4 Enhancing the Thermoelectric Performance by Decoupling the Heat and Charge Transport

In this section, by combining first-principle calculation, BTE and MD simulations, we perform a proof of concept computer experiment and provide evidence that the PF can be improved with respect to its bulk counterpart and the thermal conductivity can be decreased simultaneously by TB in the diamond-like semiconductors. Furthermore, by combining polycrystalline (normal grain boundary) and TB structures, we show that the thermal conductivity can be reduced down to extremely low values, eventually much lower than the amorphous limit, while the PF can be maintained to be at the same level or even enhanced compared to their counterpart. As a result, for the limit grain size (around 1 nm) that is achievable in experiment (Zhou et al., 2012), the ZT of bulk Si nanotwin-nanocrystalline heterostructures (NT-NC NSs) can reach as large as 0.52 at room temperature which is almost two orders of magnitude higher than that of bulk crystalline Si and twice of the polycrystalline Si. At high temperature such as 1100 K, the ZT of bulk Si NT-NC NSs can increase to 0.9.

5.4.1 Computational details

Our model structure consists of perfect $\Sigma 3$ TBs in Si which has coherent and mirror plane [(111) plane] symmetry, as shown in Figure. 5.15. Si is chosen as the model

system because the nanotwinned structures have been widely fabricated in experiments (Stoffers et al., 2015; Wang, Smirani, and Ross, 2004; Imai and Fujimoto, 2006). The atoms on the TB [red atoms in Figure. 5.15b] are stacking in the hexagonal crystal structure and the bulk atoms [yellow atoms in Figure. 5.15b] have the diamond crystal structure. Meanwhile, in order to explore the electronic structure of TB, the electronic density isosurface of TB is shown in Figure. 5.15c. The charge distribution on the TB [atoms in the red frame of Figure 5.15 (c)] has been strongly altered with respect to a pristine diamond structure [atoms in the gray frame of Figure. 5.15c], a feature which is likely expected to affect electronic transport. Meanwhile, the electronic density distribution change by displacement of the TB atoms [black circles in Figure. 5.15c and 5.15d] shows the TB mainly affects the atoms in this region and has a weak effect on bulk atoms. Four bulk Si containing TB (hereafter denoted as Si-TB) structures with different periodic length (λ_{TB}) are considered (Figure 5.15b), namely Si-TB-1(2, 3, 4) with λ_{TB} of 1.9(3.8, 5.7, 7.6) nm, respectively. All band structures of Si-TB and perfect crystalline Si are calculated using Vienna Ab-initio Simulation Package (VASP) based on the DFT (Kresse and Furthmüller, 1996). Periodic boundary conditions are applied in all three directions. The Si atoms are described by the pseudopotential containing s^2p^2 as valence states with LDA in the Project-Augmented-Wave (PAW) exchange-correlation function. A plane-wave basis is implemented with kinetic energy cutoff of 320 eV.

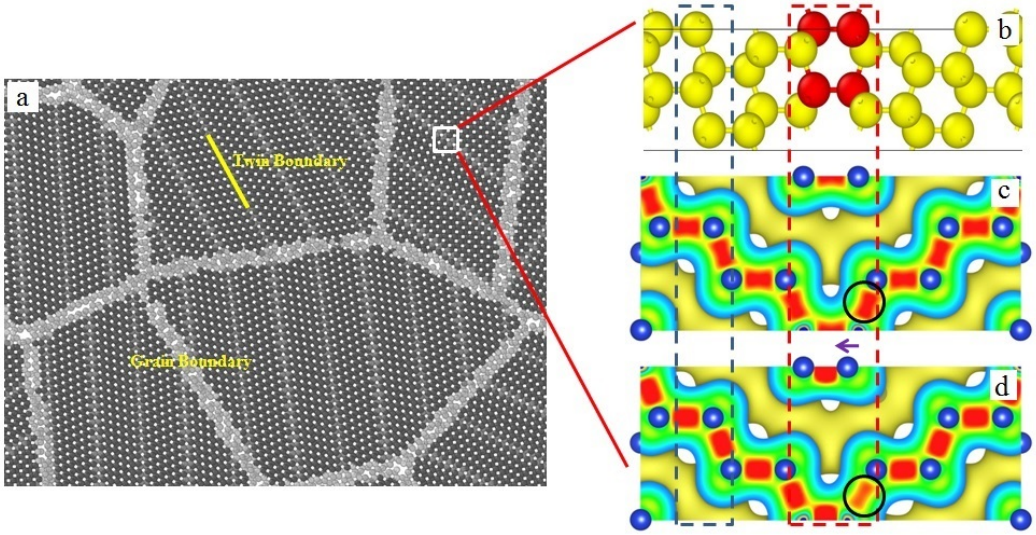


FIGURE 5.15: (a) The schematic of a representative nanostructure with Si nanotwinned structure. (b) The representative Si nanotwinned structure (periodic length of 1.9 nm). The atoms on the twin boundary that are stacking in the hexagonal crystal structure and the bulk atoms with the diamond crystal structure are highlighted in red and yellow, respectively. (c) The corresponding electrical charge density. (d) Change of electrical density distribution by displacing the twin boundary atoms (purple arrow).

At first, the lattice constant and geometry of the systems are optimized until the

energy difference and the Hellman-Feynman force are converged within $1 \times$ 10-4 eV and $5 \times$ 10-3 eV/Å, respectively, using a $4 \times 4 \times 4$ to $10 \times 10 \times 10$ shifted Monkhorst-Pack mesh of $\vec{k}$ points to sample the first Brillouin zone. Then, the electronic transport properties of the bulk crystalline Si and Si-TBs are calculated by the BoltzTrap [84] based on the semi-classical BTE. A quite dense $\vec{k}$ points mesh, $15 \times 15 \times 15$, is employed to ensure the accuracy of the Kohn-Sham eigenvalues which are used as input in the BoltzTrap. It is worth noting that the band gap computed from Kohn-Sham states is systematically underestimated (Perdew, 1986), but it does not affect directly the comparison and conclusion since all the calculations are performed with the same method, which has been proved by previous studies (Mangold, Neogi, and Donadio, 2016; Madsen and Singh, 2006; Madsen, 2006).

All the results of κ_{ph} are calculated by Green-Kubo equilibrium molecular dynamics (GK-EMD) simulations (Zhou and Hu, 2016; Zhou, Zhang, and Hu, 2017; Zhou, Yao, and Hu, 2016) (details can be found in Ref. (Zhou and Hu, 2016; Zhou, Zhang, and Hu, 2017; Zhou, Yao, and Hu, 2016)), in which the interatomic interaction is described by Tersoff potential (Tersoff, 1989). We would like to point out that, the Tersoff potential normally overestimates the κ_{ph} of bulk Si: the κ_{ph} computed by Tersoff potential is around 200 W/mK while the experimental value is 156 W/mK (Glassbrenner and Slack, 1964). However, all of our results are calculated using the same methods and interatomic potential. Therefore, this overestimation is believed to have no impact on our comparison and conclusion.

5.4.2 Results and discussions

Thermal and Electrical Transport Properties of Nanotwinned Bulk Si: Figure. 5.16a-d show the electronic transport properties in bulk Si containing TB as well as in perfect crystalline Si in the case of N-type doping [as been plotted inFigure. 5.17 below, only the conduction band is modulated by the TB structure]. Obviously, the electronic transport properties of the Si-TB structure should be direction dependent since the three crystal directions are inequivalent. Due to the degeneracy of multiple valleys and the increase of band gap (see the electronic band structure and discussion below) caused by the narrow spaced TB (Si-TB-1, Si-TB-2 and Si-TB-3), the absolute value of the Seebeck coefficient of the nanotwinned structure is unexpectedly increased with respect to bulk crystalline Si [Figure. 5.16a]. Meanwhile, it is quite interesting to find that along one of the in-plane directions ([112] direction), the electrical conductivity can be improved compared to the bulk crystalline Si due to the TB structure (detailed discussion can be found below): the smaller the λ_{TB} of the nanotwinned structure, the larger the enhancement of the electrical conductivity [Figure. 5.16b]. Following the Wiedemann-Franz law (Jonson and Mahan, 1980) (Appendix E)), the κ_{el} should have the similar trend with the electrical conductivity [Figure. 5.16c]. Finally, due to the combined effect of the Seebeck coefficient and electrical conductivity, for all the cases the PF along [112] direction can be improved and the case with λ_{TB} of 1.9

nm can be even doubled with respect to the perfect crystalline Si. The PF along [110] direction with λ_{TB} of 1.9 and 3.8 nm also increases slightly [Figure. 5.16d].

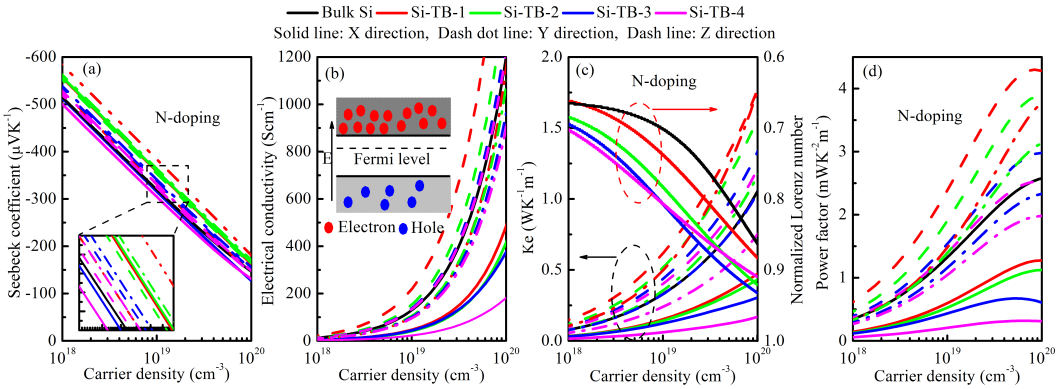


FIGURE 5.16: The electrical transport properties of the nanotwinned structure along three directions: (a) Seebeck coefficient, (b) electrical conductivity, (c) electronic thermal conductivity and Lorenz number, (d) power factor. The X, Y, and Z direction are <111>, <110> and <112> respectively.

Now, we investigate the underlying mechanism that leads to the enhancement of Seebeck coefficient and electrical conductivity for the nanotwinned structure. It is well-known that the material parameter called the thermoelectric quality factor (B) determines the optimized figure-of-merit (Wang et al., 2012; Pei et al., 2011b; Pei et al., 2012; Pei, Wang, and Snyder, 2012; DiSalvo, 1999)

$$ZT \propto B = \left(\frac{k_b}{e}\right)^2 \frac{2e(k_bT)^{3/2}}{(2\pi)^{3/2}\hbar^3} \frac{N_V \mu_0 m_b^{*3/2}}{\kappa_{ph}} T \tag{5.24}$$

where m_b^* is the band effective mass, N_v is the band degeneracy, μ_0 is the mobility at the nondegenerate limit, k_b is the Boltzmann constant, $\hbar$ is the reduced Planck constant, e is free electron mass. The traditional method to increase B is improving Seebeck coefficient via increasing m_b^* (Heremans et al., 2008)

$$S = \frac{2k_bT}{3e\hbar^2} m_d^* \left(\frac{\pi}{3n_{carrier}}\right)^{2/3} \tag{5.25}$$

with

$$m_d^* = N_V^{2/3} m_b^* \tag{5.26}$$

in which, $n_{carrier}$ is the carrier density and m_d^* is the effective mass of density of state. However, such method is detrimental to the electrical conductivity (Pei et al., 2011a) since the μ_0 can be written as (Herring and Vogt, 1956; Wang et al., 2012)

$$\mu_0 = \frac{2^{3/2}\pi^{1/2}\hbar^4 eC}{3m_I^* \left(m_b^* k_b T\right)^{3/2} \Xi^2} \tag{5.27}$$

where m_I^* is the inertial effective mass and equal to m_b^* of the concerned current

transport direction, C is the elastic constant, and Ξ is the deformation potential coefficient. Combining Eq. 5.24 and 5.27, we can know

$$ZT \propto B = \frac{2k_b^2\hbar T}{3\pi}\frac{CN_V}{3m_I^*\Xi^2\kappa_{ph}} \tag{5.28}$$

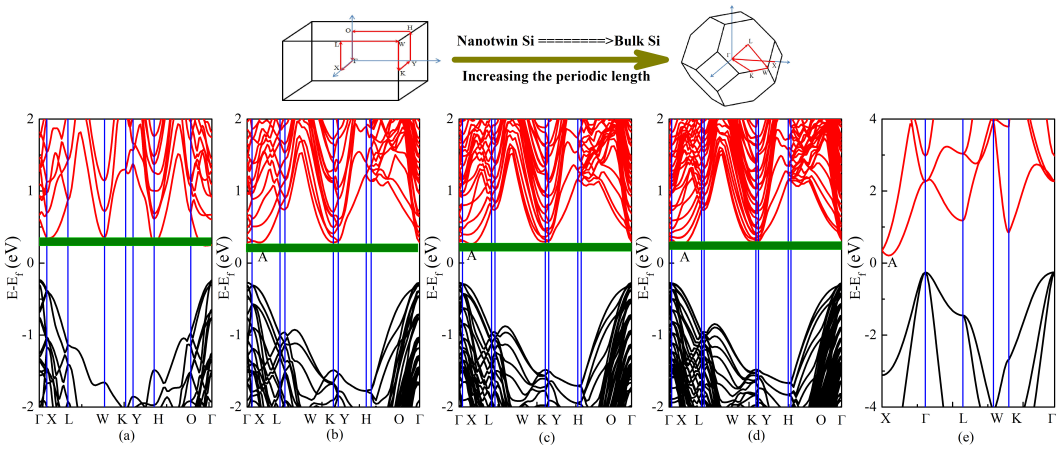


FIGURE 5.17: Band structures of the Si nanotwinned structure with various periodic length: (a) 3.8 nm, (b) 7.6 nm, (c) 11.4 nm, and (d) 15.2 nm. The horizontal lines denote the energy level of 5 kbT. (e) The results for bulk crystalline Si.

Therefore, both low effective band mass m_b^*, which can guarantee high electrical conductivity (Eq. 5.27), and large valley degeneracy N_v, which can gain large Seebeck coefficient (Eq. 5.25), are quite beneficial for achieving high figure-of-merit (Eq. 5.28). From our results [Figure. 5.17], it is clearly seen that the valley degeneracy N_v in the conduction band is effectively increased to 15 (1×Γ, 2×X, 8×W and 4×H), 9 (1×Γ, 2×A, 4×K and 2×Y), 9 (1×Γ, 2×A, 4×K and 2×Y) and 9 (1×Γ, 2×A, 4×K and 2×Y) when their band extrema are converged to have energies within a few (5) k_bT of each other. For the bulk crystalline Si, the N_v in the conduction band is only 6 (6×A). The large improvement of the N_v in the conduction band will, in return, lead to enhancement of Seebeck coefficient (Eq. 5.25 and 5.26) in the Si-TB structures as shown in Figure. 5.16a. Meanwhile, Si-TB-1 will possess the largest Seebeck coefficient where the largest N_v is found. It is worth noting that the Si-TB here can be also regarded as a special superlattice. It is well-known that the superlattice structures can be used to manipulate the symmetrically inequivalent bands to obtain high degeneracy N_v (Koga et al., 1999). At the same time, the effective band mass m_b^* of the conduction band minima (CBM) is calculated. It is easy to find that the $m^*_{b,\ y\ or\ z}$ and $m^*_{b,\ x}$ of the Si-TBs are much smaller and larger than that of the bulk crystalline Si (Table 5.2), respectively. Both the $m^*_{b,\ y\ or\ z}$ and $m^*_{b,\ x}$ increase with λ_{TB}. At the same time, as shown in Figure. 5.17, the band gap will be enlarged by the TB structure, which means that it becomes more difficult for electrons to translate from

TABLE 5.2: The effective band mass at conduction band minima [Γ point for nanotwinned Si with different periodic length (Si-TB-1/2/3/4) and A point for bulk crystalline Si]

Type	$m^*_{b,\,x}\,(m_e)$	$m^*_{b,\,y}\,(m_e)$	$m^*_{b,\,z}\,(m_e)$
Bulk Crystalline Si	1.470	1.470	0.972
Si-TB-1	0.147	0.147	0.972
Si-TB-2	0.153	0.031	0.199
Si-TB-3	0.171	0.033	0.247
Si-TB-4	0.451	0.070	0.615

valence band to conduction band, and then, is detrimental to the electrical conductivity. Therefore, there are two competing mechanisms responsible for the variation of the electrical conductivity of Si-TBs as shown in Figure. 5.16: (1) the decrease of effective band mass m^*_b leads to the improvement of mobility μ_0 (Eq. 5.27); (2) the increase of the band gap leads to the difficulty of thermal excitation of electrons from valence band to conduction band. Only when the former factor is dominant, the electrical conductivity can be improved such as z-direction ([112] direction) in the Si-TBs. For [110] direction, although the effective band mass $m^*_{b,\,y}$ is reduced, the enhancement of band gap will be dominant. Therefore, the electrical conductivity of Si-TBs along [110] will decrease slightly with respect to its bulk counterpart. For electrical conductivity along the [111] direction, both the increase of the $m^*_{b,\,x}$ and the improvement of band gap are responsible for its large reduction.

Meanwhile, there is no surprise to find that the κ_{ph} is significantly reduced with respect to the bulk crystalline Si [Figure. 5.18a], since the TB is actually a special kind of grain boundary and thus scatters the phonons. The long MFP phonons will be scattered by the TB [Figure. 5.18b]. This is because the TB will shift down the optical phonon branches, and therefore, provides more scattering channels for the low frequency region phonons [Figure. 5.18c and d]. Finally, we can know that the ZT of Si-TBs can be augmented by as large as around 3 times (up to 0.01 at room temperature) compared to the bulk crystalline counterpart. Despite the large enhancement, the pure Si-TB structure is not a good thermoelectrics since the κ_{ph} is too high.

Thermoelectric Performance of Si Nanotwin Nanomembranes: Next, we combine the nanotwin concept with the method of nanostructuring to further enhance the thermoelectric performance. Note that the nanocrystalline materials with TBs inside the grains with diamond-like structure have been fabricated in experiments (**243**). At first, the Si twin-boundary nanomembrane (denoted as Si-TBNM) is studied [Figure. 5.19a-d]. The electrical transport properties of the Si-TBNM with grain size of 3 nm and layer thickness of about 3 nm are shown in Figure. 5.19e-h (the

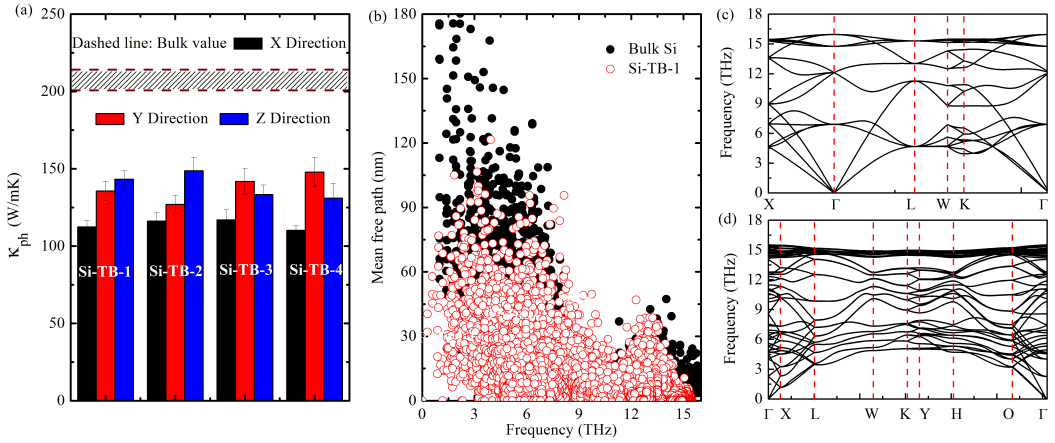


FIGURE 5.18: (a) The lattice thermal conductivity of bulk Si and Si nanotwin with various periodic lengths. (b) The mean free path of phonons for the bulk Si and Si-TB-1. (c) The corresponding phonon dispersion as discussed in (b), the high symmetry points can be found in Figure. 5.17.

calculation details can be found above). Although the electrical conductivity of Si-TBNMs is decreased compared to bulk crystalline Si, the PF of Si-TBNMs is comparable to the bulk value, due to the large enhancement of Seebeck coefficient. For the carrier density of 1×10^{20} cm^{-3}, the PF of Si-TBNMs with TB-1, TB-2, TB-3 and TB-4 incorporated is 80%, 70%, 40% and 30% of the bulk value, respectively. Meanwhile, both the simulation results and theoretical predictionsshow that the κ_{ph} of such TB-NMs can be reduced by almost two orders of magnitude with respect to the bulk value [Figure. 5.20a]. The κ_{ph} of these Si-TBNMs with grain size smaller than around 6 nm is even lower than the amorphous limit. Such phenomenon is also reported in previous studies (Zhou and Hu, 2016; Feser et al., 2013; Melis and Colombo, 2014). Increasing the thickness of the membrane leads to the increase of the κ_{ph} of Si-TBNMs due to the weakened phonon-boundary scattering [Figure. 5.20b]. This is also the reason why the Si-TBNMs with larger grain size has a stronger thickness dependence: the larger the grain size, the longer mean free path of the phonons the Si-TBNMs have [Figure. 5.20c], and then, the phonon-surface scattering is more evident. From Figure. 5.20c, we can also find that the largest MFP of phonons is much smaller than the grain size: for instance, the maximum MFP of phonons for the Si-TBNMs is only 3.5 nm when the grain size is around 8 nm. This indicates that the thermal conductivity of Si-TB nanostructures can break the Casimir limit which assumes the average MFP of phonons should be equal to the grain size (Casimir, 1938). The phonons with MFP in the range of 1.0 to 3.0 nm for the Si-TBNMs with grain size of around 8 nm contribute around 95% of total κ_{ph}. Meanwhile, both the maximum MFP of the phonons and the range of the MFP of the dominant phonons decrease with grain size decreasing. Also, relatively larger MFP phonons can exist in the TBNMs when the layer thickness increases.

From Figure. 5.21a, it is easy to find the ZT coefficient of the Si-TBNMs can reach

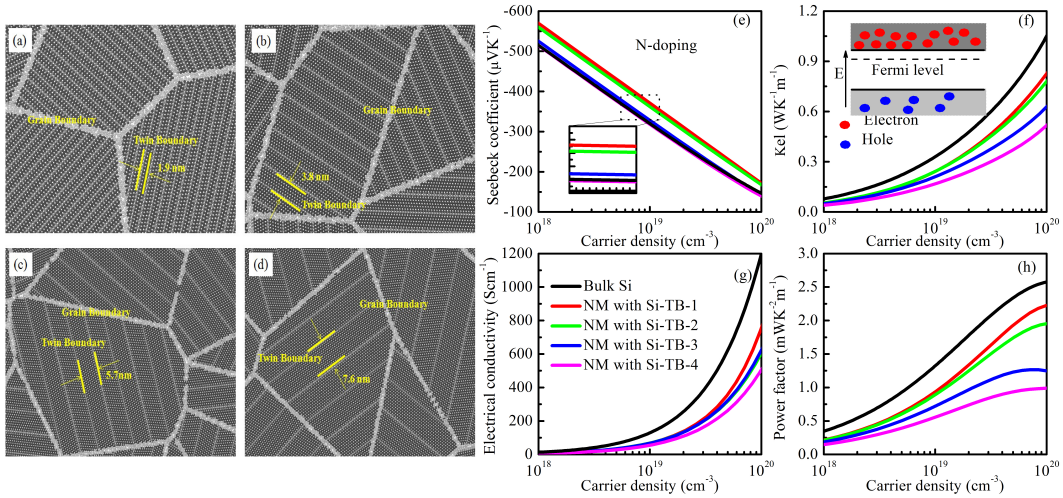


FIGURE 5.19: (a, b, c, d): the atomic structures of the Si nanotwinned membranes with different periodic lengths (a, 1.9 nm; b, 3.8 nm; c, 5.7 nm; d, 7.6 nm). Electrical transport properties of the Si nanomembranes with nanotwins inside the grains: (a) Seebeck coefficient, (b) electrical conductivity, (c) electronic thermal conductivity, and (d) power factor.

0.24 at room temperature, which is about 60 times of the bulk crystalline Si, when the grain size is around 3.0 nm. Such high ZT value is mainly due to the extremely low κ_{ph} and the bulk comparable PF. With grain size or layer thickness increasing, the ZT coefficient will be reduced which is mainly due to the increase of κ_{ph}. To further improve the thermoelectric performance, we propose three-dimensional Si nanotwin-nanocrystalline heterostructures (NT-NC HSs) which are easier to be fabricated in experiments, and calculated the corresponding ZT value. It is surprising to find that the PF of the Si NT-NC HSs can be even larger than that of bulk crystalline Si [Figure. 5.21b]. Such enhancement of the PF is mainly caused by the contribution from the other in-plane direction ([110] direction). At the same time, it is easy to know that κ_{ph} of the Si NT-NC HSs is even lower than that for the Si TBNMs with the same grain size. This is because in our models the grain boundary is rougher than the surface.

The Optimal Figure-of-merit of Si Nanotwin Nanocrystalline Heterostructures: The next question is: what is the maximum possible ZT value of the SI NT-NC HSS? From Figure. 5.21b and 5.21c, we find both PF and κ_{ph} are grain size dependent. This indicates that an optimal figure-of-merit of Si NT-NC HSs can be obtained by modulating the grain size. Figure. 5.21c shows that in the experimental limit of grain size (Zhou et al., 2012) (around 1 nm), the ZT value of the Si NT-NC HSs can be as large as 0.52 at room temperature (theoretical limit), which means Si NT-NC HS could be the highest thermoelectric material among all the Si-based bulk structures reported so far, e.g. polycrystalline Si with grain size of 100 nm (ZT: ∼0.033) (Valalaki, Vouroutzis, and Nassiopoulou, 2016), bulk SiGe alloy (maximum ZT: 0.08) (Yu et al., 2012) and nanostructured SiGe alloy (maximum ZT: ∼0.16) (Wang et al., 2008b;

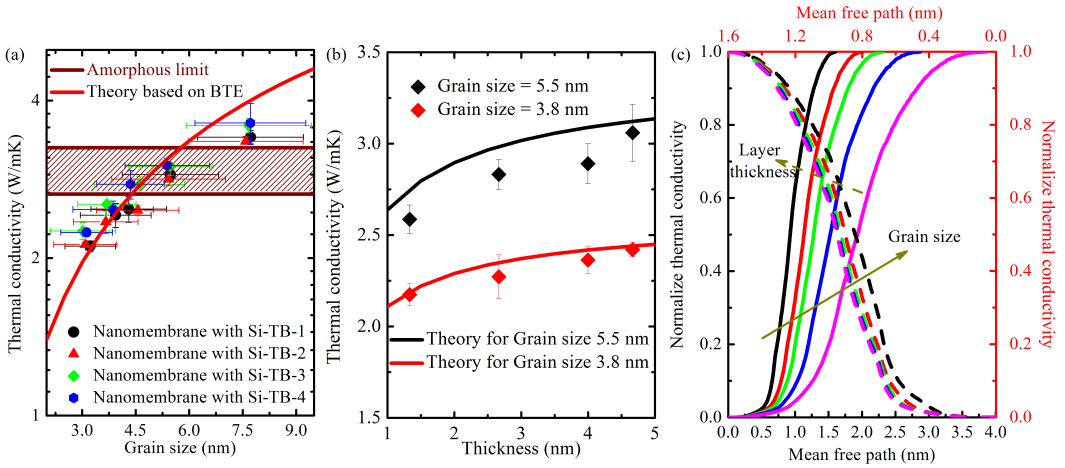


FIGURE 5.20: Grain size (a) and thickness (b) dependent lattice thermal conductivity of the Si nanomembranes incorporated with nanotwins. The symbols are results calculated by Green-Kubo equilibrium molecular dynamics simulation and the solid lines are theoretical results. (c) The phonon mean free path vs. grain size (using the black bottom-left axes) and thickness (using the red top-right axes). The dashed and solid lines are for layer thickness and grain size dependence, respectively. The arrows denote the increase direction of layer thickness and grain size.

Minnich et al., 2009a; Bera et al., 2010). Even when the grain size is increased to around 5 nm, which is the case that the bulk Si NT-NC HSs has already been fabricated in experiments (Wang, Smirani, and Ross, 2004), the ZT value of the bulk Si NT-NC HSs (0.26) is still higher than all of traditional Si-based bulk thermoelectrics. Another important factor that affects the electrical and thermal transport properties is temperature. To study the temperature effect on the thermoelectric performance of Si NT-NC HSs, we fix the grain size at the approachable experimental value (5 nm). It is clearly shown that the optimal PF will increase with temperature [white dashed line in Figure. 5.22a]. Although the electrical thermal conductivity will increase slightly with temperature due to the enhancement of electrical conductivity, the lattice will decrease slightly since high temperature can strength the inherent scattering among phonons [Figure. 5.22b and 5.22c]. It is also interesting to find that the lattice thermal conductivity shows a weak (strong) temperature dependence for the Si NT-NC HSs with small (large) grain size [red and black dashed line in Figure. 5.22c]. This is because for the small grain, the phonon-boundary scattering which is temperature independent is the dominant scattering mechanism and the effect of inherent phonon scattering processes (Umklapp scattering process) which is temperature dependent can be ignored. While for the large grain size, the Umklapp scattering process cannot be neglected, and then the lattice thermal conductivity will show temperature dependence. As a consequence, the optimal ZT can be improved to 0.7 at 1100 K [Fig. 5.22(d)]. Finally, considering the effect of both the grain size and temperature, the optimal ZT of the Si NT-NC HSs can reach 0.9 when the grain

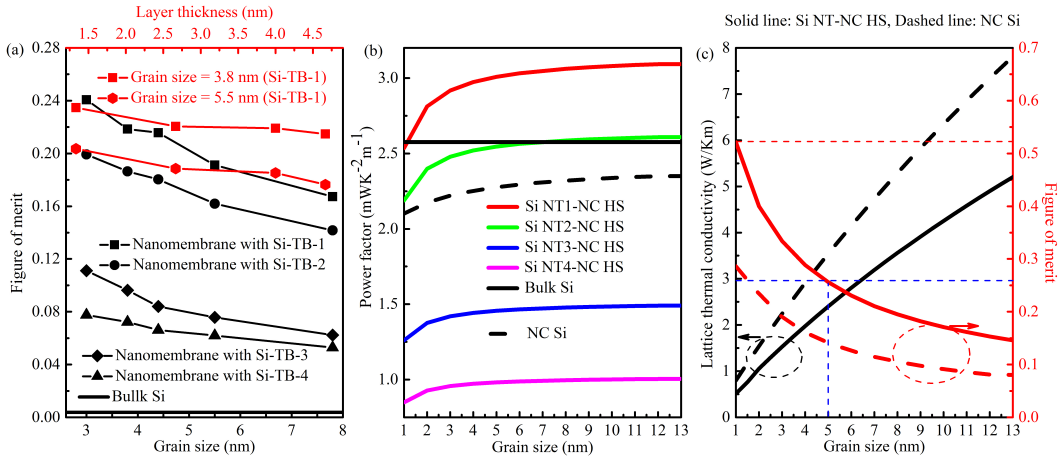


FIGURE 5.21: (a) The figure of merit (ZT) of the Si-TB NMs vs. grain size (using the black axes) and layer thickness (using the red axes) at room temperature. (b) Power factor for the Si nanotwin-nanocrystalline heterostructures with different periodic lengths and nanocrystalline Si (NT-NC HSs or NC). The black horizontal line denotes the power factor for bulk crystalline Si. (c) Lattice thermal conductivity (the black axis) and figure of merit (the red axis) of the Si NT-NC HSs (solid lines) and nanocrystalline Si (long dashed lines) vs. grain size. The square symbols are the ZT coefficient for the Si-based nanostructures reported in literature with reference number labeled. The red short dashed line represents the maximum ZT (0.52) achieved in our proposed Si NT-NC HSs (theoretical limit). The blue short dashed line represents the ZT (0.26) that can be achieved in the experimentally existing Si NT-NC HSs (grain size of 5 nm).

size is 1 nm (theoretical limit) and temperature is 1100 K [Figure. 5.22f]. It should be noted that the optimal ZT is also related to the carrier density. From our results [Figure. 5.22e], the carrier density for the optimal ZT in temperature range 300 to 1100 K and grain size range 1 to 20 nm is from 5×10^{19} cm^{-3} to 3×10^{20} cm^{-3}. Such carrier density range is easy to be obtained in experiments for Si (Zhou et al., 2012). It is also worth noting that the ZT value predicted in our paper is actually underestimated, which means the real ZT value of the bulk Si NT-NC HSs could be even higher in practice.

5.5 Conclusion

In this chapter, firstly our non-equilibrium molecular dynamics simulation results suggest that introducing a large amount of grain boundaries in NWs (the as formed polycrystalline NWs) is more efficient than the traditional structure reconstruction in terms of thermal conductivity reduction, such as decorating the NWs' surface, using supperlattice structure and modifying the surface orientation. It is found that the thermal conductivity of polycrystalline Si NWs can be reduced to a level well below the Casimir limit and is more than two orders of magnitude lower with respect to the counterpart bulk Si and pristine Si NWs, and is even only 1/3 of that for the

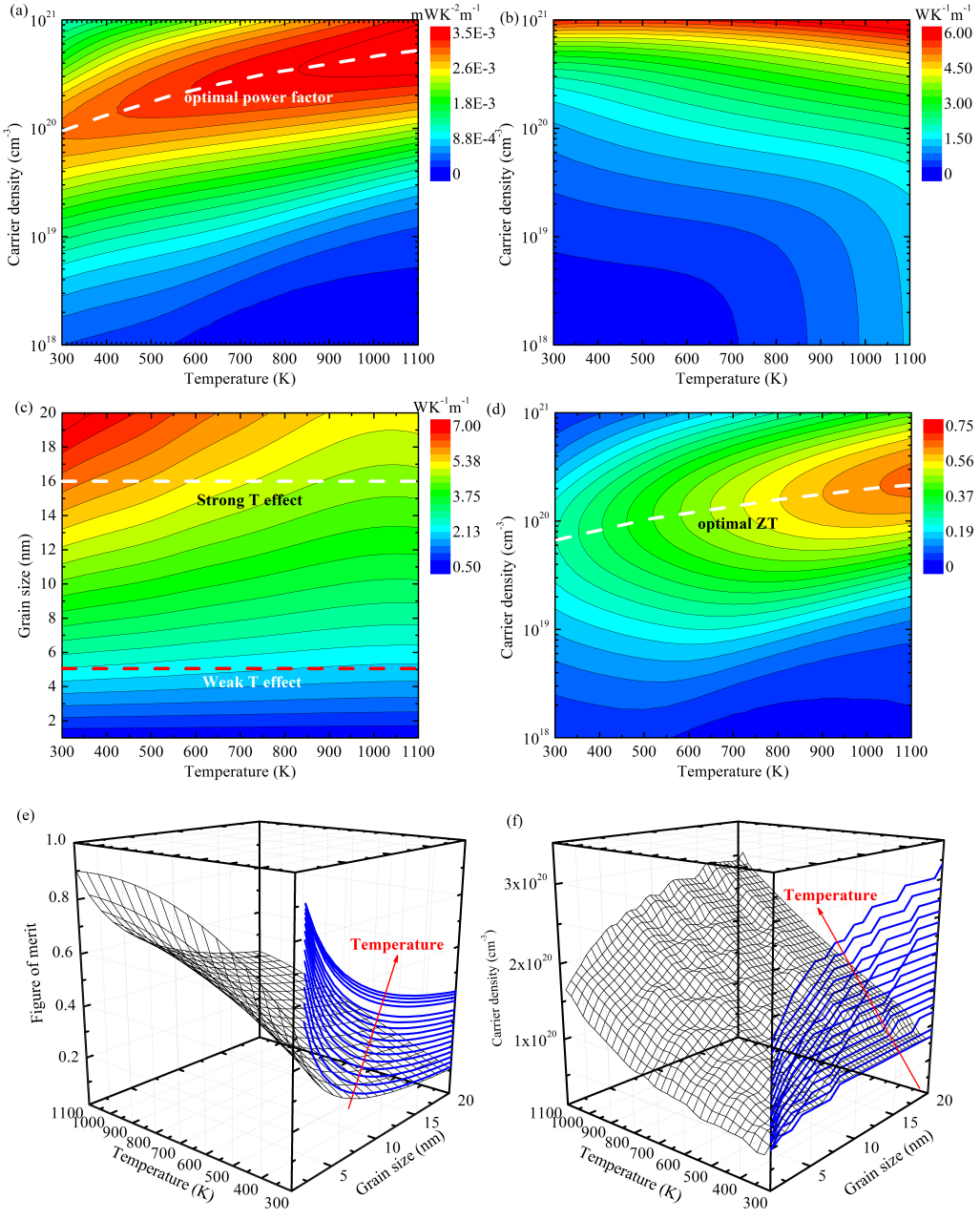


FIGURE 5.22: The power factor (a), electrical thermal conductivity (b) and figure-of-merit (d) of the Si nanotwin-nanocrystalline heterostructures with fixed grain size of 5 nm. (c) The lattice thermal conductivity. The optimal figure-of-merit (e) and the carrier density for the corresponding grain size (f).

pure amorphous Si NWs, which were generally regarded as the amorphous limit in the past (when not considering impurities and porous structures). By computing the phonon modal behavior, we explain that the drastic reduction of thermal conductivity of the polycrystalline Si NWs mainly originates from the strong localization of the vibrational modes in the middle and high frequency region, leading to a striking reduction of the effective mean free path of phonons. Furthermore, the diffusions, instead of propagons, are found to be the dominant heat carriers in polycrystalline Si NWs with respect to bulk Si, perfect Si NWs and pure amorphous Si NWs. Most of propagons in polycrystalline Si NWs are found to be strongly suppressed due to the extremely interfered phonon scattering. We also discuss the lowest possible thermal conductivity of Si NWs and we propose that, further internal treatment for the grains, such as incorporating nanotwinned structures inside the grains, could completely eliminate the contribution of propagons (i.e. only diffusons can contribute to heat conduction), and consequently a thermal conductivity value distinctly lower than the Casimir limit could be reached. Our results demonstrate that the polycrystalline form offers the most efficient pathway to decrease the thermal conductivity of NWs, and therefore has the great potential of largely enhancing the energy conversion performance of thermoelectric materials.

Next, we have designed two new structures with excellent thermoelectric performance based on the previously well-established polycrystalline structures: the polycrystalline nanostructures with SiGe superlattice and SiGe anti-superlattice inside the grains. Due to the quantum confinement effect and the reduction of the band gap caused by the superlattice structure in the grains, such structures are found to have a comparable power factor with respect to the bulk crystalline counterpart. Meanwhile, compared to the traditional nanocrystalline structures whose thermal conductivity can be reduced to a quite low value (even comparable or lower than the amorphous limit of Si when the grain size is smaller than about 4.5 nm), the thermal conductivity of the SiGe superlattice and anti-superlattice nanocrystalline heterostructures can be decreased to only 1/2 of the pure nanocrystalline Si with the same grain size due to the extra phonon scattering at Si-Ge interfaces inside the grains. Consequently, the lattice thermal conductivity of these new structures can be lower than the amorphous limit even when the grain size is relatively large (10 nm). Because of the comparable power factor to the bulk crystalline Si and the ultra-low thermal conductivity which has been decreased by at least two orders of magnitude with respect to its bulk counterpart, the ZT coefficient of the Si nanocrystalline membrane, nanomembranes with SiGe superlattices (SiGe anti-superlattices) in the grains can be as large as 0.17 and 0.26 (0.23) at room temperature, respectively. For the bulk nanocrystalline Si, SiGe superlattice and SiGe anti-superlattice nanocrystalline heterostructures, the thermal conductivity can be reduced further and the power factor can be enhanced slightly at the same time with respect to the membrane nanostructures. Therefore, the ZT value of such bulk nanostructures can be improved further compared to the membranes: the possible maximum ZT of nanocrystalline Si, SiGe

superlattice and anti-superlattice nanocrystalline heterostructures at room temperature are 0.32, 0.42 and 0.5, which is two orders of magnitude higher than that of the bulk crystalline Si. The SiGe superlattice and anti-superlattice nanocrystalline heterostructures exhibit the best ZT performance among all the bulk Si-based thermoelectrics. This work demonstrates a new strategy for enhancing thermoelectric performance by concurrently reducing the lattice thermal conductivity and preserving the high level of power factor.

At last, a new strategy based on lattice defect engineering is proposed to improve the thermoelectric performance of the diamond-structure semiconductors: simultaneously increasing the power factor and decreasing the thermal conductivity by introducing nanotwins. The enhancement of the power factor in nanotwinned structures is caused by two reasons: (1) the improvement of the Seebeck coefficient is due to the degeneracy of multiple valleys (N_V); (2) the increase of the electrical conductivity is caused by the reduction of the effective band mass (m_b^*). The reduction of the thermal conductivity (mainly lattice component) is attributed to the phonon-twin boundary scattering. Consequently, the figure-of-merit of the nanotwinned bulk Si can be improved by 3 times with respect to bulk crystalline counterpart. Furthermore, when the nano-twins are incorporated into the bulk Si nanocrystallines, surprisingly, the power factor of the Si nanotwin-nanocrystalline heterostructures can be even larger than that of bulk crystalline Si and the lattice thermal conductivity is well below the Casimir limit. As a result, the figure-of-merit of the heterostructure can reach as large as 0.52 at room temperature, which is two orders of magnitude improvement compared to bulk crystalline Si and even 100% higher than that for nanocrystalline Si. At the temperature of 1100 K, the optimal figure-of-merit can reach 0.9 for an achievable carrier density. Our results suggest that incorporating nanotwin as structure engineering is a promising strategy for breaking the bottleneck in the semiconductor thermoelectrics through decoupling the electronic and phononic transport.

Chapter 6

Conclusions and Future Works

6.1 Conclusions

The unifying theme in this thesis is that modulating the thermal conductivity or thermoelectric performance via nanostructuring.

Firstly, we start from the development of algorithm in the frame of NEMD which is a mimic of the method applied to measure thermal conductivity in experiments. That means, the models in NEMD are actually nanostructures due to the finite size of models. Two new algorithms named time domain direct decomposed method (TDDDM) and frequency domain direct decomposed method (FDDDM) in the frame of NEMD are proposed successfully to extract the modal (frequency) thermal conductivity. Then, we extend the FDDDM to the interface problem.

The new TDDDM approach is validated by studying the cases of bulk LJ Argon and SW Si and comparing the results to that by SED and TDNMA from equilibrium molecular dynamics simulation. The TDDDM approach inherently possesses the nature of both NEMD simulation and lattice dynamics. Comparing to EMD methods (SED and TDNMA), TDDDM has some distinct features and power in three aspects: (1) It provides direct evidence and quantitative analysis for the length dependence of thermal conductivity in NEMD simulation. We investigated the size effect of individual phonon mode contribution to the overall thermal conductivity in the TDDDM framework. We observe that the phonon modes with mean free path larger than the system size are truncated in TDDDM (NEMD) simulations, and therefore contribute little to the thermal conductivity. With system length increasing, phonons with mean free path longer than the system length are presented and then they are able to contribute to the thermal conductivity. (2) Using TDDDM, we prove that the thermal conductivity contributed from Gamma point is related to the momentum of the system, which is equal to zero for a stable system. Thereby the well-known common sense of the zero contribution of Gamma point can be rigorously proved using TDDDM. (3) We anticipate that TDDDM can be effectively used for studying phonon behaviors in nanostructures or under confined conditions, in particular when the structure size is significantly smaller than the characteristic MFP of the dominant phonons, which also cannot be realized by EMD methods.

The validity of our new FDDDM is assessed by comparing the results of bulk LJ Argon and SW Si to TDNMA, which is based on the equilibrium molecular dynamics simulation. Comparing with previous methods such as SED, TDNMA, and TDDDM, the new FDDDM approach has unique features and power in the following aspects: (1) Due to the inherent nature that FDDDM is based on NEMD, we can use FDDDM to explicitly investigate the size effect of frequency dependent thermal conductivity. Generally speaking, more phonons in the low frequency region, or equivalently phonons with long MFP, are present when the system size increases. (2) There is no assumption of the system temperature in our theoretic model, therefore, in principle the FDDDM can be used to observe the temperature effect of phonon mode thermal conductivity directly. Anharmonic energy transfer is found to increase with temperature increasing, which is well known but proves that our FDDDM reveals the correct physical picture of the phonon-phonon scattering. (3) The FDDDM can be directly used to study the phonon behavior of disordered systems. The amorphous Si is chosen as a benchmark system to prove the unique advantage of our FDDDM method. The contribution of phonons are found to be quite uniform, since the relaxation time of phonons in amorphous materials is substantially short and therefore the scattering is strong as compared with the crystalline materials.

Based on FDDDM, a rigorous and direct method to evaluate the two- and three-phonon scattering process at the interface within the framework of non-equilibrium molecular dynamics simulation has been developed. All possible three-phonon scattering process are taken into consideration by explicitly incorporating the three-body interaction force constants. By investigating the bulk Ar, Ar-heavy Ar and Si-Ge systems, we have validated our methodology and also revealed that combining two- and three-phonon scattering process is enough for some cases at low temperatures (Ar-heavy Ar interface). Higher order phonon scattering process should be included when the system temperature is higher. However, for Si-Ge interface, only considering two- and three-phonon scattering is far not enough even at room temperature. The higher order phonon scattering process at such interfaces can contribute more than 10% of the total thermal conductance. We also emphasize that, the three-phonon scattering process can enhance the heat transport ability through interaction with larger frequency phonons than the cut-off frequency at the interface. Four different types of three-phonon scattering process at interface, namely 1 to 2 phonon radiation, phonon full transmission, 2 to 1 radiation and phonon partial transmission, are described and their respective contribution to the overall phonon transport are explicitly assessed and compared. The 2 to 1 radiation and phonon partial transmission are found to be more important than the other two three-phonon scattering process at low temperature (lower than 30 K for Ar-heavy Ar interface). With temperature increasing, the contribution of all four three-phonon scattering process is found to be comparable. However, for Si-Ge interface, the four three-phonon process are found to have similar contribution in the entire temperature range studied, since 300 K may be already high enough to activate the phonon with frequency

above the cut-off frequency of Ge in the region near the interface of Ge side. It is also observed that there is a small group of phonons around 12 THz contributes a relatively large thermal conductance, which mainly stems from the contribution of three-phonon scattering process at interface.

Then, we care about the thermal management through nanostructuring. We have calculated the thermal conductivity of Si NWs with diverse surface orientations using NEMD simulations and the full spectrum theory. The difference of the thermal conductivity among all the NWs considered can be as large as about 2.7 $\sim$ 4.2 times. The physics responsible for this phenomenon originates from two effects: (1) different surface orientation can change the angle between the phonon wave vector and the normal vector of the surface, then alter the modal specularity, and therefore, leads to the change of thermal conductivity; (2) surface roughness changes due to the different surface structure, and thus, the thermal conductivity varies remarkably. The latter effect is found to be the main mechanism for the large difference in the thermal conductivity. Furthermore, the thermal conductivity of Si NWs is found to decrease with surface atom energy, or RMS height of roughness. Size effects, which include both the cross-section and length, are considered. The large difference among the NWs with diverse surface orientation is also found to exist for infinitely long NWs. We explain the underlying mechanism from phonon level using the vibrational density of states and spectral thermal conductivity. We find that, in the case of (110) orientation the mismatch of the VDOS between the surface atoms and the bulk atoms is smaller than that in other models, which means the stronger coupling between the surface and core atoms, and therefore, it leads to the highest thermal conductivity for (110) orientation among all the NWs studied. Meanwhile, with the help of our newly developed frequency domain direct decomposition method, we investigate the frequency dependent contribution of thermal conductivity. The largely scattered thermal conductivity among the NWs with various surface orientation is found to mainly stems from the medium frequency phonons (1.5 $\sim$ 10 THz).

Meanwhile, by using a model structure of regular Ar and heavy Ar in contact, we have presented the superiority of largely decreasing the interfacial thermal resistance by sandwiching a mass graded layer. While the widely adopted alloyed interface usually increases the overall interfacial thermal resistance by several times as compared with perfectly abrupt interface, except for atomically thin layers, the mass graded structure substantially reduces the overall resistance by 6 folders. Using atomic heat flux spectrum theory, the governing mechanisms are well explained. There are two different regimes of interfacial heat transfer across the rough interface, which originates from the competition between phonon scattering and the interface thickness. When the thickness is large enough, there is enough space for high frequency phonons to scatter then the interfacial thermal resistance will increase, while when the thickness is reduced to only a few atomic layers, there is no enough space for phonon scattering and thus the interfacial thermal resistance decreases to some extent. Moreover, the detailed phonon process for high frequency phonons across

three types of interfaces ($\omega > \omega_c^{heavy\ argon}$) are studied using wave packet method and acoustic mismatch model. For the perfectly abrupt interface, all the phonons with frequency above the cutoff frequency of heavy Ar are reflected and for the alloyed interface, the high frequency phonons gradually disappear through phonon scattering in the alloyed region. In contrast, for the mass graded interface the minor phonon reflection occurs when the phonons first reach the mass graded area. After that, the phonons can easily transmit across the subsequent multi-layers with gradually increasing transmission coefficient and hardly reflect. Consequently the major thermal energy transport turns out to be carried by medium frequency phonons. Wave packet simulation also show that, for rough interface the short and medium mean free path (corresponding to medium and high frequency) phonons have lower transmission coefficient with respect to those in perfectly abrupt interface due to the strong phonon scattering, while the long mean free path (corresponding to low frequency) phonons have the opposite trend, since they can transport across the thin layer with small interference. For the mass graded interface, almost all the phonons with frequency below the cutoff frequency of heavy Ar have significantly higher transmission coefficients, primarily due to the small mass mismatch between the adjacent layers in the interface region, and therefore, the interfacial thermal resistance is dramatically reduced.

At the same time, by performing GK-EMD simulations, we show the nonmonotonic dependence of the thermal conductivity of extremely thin Si NWs on the NW diameter. By analyzing the relative contribution of the two different three-phonon scattering process (N and U) using the BTE, we identify that, the nonmonotonic diameter dependence stems from two competing mechanisms governing the heat conduction in thin Si NWs. For Si NWs with diameter smaller than a critical value, the N process which cannot destroy their momentum are the dominant three-phonon scattering process for the low frequency phonons. Therefore, the excess momentum of these phonons gained from a temperature gradient will be redistributed by the super-strong N process with small reduction, and therefore all of these phonons will transport heat with the same drift velocity (hydrodynamic phonon flow). Consequently, the thermal conductivity of extremely thin Si NWs converges to a very high value, which can be as large as 13 folders of its bulk value for the thinnest but still thermodynamically stable Si NWs. When the NW diameter is larger than the critical value, new U scattering channels for the low frequency phonons are triggered due to the downward-shift of the surface optical phonons, and therefore breaking the dominant role of N scattering. As a result, the thermal conductivity of ultra-thin Si NWs, which is dominated by the phonon boundary scattering rather than the hydrodynamic phonon flow, increases with NW diameter increasing. Our results solve the contradictory problem (convergence vs. divergence) in the literature for the thermal conductivity of extremely thin Si NWs, and for the first time we provide an exact explanation for the mechanism underlying the converged thermal conductivity even for the thinnest possible Si NWs.

Finally, we studied how the thermoelectric performance is affected by nanostructuring. Our non-equilibrium molecular dynamics simulation results suggest that introducing a large amount of grain boundaries in NWs (the as formed polycrystalline NWs) is more efficient than the traditional structure reconstruction in terms of thermal conductivity reduction, such as decorating the NWs' surface, using supperlattice structure and modifying the surface orientation. It is found that the thermal conductivity of polycrystalline Si NWs can be reduced to a level well below the Casimir limit and is more than two orders of magnitude lower with respect to the counterpart bulk Si and pristine Si NWs, and is even only 1/3 of that for the pure amorphous Si NWs, which were generally regarded as the amorphous limit in the past (when not considering impurities and porous structures). By computing the phonon modal behavior, we explain that the drastic reduction of thermal conductivity of the polycrystalline Si NWs mainly originates from the strong localization of the vibrational modes in the middle and high frequency region, leading to a striking reduction of the effective mean free path of phonons. Furthermore, the diffusions, instead of propagons, are found to be the dominant heat carriers in polycrystalline Si NWs with respect to bulk Si, perfect Si NWs and pure amorphous Si NWs. Most of propagons in polycrystalline Si NWs are found to be strongly suppressed due to the extremely interfered phonon scattering. We also discuss the lowest possible thermal conductivity of Si NWs and we propose that, further internal treatment for the grains, such as incorporating nanotwinned structures inside the grains, could completely eliminate the contribution of propagons (i.e. only diffusons can contribute to heat conduction), and consequently a thermal conductivity value distinctly lower than the Casimir limit could be reached.

Meawhile, we have designed two new structures with excellent thermoelectric performance based on the previously well-established polycrystalline structures: the polycrystalline nanostructures with SiGe superlattice and SiGe anti-superlattice inside the grains. Due to the quantum confinement effect and the reduction of the band gap caused by the superlattice structure in the grains, such structures are found to have a comparable power factor with respect to the bulk crystalline counterpart. Meanwhile, compared to the traditional nanocrystalline structures whose thermal conductivity can be reduced to a quite low value (even comparable or lower than the amorphous limit of Si when the grain size is smaller than about 4.5 nm), the thermal conductivity of the SiGe superlattice and anti-superlattice nanocrystalline heterostructures can be decreased to only 1/2 of the pure nanocrystalline Si with the same grain size due to the extra phonon scattering at Si-Ge interfaces inside the grains. Consequently, the lattice thermal conductivity of these new structures can be lower than the amorphous limit even when the grain size is relatively large (10 nm). Because of the comparable power factor to the bulk crystalline Si and the ultra-low thermal conductivity which has been decreased by at least two orders of magnitude with respect to its bulk counterpart, the ZT coefficient of the Si nanocrystalline membrane, nanomembranes with SiGe superlattices (SiGe anti-superlattices) in the grains

can be as large as 0.17 and 0.26 (0.23) at room temperature, respectively. For the bulk nanocrystalline Si, SiGe superlattice and SiGe anti-superlattice nanocrystalline heterostructures, the thermal conductivity can be reduced further and the power factor can be enhanced slightly at the same time with respect to the membrane nanostructures. Therefore, the ZT value of such bulk nanostructures can be improved further compared to the membranes: the possible maximum ZT of nanocrystalline Si, SiGe superlattice and anti-superlattice nanocrystalline heterostructures at room temperature are 0.32, 0.42 and 0.5, which is two orders of magnitude higher than that of the bulk crystalline Si. The SiGe superlattice and anti-superlattice nanocrystalline heterostructures exhibit the best ZT performance among all the bulk Si-based thermoelectrics.

Furthermore, a new strategy based on lattice defect engineering is proposed to improve the thermoelectric performance of the diamond-structure semiconductors: simultaneously increasing the power factor and decreasing the thermal conductivity by introducing nanotwins. The enhancement of the power factor in nanotwinned structures is caused by two reasons: (1) the improvement of the Seebeck coefficient is due to the degeneracy of multiple valleys (N_V); (2) the increase of the electrical conductivity is caused by the reduction of the effective band mass (m_b^*). The reduction of the thermal conductivity (mainly lattice component) is attributed to the phonon-twin boundary scattering. Consequently, the figure-of-merit of the nanotwinned bulk Si can be improved by 3 times with respect to bulk crystalline counterpart. Furthermore, when the nano-twins are incorporated into the bulk Si nanocrystallines, surprisingly, the power factor of the Si nanotwin-nanocrystalline heterostructures can be even larger than that of bulk crystalline Si and the lattice thermal conductivity is well below the Casimir limit. As a result, the figure-of-merit of the heterostructure can reach as large as 0.52 at room temperature, which is two orders of magnitude improvement compared to bulk crystalline Si and even 100% higher than that for nanocrystalline Si. At the temperature of 1100 K, the optimal figure-of-merit can reach 0.9 for an achievable carrier density. Our results suggest that incorporating nanotwin as structure engineering is a promising strategy for breaking the bottleneck in the semiconductor thermoelectrics through decoupling the electronic and phononic transport.

6.2 Future works

There are four extensions of the work presented here:

1, The TDDDM can be extended to deal with the interface problem since it is based on NEMD. Unlike FDDDM which can only give the frequency dependent thermal conductance right now, the TDDDM can provide the modal thermal conductance directly.

2, The FDDDM can be also deduced further to obtain the *modal* level thermal conductance rather than the *frequency* dependent right now. Moreover, the FDDDM can

be also extended to study the high-order (larger than 3) phonon scattering process at interface.

3, How important of quantum effect in molecular dynamics? Are the methods of quantum corrections now accurate enough to include such quantum effect in the results of thermal conductivity calculated by MD.

4, How the twin structure affect the thermoelectric performance in these popular thermoelectric materials such as lead telluride (PbTe), lead sulphide (PbS) and Bismutch telluride *et. al.* would be another interesting topic to investigate further.

Appendix A

The Static and Thermodynamic Stability Criteria

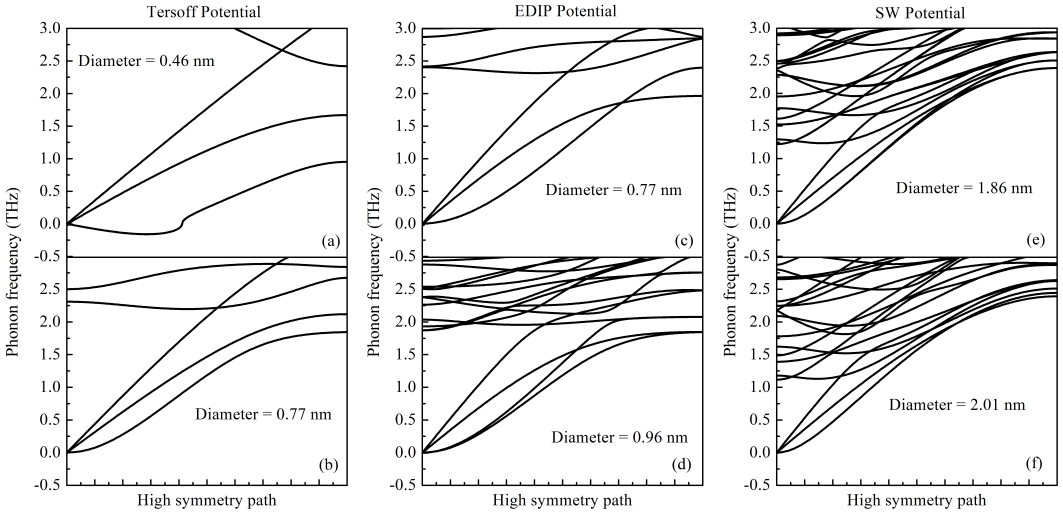


FIGURE A.1: Phonon dispersion for the smallest possible Si NWs computed by Tersoff (a, b), EDIP (c, d) and SW (e, f) potential.

It is quite popular to use the temperature and energy of system as a criterion to determine the thermodynamic stability of the system. Furthermore, the phonon dispersion is usually used as a standard to estimate the system has static stability or not. Here, both the thermodynamic and static criteria are used to decide the stability of the system. For the Tersoff potential, we can find that there is imaginary frequency in the result of the Si NW with diameter of 0.46 nm and the imaginary frequency will disappear when the diameter is increased to 0.77 nm [Figure A.1a and b]. Meanwhile, we can easily find that the temperature and energy will become thermodynamically unstable when the diameters of Si NWs are smaller than 0.77 nm (both the temperature and energy do not conserve as shown in Figure A.2). For the EDIP potential [Figure A.1c and d], although the Si NW with diameter of 0.77 nm is statically stable (there is no imaginary frequency in the phonon dispersion), it is still an unstable system since the temperature of the system cannot maintain stable at finite temperature [Figure A.2]). For the SW potential [Figure A.2e and f], we

also find that the Si NW with diameter of 1.86 nm is statically stable, while not thermodynamically stable [the temperature of the system does not stabilize as shown in Figure A.2]. Therefore, all the systems reported in our paper are both statically and thermodynamically stable. In addition, most recently, the experiment (Yu et al., 2016) find that the nanowire will become unstable when its diameter decreases to around 1 nm, which is in accordance with our simulation results here.

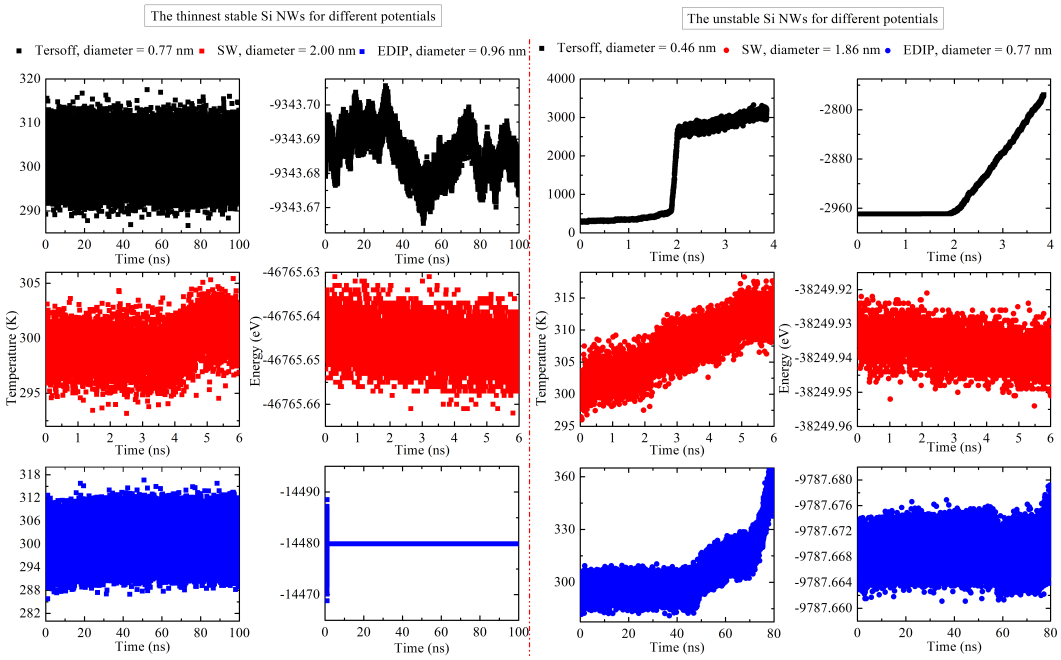


FIGURE A.2: The temperature and energy of the thinnest possible (left side of the red dot-dashed line) and the largest unstable (right side of the red dot-dashed line) Si NWs using Tersoff, SW and EDIP.

Appendix B

Effective Mean Free Path in the Callaway Model

It is usual to write the drift distribution function in the form of

$$\begin{aligned} n(\vec{k},\nu)^{drift} &= \frac{1}{e^{(\hbar\omega(\vec{k},\nu)-\vec{k}\cdot\Delta)/k_BT}-1} \\ &\approx \bar{n}(\vec{k},\nu)-\bar{n}(\vec{k},\nu)\left[1+\bar{n}(\vec{k},\nu)\right]\Delta\cdot\vec{k} \end{aligned} \tag{B.1}$$

Combing Eq. (2.27) and Eq. (B.1), we can obtain

$$\begin{aligned} n(\vec{k},\nu)-\bar{n}(\vec{k},\nu) = &-\frac{1}{\Gamma(\vec{k},\nu)^U+\Gamma(\vec{k},\nu)^N}\vec{v}(\vec{k},\nu)\cdot\nabla T\frac{\partial\bar{n}(\vec{k},\nu)}{\partial T} \\ &-\frac{\Gamma(\vec{k},\nu)^N}{\Gamma(\vec{k},\nu)^U+\Gamma(\vec{k},\nu)^N}\frac{k_BT^2}{\hbar\omega(\vec{k},\nu)}\Delta\cdot k\frac{\partial\bar{n}(\vec{k},\nu)}{\partial T} \end{aligned} \tag{B.2}$$

Due to the fact that N three phonon scattering processes conserve phonon momentum, the rate of the total momentum change should satisfy

$$\sum_{(\vec{k},\nu)}\left[n(\vec{k},\nu)-\bar{n}(\vec{k},\nu)\right]\Gamma(\vec{k},\nu)^N\cdot\vec{k}=0 \tag{B.3}$$

Using Eq. (B.1), Eq. (B.2) and Eq. (B.3), we can find

$$\begin{aligned} &\sum_{(\vec{k},\nu)}\frac{\Gamma(\vec{k},\nu)^N}{\Gamma(\vec{k},\nu)^U+\Gamma(\vec{k},\nu)^N}\left(\vec{v}(k,\nu)\cdot\nabla T\right)\vec{k}\frac{\partial\bar{n}(\vec{k},\nu)}{\partial T} = \\ &\sum_{(\vec{k},\nu)}\frac{\Gamma(\vec{k},\nu)^U\cdot\Gamma(\vec{k},\nu)^N}{\Gamma(\vec{k},\nu)^U+\Gamma(\vec{k},\nu)^N}\frac{k_BT^2}{\hbar\omega(\vec{k},\nu)}\left(\Delta\cdot k\right)\vec{k}\frac{\partial\bar{n}(\vec{k},\nu)}{\partial T} \end{aligned} \tag{B.4}$$

Assuming the thermal gradient is along the z direction, we can obtain (Cepellotti et al., 2015; Ma, Li, and Luo, 2014)

$$\frac{\Delta_z}{\nabla_z T} = \frac{1}{k_B T^2} \frac{\sum\limits_{(\vec{k},\nu)} \frac{\Gamma(\vec{k},\nu)^N}{\Gamma(\vec{k},\nu)^U + \Gamma(\vec{k},\nu)^N} \left(v_z(\vec{k},\nu)\cdot\right) k_z \bar{n}(\vec{k},\nu) \left[1+\bar{n}(\vec{k},\nu)\right]}{\sum\limits_{(\vec{k},\nu)} \frac{\Gamma(\vec{k},\nu)^U \cdot \Gamma(\vec{k},\nu)^N}{\Gamma(\vec{k},\nu)^U + \Gamma(\vec{k},\nu)^N} k_z k_z \bar{n}(\vec{k},\nu) \left[1+\bar{n}(\vec{k},\nu)\right]} \tag{B.5}$$

Meanwhile, the heat current along z direction due to the small temperature gradient can be written as (Li et al., 2014)

$$J_z = \frac{1}{NV} \sum_{(\vec{k},\nu)} \hbar\omega(\vec{k},\nu) v_z(\vec{k},\nu) \left[n(\vec{k},\nu) - \bar{n}(\vec{k},\nu)\right] \tag{B.6}$$

It has been known that the Fourier's law is invalid when the heat current is quite large (Guo et al., 2007), here we assume that temperature gradient is quite small and then Fourier's law still holds. Therefore, we have

$$k_{zz} = -\frac{1}{NV} \sum_{(\vec{k},\nu)} \frac{\hbar\omega(\vec{k},\nu) v_z(\vec{k},\nu) \left[n(\vec{k},\nu) - \bar{n}(\vec{k},\nu)\right]}{\nabla_z T} \tag{B.7}$$

Recasting Eq. (B.2) and Eq. (B.5) into Eq. (B.7), we can find

$$\begin{aligned} k_{zz} =& \frac{1}{k_B T^2 NV} \sum_{(\vec{k},\nu)} \frac{\left(\hbar\omega(\vec{k},\nu)\right)^2 v_z(\vec{k},\nu) v_z(\vec{k},\nu) \bar{n}(\vec{k},\nu) \left[1+\bar{n}(\vec{k},\nu)\right]}{\Gamma(\vec{k},\nu)^U + \Gamma(\vec{k},\nu)^N} + \\ & \frac{1}{k_B T^2 NV} \frac{\left\{ \sum\limits_{(\vec{k},\nu)} \frac{\Gamma(\vec{k},\nu)^N \hbar\omega(\vec{k},\nu) v_z(\vec{k},\nu) k_z \bar{n}(\vec{k},\nu)\left[1+\bar{n}(\vec{k},\nu)\right]}{\Gamma(\vec{k},\nu)^U + \Gamma(\vec{k},\nu)^N} \right\}^2}{\sum\limits_{(\vec{k},\nu)} \frac{\Gamma(\vec{k},\nu)^U \Gamma(\vec{k},\nu)^N k_z k_z \bar{n}(\vec{k},\nu)\left[1+\bar{n}(\vec{k},\nu)\right]}{\Gamma(\vec{k},\nu)^U + \Gamma(\vec{k},\nu)^N}} \end{aligned} \tag{B.8}$$

Here, we still assume that thermal conductivity can be written in the similar form with that of single mode relaxation time approximation. Then we have

$$k_{zz} = \frac{1}{k_B T^2 NV} \sum_{(\mathbf{k},\nu)} \left(\hbar\omega(\vec{k},\nu)\right)^2 v_z(\vec{k},\nu) \Lambda_z^{effective}(\vec{k},\nu) \bar{n}(\vec{k},\nu) \left[1+\bar{n}(\vec{k},\nu)\right] \tag{B.9}$$

where $\Lambda_z^{effective}$ is the effective mean free path of phonon mode $(\vec{k},\nu)$. Comparing Eq. (B.8) and Eq. (B.10), we can know that

$$\Lambda_z^{effective}(\vec{k},\nu) = \frac{1}{\Gamma(\vec{k},\nu)^U + \Gamma(\vec{k},\nu)^N}\left\{ v_z(\vec{k},\nu) + \frac{k_z\Gamma(\vec{k},\nu)^N\left\{\sum_{(\vec{k}',\nu')}\frac{\Gamma(\vec{k}',\nu')^N\hbar\omega(\vec{k}',\nu')v_z(\vec{k}',\nu')k'_z\bar{n}(\vec{k}',\nu')\left[1+\bar{n}(\vec{k}',\nu')\right]}{\Gamma(\vec{k}',\nu')^U+\Gamma(\vec{k}',\nu')^N}\right\}}{\hbar\omega(\vec{k},\nu)\sum_{(\vec{k}',\nu')}\frac{\Gamma(\vec{k}',\nu')^U\Gamma(\vec{k}',\nu')^N k'_z k'_z\bar{n}(\vec{k}',\nu')\left[1+\bar{n}(\vec{k}',\nu')\right]}{\Gamma(\vec{k}',\nu')^U+\Gamma(\vec{k}',\nu')^N}} \right\} \tag{B.10}$$

Appendix C

Inherent Relaxation Time of Carriers

Here, to obtain the inherent electron relaxation time, we fit the experimental results rather than calculate it directly. It is easy to know the mobility of electrons in bulk Si (Irvin, 1962; Baccarani and Ostoja, 1975), then by applying

$$\langle \tau_{el} \rangle = \frac{\mu_0 m_b^*}{e} \tag{C.1}$$

in which, μ_0, $m_b^*$and e are the mobility, average band effective mass and elementary charge of electrons, respectively. From the experimental results of Figure C.1, we can easily find that it is quite suitable to regard the inherent electron relaxation time as a constant for the carrier density ($1 \times 10^{18} - 1 \times 10^{20}\ cm^{-3}$) considered in our thesis.

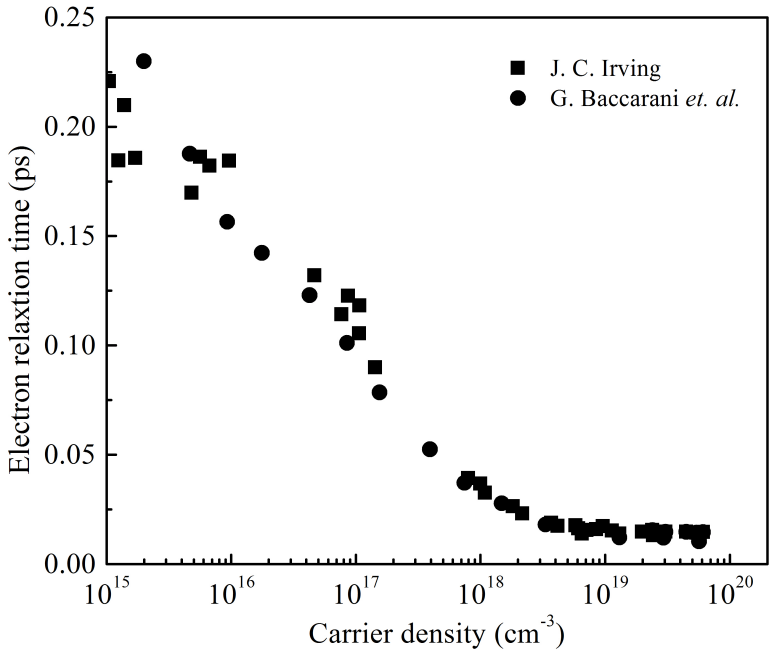


FIGURE C.1: Inherent relaxation time of electrons in bulk Si measured by experiments.

Appendix D

The Power Factor of the Bulk Superlattice Nanocrystalline Heterostructures

Figure D.1 shows the power factor (PF) of the bulk nanostructures with grain size of 3 nm. It is clearly shown that the PF will increase a little with respect to the nano membranes (Figure 5.8 in our main text).

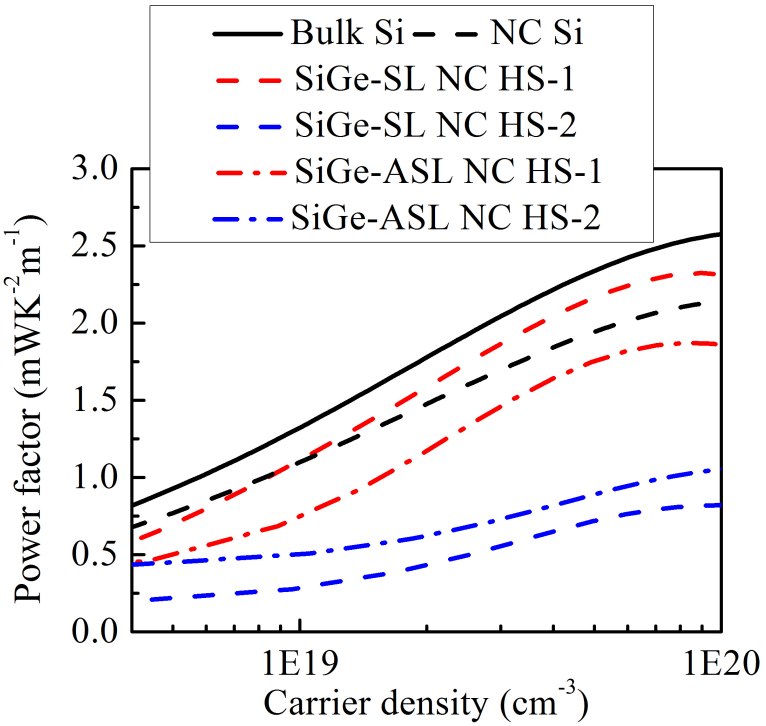


FIGURE D.1: The power factor of the bulk nanostructures with superlattice and anti-superlattice inside the grains.

Appendix E

The Calculation of Lorenz Number

The Wiedemann-Franz law shows the electrical thermal conductivity can be shown as

$$\kappa_e = L\sigma T \tag{E.1}$$

in which, σ and T are the electrical conductivity and temperature, respectively. L is the Lorenz number and can be obtained

$$L = \left(\frac{k_b}{e}\right)^2 \left[\frac{3F_2}{F_0} - \left(\frac{2F_1}{F_0}\right)^2\right] \tag{E.2}$$

With the reduced Fermi energy η, we have

$$F_i(\eta) = \int_0^\infty \frac{x^i}{e^{(x-\eta)}+1} dx \tag{E.3}$$

Appendix F

Curriculum Vitae

Personal Data

Name: Yanguang Zhou
Data of Birth: October 15th, 1987
Place of Birth: Hunan, China

Education

2007-2011 Mechanical design manufacturing and automation, China University of Geosciences (CUG), Beijing
2011-2014 Solid Mechanics, Beihang University (BUAA), Beijing
2014-2017 Computational Science Engineering, RWTH-Aachen University, Germany

Publications

1. **Y. G. Zhou**, X. L. Zhang and M. Hu, Nonmonotonic Diameter Dependence of Thermal Conductivity of Extremely Thin Si Nanowires: Competition between Hydrodynamic Phonon Flow and Boundary Scattering, Nano Letters, 17 (2017): 1269.
2. **Y. G. Zhou** and M. Hu, Record Low Thermal Conductivity of Polycrystalline Si Nanowire: Breaking the Casimir Limit by Severe Suppression of Propagons, Nano Letters, 16 (2016): 6178.
3. **Y. G. Zhou**, Y. G. Yao and M. Hu, Boundary Scattering Effect on Thermal Conductivity of Nanowires, Semiconductor Science and Technology, 31 (2016): 74004.
4.**Y. G. Zhou**, Y. L. Chen and M. Hu, Strong Surface Orientation Dependent Thermal Transport in Si Nanowires, Scientific Reports, 6 (2016): 24903.
5. **Y. G. Zhou**, X. L. Zhang and M. Hu, Excellent Candidate for Largely Reducing Interfacial Thermal Resistance: Confined Mass Graded Interface, Nanoscale, 8 (2016): 1994.
6. **Y. G. Zhou** and M. Hu, Quantitatively Analyzing Phonon Spectral Contribution of Thermal Conductivity Based on Non-equilibrium Molecular Dynamics Simulation II: From Time Fourier Transform, Physical Review B, 92 (2015): 195205.
7. **Y. G. Zhou**, X. L. Zhang and M. Hu, Quantitatively Analyzing Phonon Spectral Contribution of Thermal Conductivity Based on Non-equilibrium Molecular Dynamics Simulation I: From Space Fourier Transform, Physical Review B, 92 (2015): 195204.

8. **Y. G. Zhou**, W. W. Yang, M. Hu and Z. Y. Yang, The Typical Manners of Dynamic Crack Propagation Along the Metal/ceramics Interfaces: A Molecular Dynamics Study, Computational Materials Science, 112 (2016): 27.
9.**Y. G. Zhou**, Y. L. Chen, B. Liu, S. T. Wang, Z. Y. Yang, M. Hu, Mechanics of Nanoscale Wrinkling of Graphene on a Non-developable Spherical Surface, Carbon, 84 (2015): 263.
10. X. L. Zhang, X. J. Gong, **Y. G. Zhou** and M. Hu, Full Tailoring Thermal Conductivity of AlN Films by Periodically Aligned Surface Nano-grooves, Applied Physics Letters, 109 (2016): 133107.
11. **Y. G. Zhou** and M. Hu, Mechanical behaviors of nanocrystalline Cu/SiC nanocomposites: Atomistic investigation, Computational Materials Science, 129 (2017): 129.
12. **Y. G. Zhou** and M. Hu, Full Quantification of Three-phonon Scattering Process at Interface from Non-Equilibrium Molecular Dynamics Simulation, Physical Review B, 95 (2017): 115313.
13. **Y. G. Zhou**, X. J. Gong and M. Hu, Giant Enhancement of Thermoelectric Figure-of-merit in Nanostructured N-type Silicon-based superlattice, Journal of Applied Physics, 122 (2017):085105.
14. **Y. G. Zhou**, X. J. Gong, B. Xu and M. Hu, Decouple Electronic and Phononic Transport in Nanotwinned Structure: A New Strategy for Enhancing the Figure-of-merit of Thermoelectrics, Nanoscale, 28 (2017): 9987.
15. Y. Han, **Y. G. Zhou**, G. Z. Qin, J. M. Dong, D. S. Galvao and M. Hu, Anomalous Increase of the Lattice Thermal Conductivity of Auxetic Carbon Crystals under Tensile Strain, Carbon, 122 (2017): 374.
16. **Y. G. Zhou**, J. Y. Yang and M. Hu, Bi- or Tri-modal Phonon Scattering Induced Giant Reduction of Thermal Conductivity in PbTe Nanotwin Boundary, (submitted to Nano Letters).

Conferences and Workshops

1, **Y. G. Zhou**, Prediction of Giant Thermoelectric Effciency Induced by Nanotwin Structures, XingHai forum (2017), Dilian (China).
2, **Y. G. Zhou** and M. Hu, Giant Enhancement of Thermoelectric Figure-of-merit in Si-based Materials by Nanostructuring, European Materials Research Society (2017), Strasbourg (France).
3, **Y. G. Zhou** and M. Hu, Full Quantification of Three-phonon Scattering Process at Interface, Nanoscale and Microscale Heat Transfer V (2016), Santorini (Greece).
4, **Y. G. Zhou**, X. L. Zhang and M. Hu, Predicting Phonon Mode Contribution Based on Non-equilibrium Molecular Dynamics Simulation, International Mechanical Engineering Congress and Exposition (2015), Houston (United States).
5, **Y. G. Zhou** and M. Hu, Surface Orientation Dependent Thermal Transport in Thin Silicon Nanowires, Workshop on Thermal Nanosciences and Nanotechnology (2015), Pairs (France).

6, **Y. G. Zhou**, X. L. Zhang and M. Hu, Excellent Candidates for Enhancing and Reducing Interfacial Thermal Resistance: Rough and Mass Grading Interfaces, Workshop: Hot Nanostructures: Thermal Transport and Radiation at the Nanoscale (2015), Mainz (Germany).
7, **Y. G. Zhou** and M. Hu, Characterizing Frequency Dependent Thermal Conductivity Contribution Based on Non-equilibrium Molecular Dynamics Simulation, 3rd ECCOMAS Young Investigators Conference (2015), Aachen (Germany).

Bibliography

Aksamija, Z and I Knezevic (2010). "Anisotropy and boundary scattering in the lattice thermal conductivity of silicon nanomembranes". In: *Physical Review B* 82.4, p. 045319.

— (2011). "Lattice thermal conductivity of graphene nanoribbons: Anisotropy and edge roughness scattering". In: *Applied Physics Letters* 98.14, p. 141919.

Alerhand, OL et al. (1988). "Spontaneous formation of stress domains on crystal surfaces". In: *Physical Review Letters* 61.17, p. 1973.

Allen, Philip B and Joseph L Feldman (1993). "Thermal conductivity of disordered harmonic solids". In: *Physical Review B* 48.17, p. 12581.

Alvarez, FX and D Jou (2008). "Size and frequency dependence of effective thermal conductivity in nanosystems". In: *Journal of Applied Physics* 103.9, p. 094321.

Alvarez, FX, D Jou, and A Sellitto (2009). "Phonon hydrodynamics and phonon-boundary scattering in nanosystems". In: *Journal of Applied Physics* 105.1, p. 014317.

Amato, Michele and Riccardo Rurali (2015). "Shell-Thickness Controlled Semiconductor–Metal Transition in Si–SiC Core–Shell Nanowires". In: *Nano Letters* 15.5, pp. 3425–3430.

Ashcroft, NW and D Stroud (1978). "Theory of the thermodynamics of simple liquid metals". In: *Solid State Physics* 33, pp. 1–81.

Baccarani, G and P Ostoja (1975). "Electron mobility empirically related to the phosphorus concentration in silicon". In: *Solid-State Electronics* 18.6, pp. 579–580.

Bazant, Martin Z, Efthimios Kaxiras, and Joao F Justo (1997). "Environment-dependent interatomic potential for bulk silicon". In: *Physical Review B* 56.14, p. 8542.

Bera, Chandan et al. (2010). "Thermoelectric properties of nanostructured Si 1- x Ge x and potential for further improvement". In: *Journal of Applied Physics* 108.12, p. 124306.

Bergman, Theodore L et al. (2011). *Fundamentals of heat and mass transfer*. John Wiley & Sons.

Berman, R, FE Simon, and JM Ziman (1953). "The thermal conductivity of diamond at low temperatures". In: 220.1141, pp. 171–183.

Biswas, Kanishka et al. (2012). "High-performance bulk thermoelectrics with all-scale hierarchical architectures". In: *Nature* 489.7416, pp. 414–418.

Bodapati, Arun et al. (2006). "Vibrations and thermal transport in nanocrystalline silicon". In: *Physical Review B* 74.24, p. 245207.

Bolding, Barry C and Hans C Andersen (1990). "Interatomic potential for silicon clusters, crystals, and surfaces". In: *Physical Review B* 41.15, p. 10568.

Boukai, Akram I et al. (2008). "Silicon nanowires as efficient thermoelectric materials". In: *Nature* 451.7175, pp. 168–171.

Brenner, Donald W and Barbara J Garrison (1988). "Microscopic mechanisms of reactions associated with silicon MBE: A molecular dynamics investigation". In: *Surface Science* 198.1-2, pp. 151–166.

Broido, DA and TL Reinecke (1995). "Effect of superlattice structure on the thermoelectric figure of merit". In: *Physical Review B* 51.19, p. 13797.

— (2000). "Thermoelectric power factor in superlattice systems". In: *Applied Physics Letters* 77.5, pp. 705–707.

Cahill, David G et al. (2014). "Nanoscale thermal transport. II. 2003–2012". In: *Applied Physics Reviews* 1.1, p. 011305.

Callaway, Joseph (1959). "Model for lattice thermal conductivity at low temperatures". In: *Physical Review* 113.4, p. 1046.

Carrete, Jesús et al. (2011). "Surface roughness and thermal conductivity of semiconductor nanowires: Going below the Casimir limit". In: *Physical Review B* 84.7, p. 075403.

Cartoixa, Xavier, Luciano Colombo, and Riccardo Rurali (2015). "Thermal Rectification by Design in Telescopic Si Nanowires". In: *Nano Letters* 15.12, pp. 8255–8259.

Cartoixà, Xavier et al. (2016a). "Thermal transport in porous Si nanowires from approach-to-equilibrium molecular dynamics calculations". In: *Applied Physics Letters* 109.1, p. 013107.

— (2016b). "Thermal transport in porous Si nanowires from approach-to-equilibrium molecular dynamics calculations". In: *Applied Physics Letters* 109.1, p. 013107.

Casimir, HBG (1938). "Note on the Conduction of Heat in Crystals". In: *Physica* 5.6, pp. 495–500.

Cattaneo, C (1958). "A form of heat conduction equation which eliminates the paradox of instantaneous propagation". In: *Compte Rendus* 247.4, pp. 431–433.

Cepellotti, Andrea et al. (2015). "Phonon hydrodynamics in two-dimensional materials". In: *Nature Communications* 6, p. 6400.

Chadi, DJ (1979). "Atomic and electronic structures of reconstructed Si (100) surfaces". In: *Physical Review Letters* 43.1, p. 43.

Chalopin, Yann and Sebastian Volz (2013). "A microscopic formulation of the phonon transmission at the nanoscale". In: *Applied Physics Letters* 103.5, p. 051602.

Chalopin, Yann et al. (2012). "Thermal interface conductance in Si/Ge superlattices by equilibrium molecular dynamics". In: *Physical Review B* 85.19, p. 195302.

Chalopin, Yann et al. (2014). "Equilibrium molecular dynamics simulations on interfacial phonon transport". In: *Annual Review of Heat Transfer* 17, pp. 147–176.

Chen, Jie, Gang Zhang, and Baowen Li (2012). "Impacts of atomistic coating on thermal conductivity of germanium nanowires". In: *Nano letters* 12.6, pp. 2826–2832.

Chen, Renkun et al. (2008). "Thermal conductance of thin silicon nanowires". In: *Physical review letters* 101.10, p. 105501.

Chu, Steven and Arun Majumdar (2012). "Opportunities and challenges for a sustainable energy future". In: *Nature* 488.7411, pp. 294–303.

Conrad, D, K Scheerschmidt, and U Gösele (1996). "Molecular dynamics simulations of silicon wafer bonding". In: *Applied Physics A* 62.1, pp. 7–12.

Dammak, Hichem et al. (2009). "Quantum thermal bath for molecular dynamics simulation". In: *Physical Review Letters* 103.19, p. 190601.

De Tomas, C et al. (2015). "Enhancing of optic phonon contribution in hydrodynamic phonon transport". In: *Journal of Applied Physics* 118.13, p. 134305.

Debernardi, Alberto, Stefano Baroni, and Elisa Molinari (1995). "Anharmonic phonon lifetimes in semiconductors from density-functional perturbation theory". In: *Physical Review Letters* 75.9, p. 1819.

Deinzer, Gernot, Gerd Birner, and Dieter Strauch (2003). "Ab initio calculation of the linewidth of various phonon modes in germanium and silicon". In: *Physical Review B* 67.14, p. 144304.

DiSalvo, Francis J (1999). "Thermoelectric cooling and power generation". In: *Science* 285.5428, pp. 703–706.

Dobson, P et al. (2013). "S. Cecchi, T. Etzelstorfer, E. Müller, A. Samarelli, L. Ferre Llin, D. Chrastina, G. Isella, J. Stangl, JMR Weaver". In: *Journal of Electronical Material* 42, pp. 2030–2034.

Donadio, Davide and Giulia Galli (2009). "Atomistic simulations of heat transport in silicon nanowires". In: *Physical Review Letters* 102.19, p. 195901.

— (2010). "Temperature dependence of the thermal conductivity of thin silicon nanowires". In: *Nano Letters* 10.3, pp. 847–851.

Dong, Yuan, Bing-Yang Cao, and Zeng-Yuan Guo (2014). "Size dependent thermal conductivity of Si nanosystems based on phonon gas dynamics". In: *Physica E: Low-dimensional Systems and Nanostructures* 56, pp. 256–262.

Dove, Martin T (1993). *Introduction to lattice dynamics*. Vol. 4. Cambridge University Press.

Duda, John C et al. (2011). "Implications of cross-species interactions on the temperature dependence of Kapitza conductance". In: *Physical Review B* 84.19, p. 193301.

English, Timothy S et al. (2012). "Enhancing and tuning phonon transport at vibrationally mismatched solid-solid interfaces". In: *Physical review B* 85.3, p. 035438.

Evans, E and DL Mills (1972). "Theory of surface polarons". In: *Solid State Communications* 11.9, pp. 1093–1098.

Feng, Tianli and Xiulin Ruan (2014). "Prediction of spectral phonon mean free path and thermal conductivity with applications to thermoelectrics and thermal management: a review". In: *Journal of Nanomaterials* 2014.

Feser, Joseph P et al. (2013). "Ultralow thermal conductivity in polycrystalline CdSe thin films with controlled grain size". In: *Nano Letters* 13.5, pp. 2122–2127.

France-Lanord, Arthur et al. (2014). "Atomistic amorphous/crystalline interface modelling for superlattices and core/shell nanowires". In: *Journal of Physics: Condensed Matter* 26.5, p. 055011.

Fritzen, Felix, Thomas Böhlke, and Eckart Schnack (2008). "Periodic three-dimensional mesh-generation for Voronoi tessellations with application to cubic crystal aggregates". In: *PAMM* 8.1, pp. 10545–10546.

Fugallo, Giorgia et al. (2013). "Ab initio variational approach for evaluating lattice thermal conductivity". In: *Physical Review B* 88.4, p. 045430.

Garg, Jivtesh et al. (2011). "Role of disorder and anharmonicity in the thermal conductivity of silicon-germanium alloys: A first-principles study". In: *Physical Review Letters* 106.4, p. 045901.

Glassbrenner, CJ and Glen A Slack (1964). "Thermal conductivity of silicon and germanium from 3 K to the melting point". In: *Physical Review* 134.4A, A1058.

Goicochea, Javier V, Marcela Madrid, and Cristina Amon (2010). "Thermal properties for bulk silicon based on the determination of relaxation times using molecular dynamics". In: *Journal of Heat Transfer* 132.1, p. 012401.

Gordiz, Kiarash and Asegun Henry (2016). "Phonon transport at crystalline Si/Ge interfaces: the role of interfacial modes of vibration". In: *Scientific reports* 6, p. 23139.

Gu, Xiaokun, Xiaobo Li, and Ronggui Yang (2015). "Phonon transmission across Mg 2 Si/Mg 2 Si 1- x Sn x interfaces: A first-principles-based atomistic Green's function study". In: *Physical Review B* 91.20, p. 205313.

Guo, ZY et al. (2007). "State equation of phonon gas and conservation equations for phonon gas motion". In: *Acta Phys. Sin* 56, pp. 3306–3311.

Gupta, Rajeev et al. (2003). "Surface optical phonons in gallium phosphide nanowires". In: *Nano Letters* 3.12, pp. 1745–1750.

Haile, Sossina M (2014). "News and analysis on materials solutions to energy challenges". In: *MRS Bulletin* 39.03, pp. 213–213.

Hara, S et al. (2005). "Surface energy, stress and structure of well-relaxed amorphous silicon: A combination approach of ab initio and classical molecular dynamics". In: *Surface Science* 585.1, pp. 17–24.

He, Yuping, Davide Donadio, and Giulia Galli (2011). "Heat transport in amorphous silicon: Interplay between morphology and disorder". In: *Applied physics letters* 98.14, p. 144101.

He, Yuping and Giulia Galli (2012). "Microscopic origin of the reduced thermal conductivity of silicon nanowires". In: *Physical Review Letters* 108.21, p. 215901.

He, Yuping et al. (2011). "Thermal transport in nanoporous silicon: interplay between disorder at mesoscopic and atomic scales". In: *Acs Nano* 5.3, pp. 1839–1844.

Hellman, Olle, IA Abrikosov, and SI Simak (2011). "Lattice dynamics of anharmonic solids from first principles". In: *Physical Review B* 84.18, p. 180301.

Hellman, Olle et al. (2013). "Temperature dependent effective potential method for accurate free energy calculations of solids". In: *Physical Review B* 87.10, p. 104111.

Henry, Asegun S and Gang Chen (2008). "Spectral phonon transport properties of silicon based on molecular dynamics simulations and lattice dynamics". In: *Journal of Computational and Theoretical Nanoscience* 5.2, pp. 141–152.

Heremans, Joseph P et al. (2008). "Enhancement of thermoelectric efficiency in PbTe by distortion of the electronic density of states". In: *Science* 321.5888, pp. 554–557.

Herring, Conyers and Erich Vogt (1956). "Transport and deformation-potential theory for many-valley semiconductors with anisotropic scattering". In: *Physical Review* 101.3, p. 944.

Hicks, LD and MS Dresselhaus (1993a). "Effect of quantum-well structures on the thermoelectric figure of merit". In: *Physical Review B* 47.19, p. 12727.

— (1993b). "Thermoelectric figure of merit of a one-dimensional conductor". In: *Physical Review B* 47.24, p. 16631.

Hinsche, Nicki F, Ingrid Mertig, and Peter Zahn (2011). "Effect of strain on the thermoelectric properties of silicon: an ab initio study". In: *Journal of Physics: Condensed Matter* 23.29, p. 295502.

Hochbaum, Allon I et al. (2008). "Enhanced thermoelectric performance of rough silicon nanowires". In: *Nature* 451.7175, pp. 163–167.

Hohenberg, Pierre and Walter Kohn (1964). "Inhomogeneous electron gas". In: *Physical Review* 136.3B, B864.

Hohensee, Gregory T, RB Wilson, and David G Cahill (2015). "Thermal conductance of metal–diamond interfaces at high pressure". In: *Nature Communications* 6.

Holland, MG (1964). "Phonon scattering in semiconductors from thermal conductivity studies". In: *Physical Review* 134.2A, A471.

Holmes, Justin D et al. (2000). "Control of thickness and orientation of solution-grown silicon nanowires". In: *Science* 287.5457, pp. 1471–1473.

Hopkins, Patrick E et al. (2010). "Effects of surface roughness and oxide layer on the thermal boundary conductance at aluminum/silicon interfaces". In: *2010 14th International Heat Transfer Conference*. American Society of Mechanical Engineers, pp. 313–319.

Hopkins, Patrick E et al. (2011). "Controlling thermal conductance through quantum dot roughening at interfaces". In: *Physical Review B* 84.3, p. 035438.

Hsu, Kuei Fang et al. (2004a). "Cubic AgPbmSbTe2+ m: bulk thermoelectric materials with high figure of merit". In: *Science* 303.5659, pp. 818–821.

— (2004b). "Cubic AgPbmSbTe2+ m: bulk thermoelectric materials with high figure of merit". In: *Science* 303.5659, pp. 818–821.

Hu, Ming and Dimos Poulikakos (2012). "Si/Ge superlattice nanowires with ultralow thermal conductivity". In: *Nano Letters* 12.11, pp. 5487–5494.

Hua, Yu-Chao and Bing-Yang Cao (2016). "Ballistic-diffusive heat conduction in multiply-constrained nanostructures". In: *International Journal of Thermal Sciences* 101, pp. 126–132.

Huang, Quan et al. (2014). "Nanotwinned diamond with unprecedented hardness and stability". In: *Nature* 510.7504, pp. 250–253.

Imai, Shigeki and Masayuki Fujimoto (2006). "Formation of (111) nanotwin lamellae hillocks in polycrystalline silicon thin films caused by deposition of silicon dioxide layer". In: *Applied Physics Letters* 88.2, p. 021912.

Irvin, John C (1962). "Resistivity of bulk silicon and of diffused layers in silicon". In: *Bell Labs Technical Journal* 41.2, pp. 387–410.

Irving, JH and John G Kirkwood (1950). "The statistical mechanical theory of transport processes. IV. The equations of hydrodynamics". In: *The Journal of chemical physics* 18.6, pp. 817–829.

Ismail, K et al. (1993). "Electron transport properties of Si/SiGe heterostructures: Measurements and device implications". In: *Applied Physics Letters* 63.5, pp. 660–662.

Jain, Ankit and Alan JH McGaughey (2015). "Effect of exchange–correlation on first-principles-driven lattice thermal conductivity predictions of crystalline silicon". In: *Computational Materials Science* 110, pp. 115–120.

Jiang, Jin-Wu et al. (2013). "Modulation of thermal conductivity in kinked silicon nanowires: Phonon interchanging and pinching effects". In: *Nano Letters* 13.4, pp. 1670–1674.

Jonson, M and GD Mahan (1980). "Mott's formula for the thermopower and the Wiedemann-Franz law". In: *Physical Review B* 21.10, p. 4223.

Joshi, Giri et al. (2008). "Enhanced thermoelectric figure-of-merit in nanostructured p-type silicon germanium bulk alloys". In: *Nano Letters* 8.12, pp. 4670–4674.

Khadem, Masoud H and Aaron P Wemhoff (2013). "Comparison of Green–Kubo and NEMD heat flux formulations for thermal conductivity prediction using the Tersoff potential". In: *Computational Materials Science* 69, pp. 428–434.

Kim, Sang Il et al. (2015a). "Dense dislocation arrays embedded in grain boundaries for high-performance bulk thermoelectrics". In: *Science* 348.6230, pp. 109–114.

Kim, SJ et al. (2015b). "Thermoelectric properties of 50-nm-wide n-and p-type silicon nanowires". In: *Applied Physics A* 120.1, pp. 265–269.

Klemens, PG (1951). "The thermal conductivity of dielectric solids at low temperatures (theoretical)". In: 208.1092, pp. 108–133.

— (1955). "The scattering of low-frequency lattice waves by static imperfections". In: *Proceedings of the Physical Society. Section A* 68.12, p. 1113.

— (1958). "Thermal conductivity and lattice vibrational modes". In: *Solid state physics* 7, pp. 1–98.

Koga, T et al. (1999). "Carrier pocket engineering applied to "strained" Si/Ge superlattices to design useful thermoelectric materials". In: *Applied Physics Letters* 75.16, pp. 2438–2440.

Koga, T et al. (2000). "Experimental proof-of-principle investigation of enhanced Z 3D T in (001) oriented Si/Ge superlattices". In: *Applied Physics Letters* 77.10, pp. 1490–1492.

Kohn, Walter and Lu Jeu Sham (1965). "Self-consistent equations including exchange and correlation effects". In: *Physical Review* 140.4A, A1133.

Kresse, Georg and Jürgen Furthmüller (1996). "Efficient iterative schemes for ab initio total-energy calculations using a plane-wave basis set". In: *Physical Review B* 54.16, p. 11169.

Kubo, Rep (1966). "The fluctuation-dissipation theorem". In: *Reports on Progress in Physics* 29.1, p. 255.

Kubo, Ryogo (1957). "Statistical-mechanical theory of irreversible processes. I. General theory and simple applications to magnetic and conduction problems". In: *Journal of the Physical Society of Japan* 12.6, pp. 570–586.

Ladd, Anthony JC, Bill Moran, and William G Hoover (1986). "Lattice thermal conductivity: A comparison of molecular dynamics and anharmonic lattice dynamics". In: *Physical Review B* 34.8, p. 5058.

Lan, Yucheng et al. (2010). "Enhancement of thermoelectric figure-of-merit by a bulk nanostructuring approach". In: *Advanced Functional Materials* 20.3, pp. 357–376.

Landry, Eric S and Alan JH McGaughey (2010). "Effect of film thickness on the thermal resistance of confined semiconductor thin films". In: *Journal of Applied Physics* 107.1, p. 013521.

Larkin, Jason M and Alan JH McGaughey (2013). "Predicting alloy vibrational mode properties using lattice dynamics calculations, molecular dynamics simulations, and the virtual crystal approximation". In: *Journal of Applied Physics* 114.2, p. 023507.

— (2014). "Thermal conductivity accumulation in amorphous silica and amorphous silicon". In: *Physical Review B* 89.14, p. 144303.

Lee, Jinwoo, Jaeyun Kim, and Taeghwan Hyeon (2006). "Recent progress in the synthesis of porous carbon materials". In: *Advanced Materials* 18.16, pp. 2073–2094.

Lee, Sangyeop et al. (2015). "Hydrodynamic phonon transport in suspended graphene". In: *Nature Communications* 6, p. 6290.

Li, Deyu et al. (2003). "Thermal conductivity of individual silicon nanowires". In: *Applied Physics Letters* 83.14, pp. 2934–2936.

Li, Wu et al. (2014). "ShengBTE: A solver of the Boltzmann transport equation for phonons". In: *Computer Physics Communications* 185.6, pp. 1747–1758.

Li, Xiaobo and Ronggui Yang (2012). "Effect of lattice mismatch on phonon transmission and interface thermal conductance across dissimilar material interfaces". In: *Physical Review B* 86.5, p. 054305.

Lienhard, John H (2013). *A heat transfer textbook*. Courier Corporation.

Lim, Jongwoo et al. (2012). "Quantifying surface roughness effects on phonon transport in silicon nanowires". In: *Nano Letters* 12.5, pp. 2475–2482.

Lindsay, L and DA Broido (2008). "Three-phonon phase space and lattice thermal conductivity in semiconductors". In: *Journal of Physics: Condensed Matter* 20.16, p. 165209.

Liu, Sha et al. (2014). "Anomalous heat diffusion". In: *Physical Review Letters* 112.4, p. 040601.

Losego, Mark D et al. (2012). "Effects of chemical bonding on heat transport across interfaces". In: *Nature Materials* 11.6, pp. 502–506.

Luckyanova, Maria N et al. (2012). "Coherent phonon heat conduction in superlattices". In: *Science* 338.6109, pp. 936–939.

Luo, Tengfei and Gang Chen (2013). "Nanoscale heat transfer–from computation to experiment". In: *Physical Chemistry Chemical Physics* 15.10, pp. 3389–3412.

Ma, Jinlong, Wu Li, and Xiaobing Luo (2014). "Examining the Callaway model for lattice thermal conductivity". In: *Physical Review B* 90.3, p. 035203.

Madsen, Georg KH (2006). "Automated search for new thermoelectric materials: the case of LiZnSb". In: *Journal of the American Chemical Society* 128.37, pp. 12140–12146.

Madsen, Georg KH and David J Singh (2006). "BoltzTraP. A code for calculating band-structure dependent quantities". In: *Computer Physics Communications* 175.1, pp. 67–71.

Mangold, Claudia, Sanghamitra Neogi, and Davide Donadio (2016). "Optimal thickness of silicon membranes to achieve maximum thermoelectric efficiency: A first principles study". In: *Applied Physics Letters* 109.5, p. 053902.

Maradudin, AA and AE Fein (1962). "Scattering of neutrons by an anharmonic crystal". In: *Physical Review* 128.6, p. 2589.

Martin, Pierre N et al. (2010). "Reduced thermal conductivity in nanoengineered rough Ge and GaAs nanowires". In: *Nano Letters* 10.4, pp. 1120–1124.

McGaughey, AJH and M Kaviany (2004a). "Thermal conductivity decomposition and analysis using molecular dynamics simulations. Part I. Lennard-Jones argon". In: *International Journal of Heat and Mass Transfer* 47.8, pp. 1783–1798.

— (2004b). "Thermal conductivity decomposition and analysis using molecular dynamics simulations: Part II. Complex silica structures". In: *International Journal of Heat and Mass Transfer* 47.8, pp. 1799–1816.

McGaughey, Alan JH and Ankit Jain (2012). "Nanostructure thermal conductivity prediction by Monte Carlo sampling of phonon free paths". In: *Applied Physics Letters* 100.6, p. 061911.

McGaughey, Alan JH and Jason M Larkin (2014). "Predicting phonon properties from equilibrium molecular dynamics simulations". In: *Ann. Rev. Heat Transfer* 17, pp. 49–87.

Melis, Claudio and Luciano Colombo (2014). "Lattice thermal conductivity of Si 1- x Ge x nanocomposites". In: *Physical Review Letters* 112.6, p. 065901.

Mingo, N (2003). "Calculation of Si nanowire thermal conductivity using complete phonon dispersion relations". In: *Physical Review B* 68.11, p. 113308.

Mingo, Natalio et al. (2003). "Predicting the thermal conductivity of Si and Ge nanowires". In: *Nano Letters* 3.12, pp. 1713–1716.

Minnich, AJ et al. (2009a). "Modeling study of thermoelectric SiGe nanocomposites". In: *Physical Review B* 80.15, p. 155327.

Minnich, AJl et al. (2009b). "Bulk nanostructured thermoelectric materials: current research and future prospects". In: *Energy & Environmental Science* 2.5, pp. 466–479.

Mu, Xin et al. (2014). "Thermal transport in graphene oxide–from ballistic extreme to amorphous limit". In: *Scientific Reports* 4, p. 3909.

Nakamura, Yoshiaki et al. (2015). "Anomalous reduction of thermal conductivity in coherent nanocrystal architecture for silicon thermoelectric material". In: *Nano Energy* 12, pp. 845–851.

Neogi, Sanghamitra et al. (2015). "Tuning thermal transport in ultrathin silicon membranes by surface nanoscale engineering". In: *ACS nano* 9.4, pp. 3820–3828.

Omini, M and A Sparavigna (1995). "An iterative approach to the phonon Boltzmann equation in the theory of thermal conductivity". In: *Physica B: Condensed Matter* 212.2, pp. 101–112.

— (1996). "Beyond the isotropic-model approximation in the theory of thermal conductivity". In: *Physical Review B* 53.14, p. 9064.

Pan, Ying et al. (2016). "Surface Chemical Tuning of Phonon and Electron Transport in Free-Standing Silicon Nanowire Arrays". In: *Nano Letters* 16.10, pp. 6364–6370.

Pei, Yanzhong, Heng Wang, and GJ Snyder (2012). "Band engineering of thermoelectric materials". In: *Advanced Materials* 24.46, pp. 6125–6135.

Pei, Yanzhong et al. (2011a). "Convergence of electronic bands for high performance bulk thermoelectrics". In: *Nature* 473.7345, pp. 66–69.

Pei, Yanzhong et al. (2011b). "Stabilizing the optimal carrier concentration for high thermoelectric efficiency". In: *Advanced Materials* 23.47, pp. 5674–5678.

Pei, Yanzhong et al. (2012). "Low effective mass leading to high thermoelectric performance". In: *Energy & Environmental Science* 5.7, pp. 7963–7969.

Peierls, Rudolf Ernst (1955). *Quantum theory of solids*. 23. Oxford University Press.

People, R et al. (1984). "Modulation doping in Ge x Si1- x/Si strained layer heterostructures". In: *Applied Physics Letters* 45.11, pp. 1231–1233.

Perdew, John P (1986). "Density functional theory and the band gap problem". In: *International Journal of Quantum Chemistry* 30.3, pp. 451–451.

Plimpton, Steve (1995). "Fast parallel algorithms for short-range molecular dynamics". In: *Journal of computational physics* 117.1, pp. 1–19.

Ponomareva, Inna, Deepak Srivastava, and Madhu Menon (2007). "Thermal conductivity in thin silicon nanowires: phonon confinement effect". In: *Nano Letters* 7.5, pp. 1155–1159.

Poudel, Bed et al. (2008a). "High-thermoelectric performance of nanostructured bismuth antimony telluride bulk alloys". In: *Science* 320.5876, pp. 634–638.

— (2008b). "High-thermoelectric performance of nanostructured bismuth antimony telluride bulk alloys". In: *Science* 320.5876, pp. 634–638.

Qiu, Bo et al. (2012). "Molecular dynamics simulations of lattice thermal conductivity and spectral phonon mean free path of PbTe: Bulk and nanostructures". In: *Computational Materials Science* 53.1, pp. 278–285.

Ramayya, EB et al. (2012). "Thermoelectric properties of ultrathin silicon nanowires". In: *Physical Review B* 86.11, p. 115328.

Romero, AH et al. (2015). "Thermal conductivity in PbTe from first principles". In: *Physical Review B* 91.21, p. 214310.

Sääskilahti, K et al. (2014). "Role of anharmonic phonon scattering in the spectrally decomposed thermal conductance at planar interfaces". In: *Physical Review B* 90.13, p. 134312.

Sääskilahti, K et al. (2015). "Frequency-dependent phonon mean free path in carbon nanotubes from nonequilibrium molecular dynamics". In: *Physical Review B* 91.11, p. 115426.

Sansoz, Frederic (2011). "Surface faceting dependence of thermal transport in silicon nanowires". In: *Nano Letters* 11.12, pp. 5378–5382.

Schelling, Patrick K, Simon R Phillpot, and Pawel Keblinski (2002a). "Comparison of atomic-level simulation methods for computing thermal conductivity". In: *Physical Review B* 65.14, p. 144306.

Schelling, PK and SR Phillpot (2003a). "Multiscale simulation of phonon transport in superlattices". In: *Journal of Applied Physics* 93.9, pp. 5377–5387.

— (2003b). "Multiscale simulation of phonon transport in superlattices". In: *Journal of Applied Physics* 93.9, pp. 5377–5387.

Schelling, PK, SR Phillpot, and P Keblinski (2002b). "Phonon wave-packet dynamics at semiconductor interfaces by molecular-dynamics simulation". In: *Applied Physics Letters* 80.14, pp. 2484–2486.

Schrödinger, Erwin (1926). "An undulatory theory of the mechanics of atoms and molecules". In: *Physical Review* 28.6, p. 1049.

Schuberth, G et al. (1991). "High electron mobility in modulation-doped Si/SiGe quantum well structures". In: *Applied Physics Letters* 59.25, pp. 3318–3320.

Sellan, Daniel P et al. (2010a). "Cross-plane phonon transport in thin films". In: *Journal of Applied Physics* 108.11, p. 113524.

Sellan, Daniel P et al. (2010b). "Size effects in molecular dynamics thermal conductivity predictions". In: *Physical Review B* 81.21, p. 214305.

Shi, Lihong et al. (2009). "Size dependent thermoelectric properties of silicon nanowires". In: *Applied Physics Letters* 95.6, p. 063102.

Singh, N et al. (2006). "High-performance fully depleted silicon nanowire (diameter/spl les/5 nm) gate-all-around CMOS devices". In: *IEEE Electron Device Letters* 27.5, pp. 383–386.

Sinha, S et al. (2005). "Scattering of g-process longitudinal optical phonons at hotspots in silicon". In: *Journal of Applied Physics* 97.2, p. 023702.

Snyder, G Jeffrey and Eric S Toberer (2008a). "Complex thermoelectric materials". In: *Nature Materials* 7.2, pp. 105–114.

— (2008b). "Complex thermoelectric materials". In: *Nature Materials* 7.2, pp. 105–114.

Son, Jae Sung et al. (2012). "n-Type nanostructured thermoelectric materials prepared from chemically synthesized ultrathin Bi2Te3 nanoplates". In: *Nano Letters* 12.2, pp. 640–647.

Soni, Ajay et al. (2012). "Enhanced Thermoelectric Properties of Solution Grown Bi2Te3–x Se x Nanoplatelet Composites". In: *Nano Letters* 12.3, pp. 1203–1209.

Sosso, Gabriele C et al. (2012). "Thermal transport in phase-change materials from atomistic simulations". In: *Physical Review B* 86.10, p. 104301.

Srivastava, Gyaneshwar P (1990). *The physics of phonons*. CRC press.

Stillinger, Frank H and Thomas A Weber (1985). "Computer simulation of local order in condensed phases of silicon". In: *Physical Review B* 31.8, p. 5262.

Stoffers, Andreas et al. (2015). "Complex Nanotwin Substructure of an Asymmetric Σ 9 Tilt Grain Boundary in a Silicon Polycrystal". In: *Physical Review Letters* 115.23, p. 235502.

Sumiya, H and T Irifune (2007). "Hardness and deformation microstructures of nano-polycrystalline diamonds synthesized from various carbons under high pressure and high temperature". In: *Journal of Materials Research* 22.08, pp. 2345–2351.

Swartz, Eric T and Robert O Pohl (1989). "Thermal boundary resistance". In: *Reviews of Modern Physics* 61.3, p. 605.

Tersoff, J (1989). "Modeling solid-state chemistry: Interatomic potentials for multicomponent systems". In: *Physical Review B* 39.8, p. 5566.

Tian, Zhiting, Keivan Esfarjani, and Gang Chen (2012). "Enhancing phonon transmission across a Si/Ge interface by atomic roughness: First-principles study with the Green's function method". In: *Physical Review B* 86.23, p. 235304.

Togo, Atsushi, Fumiyasu Oba, and Isao Tanaka (2008). "First-principles calculations of the ferroelastic transition between rutile-type and CaCl 2-type SiO 2 at high pressures". In: *Physical Review B* 78.13, p. 134106.

Torii, Daichi, Takeo Nakano, and Taku Ohara (2008). "Contribution of inter-and intramolecular energy transfers to heat conduction in liquids". In: *The Journal of Chemical Physics* 128.4, p. 044504.

Tritt, Terry (2000). *Recent Trends in Thermoelectric Materials Research, Part Two*. Vol. 70. Academic Press.

Tritt, Terry M, Harald Böttner, and Lidong Chen (2008). "Thermoelectrics: Direct solar thermal energy conversion". In: *MRS bulletin* 33.04, pp. 366–368.

Turney, JE, AJH McGaughey, and CH Amon (2009). "Assessing the applicability of quantum corrections to classical thermal conductivity predictions". In: *Physical Review B* 79.22, p. 224305.

Turney, JE et al. (2009). "Predicting phonon properties and thermal conductivity from anharmonic lattice dynamics calculations and molecular dynamics simulations". In: *Physical Review B* 79.6, p. 064301.

Turney, Joseph E, Alan JH McGaughey, and Cristina H Amon (2010). "In-plane phonon transport in thin films". In: *Journal of Applied Physics* 107.2, p. 024317.

Valalaki, K, N Vouroutzis, and AG Nassiopoulou (2016). "Significant enhancement of the thermoelectric figure of merit of polycrystalline Si films by reducing grain size". In: *Journal of Physics D: Applied Physics* 49.31, p. 315104.

Venkatasubramanian, Rama et al. (2001). "Thin-film thermoelectric devices with high room-temperature figures of merit". In: *Nature* 413.6856, pp. 597–602.

Verlet, Loup (1967). “Computer" experiments" on classical fluids. I. Thermodynamical properties of Lennard-Jones molecules”. In: *Physical Review* 159.1, p. 98.

Vernotte, P (1958). “Paradoxes in the continuous theory of the heat equation”. In: *CR Acad. Sci* 246.3, pp. 154–3.

Vineis, Christopher J et al. (2010). “Nanostructured thermoelectrics: big efficiency gains from small features”. In: *Advanced Materials* 22.36, pp. 3970–3980.

Vo, Trinh TM et al. (2008). “Atomistic design of thermoelectric properties of silicon nanowires”. In: *Nano Letters* 8.4, pp. 1111–1114.

Volz, Sebastian G and Gang Chen (1999). “Molecular dynamics simulation of thermal conductivity of silicon nanowires”. In: *Applied Physics Letters* 75.14, pp. 2056–2058.

— (2000). “Molecular-dynamics simulation of thermal conductivity of silicon crystals”. In: *Physical Review B* 61.4, p. 2651.

Wang, Chao et al. (2008a). “Ultrathin Au nanowires and their transport properties”. In: *Journal of the American Chemical Society* 130.28, pp. 8902–8903.

Wang, CZ, CT Chan, and KM Ho (1990). “Tight-binding molecular-dynamics study of phonon anharmonic effects in silicon and diamond”. In: *Physical Review B* 42.17, p. 11276.

Wang, Heng et al. (2012). “Weak electron–phonon coupling contributing to high thermoelectric performance in n-type PbSe”. In: *Proceedings of the National Academy of Sciences* 109.25, pp. 9705–9709.

Wang, Shuai-chuang et al. (2009). “Thermal conductivity of silicon nanowire by nonequilibrium molecular dynamics simulations”. In: *Journal of Applied Physics* 105.1, p. 014316.

Wang, XW et al. (2008b). “Enhanced thermoelectric figure of merit in nanostructured n-type silicon germanium bulk alloy”. In: *Applied Physics Letters* 93.19, p. 193121.

Wang, YQ, R Smirani, and GG Ross (2004). “Nanotwinning in silicon nanocrystals produced by ion implantation”. In: *Nano Letters* 4.10, pp. 2041–2045.

Ward, A and DA Broido (2010). “Intrinsic phonon relaxation times from first-principles studies of the thermal conductivities of Si and Ge”. In: *Physical Review B* 81.8, p. 085205.

Ward, Alistair et al. (2009). “Ab initio theory of the lattice thermal conductivity in diamond”. In: *Physical Review B* 80.12, p. 125203.

Wingert, Matthew C et al. (2015). “Sub-amorphous thermal conductivity in ultrathin crystalline silicon nanotubes”. In: *Nano Letters* 15.4, pp. 2605–2611.

Wu, CL et al. (1994). “Mobility enhancement in double δ-doped GaAs/In x Ga1- x As/GaAs pseudomorphic structures by grading the heterointerfaces”. In: *Applied physics letters* 64.22, pp. 3027–3029.

Wu, Xuanzhi (2004). “High-efficiency polycrystalline CdTe thin-film solar cells”. In: *Solar energy* 77.6, pp. 803–814.

Wu, Yue et al. (2004a). “Controlled growth and structures of molecular-scale silicon nanowires”. In: *Nano letters* 4.3, pp. 433–436.

— (2004b). "Controlled growth and structures of molecular-scale silicon nanowires". In: *Nano letters* 4.3, pp. 433–436.

Yan, Hong, Xiao Hu, and Hannes Jónsson (1994). "Atomic structure of β-SiC (100) surfaces: a study using the Tersoff potential". In: *Surface Science* 316.1-2, pp. 181–188.

Yang, Ho-Soon et al. (2002). "Interfacial thermal resistance in nanocrystalline yttria-stabilized zirconia". In: *Acta Materialia* 50.9, pp. 2309–2317.

Yang, Lina, Nuo Yang, and Baowen Li (2014). "Extreme low thermal conductivity in nanoscale 3D Si phononic crystal with spherical pores". In: *Nano Letters* 14.4, pp. 1734–1738.

Yang, Nuo, Gang Zhang, and Baowen Li (2008). "Ultralow thermal conductivity of isotope-doped silicon nanowires". In: *Nano Letters* 8.1, pp. 276–280.

— (2010). "Violation of Fourier's law and anomalous heat diffusion in silicon nanowires". In: *Nano Today* 5.2, pp. 85–90.

Yang, Zhenyu, Zixing Lu, and Ya-Pu Zhao (2009). "Shape effects on the yield stress and deformation of silicon nanowires: A molecular dynamics simulation". In: *Journal of Applied Physics* 106.2, p. 023537.

Yang, Zhenyu et al. (2014). "Crack propagation behaviors at Cu/SiC interface by molecular dynamics simulation". In: *Computational Materials Science* 82, pp. 17–25.

Yao, Donglai, Gang Zhang, and Baowen Li (2008). "A universal expression of band gap for silicon nanowires of different cross-section geometries". In: *Nano Letters* 8.12, pp. 4557–4561.

Yasaei, Poya et al. (2015). "Bimodal phonon scattering in graphene grain boundaries". In: *Nano Letters* 15.7, pp. 4532–4540.

Yu, Bo et al. (2012). "Enhancement of thermoelectric properties by modulation-doping in silicon germanium alloy nanocomposites". In: *Nano Letters* 12.4, pp. 2077–2082.

Yu, Yi et al. (2016). "Atomic structure of ultrathin gold nanowires". In: *Nano Letters* 16.5, pp. 3078–3084.

Zaoui, Hayat et al. (2016). "Length dependence of thermal conductivity by approach-to-equilibrium molecular dynamics". In: *Physical Review B* 94.5, p. 054304.

Zebarjadi, Mona et al. (2011). "Power factor enhancement by modulation doping in bulk nanocomposites". In: *Nano letters* 11.6, pp. 2225–2230.

Zhang, Xiao and Li-Dong Zhao (2015). "Thermoelectric materials: energy conversion between heat and electricity". In: *Journal of Materiomics* 1.2, pp. 92–105.

Zhang, Xiaoliang et al. (2014). "Thermal conductivity of silicene calculated using an optimized Stillinger-Weber potential". In: *Physical Review B* 89.5, p. 054310.

Zhao, Li-Dong et al. (2009). "Effect of mixed grain sizes on thermoelectric performance of Bi 2 Te 3 compound". In: *Journal of Applied Physics* 105.2, p. 023704.

Zheng, XF et al. (2014). "A review of thermoelectrics research–Recent developments and potentials for sustainable and renewable energy applications". In: *Renewable and Sustainable Energy Reviews* 32, pp. 486–503.

Zhou, Chen et al. (2012). "Grain size effects in polycrystalline gold nanoparticles". In: *Nanoscale* 4.14, pp. 4228–4233.

Zhou, Jun et al. (2010). "Semiclassical model for thermoelectric transport in nanocomposites". In: *Physical Review B* 82.11, p. 115308.

Zhou, Yanguang, Yuli Chen, and Ming Hu (2016). "Strong surface orientation dependent thermal transport in Si nanowires". In: *Scientific Reports* 6, p. 24903.

Zhou, Yanguang and Ming Hu (2015). "Quantitatively analyzing phonon spectral contribution of thermal conductivity based on nonequilibrium molecular dynamics simulations. II. from time Fourier transform". In: *Physical Review B* 92.19, p. 195205.

— (2016). "Record Low Thermal Conductivity of Polycrystalline Si Nanowire: Breaking the Casimir Limit by Severe Suppression of Propagons". In: *Nano Letters* 16.10, pp. 6178–6187.

Zhou, Yanguang, Zhenyu Yang, and Zixing Lu (2014). "Dynamic crack propagation in copper bicrystals grain boundary by atomistic simulation". In: *Materials Science and Engineering: A* 599, pp. 116–124.

Zhou, Yanguang, Yagang Yao, and Ming Hu (2016). "Boundary scattering effect on the thermal conductivity of nanowires". In: *Semiconductor Science and Technology* 31.7, p. 074004.

Zhou, Yanguang, Xiaoliang Zhang, and Ming Hu (2015). "Quantitatively analyzing phonon spectral contribution of thermal conductivity based on nonequilibrium molecular dynamics simulations. I. from space Fourier transform". In: *Physical Review B* 92.19, p. 195204.

— (2017). "Nonmonotonic Diameter Dependence of Thermal Conductivity of Extremely Thin Si Nanowires: Competition between Hydrodynamic Phonon Flow and Boundary Scattering". In: *Nano Letters* 17.2, pp. 1269–1276.

Zhou, Yanguang et al. (2016). "The typical manners of dynamic crack propagation along the metal/ceramics interfaces: A molecular dynamics study". In: *Computational Materials Science* 112, pp. 27–33.

Ziman, John M (1960). *Electrons and phonons: the theory of transport phenomena in solids*. Oxford university press.

Zou, Jie and Alexander Balandin (2001). "Phonon heat conduction in a semiconductor nanowire". In: *Journal of Applied Physics* 89.5, pp. 2932–2938.